

1 **Fetal monitoring for high-risk pregnancies using a wearable ultrasound patch**

2

3 Geonho Park^{1,2,12}, Yizhou Bian^{1,12}, Hao Huang^{1,12}, Sai Zhou^{3,12}, Siyu Qin⁴, Muyang Lin¹, Xinyi
4 Yang³, Aaron Lee⁵, Anand Ramkumar⁶, Mariana Tome⁶, Jayne Lander⁶, Xiangjun Chen³,
5 Shenghan Wang¹, Pranavi Bheemreddy⁴, Liam Stanton¹, Ren Sheng⁷, Guihuan Guo¹, Mabel
6 Shehada⁵, Ruotao Wang¹, Alexa Roa⁵, Chengchangfeng Lu⁴, Wentong Yue¹, Ray S. Wu¹,
7 Xiaoxiang Gao¹, Hongjie Hu¹, Amer Yaghi¹, Mark Liu⁸, Lawrence Impey⁶, Sally L. Collins⁶,
8 Aris T Papageorgiou⁶, Louise C. Laurent⁹, Keith A. Wear¹⁰, Antoniya Georgieva^{6#}, Sheng
9 Xu^{1,2,3,4,11#}

10

11 ¹Aiiso Yufeng Li Family Department of Chemical and Nano Engineering, University of
12 California San Diego, La Jolla, CA 92093, USA.

13 ²Department of Anesthesiology, Perioperative and Pain Medicine, Stanford University, Stanford,
14 CA 94304, USA.

15 ³Materials Science and Engineering Program, University of California San Diego, La Jolla, CA
16 92093, USA.

17 ⁴Department of Electrical and Computer Engineering, University of California San Diego, La
18 Jolla, CA 92093, USA.

19 ⁵Shu Chien–Gene Lay Department of Bioengineering, University of California San Diego, La
20 Jolla, CA 92093, USA.

21 ⁶Nuffield Department of Women’s and Reproductive Health, University of Oxford, Oxford OX3
22 9DU, UK.

23 ⁷Department of Computer Science and Engineering, University of California San Diego, La
24 Jolla, CA 92093, USA.

25 ⁸Qualcomm Institute Makerspace, University of California San Diego, La Jolla, CA 92093,
26 USA.

27 ⁹Department of Obstetrics, Gynecology, and Reproductive Sciences, University of California
28 San Diego, La Jolla, CA 92093, USA.

29 ¹⁰Independent Researcher, Rockville, MD 20852, USA.

30 ¹¹Department of Radiology, University of California San Diego, La Jolla, CA 92093, USA.

31 ¹²These authors contributed equally to this work: Geonho Park, Yizhou Bian, Hao Huang, Sai
32 Zhou.

33 #e-mail: shengxu@stanford.edu, antoniya.georgieva@wrh.ox.ac.uk

34 **Ultrasonography is a cornerstone of fetal monitoring, but it requires specialized**
35 **sonographers and is limited to providing snapshot evaluations at discrete intervals. Here**
36 **we report a wearable ultrasound patch (UPatch) for continuous and autonomous fetal**
37 **monitoring. The UPatch can acquire anatomical structures and blood flow velocities,**
38 **demonstrating high agreement with a handheld clinical ultrasound device on 62**
39 **pregnancies. Real-time image segmentation allows autonomous tracking of target vessels**
40 **and thus the acquisition of continuous blood flow spectra during fetal and maternal**
41 **movements without a sonographer. Continuous monitoring data for 1–3 h from 52**
42 **pregnant women aligned with stratified perinatal conditions, including healthy, small for**
43 **gestational age, large for gestational age, gestational diabetes, pre-eclampsia, and**
44 **gestational hypertension. Additionally, integration with a miniaturized circuit could enable**
45 **fully wireless operation and greater patient mobility. The UPatch could provide evidence of**
46 **fetal complications in high-risk pregnancies, expanding prenatal-care capabilities.**

47

48 The physiological maturation of the fetus in the uterus is supported by cardiovascular
49 exchanges between the maternal, placental, and fetal circulations¹. Any disruption of this delicate
50 exchange system can precipitate fetal complications, such as hypoxia², intrauterine growth
51 restriction³, and cerebral palsy⁴, with stillbirth⁵ being the most extreme outcome. Despite
52 decades of research, many such fetal complications remain undiagnosed and unexplained, with
53 existing methods relying mostly on postmortem investigations^{6,7}. Continuous monitoring of fetal
54 anatomy and hemodynamics throughout pregnancy not only provides insights into the
55 pathophysiological mechanisms of fetal complications but also allows the early detection and

56 mitigation of emerging issues, helping to prevent adverse outcomes (Supplementary Discussion
57 1)^{8,9}.

58 Continuous fetal monitoring currently relies predominantly on cardiotocography, which
59 measures the fetal heart rate and uterine contractions (Supplementary Fig. 1 and Supplementary
60 Discussion 2)^{10,11}. However, given the complexity of fetal physiology, these measurements do
61 not correlate well with fetal health and yield false positive rates up to 50% (Supplementary
62 Discussion 3)¹²⁻¹⁵. Other continuous monitoring devices based on electrocardiography¹⁶, pulse
63 oximetry¹⁷, or accelerometry¹⁸ cannot reliably differentiate fetal from maternal signals and are
64 not commonly used in clinical practice. Ultrasonography is widely used to measure fetal
65 biometry and blood flow (Supplementary Discussion 4)¹⁹⁻²¹, and standardized reference indices
66 have been established throughout gestation to evaluate fetal health (Supplementary Discussion
67 5)²²⁻²⁵. However, conventional ultrasonography is heavily dependent on the skills of the operator,
68 and measurements are limited to snapshots that can fail to capture the patterns and critical
69 moments of fetal hemodynamics^{26,27}. Although wearable ultrasound devices have been
70 developed for continuous monitoring of physiological signals²⁸⁻³¹, they are unsuitable for fetal
71 monitoring due to weak blood flow signals from deep fetal vessels and signal loss during large
72 fetal movements.

73 Here we report a wearable ultrasound patch (UPatch) that can continuously image the
74 fetus and autonomously measure fetal blood flow in real time (Supplementary Discussion 6). To
75 enhance the signal-to-noise ratio and imaging resolution, we integrated transducers fabricated by
76 super multipass dicing, as well as an acoustic lens and a soft Faraday cage (Extended Data Fig.
77 1). To identify and track moving targets, we used segmentation-based algorithms to place sample
78 gates in vessel images. Blood flow spectra can be acquired continuously and autonomously in

79 real time, even during large fetal movements. We conducted a prospective study with 62
80 pregnant participants to validate the accuracy of the UPatch using a handheld clinical ultrasound
81 device. Furthermore, we used the UPatch to continuously monitor the umbilical cord blood flow
82 in 52 participants, generating longitudinal measurements that distinguished transient fluctuations
83 from sustained compromise. We found that Doppler indices exhibited monotonic relationship
84 with gestational age and differentiated high-risk from healthy pregnancies. In a pre-eclamptic
85 case, the UPatch revealed the severity of intrauterine growth restriction, leading to Cesarean
86 delivery to prevent stillbirth.

87

88 **Design of the UPatch**

89 Fetal structures and vessels vary in size and are distributed over a wide range of depths in
90 the uterus (Fig. 1a, left)³². Brightness-mode imaging is based on echoes from tissue interfaces
91 and distributed scattering within tissues³³. On the other hand, color Doppler imaging and spectral
92 Doppler waveforms of blood flow are based on the much weaker echoes from red blood
93 cells^{33,34}.

94 We adopted three strategies to strengthen the echoes from red blood cells in deep fetal
95 vessels. First, the UPatch contains a 2.5-MHz PZT-5H 1–3 composite with a conductive epoxy
96 backing layer at a pitch of 0.65 ultrasound wavelength (Fig. 1a, right). We used super multipass
97 dicing, which reduced the kerf and thus increased the element width by 58% (Fig. 1b, Methods,
98 Supplementary Figs 2 and 3, and Supplementary Discussion 7). This improved the signal-to-
99 noise ratio by 7.2 dB without increasing the crosstalk between adjacent elements (Supplementary
100 Fig. 4). Second, we designed an acoustic lens to improve elevational focusing, which reduced the
101 focal beamwidth by 25% and thus enhanced the spatial resolution and color Doppler signal

102 sensitivity (Fig. 1c, Methods, Supplementary Figs 5–8, and Supplementary Discussion 8)³⁵.
103 Additionally, the acoustic lens moved the beam elevational focal depth from 14 to 10 cm, on par
104 with clinical devices, to balance the spatial resolution throughout the entire uterus (Fig. 1c and
105 Supplementary Fig. 7). Third, we developed a soft Faraday cage by connecting the
106 electromagnetic shielding layer to the mesh ground electrode layer using vertical interconnect
107 accesses (Methods, Supplementary Figs 9 and 10, and Supplementary Discussion 9). The cage
108 fully encapsulated the elements and reduced the electromagnetic interference by 11.7 dB/Hz
109 (Fig. 1d and Supplementary Figs 11–13)³⁶. Additionally, we used two signal electrode layers that
110 can individually address each element with a minimal electrode footprint (Supplementary Fig. 9).
111 The UPatch was mechanically compliant (Fig. 1e) and showed negligible constraints on the
112 movement of pregnant participants in various positions (Supplementary Fig. 14).

113 To quantify the UPatch performance, we characterized its brightness, color Doppler, and
114 spectral Doppler modes following the Institute of Physics and Engineering in Medicine protocols
115 (Methods)³⁷. On a phantom filled with monofilament wires and tissue-mimicking contrast
116 targets, the axial and lateral resolutions, dynamic range, and contrast-to-noise ratio of the UPatch
117 in brightness mode were comparable to those of a handheld clinical ultrasound device
118 (Supplementary Fig. 15)³⁸. On a flow phantom with blood-mimicking fluids, the color Doppler
119 sensitivity and the spectral Doppler accuracy of the UPatch at different depths and velocities
120 were similar to those of the clinical device (Supplementary Figs 16 and 17)³⁹. On a customized
121 umbilical cord flow phantom, the UPatch reliably acquired flow signals regardless of phantom
122 orientation (Extended Data Fig. 2, Supplementary Figs 18 and 19, and Supplementary
123 Discussion 10). On a healthy adult participant, all three modes of the UPatch and the clinical
124 device were comparable in quality (Supplementary Figs 20 and 21).

125

126 **Acoustic safety characterizations**

127 Minimal acoustic intensity is necessary for the fetus to avoid potential side effects
128 associated with ultrasound exposure⁴⁰. We examined the biological effects of the UPatch in vitro
129 in all three modes following the guidelines from the American Institute of Ultrasound in
130 Medicine (AIUM)⁴¹, British Medical Ultrasound Society (BMUS)⁴², and Food and Drug
131 Administration (FDA)⁴³ (Methods and Supplementary Discussion 11). The maximum spatial
132 average temporal average intensity was 0.72 mW/cm² (< 20 mW/cm² is recommended by the
133 FDA⁴³, and 5 mW/cm² is the value reported for the GE Corometrics 250CX⁴⁴). Furthermore, the
134 maximum derated spatial peak pulse average intensity was 16.42 W/cm² (< 190 W/cm² is
135 recommended by the FDA⁴³), the maximum derated spatial peak temporal average intensity was
136 58.5 mW/cm² (< 94 mW/cm² is recommended by the FDA⁴³), and the mechanical index was 0.20
137 for duplex (combined brightness and color Doppler) imaging and 0.38 for spectral Doppler (<
138 1.9 is recommended by the FDA⁴³ and ≤ 0.7 is recommended by the BMUS⁴²) (Fig. 1f and
139 Supplementary Discussion 12).

140 We also evaluated the thermal characteristics of the UPatch^{45,46}. Surface temperatures
141 were tested using a thermocouple on a phantom and in air (Methods). In both experiments, the
142 temperature increase was < 0.7 °C during 48 h of continuous UPatch activation (Supplementary
143 Fig. 22). To calculate the thermal index, acoustic power was measured and cross-checked using a
144 hydrophone and radiation force balance (Methods, Supplementary Figs 23 and 24)⁴⁶. The soft
145 tissue thermal index, bone thermal index, and cranium thermal index were 0.02, 0.05, and 0.05
146 for duplex imaging, and 0.1, 0.38, and 0.17 for spectral Doppler, respectively (Fig. 1f). All

147 results were well below the maximum level of 0.7 recommended by the AIUM and BMUS for
148 continuous monitoring^{41,42}.

149

150 **Fetal monitoring and validation**

151 Duplex imaging can reveal fetal anatomical abnormalities, quantify fetal biometry, and
152 facilitate the recording of spectral Doppler waveforms⁴⁷. Correcting the phase aberration induced
153 by the maternal abdomen allowed the acquisition of high-quality signals from the UPatch
154 (Supplementary Fig. 25 and Supplementary Discussion 13). The UPatch was able to image the
155 two arteries and a vein in the helical umbilical cord and the middle cerebral artery from the circle
156 of Willis (Fig. 2a,b). Detailed blood flow velocities were acquired from all of these vessels (Fig.
157 2c and Supplementary Discussion 5). The cerebroplacental ratio (the pulsatility index of the
158 middle cerebral artery divided by that of the umbilical artery) quantifies the fetal brain-sparing
159 effect during prolonged hypoxia or in placental insufficiency, and the measurements acquired by
160 the UPatch and a clinical device were comparable (Fig. 2d)⁴⁸. The UPatch accurately measured
161 anatomical structures (such as the biparietal diameter, head circumference, abdominal
162 circumference, and femur length), providing a fetal weight estimate for the diagnosis of growth-
163 related complications (Fig. 2e, Methods, and Supplementary Fig. 26)⁴⁹.

164 The UPatch accuracy was validated against a clinical device on 62 participants with
165 various vessel depths, orientations, and placental locations (Table 1, Methods, Extended Data
166 Fig. 3, and Supplementary Figs 27 and 28). From the spectral Doppler waveforms, an envelope
167 extraction algorithm can derive peak systolic velocity, end diastolic velocity, and fetal heart rate
168 to calculate the systolic-to-diastolic ratio, pulsatility index, and resistance index (Supplementary
169 Fig. 29)⁵⁰. Based on Bland–Altman analysis, the mean differences \pm standard deviations between

170 the UPatch and clinical device were -0.019 ± 0.274 for the systolic-to-diastolic ratio (-0.72%
171 relative mean difference), -0.010 ± 0.117 for the pulsatility index (-0.92%), -0.004 ± 0.044 for
172 the resistance index (-0.64%), and 0.95 ± 2.91 beats per minute (bpm) for the fetal heart rate
173 (0.68% ; Fig. 2f and Supplementary Fig. 30). Pearson correlation coefficients demonstrated
174 strong linear relationship between the two devices (Extended Data Fig. 4).

175

176 **Autonomous vessel tracking**

177 The umbilical cord facilitates gas exchange and nutrient transfer between the placenta
178 and fetus¹. Spectral Doppler waveforms of the umbilical blood flow can monitor the
179 fetoplacental circulation (Supplementary Discussions 4 and 5)³. However, the umbilical cord is a
180 moving target due to fetal and maternal movements, respiration, and uterine contractions
181 (Supplementary Discussion 14)²¹. In clinical practice, sonographers manually adjust the color-
182 flow box and set a sample gate to acquire spectral Doppler signals from the target vessel, which
183 is time-consuming and operator-dependent (Supplementary Fig. 31)⁵¹. In low-resource settings
184 where the incidence of pregnancy complications remains high, such sonographers are often
185 limited in number^{52,53}.

186 To reduce the need for manual operators and the corresponding healthcare burden, we
187 developed an image segmentation-based algorithm that can autonomously identify and track
188 moving vessels (Fig. 3a and Supplementary Discussion 15). We used a diverging beam to cover
189 a large field of view, ensuring that the moving vessel remains consistently visible within the
190 ultrasonographic window (Supplementary Fig. 32)⁵⁴. The UPatch stably acquired the umbilical
191 cord signals without repositioning across common maternal postures (Extended Data Fig. 5). By
192 segmenting the reconstructed duplex images, the tracking algorithm identifies pulsatile signals

193 by calculating the variance in color Doppler pixel intensity over several consecutive frames (Fig.
194 3a, Extended Data Fig. 6, and Supplementary Discussion 16). Then, the algorithm identifies the
195 primary region of the pulsatile signals and registers the spatial centroid of the primary region as
196 the sample gate, where a focused beam is directed to acquire blood flow spectra with enhanced
197 signal intensity (Fig. 3a and Supplementary Figs 33 and 34)⁵⁴. This autonomous sample gate
198 registration enabled continuous blood flow monitoring of a moving vessel in real time (Fig. 3b,c,
199 Supplementary Video 1, and Supplementary Discussion 17). Without the tracking algorithm,
200 blood flow signals were lost during vessel movements (Fig. 3c).

201 To validate the accuracy of the autonomous tracking algorithm, we compared its sample
202 gates with those registered by a sonographer in a double-blind test (Fig. 3d, Methods, and
203 Supplementary Discussion 18). We found that 91.9% and 90.5% of the sample gates were within
204 a 2-mm discrepancy (an accepted clinical standard) in the lateral and axial directions,
205 respectively (Fig. 3e and Supplementary Discussion 19)⁴⁷. In a separate test, the sample gates
206 registered by the tracking algorithm were considered accurate by three sonographers in 94.2% of
207 the images acquired using the clinical device (with some images affected by fast cord
208 movements), and in 91.2% of the images acquired using the UPatch (due to slight differences in
209 image quality, Methods, Extended Data Fig. 7, and Supplementary Discussion 18). We used
210 Bland–Altman analysis to compare the systolic-to-diastolic ratio from the sample gates acquired
211 by the tracking algorithm and a sonographer (Methods and Supplementary Discussion 18). The
212 mean difference \pm standard deviation was only 0.036 ± 0.124 (Fig. 3f). While its accuracy is
213 similar to that of U-Net⁵⁵ and ConvLSTM⁵⁶, the tracking algorithm achieved more than a tenfold
214 reduction in processing time, enabling real-time image processing (Supplementary Fig. 35 and
215 Supplementary Discussion 18).

216

217 **Continuous monitoring of pregnant participants**

218 The continuous monitoring of umbilical artery blood flow is important for assessing fetal
219 growth restriction (Supplementary Discussions 4 and 5)⁵⁷. Abnormal waveforms (such as absent
220 or reversed end diastolic velocities) often indicate fetal pathology due to placental insufficiency,
221 and even subtler abnormalities (such as increased Doppler indices) indicate an elevated risk^{58,59}.
222 Continuous monitoring of these changes can inform the optimal delivery time, helping avoid
223 both premature birth, which may lead to postnatal complications⁶⁰, and delayed birth, which
224 heightens the risk of asphyxia, cerebral palsy, and stillbirth⁶¹.

225 We used the UPatch to compare a healthy (32 weeks 6 days) and a pre-eclamptic (28
226 weeks 3 days gestational age) participant. The participants were in a semi-recumbent position
227 with the UPatch placed on the maternal abdomen to monitor the blood flow continuously at the
228 placental cord insertion (Fig. 4a and Supplementary Discussion 20). We derived the fetal heart
229 rate and Doppler indices, including resistance index, pulsatility index, and systolic-to-diastolic
230 ratio, which are independent of the ultrasound incident angle (Supplementary Discussion 21)¹⁹.
231 Both participants showed similar fetal heart rate patterns (Fig. 4b–d). The average fetal heart
232 rates were 149.5 bpm for the healthy and 143.3 bpm for the pre-eclamptic participant, with
233 variabilities of 20.3 and 21.5 bpm, respectively (Fig. 4b and Supplementary Discussion 22). The
234 UPatch could detect transient fetal heart rate accelerations, which indicate a healthy fetal state
235 (Fig. 4c and Supplementary Fig. 36)⁶². However, the Doppler indices of the participants showed
236 distinct features. There was minimal variability in the Doppler indices of the healthy participant,
237 indicating stable blood flow. The mean resistance index of 0.62, pulsatility index of 1.04, and
238 systolic-to-diastolic ratio of 2.61 aligned with the 50th percentile of established reference norms,

239 indicating a healthy fetus²³. In contrast, the pre-eclamptic participant showed large fluctuations
240 in the Doppler indices, and the end diastolic velocity was absent 24.9% of the time (Fig. 4b,d,
241 Supplementary Fig. 37, and Supplementary Discussion 22). The mean resistance index of 0.85,
242 pulsatility index of 2.04, and systolic-to-diastolic ratio of 5.11 were above the 97.5th percentile,
243 suggesting severe placental dysfunction²³. Following the detection of compromised fetal health
244 using the UPatch, the pre-eclamptic participant underwent intensive monitoring, and the baby
245 was delivered via Cesarean section 4 days later.

246 Current obstetric practice relies on a two-step process of cardiotocography for fetal heart
247 rate and separate manual Doppler ultrasound for Doppler indices (Supplementary Discussion 23)⁵⁷.
248 We used the UPatch to continuously monitor both signals simultaneously in 52 pregnancies
249 (Supplementary Figs 36–91 and Supplementary Discussion 24). Cohort analysis showed that the
250 fetal heart rate and Doppler indices are not correlated, highlighting their potential to provide
251 complementary clinical insights (Fig. 4e and Supplementary Fig. 92). Additionally, continuous
252 monitoring results revealed that transient physiological fluctuations can temporarily alter Doppler
253 indices to abnormal values (Supplementary Figs 36–91). With conventional ultrasound devices,
254 these transient fluctuations may be misinterpreted as pathological and trigger unnecessary
255 interventions, whereas continuous monitoring with the UPatch establishes a personalized baseline
256 and temporal context to distinguish transient fluctuations from sustained compromise. While fetal
257 heart rate decelerations were observed, the substantial beat-to-beat variability and absence of a
258 defined gestational reference trend make interpretation challenging (Fig. 4f and Supplementary
259 Fig. 93)⁶³. In contrast, Doppler indices exhibited monotonic relationships with gestational age,
260 consistent with established reference ranges²³, supporting their use as objective, clinically
261 actionable information for assessing fetal vascular resistance and identifying high-risk pregnancies

262 (Fig. 4g and Supplementary Figs 93 and 94). The data were also stratified by perinatal conditions,
263 including healthy, small for gestational age, large for gestational age, gestational diabetes, pre-
264 eclampsia, and gestational hypertension. Fetal heart rate distributions overlapped substantially
265 among all conditions, showing minimal discrimination (Fig. 4h). In contrast, Doppler indices
266 differed, particularly for small for gestational age, pre-eclampsia, and hypertension, illustrating the
267 UPatch’s potential to identify high-risk pregnancies in real time (Fig. 4i, Supplementary Figs 95
268 and 96, and Supplementary Discussion 25).

269

270 **Discussion**

271 The UPatch can visualize fetal anatomy and measure fetal heart rate and blood flow with
272 high sensitivity and accuracy, offering complementary insights to existing approaches to evaluate
273 fetal health. Whereas standard clinical regimens mandate periodic blood flow assessments
274 performed by sonographers, typically at weekly intervals in outpatient settings and up to three
275 times per week for inpatients, these evaluations are labor-intensive and prone to errors⁵⁸. In
276 contrast, the UPatch adheres directly to the maternal abdomen for hands-free use and employs an
277 image segmentation algorithm to differentiate and track blood vessels autonomously, enabling
278 continuous and accurate blood flow measurements without the need for a sonographer.

279 Several strategies could be pursued to improve the UPatch further. First, the tracking
280 algorithm cannot generate uninterrupted spectral Doppler waveforms during motion because
281 vessel tracking and spectral Doppler acquisition occur sequentially. This problem can be solved
282 by integrating a separate image segmentation algorithm to detect signal loss in real time,
283 allowing the system to pause the spectral Doppler sequence and track the target vessel in the
284 duplex image. Leveraging advanced graphics processing units would substantially accelerate

285 computation, enabling simultaneous duplex imaging and spectral Doppler acquisition
286 (Supplementary Discussion 17)^{64,65}.

287 Second, the UPatch currently needs to be wired to a backend system (Vantage 256,
288 Verasonics) for both power and high-bandwidth data transmission, like many existing wearable
289 devices^{28,31,66-70}. While this configuration is appropriate for inpatient settings, it limits mobility
290 and broader applicability. Future developments could incorporate wireless circuits to expand the
291 range of clinical scenarios. A compact circuit was recently developed to interface a transducer
292 array with a single transceiver for vessel pulsation monitoring, but it is not capable of Doppler
293 imaging (Supplementary Discussion 26)⁷¹. Developing a more advanced circuit with multiple
294 transceivers for Doppler imaging would enhance patient mobility, help assess the impact of
295 maternal posture and physical activity on fetal health, and show how maternal circulation affects
296 fetal hemodynamics⁷².

297 Third, further investigations are necessary to establish the UPatch as a diagnostic tool to
298 identify specific conditions or diseases⁷³. Continuous hemodynamic monitoring with a particular
299 focus on the frequency and duration of critical changes (such as decreased or absent end diastolic
300 velocity), is essential for assessing the severity of hypoxia and identifying optimal intervention
301 windows to prevent adverse perinatal outcomes⁷⁴. The UPatch can define individualized
302 baselines that characterize the normal range of short-term fluctuations for each patient while
303 highlighting patterns of sustained abnormalities that indicate evolving pathology. This
304 personalized calibration reduces false alarms triggered by normal transient events and allows
305 clinicians to focus on persistent deviations that truly indicate risk. These studies could establish
306 the real-world clinical utility of the UPatch.

307 Finally, this study was limited to using only the UPatch. Future work could focus on
308 integrating UPatch data streams (such as fetal heart rate and Doppler indices) with additional
309 physiological metrics from both the fetus (such as electrocardiogram) and the mother (such as
310 blood pressure, pulse oximetry, and tocodynamometry). Such multimodal integration would
311 provide a more comprehensive and accurate understanding of the dynamic interactions between
312 fetus and mother¹¹. Additionally, applying big data analysis to correlate UPatch data streams
313 with postnatal and postmortem results would yield unprecedented insights into the mechanisms
314 of fetal complications, advancing diagnosis and intervention strategies⁷⁵.

315

316 **Acknowledgements**

317 We thank all pregnant volunteers for their participation. We thank M. Selvaraj, S. La
318 Belle, J. Murillo, H. Valentine, S. Collins, A. Rondoni, E. D'Alberti, I. Noakes, A. Anton, G.
319 James, R. Craik, D. Hedgecote, and L. Bozhilova for assistance with subject recruitment and
320 clinical tests. We also thank C. Deane and S. Stock for their discussions and C. Bevan for her
321 public involvement. This work was supported by Wellcome Leap HER01430 (A.G., S.X.), the
322 National Institutes of Health 1R01EB033464-01 (S.X.) and 1R01HL171652-01 (S.X.), and
323 Accelerating Innovation to Market at UC San Diego (S.X.). The content is solely the
324 responsibility of the authors and does not represent the official views of the Wellcome Leap or
325 the National Institutes of Health. G.P. is supported by the Siebel Foundation, Merkin Graduate
326 Fellowship Program, and Asan Foundation. A.T.P. is supported by the National Institute for
327 Health Research Oxford Biomedical Research Centre. All biological experiments were
328 conducted in accordance with the ethical guidelines of the National Institutes of Health and with
329 the approval of the Institutional Review Board of the University of California San Diego and the

330 UK Research Ethics Committee. The mention of commercial products, their sources, or their use
331 in connection with material reported herein is not to be construed as either an actual or implied
332 endorsement of such products by the Department of Health and Human Services.

333

334 **Author contributions**

335 G.P., A.G., and S.X. conceived the project. G.P., Y.B., H.H., S.Y.Q., M.Y.L., S.W., P.B.,
336 G.G., R.T.W., A.X.R., C.C.F.L., X.X.G., H.J.H., A.Y., M.L., and S.X. developed the UPatch.
337 G.P., X.Y.Y., X.J.C., W.T.Y., R.S.W., and K.A.W. carried out the acoustic safety
338 characterization. G.P., Y.B., H.H., A.R., M.T., J.L., A.T.P., L.I., S.L.C., L.C.L., and A.G.
339 performed the clinical studies. G.P., Y.B., H.H., S.Z., R.S. and S.X. processed and analyzed the
340 data. G.P. H.H., A.L., L.S., and M.S. prepared the figures. G.P. and S.X. wrote the paper. All
341 authors provided constructive and valuable feedback on the manuscript.

342

343 **Competing interests**

344 S.X. is a cofounder of Softsonics LLC. M.T., L.I., and A.G. are cofounders of Safer Birth
345 LTD. A.T.P. is a Senior Scientific Advisor of Intelligent Ultrasound Ltd. All other authors
346 declare no competing interests.

347

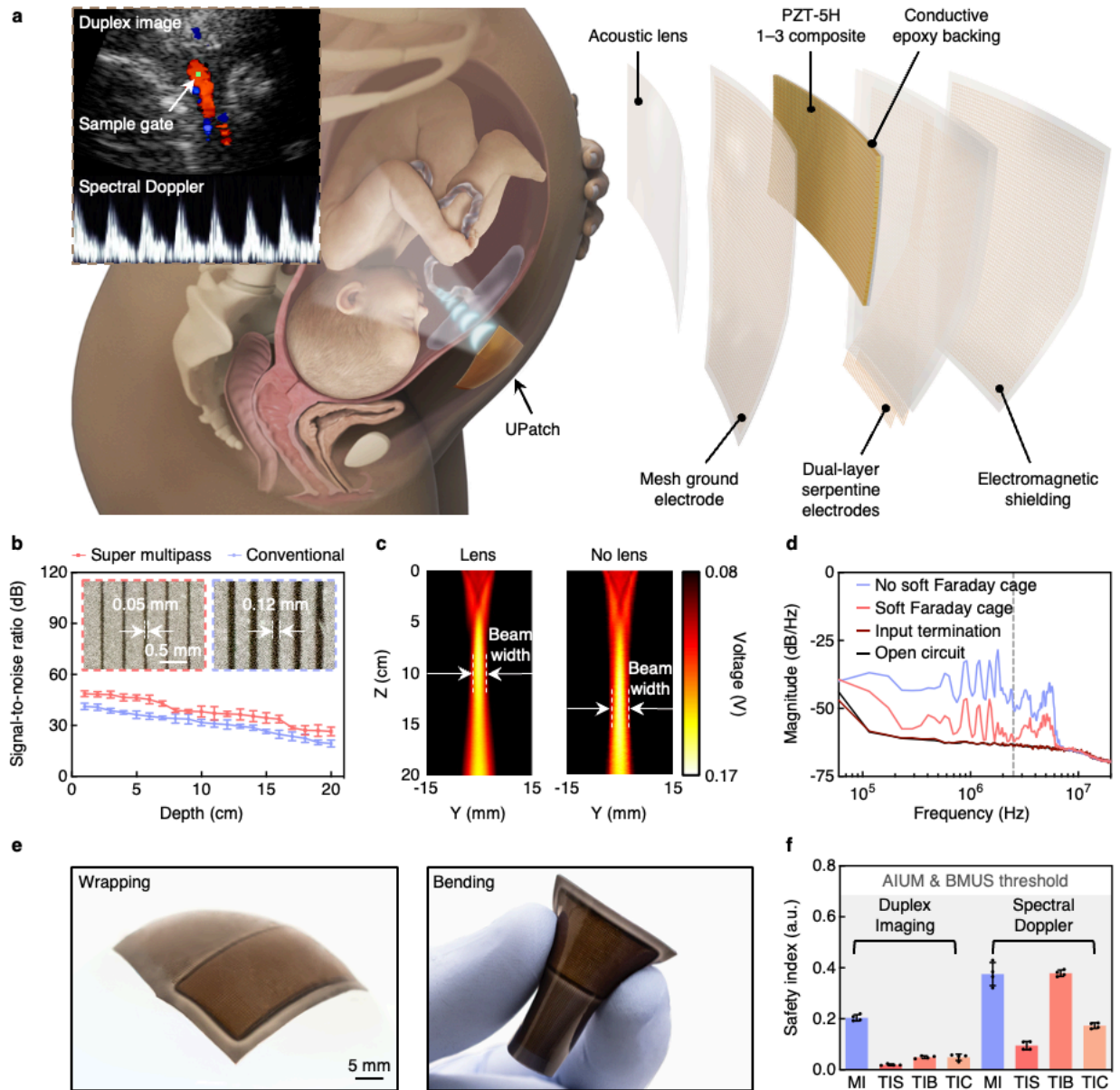
348 **Table 1 | Participant demographics in the validation study.** The demographic
 349 information includes race/ethnicity, age, height, weight, body mass index, gestational age, and
 350 placental location at the time of the study. The validation was performed on a diverse participant
 351 cohort, ensuring the broad applicability of the UPatch.

Race/ethnicity	n (percentage)
White	45 (72.6%)
Asian	5 (8.1%)
Mixed, American Indian	8 (12.9%)
Unknown*	4 (6.4%)
At the time of study	Mean ± standard deviation
Age (years)	31.45 ± 4.88
Height (cm)	164.44 ± 7.34
Weight (kg)	73.33 ± 18.11
Body mass index	27.17 ± 6.92
Gestational age (days)	238.90 ± 26.68
Placental location	n (percentage)
Anterior	36 (58.1%)
Posterior	17 (27.4%)
Lateral	4 (6.5%)
Fundal	5 (8.1%)

352 *The participants refused to provide this information.

353

354 **Figures and figure legends**



355

356

Fig. 1 | Overview of the UPatch. a, Schematics of the working principle for fetal

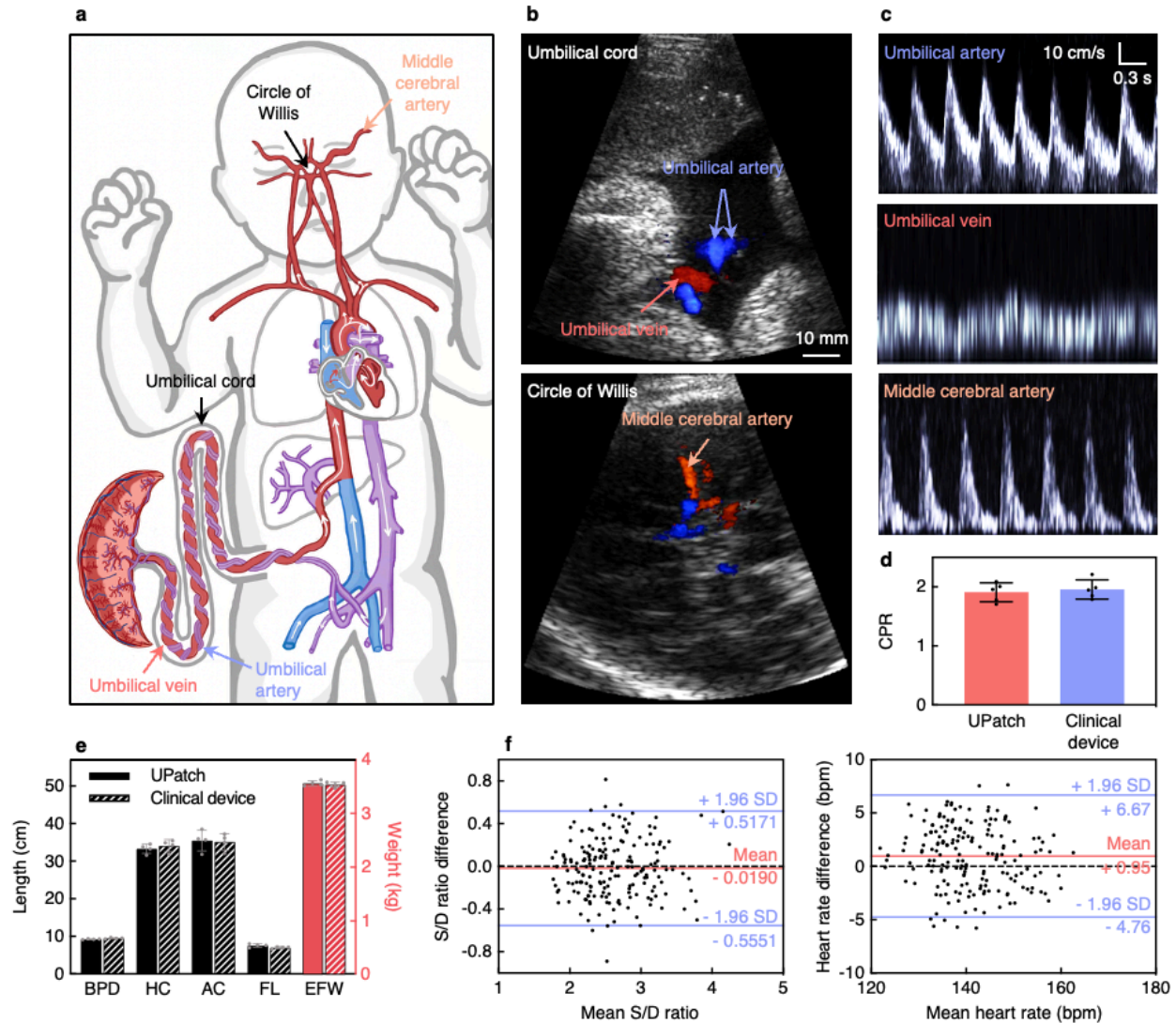
357 monitoring (left) and a structurally exploded view (right). The UPatch is attached to the maternal

358 abdomen to monitor fetal anatomical structures and hemodynamics continuously with duplex

359 imaging. A sample gate, indicated by the green dot, provides blood flow measurements from

360 fetal vessels. A diverging beam is used for imaging, and a focused beam for blood flow

361 measurement. The UPatch is multilayered to enhance its signals from red blood cells and
362 minimize its form factors. **b**, Comparison of signal-to-noise ratios between the conventional
363 method and transducers diced with the super multipass method ($n = 12$). The insets are optical
364 images showing the results from the two methods. The images share the same scale bar. **c**,
365 Acoustic fields measured using a hydrophone in the elevational plane of the UPatch with (left)
366 and without (right) an acoustic lens. **d**, The power spectral density analysis of the UPatch with
367 and without the soft Faraday cage, input termination at 50Ω , and open circuit of the backend
368 system. The soft Faraday cage reduces noise coupling from electromagnetic interference by 11.7
369 dB/Hz at 2.5 MHz (gray dashed line), the center frequency of the UPatch. **e**, Photographs of the
370 UPatch demonstrating its mechanical compliance in wrapping (left) and bending (right) shapes.
371 **f**, UPatch safety measurements. The mechanical index (MI), soft tissue thermal index (TIS),
372 bone thermal index (TIB), and cranium thermal index (TIC) were all well below the thresholds
373 of 0.7 recommended by the AIUM⁴¹ and BMUS⁴² for continuous monitoring ($n = 4$). Data in **b**
374 and **f** are presented as mean \pm standard deviations.



375

376

Fig. 2 | Measurements and validations of the UPatch for fetal monitoring. a,

377

Schematics illustrating the fetal cardiovascular system. The umbilical cord shows coiling of the

378

two umbilical arteries and the umbilical vein. The middle cerebral artery is located within the

379

circle of Willis. **b**, Duplex images from the umbilical cord and circle of Willis recorded with the

380

UPatch. The images share the same scale bar. **c**, Blood flow spectra from three key vessels

381

recorded with the UPatch. The spectra share the same scale bar. **d**, Comparison of the

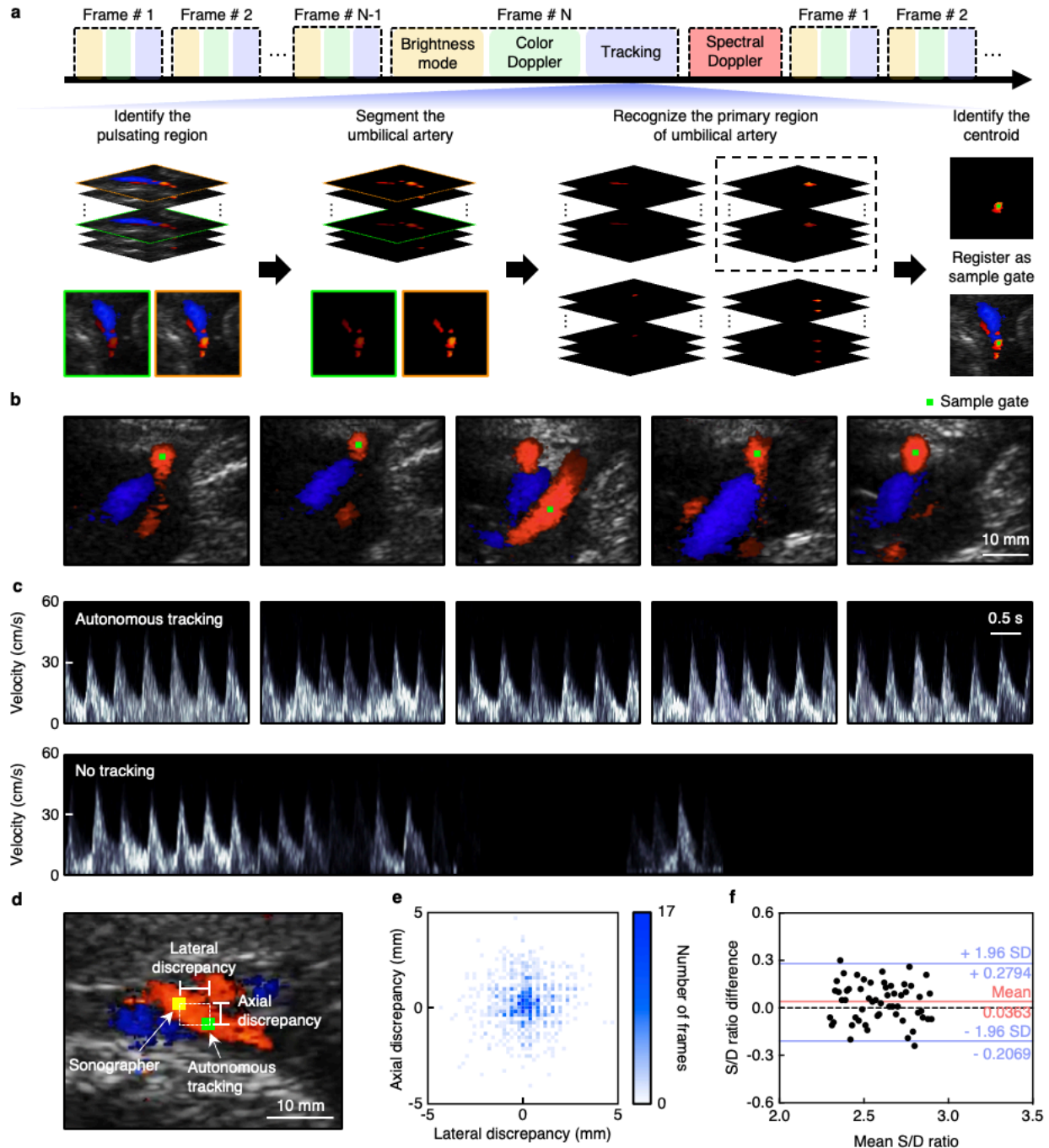
382

cerebroplacental ratio (CPR) measured with the UPatch and a handheld clinical ultrasound

383

device (n = 5). **e**, Comparison of fetal biometry measured with the UPatch and a handheld

384 clinical ultrasound device. Biparietal diameter (BPD), head circumference (HC), abdominal
385 circumference (AC), and femur length (FL) were used to calculate estimated fetal weight (EFW)
386 ($n = 4$)⁴⁹. **f**, Bland–Altman plots for the systolic-to-diastolic ratio (S/D ratio, left) and fetal heart
387 rate (right) measured using the UPatch and a handheld clinical ultrasound device (Voluson E10,
388 GE). Solid red lines are the mean differences between the two devices, solid blue lines are 95%
389 limits of agreement (1.96 standard deviations above and below the mean differences), and black
390 dashed lines are the zero difference between the two devices. Each plot has three measurement
391 pairs by repeating three times with the same devices on the same participant for each of the 62
392 participants. Data in **d** and **e** are presented as mean \pm standard deviations.



393

394

Fig. 3 | Autonomous vessel tracking by image segmentation. a, Beamforming

395

sequence and working principle of the image segmentation-based vessel tracking algorithm. The

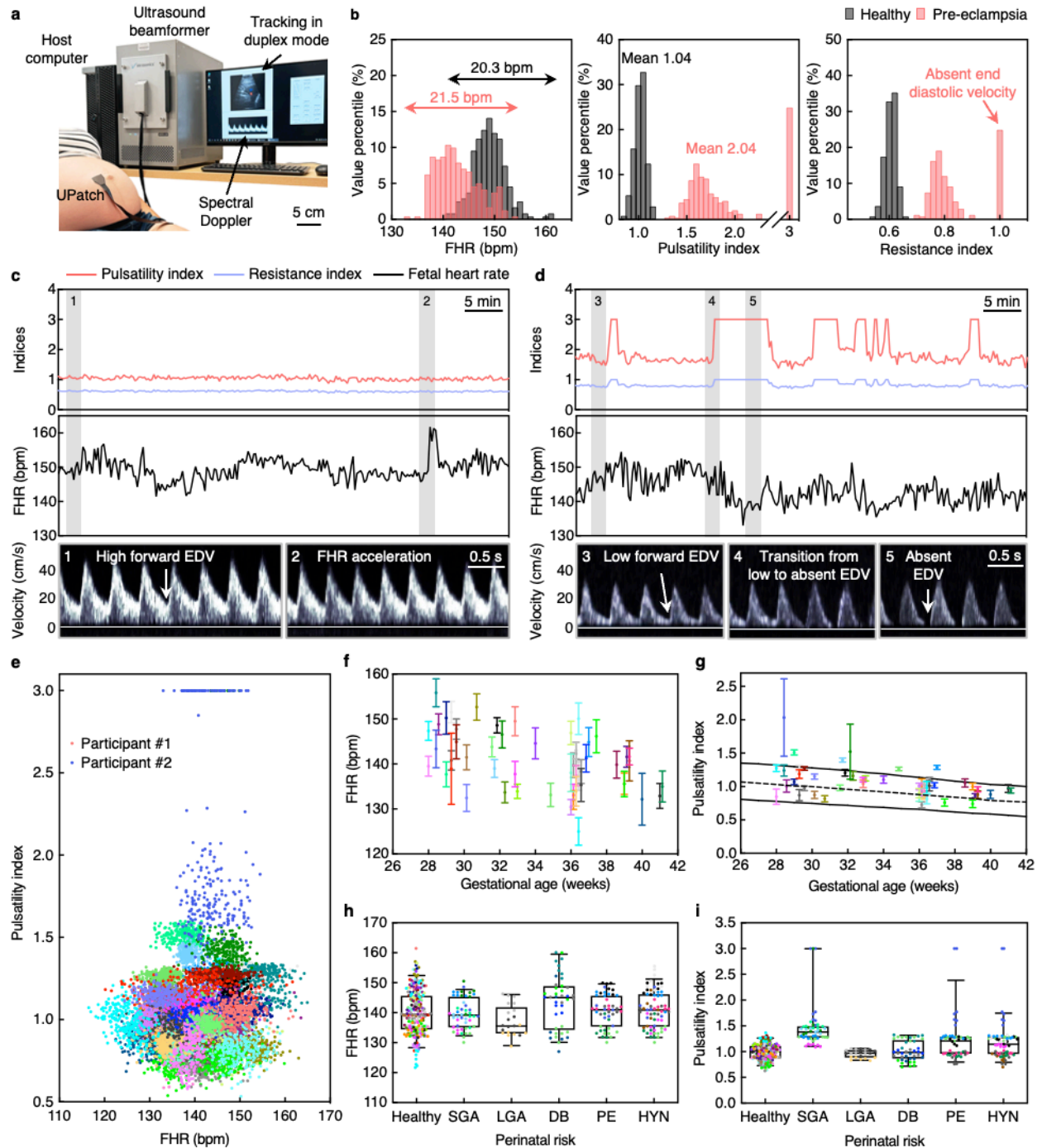
396

tracking algorithm is integrated between the duplex imaging and spectral Doppler (top). The

397

algorithm identifies the pulsating regions in consecutive frames, segments the umbilical artery,

398 recognizes the primary region, and registers the spatial centroid as the sample gate (bottom).
399 Images with green and orange boundaries represent the end diastole and peak systole,
400 respectively. In these two images, the blue regions are similar, indicating the umbilical vein,
401 whereas the red regions differ in intensity, indicating the pulsating umbilical artery. Among the
402 four segmented areas, the primary region is defined as the largest segmented area (denoted with
403 the black dashed box), which has the strongest signal intensity. **b**, Tracking a moving umbilical
404 artery and registering a sample gate using the UPatch with the autonomous algorithm. All images
405 share the same scale bar. **c**, The autonomous algorithm allows the measurement of blood flow
406 from a moving vessel continuously (top). Without the autonomous tracking algorithm, a
407 predefined sample gate results in signal loss due to vessel movements (bottom). The spectra
408 share the same scale bar. **d**, A representative image showing the difference between the sample
409 gate labeled by the autonomous tracking algorithm and by a sonographer. **e**, Summary of the
410 lateral and axial discrepancies in the sample gates labeled by the autonomous tracking algorithm
411 and by a sonographer. **f**, Bland–Altman plot for the systolic-to-diastolic ratios (S/D ratio)
412 measured by the autonomous tracking algorithm and a sonographer. The solid red line is the
413 mean difference between the two methods, the solid blue lines are 95% limits of agreement (1.96
414 standard deviations above and below the mean differences), and the black dashed line is the zero
415 difference between the two methods.



416

417

Fig. 4 | Continuous monitoring of pregnant participants. a, Photograph of the

418

measurement setup, with participants in a semi-recumbent position. The UPatch was laminated

419

on the maternal abdomen and connected to an ultrasound beamformer and a host computer,

420

which displays the duplex image, tracks the sample gate, and measures spectral Doppler signals

421 from the umbilical artery. **b**, Histograms of the fetal heart rate (FHR, left), pulsatility index
422 (middle), and resistance index (right) from the healthy (grey) and pre-eclamptic (red)
423 participants. **c**, Pulsatility index, resistance index (top), and FHR (middle) recording from the
424 healthy participant, with highlighted spectral Doppler signals from the shaded regions (bottom).
425 The recorded traces share the same scale bar. The spectra share the same scale bar. **d**, Pulsatility
426 index, resistance index (top), and FHR (middle) recording from the pre-eclamptic participant,
427 with highlighted spectral Doppler signals from the shaded regions (bottom). The recorded traces
428 share the same scale bar. The spectra share the same scale bar. **e**, Scatterplot of pulsatility index
429 against FHR with each color in the data points corresponding to an individual participant.
430 Participant #1 corresponds to the healthy participant and Participant #2 corresponds to the pre-
431 eclamptic participant in **b** and **c**. The corresponding color scheme for all participants is provided
432 in Supplementary Figs 88–91. **f**, FHR plotted against gestational age ($n = 241$). **g**, Pulsatility
433 index plotted against gestational age ($n = 241$). The black dashed line is the 50th percentile, and
434 the solid black lines are the 5th and 95th percentiles of a widely used reference population²³. Data
435 in **f** and **g** are presented as mean \pm standard deviations. **h,i**, Box plots of (**h**) FHR and (**i**)
436 pulsatility index stratified by perinatal conditions: healthy (31 participants, 217 data points),
437 small for gestational age (SGA; 7 participants, 49 data points), large for gestational age (LGA; 3
438 participants, 21 data points), diabetes (DB; 6 participants, 42 data points), pre-eclampsia (PE; 7
439 participants, 49 data points), and maternal hypertension (HYN; 10 participants, 70 data points).
440 Each box represents the interquartile range (25th to 75th percentiles), the whiskers denote the 5th
441 to 95th percentile range, and the midline indicates the median. Each participant's data was
442 segmented into 10-min intervals ($n = 7$ per participant). The color schemes in **e–i** are the same.

443 **References**

444 1 Woodward, P. J., Kennedy, A. & Sohaey, R. *Diagnostic imaging: obstetrics*. (Elsevier,
445 2021).

446 2 Hutter, D., Kingdom, J. & Jaeggi, E. Causes and Mechanisms of Intrauterine Hypoxia and
447 Its Impact on the Fetal Cardiovascular System: A Review. *International Journal of*
448 *Pediatrics* **2010**, 401323 (2010).

449 3 Berkley, E., Chauhan, S. P. & Abuhamad, A. Doppler assessment of the fetus with
450 intrauterine growth restriction. *American Journal of Obstetrics and Gynecology* **206**, 300-
451 308 (2012).

452 4 Nelson, K. B. & Grether, J. K. Causes of cerebral palsy. *Current Opinion in Pediatrics* **11**,
453 487-491 (1999).

454 5 McClure, E. *et al.* Global Network for Women's and Children's Health Research: probable
455 causes of stillbirth in low- and middle- income countries using a prospectively defined
456 classification system. *BJOG: An International Journal of Obstetrics & Gynaecology* **125**,
457 131-138 (2018).

458 6 Smith, G. C. S. & Fretts, R. C. Stillbirth. *The Lancet* **370**, 1715-1725 (2007).

459 7 Lawn, J. E. *et al.* Stillbirths: rates, risk factors, and acceleration towards 2030. *The Lancet*
460 **387**, 587-603 (2016).

461 8 Rouse, D. J. Antepartum fetal surveillance ACOG practice bulletin, number 229. *Obstet*
462 *Gynecol* **137**, E116-E127 (2021).

463 9 Rouse, D. J., Owen, J., Goldenberg, R. L. & Cliver, S. P. Determinants of the optimal time
464 in gestation to initiate antenatal fetal testing: a decision-analytic approach. *Am J Obstet*
465 *Gynecol* **173**, 1357-1363 (1995).

466 10 Harkey, K. T., Casale, M. B., Pantelopoulos, A. A. & Zurcher, M. A. Assessing the Clinical
467 Use of a Novel, Mobile Fetal Monitoring Device. *Obstetrics & Gynecology* **123**, 55S
468 (2014).

469 11 Ryu, D. *et al.* Comprehensive pregnancy monitoring with a network of wireless, soft, and
470 flexible sensors in high- and low-resource health settings. *Proceedings of the National*
471 *Academy of Sciences* **118**, e2100466118 (2021).

472 12 Freeman, R. K. Problems with intrapartum fetal heart rate monitoring interpretation and
473 patient management. *Obstet Gynecol* **100**, 813-826 (2002).

474 13 Grivell, R. M., Alfirevic, Z., Gyte, G. M. & Devane, D. Antenatal cardiotocography for
475 fetal assessment. *Cochrane Database of Systematic Reviews* **9**, CD007863 (2015).

476 14 Alfirevic, Z., Devane, D., Gyte, G. M. & Cuthbert, A. Continuous cardiotocography (CTG)
477 as a form of electronic fetal monitoring (EFM) for fetal assessment during labour.
478 *Cochrane Database Syst Rev* **2**, CD006066-CD006066 (2017).

479 15 Marzbanrad, F., Stroux, L. & Clifford, G. D. Cardiotocography and beyond: a review of
480 one-dimensional Doppler ultrasound application in fetal monitoring. *Physiological*
481 *Measurement* **39**, 08TR01 (2018).

482 16 Hayes - Gill, B. R. Monica Healthcare: From the research laboratory to commercial
483 reality—A real - life case study. *Healthcare Technology Letters* **8**, 1-10 (2021).

484 17 Gunther, J. E., Jayet, B., Sekar, S. K. V., Kainerstorfer, J. M. & Andersson - Engels, S.
485 Review of optical methods for fetal monitoring in utero. *Journal of Biophotonics* **15**,
486 e202100343 (2022).

487 18 Du, Y.-C., Yen, L. B., Kuo, P.-L. & Tsai, P.-Y. A Wearable Device for Evaluation of
488 Relative Position, Force, and Duration of Fetal Movement for Pregnant Woman Care. *IEEE*
489 *Sensors Journal* **21**, 19341-19350 (2021).

490 19 Kypros Nicolaidis, G. R., Kurt Hecher, Renato Ximenes. *Doppler in Obstetrics*. (2002).

491 20 Salomon, L. J. *et al.* ISUOG Practice Guidelines: ultrasound assessment of fetal biometry
492 and growth. *Ultrasound in Obstetrics & Gynecology* **53**, 715-723 (2019).

493 21 Bhide, A. *et al.* ISUOG Practice Guidelines (updated): use of Doppler velocimetry in
494 obstetrics. *Ultrasound in Obstetrics & Gynecology* **58**, 331-339 (2021).

495 22 Oros, D. *et al.* Reference ranges for Doppler indices of umbilical and fetal middle cerebral
496 arteries and cerebroplacental ratio: systematic review. *Ultrasound in Obstetrics &*
497 *Gynecology* **53**, 454-464 (2019).

498 23 Drukker, L. *et al.* International gestational age-specific centiles for umbilical artery
499 Doppler indices: a longitudinal prospective cohort study of the INTERGROWTH-21st
500 Project. *American Journal of Obstetrics and Gynecology* **222**, 602.e601-602.e615 (2020).

501 24 Kiserud, T. *et al.* The World Health Organization Fetal Growth Charts: A Multinational
502 Longitudinal Study of Ultrasound Biometric Measurements and Estimated Fetal Weight.
503 *PLOS Medicine* **14**, e1002220 (2017).

504 25 Papageorgiou, A. T. *et al.* International standards for fetal growth based on serial
505 ultrasound measurements: the Fetal Growth Longitudinal Study of the INTERGROWTH-
506 21st Project. *The Lancet* **384**, 869-879 (2014).

507 26 Goldenberg, R. L., Harrison, M. S. & McClure, E. M. Stillbirths: The Hidden Birth
508 Asphyxia — US and Global Perspectives. *Clinics in Perinatology* **43**, 439-453 (2016).

509 27 AIUM Practice Parameter for the Performance of Standard Diagnostic Obstetric
510 Ultrasound. *Journal of Ultrasound in Medicine* **43**, E20-E32 (2024).

511 28 Wang, C. *et al.* Bioadhesive ultrasound for long-term continuous imaging of diverse organs.
512 *Science* **377**, 517-523 (2022).

513 29 Hu, H. *et al.* A wearable cardiac ultrasound imager. *Nature* **613**, 667-675 (2023).

514 30 Du, W. *et al.* Conformable ultrasound breast patch for deep tissue scanning and imaging.
515 *Science Advances* **9**, eadh5325 (2023).

516 31 Zhang, L. *et al.* A conformable phased-array ultrasound patch for bladder volume
517 monitoring. *Nature Electronics* **7**, 77-90 (2023).

518 32 Khalil, A. *et al.* ISUOG Practice Guidelines: performance of third - trimester obstetric
519 ultrasound scan. *Ultrasound in Obstetrics & Gynecology* **63**, 131-147 (2024).

520 33 Hoskins, P. R., Martin, K. & Thrush, A. *Diagnostic Ultrasound Physics and Equipment*.
521 (CRC Press, 2019).

522 34 Evans, D. H., Jensen, J. A. & Nielsen, M. B. Ultrasonic colour Doppler imaging. *Interface*
523 *Focus* **1**, 490-502 (2011).

524 35 Zhang, L., Du, W., Kim, J.-H., Yu, C.-C. & Dagdeviren, C. An Emerging Era:
525 Conformable Ultrasound Electronics. *Advanced Materials* **36**, 2307664 (2024).

526 36 Aksoy, B. *et al.* Shielded soft force sensors. *Nature Communications* **13**, 4649 (2022).

527 37 IPeM. *Report 102 Quality Assurance of Ultrasound Imaging Systems*. (Institute of Physics
528 and Engineering in Medicine, 2010).

529 38 Thijssen, J. M., van Wijk, M. C. & Cuyper, M. H. M. Performance testing of medical
530 echo/Doppler equipment. *European Journal of Ultrasound* **15**, 151-164 (2002).

531 39 Browne, J. E. A review of Doppler ultrasound quality assurance protocols and test devices.
532 *Physica Medica* **30**, 742-751 (2014).

533 40 Haar, G. t. *The Safe Use of Ultrasound in Medical Diagnosis*. (The British Institute of
534 Radiology, 2012).

535 41 AIUM Official Statement for Recommended Maximum Scanning Times for Displayed

536 Thermal Index Values. *Journal of Ultrasound in Medicine* **42**, E74-E75 (2023).

537 42 Safety Group of the British Medical Ultrasound Society. Guidelines for the safe use of
538 diagnostic ultrasound equipment. *Ultrasound* **18**, 52-59 (2010).

539 43 Food and Drug Administration. Marketing clearance of diagnostic ultrasound systems and
540 transducers: Guidance for industry and food and drug administration staff. *U.S. Food and*
541 *Drug Administration, Silver Spring, MD, USA*, Tech. Rep. FDA-2017-D-5372 (2023).

542 44 [https://my.getzhealthcare.com/getzhealthcare/products/ge-healthcare/corometrics-](https://my.getzhealthcare.com/getzhealthcare/products/ge-healthcare/corometrics-250cx/corometrics250cx_datasheet.pdf)
543 [250cx/corometrics250cx_datasheet.pdf](https://my.getzhealthcare.com/getzhealthcare/products/ge-healthcare/corometrics-250cx/corometrics250cx_datasheet.pdf).

544 45 Hekkenberg, R. T. & Bezemer, R. A. Aspects concerning the measurement of surface
545 temperature of ultrasonic diagnostic transducers, Part 2: on a human and artificial tissue.
546 *TNO Prevention and Health report*, Leiden (2003).

547 46 International Electrotechnical Commission. IEC 62359:2010/AMD1:2017 "Ultrasonics:
548 Field Characterization—Test Methods for the Determination of Thermal and Mechanical
549 Indices Related to Medical Diagnostic Ultrasonic Fields". *International Electrotechnical*
550 *Commission, Geneva, Switzerland*, Ed. 2.1 (2017).

551 47 Maulik, D. & Lees, C. C. *Doppler Ultrasound in Obstetrics and Gynecology*. (Springer,
552 2023).

553 48 Conde - Agudelo, A., Villar, J., Kennedy, S. H. & Papageorghiou, A. T. Predictive
554 accuracy of cerebroplacental ratio for adverse perinatal and neurodevelopmental outcomes
555 in suspected fetal growth restriction: systematic review and meta - analysis. *Ultrasound in*
556 *Obstetrics & Gynecology* **52**, 430-441 (2018).

557 49 Hadlock, F. P., Harrist, R. B., Sharman, R. S., Deter, R. L. & Park, S. K. Estimation of
558 fetal weight with the use of head, body, and femur measurements--a prospective study. *Am*
559 *J Obstet Gynecol* **151**, 333-337 (1985).

560 50 Zhou, S. *et al.* Transcranial volumetric imaging using a conformal ultrasound patch. *Nature*
561 **629**, 810-818 (2024).

562 51 Oates, C. *Ultrasound Technology for Clinical Practitioners*. (Wiley, 2023).

563 52 Ali, S. *et al.* Prognostic accuracy of antenatal Doppler ultrasound for adverse perinatal
564 outcomes in low-income and middle-income countries: a systematic review. *BMJ Open* **11**,
565 e049799 (2021).

566 53 Ali, S. *et al.* Standardization and quality control of Doppler and fetal biometric ultrasound
567 measurements in low - income setting. *Ultrasound in Obstetrics & Gynecology* **61**, 481-
568 487 (2023).

569 54 Demi, L. Practical Guide to Ultrasound Beam Forming: Beam Pattern and Image
570 Reconstruction Analysis. *Applied Sciences* **8**, 1544 (2018).

571 55 Ronneberger, O., Fischer, P. & Brox, T. U-Net: Convolutional Networks for Biomedical
572 Image Segmentation. in *Medical Image Computing and Computer-Assisted Intervention*.
573 234-241 (2015).

574 56 Shi, X. *et al.* Convolutional LSTM Network: A Machine Learning Approach for
575 Precipitation Nowcasting. in *Advances in Neural Information Processing Systems*. **28**, 802-
576 810 (2015).

577 57 Alfrevic, Z., Stampalija, T. & Dowswell, T. Fetal and umbilical Doppler ultrasound in
578 high-risk pregnancies. *Cochrane Database of Systematic Reviews* **6**, CD007529 (2017).

579 58 Lees, C. C. *et al.* ISUOG Practice Guidelines: diagnosis and management of small - for -
580 gestational - age fetus and fetal growth restriction. *Ultrasound in Obstetrics & Gynecology*
581 **56**, 298-312 (2020).

582 59 Sotiriadis, A. *et al.* ISUOG Practice Guidelines: role of ultrasound in screening for and
583 follow - up of pre - eclampsia. *Ultrasound in Obstetrics & Gynecology* **53**, 7-22 (2019).
584 60 Vogel, J. P. *et al.* The global epidemiology of preterm birth. *Best Practice & Research*
585 *Clinical Obstetrics & Gynaecology* **52**, 3-12 (2018).
586 61 Gardosi, J., Madurasinghe, V., Williams, M., Malik, A. & Francis, A. Maternal and fetal
587 risk factors for stillbirth: population based study. *BMJ* **346**, f108-f108 (2013).
588 62 Freeman, R. K., Garite, T. J., Nageotte, M. P. & Miller, L. A. *Fetal Heart Rate Monitoring*.
589 (Lippincott Williams & Wilkins, 2012).
590 63 Pildner Von Steinburg, S. *et al.* What is the “normal” fetal heart rate? *PeerJ* **1**, e82 (2013).
591 64 Chang, L. W., Hsu, K. H. & Li, P. C. Graphics Processing Unit-Based High-Frame-Rate
592 Color Doppler Ultrasound Processing. *IEEE Transactions on Ultrasonics, Ferroelectrics,*
593 *and Frequency Control* **56**, 1856-1860 (2009).
594 65 So, H., Chen, J., Yiu, B. & Yu, A. Medical Ultrasound Imaging: To GPU or Not to GPU?
595 *IEEE Micro* **31**, 54-65 (2011).
596 66 Lee, W. *et al.* Universal assembly of liquid metal particles in polymers enables elastic
597 printed circuit board. *Science* **378**, 637-641 (2022).
598 67 You, I. *et al.* Artificial multimodal receptors based on ion relaxation dynamics. *Science*
599 **370**, 961-965 (2020).
600 68 Wang, S. *et al.* Skin electronics from scalable fabrication of an intrinsically stretchable
601 transistor array. *Nature* **555**, 83-88 (2018).
602 69 Son, D. *et al.* Multifunctional wearable devices for diagnosis and therapy of movement
603 disorders. *Nature Nanotechnology* **9**, 397-404 (2014).
604 70 Liu, Z. *et al.* A three-dimensionally architected electronic skin mimicking human
605 mechanosensation. *Science* **384**, 987-994 (2024).
606 71 Lin, M. *et al.* A fully integrated wearable ultrasound system to monitor deep tissues in
607 moving subjects. *Nature Biotechnology* **42**, 448-457 (2024).
608 72 Skow, R. J. *et al.* Effects of prenatal exercise on fetal heart rate, umbilical and uterine blood
609 flow: a systematic review and meta-analysis. *British Journal of Sports Medicine* **53**, 124-
610 133 (2019).
611 73 Kim, J. *et al.* Skin-interfaced wireless biosensors for perinatal and paediatric health. *Nature*
612 *Reviews Bioengineering* **1**, 631-647 (2023).
613 74 Rees, S. *et al.* Fetal Brain Injury Following Prolonged Hypoxemia and Placental
614 Insufficiency: A Review. *Comparative Biochemistry and Physiology Part A: Molecular &*
615 *Integrative Physiology* **119**, 653-660 (1998).
616 75 Georgieva, A., Abry, P., Nunes, I. & Frasch, M. G. Editorial: Fetal-maternal monitoring in
617 the age of artificial intelligence and computer-aided decision support: A multidisciplinary
618 perspective. *Frontiers in Pediatrics* **10**, 2296-2360 (2022).
619

620 **Methods**

621 **Fabrication of the UPatch**

622 The fabrication process can be divided into three steps: (1) transducer assembly, (2)
623 electrode printing and acoustic lens integration, and (3) device packaging.

624 (1) Transducer assembly: A silicone (Ecoflex-0030, Smooth-On) layer was first spin-
625 coated at 3000 rpm for 60 s on two glass slides and cured in an 80 °C oven as temporary
626 substrates. Conductive epoxy (Von Roll 3022 E-Solder, EIS) was prepared as the backing layer
627 by mixing an Ag-epoxy composite with a hardener in a 12.5:1 weight ratio and subsequently
628 degassed in a vacuum desiccator. Then, a 1-3 composite (Del Piezo Specialties) was placed on
629 the silicone surface of one glass slide. The degassed conductive epoxy was placed on top and
630 covered by the other silicone-coated glass slide, followed by curing at room temperature for 24
631 h. The thickness of the backing layer (400 μm in this study) was controlled by placing certain
632 spacers in between the two glass slides.

633 After curing, the glass slides were removed, and the transducer made of 1-3
634 composite/backing was diced. To ensure direct transfer of the backing layer side of the
635 transducer to the signal electrodes, the 1-3 composite side of the transducer was first placed on
636 an ultraviolet tape (UHP-110M3, Denka) with a frame film applicator (UH114, Ultron Systems,
637 Inc.). Then, the transducer was diced with a dicing machine (DAD3221, Disco) to 25.55 mm by
638 12 mm using a diamond blade (ZH14-SD1700-V1-90 GE, Disco) at 25,000 spindle rotations
639 per minute (rpm) and 0.5 mm/s feed speed. A second diamond blade (Z09-SD4000-Y1-60,
640 Disco) was used to dice the 0.05 mm kerf of the transducer. Super multipass dicing was
641 performed with 50 μm depth stepwise cuts at 50,000 spindle rpm and 10 mm/s feed speed to
642 minimize blade and transducer vibration during dicing (Supplementary Fig. 2 and Supplementary
643 Discussion 7). Finally, the diced transducers were detached from the ultraviolet tape by an
644 ultraviolet curing system (UH104, Ultron Systems Inc.).

645 (2) Electrode printing and acoustic lens integration: The substrate for electrode printing
646 was prepared by spin-coating polydimethylsiloxane (Sylgard 184) at 3000 rpm for 60 s on a
647 glass slide, followed by curing in an 80 °C oven as a temporary substrate. Then,
648 polyimide/copper laminates (AC181200EN, DuPont) and the polydimethylsiloxane-coated glass
649 slide were activated by ultraviolet light (PSD series Digital UV Ozone System, Novascan) and
650 bonded together. Electrode patterns (such as electromagnetic shielding, mesh ground electrode,
651 and two signal electrodes) designed with AutoCAD (Autodesk) were laser ablated (G4 Pulsed
652 Fiber Laser, wavelength 1095 to 1065 nm, energy 0.228 mJ, frequency 35 kHz, speed 300 mm/s,
653 and pulse width 500 ns) on the polyimide/copper laminate (Supplementary Fig. 9). Two
654 polyimide masks were prepared by laser ablation for dispensing conductive epoxy on the
655 transducer bonding pads of the two signal electrode layers.

656 For acoustic lens integration, an aluminum block mold was designed with Solidworks
657 (Dassault Systemes) and machined using a computer-numerically controlled machining
658 (Tormach 1100MX, Tormach Inc.) at a spindle speed of 10,000 rpm and feed rate of 40 in/min
659 (Supplementary Fig. 6 and Supplementary Discussion 8). The mold was cleaned with
660 isopropanol before silicon elastomer was cured in the mold and used as the acoustic lens.

661 (3) Device packaging: First, polyimide tapes were adhered to two glass slides to ensure
662 device detachment after final packaging. Silicone (Ecoflex-0030, Smooth-On) mixed with black
663 dye was spin-coated on the polyimide tape at 4000 rpm for 60 s, followed by curing at room
664 temperature for 2 h. The electromagnetic shielding layer, which was transferred onto a water-
665 soluble tape (AQUASOL), and the silicone-coated glass slide was activated by ultraviolet light
666 and bonded together, followed by heating in an 80 °C oven for 30 min. After the water-soluble

667 tape was dissolved, a silicone layer was spin-coated on top at 4000 rpm for 60 s followed by
668 curing.

669 Similarly, the first layer of the signal electrode was aligned and transferred onto the
670 electromagnetic shielding layer via a water-soluble tape. A polyimide mask was placed on the
671 signal electrode to protect the transducer bonding pads of the electrode from another silicone
672 layer spin-coated on top. After the polyimide mask was removed and the silicone layer was
673 cured, the second layer of the signal electrode was aligned and stacked onto the first layer of the
674 signal electrode. Conductive epoxy was dispensed onto the transducer bonding pads of both
675 signal electrodes through a polyimide mask. After the mask was removed, the backing layer side
676 of the diced transducers was aligned and bonded by curing the conductive epoxy for 8 h at room
677 temperature and then 2 h at 40 °C. Flexible printed circuit cables were bonded to the signal
678 electrodes via solder paste ($\text{Sn}_{42}\text{Bi}_{57.6}\text{Ag}_{0.4}$, m.p. 138 °C).

679 The mesh ground electrode was bonded to a silicone-coated glass slide. After conductive
680 epoxy was dispensed using a polyimide mask, the mesh ground electrode was aligned and cured
681 onto the transducers. The exterior boundaries of the mesh ground electrode and electromagnetic
682 shielding layer were connected with vertical interconnect accesses by soldering copper wires
683 (Remington Industries) to create a Faraday cage (Supplementary Fig. 10 and Supplementary
684 Discussion 9)⁷⁶. After the device was fully encapsulated with silicone elastomer, the glass slides
685 were removed. Finally, the acoustic lens was aligned and bonded with silicone elastomer onto
686 the packaged transducers.

687

688 **Quality assurance**

689 The UPatch was transmitted at a frequency of 2.5 MHz with a sampling rate of 10 MHz.
690 Apodization was uniform across 64 channels with the imaging view angle of 45°. The number of
691 compounding angles was 21 with a step size of 0.75° for B-mode imaging. The ensemble length
692 was 14 for color flow mode. Doppler modes utilized a pulse repetition frequency of 3000 Hz.
693 The sample gate size for spectral Doppler was 2 mm.

694 The UPatch was characterized using two phantom setups and compared to a handheld
695 clinical ultrasound device (P4-1, ATL), both transmitting at 2.5 MHz. Both the UPatch and the
696 handheld clinical ultrasound device (P4-1, ATL) were connected to the Vantage 256
697 (Verasonics), rather than connecting the P4-1 device to a clinical backend system (Voluson E10,
698 GE). This method allows comparison of the probe performance more fairly and avoids
699 confounding effects from differences in backend signal processing.

700 First, the brightness mode was characterized with a multipurpose phantom (CIRS ATS
701 539, CIRS Inc.) (Supplementary Fig. 15)^{37,38}. Monofilament wires were used to determine the
702 axial and lateral resolutions. A volume of water on top of the phantom was used as a standoff to
703 characterize depths up to 20 cm. The distance between two adjacent pixels in the axial and lateral
704 directions was calculated as:

$$705 \quad \Delta y = \frac{depth}{N_{pixel,axial} - 1} \quad (1)$$

$$706 \quad \Delta x = \frac{depth}{N_{pixel,lateral} - 1} \quad (2)$$

707 The full width at half maximum of the point spread function for each wire in the axial
708 and lateral directions was measured. The axial and lateral resolutions were calculated by
709 multiplying the number of pixels within the full width at half maximum and adjacent pixel

710 distance. The six tissue–mimicking contrast targets in the phantom were used to characterize the
711 dynamic range and contrast-to-noise ratio³⁸. The dynamic range was calculated by linearly fitting
712 among the six greyscale targets and finding the maximum positive and negative contrasts
713 corresponding to grey values of 255 and 0. Then, the negative one was subtracted from the other.
714 The contrast-to-noise ratio was calculated by:

$$715 \quad \text{Contrast-to-noise ratio} = \frac{|\mu_{in} - \mu_{out}|}{\sqrt{\sigma_{in}^2 + \sigma_{out}^2}} \quad (3)$$

716 where μ_{in} and σ_{in} are the mean and standard deviation of pixel intensities within each target, and
717 μ_{out} and σ_{out} are the mean and standard deviation of pixel intensities outside each target. The
718 contrast and contrast-to-noise ratio were computed based on displayed images rather than raw
719 radiofrequency signals or in-phase and quadrature (I/Q) data, meaning that the values were
720 derived from log-compressed images⁷⁷.

721 The color and spectral Doppler modes were characterized with Doppler fluid (769DF,
722 CIRS Inc.) pumped into a Doppler phantom (CIRS ATS 523A, CIRS Inc.) with 2, 4, 6, and 8
723 mm diameter using a peristaltic pump (Supplementary Fig. 16)³⁹. The UPatch was positioned at
724 varying distances from 30 mm to 120 mm at intervals of 10 mm from the phantom. The signal-
725 to-noise ratio in the color flow images was calculated by increasing the color gain to maximum
726 to obtain a noise level in the tissue mimicking phantom. The accuracy of spectral Doppler was
727 measured by comparison to a known velocity from the peristaltic pump at different depths and
728 velocities.

729

730 **Acoustic exposure and thermal measurement protocols**

731 (1) Hydrophone: A needle hydrophone (HNP-0400, ONDA) was connected to a right-
 732 angle adapter (ONDA), pre-amplifier (AH-2010-100, ONDA), and DC block (BNP, ONDA)
 733 and suspended in deionized water (Supplementary Fig. 24)⁷⁸. The signals were read with an
 734 oscilloscope (PicoScope 5000 Series, Pico Technology, Cambridgeshire). At 2.5 MHz, the
 735 effective sensitive element diameter (a more meaningful measure of spatial resolution than the
 736 geometrical sensitive element diameter, which was 400 μm) was estimated to be 480 μm ⁷⁹. The
 737 uncertainties of hydrophone-based pressure, intensity, and power measurements are $\sim 15\%$ ⁸⁰.

738 The hydrophone system was calibrated < 1 year before the measurement. The calibration $M_c(f)$
 739 is the hydrophone end-of-cable open circuit sensitivity, which can be converted by:

$$740 \quad M_C(f)_{V/Pa} = 10^{\frac{M_C(f)_{dB \text{ re. } 1V/\mu Pa} + 120}{20}} \quad (4)$$

741 where $M_C(f)_{V/Pa}$ is the sensitivity in volts per pascal and $M_C(f)_{dB \text{ re. } 1V/\mu Pa}$ is the sensitivity in
 742 decibels relative to 1 volt per micropascals⁷⁸. The manufacturer's sensitivity magnitude data (i.e.,
 743 relative calibration from 1 to 20 MHz) was used to perform magnitude-based waveform
 744 deconvolution to compensate for the hydrophone's nonuniform frequency response in the signal
 745 spectrum (Supplementary Fig. 24). Magnitude-based deconvolution has been shown to be nearly
 746 as effective as complex deconvolution for improving the accuracy of pressure and intensity
 747 measurements⁸¹. Additionally, because the ratio of the hydrophone sensitive element diameter d_g
 748 to the product of the wavelength λ and $F/\#$ (ratio of focal distance to aperture width) $\ll 1$, a
 749 hydrophone spatial averaging correction was not necessary⁸².

750 Considering the capacitive load of the preamplifier when converting the voltage
 751 measurements to pressure values, the loaded sensitivity $M_L(f)$ can be estimated as:

752
$$M_L(f) = G(f)M_C(f)_{V/Pa} \frac{C_H}{C_H + C_A + C_C} \quad (5)$$

753 where $G(f)$ is the preamplifier gain (20 dB in this study), C_H is the capacitance of hydrophone
 754 (70 pF in this study), C_A is the capacitance of preamplifier (7 pF in this study), and C_C is the
 755 capacitance of right-angle adapter (1.6 pF in this study)⁷⁸.

756 A hydrophone controlled by a 3D linear motor in a water tank was used to measure the
 757 acoustic signal intensity (Supplementary Fig. 24). Transverse scans with scanning increments of
 758 $\Delta x = 0.5$ mm (approximately one effective hydrophone diameter) and $\Delta y = 0.5$ mm and an axial
 759 scan with scanning increments of $\Delta z = 0.5$ mm from break-point depth to focal depth were
 760 performed (Supplementary Discussion 11)⁸³. Two different beamforming methods were
 761 measured separately: diverging beam (for brightness and color flow mode) and focused beam
 762 (for spectral Doppler mode) that was focused at every 1 cm depth (between 5 to 15 cm) along the
 763 beam axis. The UPatch was activated at 30 V with a pulse repetition frequency of 3000 Hz.
 764 Power was derived from the hydrophone by integrating over a transverse plane within the beam
 765 cross-sectional area where the intensity was at least -26.2 dB of the peak value. All
 766 measurements were calculated based on the settings used for duplex imaging and spectral
 767 Doppler because these were the modes utilized during continuous monitoring in this study.

768 (2) Radiation force balance: Power measurements were obtained from a radiation force
 769 balance (RFB-2000, ONDA, Sunnyvale, CA) with a flat absorbing target, which could
 770 accurately measure power levels up to 2 W (Supplementary Fig. 25)⁸⁴. First, a 1 g weight was
 771 used to calibrate the radiation force balance. The calibration constant obtained was 0.9699 A/N,
 772 which fell in the range designed by ONDA, 0.9–1.1 A/N. The distance between the radiation
 773 force balance and the UPatch was set to ≥ 1 cm to avoid thermal and electrical coupling effects

774 between the radiation force balance and the UPatch. Acoustic output power was obtained from
775 the entire aperture of the UPatch, and the bounded-square output power over a 1 cm² area was
776 measured by masking the UPatch.

777 The thermal index was calculated based on acoustic output power measurements from
778 both the radiation force balance and hydrophone scan in the transverse plane, providing two
779 independent measurements to minimize uncertainty in the calculation⁴⁶.

780 (3) Surface temperature testing: The surface temperature of the UPatch was evaluated
781 under two scenarios to simulate clinical conditions based on IEC 60601-2-37 (ref. ⁸⁵). Although
782 the standard requires only 30-min testing⁸⁵, we extended the assessments to 48 h to ensure
783 compliance with regulatory standards even under prolonged operation.

784 First, a phantom test was performed to replicate the setup in the hospital (Supplementary
785 Fig. 23). The phantom consisted of a silicone-based skin (NPL, UK) and agar-based tissue (NPL,
786 UK) with acoustic and thermal properties similar to those of human skin and tissue, respectively.
787 A type K thermocouple (5SRTC-TT-KI-40-1M, OMEGA, Norwalk, Connecticut) with a
788 thickness of 75 μm (\ll ultrasound wavelength at 2.5 MHz) was placed on top of the skin
789 mimicking phantom to measure the surface temperature of the UPatch⁴⁵.

790 Second, to evaluate thermal changes when the UPatch was activated in air, surface
791 temperature was measured. Because the UPatch/air interface has a higher acoustic impedance
792 mismatch compared to that of the UPatch/tissue phantom interface, more heat is expected to be
793 generated in the air⁴⁵. The UPatch was suspended on a clean surface in a stationary position with
794 minimal airflow across the transducer area. The same thermocouple was adhered to the UPatch
795 for temperature measurement.

796

797 **Evaluation of the vessel-tracking algorithm**

798 The comparative analysis of the lateral and axial discrepancies in defining the sample
799 gates between the tracking algorithm and a sonographer was performed using double-blind
800 method (Supplementary Discussion 18). The tracking algorithm and the sonographer each
801 selected sample gates independently from 1,000 duplex images, without access to the other's
802 chosen locations. This design was used to prevent bias in sample gate placement and to ensure an
803 objective comparison between algorithm-selected and sonographer-selected measurements, with
804 discrepancies quantified by the spatial distance between the selected gates. The lateral and axial
805 discrepancies were calculated between the two sample gates (Fig. 3d). A 2 mm sample gate
806 length is commonly employed in hospitals (Supplementary Discussion 19)¹. Thus, within a 2 mm
807 discrepancy between the tracking algorithm and the sonographer, the sample gate was considered
808 to acquire spectral Doppler signals accurately.

809 Additionally, a new dataset was acquired, containing 500 duplex images from scanning
810 the clinical device on a participant and 500 duplex images from the UPatch on another
811 participant. The tracking algorithm identified the sample gates in all 1,000 images. We engaged
812 three experienced sonographers, each with 30, 8, and 20 years of fetal ultrasonography
813 experience, to independently assess the tracking performance on 1,000 images (Supplementary
814 Fig. 39). This validation method aligns with the recently FDA-cleared cardiac Doppler tracking
815 algorithm⁸⁶, which also relied on three sonographers and evaluated only 168 images. All three
816 sonographers evaluated the tracking algorithm with a customized graphical user interface in
817 Matlab R2023b (Mathworks). “Optimal” was defined by the sonographer as the tracked sample

818 gate that could potentially be used for spectral Doppler acquisition, “Sub-optimal” was defined
819 as the sample gate potentially providing low-quality spectral Doppler signals, and “Non-
820 diagnostic” was defined as the sample gate that could not provide any spectral Doppler signal
821 (Supplementary Fig. 39 and Supplementary Discussion 18).

822 Finally, the tracking algorithm was evaluated with the UPatch based on the systolic-to-
823 diastolic ratio of a participant (Supplementary Discussion 18). Each pair of measurements was
824 acquired sequentially by a sonographer and the tracking algorithm. For the mean difference \pm
825 standard deviation between the UPatch and clinical device, it is expected that the device
826 differences and physiological variability increase the spread of values, even when the overall
827 bias remains very small (Fig. 2f). By eliminating inter-device variability and focusing merely on
828 sample gate selection, the tracking algorithm analysis yields a narrower distribution, even though
829 the mean offset is slightly larger (Fig. 3f). Notably, the mean values reflect different reference
830 comparisons and are not expected to be identical, whereas the reduced standard deviation reflects
831 the elimination of device-related variability.

832

833 **Human test protocol**

834 All human tests were approved by the Institutional Review Board of the University of
835 California San Diego (#804817) and the UK Research Ethics Committee (23/WA/0032). The
836 participants all gave voluntary consent to the UPatch tests, and all measurements were conducted
837 by a clinician. The study included 62 participants for accuracy validation (Fig. 2f, Table 1, and
838 Supplementary Fig. 32) and 52 participants for continuous monitoring (Supplementary Figs 40–
839 95). This dataset captures a broad range of clinical conditions across the study cohort, including

840 variations in fetal biometry (e.g., small and large for gestational age) (Fig. 4e–i and
841 Supplementary Figs 96 and 97) and gestational age (Table 1). For the validation test, three pairs
842 of measurements were acquired from the UPatch and a handheld clinical ultrasound device
843 (Voluson E10, GE) on 62 participants. For continuous monitoring, the clinical device was used
844 to locate the position of the vessel. Then, the UPatch was taped on the maternal abdomen for
845 continuous monitoring. The current study was conducted under inpatient conditions, where
846 pregnant participants were free to move within the limits of standard clinical monitoring. During
847 the recordings, the pregnant participants naturally moved within their beds, accompanied by
848 various fetal behavioral states, fetal movements, and uterine contractions.

849 While healthy pregnancies typically exhibit strong forward end diastolic flow, severe
850 pathological pregnancies can have reduced forward end diastolic flow, absent end diastolic flow,
851 or reversed end diastolic flow, resulting in weaker diastolic spectral content and increased
852 waveform variability^{3,87}. In these cases, pulse repetition frequency of Doppler ultrasound
853 becomes particularly critical: if it is too high, low velocity components are compressed near the
854 waveform baseline and become difficult to distinguish from noise, while a pulse repetition
855 frequency that is too low risks aliasing at peak systolic velocities³³. To ensure a fair and
856 clinically relevant comparison across healthy and severe pathological conditions, validation was
857 performed using matched pulse repetition frequency settings between the UPatch and clinical
858 ultrasound system.

859 The UPatch was designed for easy repositioning as needed. It is movable, can be
860 sanitized with alcohol wipes, and can be repositioned without compromising functionality. This
861 allows adaptability in clinical use while maintaining hygiene and patient comfort.

862 For fetal biometry, estimated fetal weight (*EFW*) was calculated based on Hadlock's IV
863 formula⁴⁹:
864 $EFW = 1.3596 - 0.00386AC \cdot FL + 0.0064HC + 0.00061BPD \cdot AC + 0.0424AC + 0.174FL$ (6)
865 where *AC* is abdominal circumference, *FL* is femur length, *HC* is head circumference, and *BPD*
866 is biparietal diameter.

867

868 **Data availability**

869 The data supporting the findings of this study are available in the main text or the
870 Supplementary Information.

871

872 **Code availability**

873 The code used in this study is available from GitHub
874 (<https://github.com/ParkingTom/Autonomous-tracking-algorithm>).

875

876 **Methods references**

- 877 76 Huang, Z. *et al.* Three-dimensional integrated stretchable electronics. *Nature Electronics*
878 **1**, 473-480 (2018).
879 77 Kempski, K. M., Graham, M. T., Gubbi, M. R., Palmer, T. & Lediju Bell, M. A.
880 Application of the generalized contrast-to-noise ratio to assess photoacoustic image quality.
881 *Biomed Opt Express* **11**, 3684-3698 (2020).
882 78 <https://www.ondacorp.com/Handbook/>.
883 79 Wear, K. A. & Shah, A. Nominal Versus Actual Spatial Resolution: Comparison of
884 Directivity and Frequency-Dependent Effective Sensitive Element Size for Membrane,
885 Needle, Capsule, and Fiber-Optic Hydrophones. *IEEE Transactions on Ultrasonics,*
886 *Ferroelectrics, and Frequency Control* **70**, 112-119 (2023).

887 80 Harris, G. R. *et al.* Hydrophone Measurements for Biomedical Ultrasound Applications: A
888 Review. *IEEE Transactions on Ultrasonics, Ferroelectrics, and Frequency Control* **70**, 85-
889 100 (2023).

890 81 Wear, K. A., Gammell, P. M., Maruvada, S., Liu, Y. & Harris, G. R. Improved
891 measurement of acoustic output using complex deconvolution of hydrophone sensitivity.
892 *IEEE Transactions on Ultrasonics, Ferroelectrics, and Frequency Control* **61**, 62-75
893 (2014).

894 82 Wear, K. A. Hydrophone Spatial Averaging Correction for Acoustic Exposure
895 Measurements From Arrays-Part I: Theory and Impact on Diagnostic Safety Indexes. *IEEE*
896 *Trans Ultrason Ferroelectr Freq Control* **68**, 358-375 (2021).

897 83 Szabo, T. L. *Diagnostic Ultrasound Imaging: Inside Out*. (Academic Press, 2014).

898 84 [https://www.ondacorp.com/radiation-
899 force/#:~:text=Designed%20specifically%20for%20easy%20Ultrasound,and%20with%20
900 0associated%20IEC%20standards.](https://www.ondacorp.com/radiation-force/#:~:text=Designed%20specifically%20for%20easy%20Ultrasound,and%20with%20associated%20IEC%20standards.)

901 85 International Electrotechnical Commission. IEC 60601-2-37:2024 “Medical electrical
902 equipment - Part 2-37: Particular requirements for the basic safety and essential
903 performance of ultrasonic medical diagnostic and monitoring equipment”. *International*
904 *Electrotechnical Commission, Geneva, Switzerland*, Ed. 3.0 (2024).

905 86 https://www.accessdata.fda.gov/cdrh_docs/pdf23/K232145.pdf.

906 87 Kennedy, A. M. & Woodward, P. J. A Radiologist’s Guide to the Performance and
907 Interpretation of Obstetric Doppler US. *RadioGraphics* **39**, 893-910 (2019).
908

909 **Additional information**

910 **Supplementary Information** is available for this paper.

911 **Correspondence and requests for materials** should be addressed to Sheng Xu and Antoniya
912 Georgieva.

913 **Reprints and permissions information** is available at <http://www.nature.com/reprints>.
914

Table of Contents

1		
2	Supplementary Discussion 1: Continuous prenatal monitoring.....	4
3	Supplementary Discussion 2: Wearable fetal monitors.....	4
4	Supplementary Discussion 3: Implications and limitations of cardiocography.....	6
5	Supplementary Discussion 4: Blood flow monitoring with ultrasonography.....	8
6	Supplementary Discussion 5: Clinically relevant vessels for monitoring.....	9
7	Supplementary Discussion 6: Novelty of the UPatch.....	10
8	Supplementary Discussion 7: Transducer dicing.....	11
9	Supplementary Discussion 8: Acoustic lens.....	13
10	Supplementary Discussion 9: Soft Faraday cage.....	14
11	Supplementary Discussion 10: Umbilical cord phantom.....	17
12	Supplementary Discussion 11: Acoustic exposure safety parameters.....	18
13	Supplementary Discussion 12: Thermal safety of the UPatch.....	20
14	Supplementary Discussion 13: Beamforming of the UPatch on the abdomen.....	21
15	Supplementary Discussion 14: Vessel tracking algorithms.....	21
16	Supplementary Discussion 15: Working principles of vessel tracking algorithm.....	23
17	Supplementary Discussion 16: Umbilical vein tracking.....	23
18	Supplementary Discussion 17: Response time during image segmentation.....	24
19	Supplementary Discussion 18: Evaluation of the autonomous tracking algorithm.....	25
20	Supplementary Discussion 19: Ultrasound sample gate.....	26
21	Supplementary Discussion 20: Continuous monitoring of the umbilical artery.....	27
22	Supplementary Discussion 21: Ultrasound incident angle.....	28
23	Supplementary Discussion 22: Abnormality in a pre-eclamptic participant.....	29
24	Supplementary Discussion 23: Clinical importance of continuous monitoring of blood flow.....	30
25	Supplementary Discussion 24: Data processing.....	31
26	Supplementary Discussion 25: Predictive modeling.....	31
27	Supplementary Discussion 26: Circuit integration.....	32
28	Supplementary Fig. 1 Existing wearable fetal monitors.....	33
29	Supplementary Fig. 2 Dicing strategies.....	34
30	Supplementary Fig. 3 1–3 composite side of the transducers diced with different strategies....	35
31	Supplementary Fig. 4 Comparison of transducers diced with different strategies.....	36
32	Supplementary Fig. 5 Design of the acoustic lens.....	37
33	Supplementary Fig. 6 Fabrication of the acoustic lens.....	38
34	Supplementary Fig. 7 Characterization of the acoustic lens.....	39
35	Supplementary Fig. 8 Elevational beamwidth during beam steering.....	40
36	Supplementary Fig. 9 Photographs of each layer of electrodes.....	41
37	Supplementary Fig. 10 Faraday cages.....	42
38	Supplementary Fig. 11 Effects of the soft Faraday cage on phantom measurements.....	43
39	Supplementary Fig. 12 Effects of the soft Faraday cage on adult carotid artery measurements.....	44
40	Supplementary Fig. 13 Effects of the soft Faraday cage on noise levels in duplex imaging.....	45
41	Supplementary Fig. 14 Photographs of the UPatch on a pregnant woman.....	46
42	Supplementary Fig. 15 Brightness mode characterizations.....	47
43	Supplementary Fig. 16 Doppler characterizations.....	48
44	Supplementary Fig. 17 Blood flow measurement accuracy.....	50
45	Supplementary Fig. 18 Design of the umbilical cord phantom.....	51
46	Supplementary Fig. 19 Stereolithographic fabrication of the umbilical cord phantom.....	52

47	Supplementary Fig. 20	Measurements on the carotid artery of a healthy adult.....	53
48	Supplementary Fig. 21	Measurements on the abdominal cross-section of a healthy adult	54
49	Supplementary Fig. 22	Surface temperature characterizations.....	56
50	Supplementary Fig. 23	Safety measurements with a hydrophone	58
51	Supplementary Fig. 24	Safety measurements with a radiation force balance.....	59
52	Supplementary Fig. 25	Deformation of the UPatch.....	60
53	Supplementary Fig. 26	Fetal biometry	62
54	Supplementary Fig. 27	Spectral Doppler of the umbilical artery	63
55	Supplementary Fig. 28	Spectral Doppler of the umbilical vein.....	64
56	Supplementary Fig. 29	Envelope extraction from spectral Doppler signals.....	65
57	Supplementary Fig. 30	Statistical analysis of the pulsatility index and the resistance index	66
58	Supplementary Fig. 31	Imaging with a handheld clinical ultrasound device	67
59	Supplementary Fig. 32	Data acquisition processes of the UPatch.....	68
60	Supplementary Fig. 33	Recognition of the primary region of the umbilical artery	69
61	Supplementary Fig. 34	Identification of the centroid for sample gate placement	70
62	Supplementary Fig. 35	Benchmarking the tracking algorithm against deep learning methods..	71
63	Supplementary Fig. 36	Continuous fetal monitoring using the UPatch in Participant #1	72
64	Supplementary Fig. 37	Continuous fetal monitoring using the UPatch in Participant #2	73
65	Supplementary Fig. 38	Continuous fetal monitoring using the UPatch in Participant #3	74
66	Supplementary Fig. 39	Continuous fetal monitoring using the UPatch in Participant #4	75
67	Supplementary Fig. 40	Continuous fetal monitoring using the UPatch in Participant #5	76
68	Supplementary Fig. 41	Continuous fetal monitoring using the UPatch in Participant #6	77
69	Supplementary Fig. 42	Continuous fetal monitoring using the UPatch in Participant #7	78
70	Supplementary Fig. 43	Continuous fetal monitoring using the UPatch in Participant #8	79
71	Supplementary Fig. 44	Continuous fetal monitoring using the UPatch in Participant #9	80
72	Supplementary Fig. 45	Continuous fetal monitoring using the UPatch in Participant #10	81
73	Supplementary Fig. 46	Continuous fetal monitoring using the UPatch in Participant #11	82
74	Supplementary Fig. 47	Continuous fetal monitoring using the UPatch in Participant #12	83
75	Supplementary Fig. 48	Continuous fetal monitoring using the UPatch in Participant #13	84
76	Supplementary Fig. 49	Continuous fetal monitoring using the UPatch in Participant #14	85
77	Supplementary Fig. 50	Continuous fetal monitoring using the UPatch in Participant #15	86
78	Supplementary Fig. 51	Continuous fetal monitoring using the UPatch in Participant #16	87
79	Supplementary Fig. 52	Continuous fetal monitoring using the UPatch in Participant #17	88
80	Supplementary Fig. 53	Continuous fetal monitoring using the UPatch in Participant #18	89
81	Supplementary Fig. 54	Continuous fetal monitoring using the UPatch in Participant #19	90
82	Supplementary Fig. 55	Continuous fetal monitoring using the UPatch in Participant #20	91
83	Supplementary Fig. 56	Continuous fetal monitoring using the UPatch in Participant #21	92
84	Supplementary Fig. 57	Continuous fetal monitoring using the UPatch in Participant #22	93
85	Supplementary Fig. 58	Continuous fetal monitoring using the UPatch in Participant #23	94
86	Supplementary Fig. 59	Continuous fetal monitoring using the UPatch in Participant #24	95
87	Supplementary Fig. 60	Continuous fetal monitoring using the UPatch in Participant #25	96
88	Supplementary Fig. 61	Continuous fetal monitoring using the UPatch in Participant #26	97
89	Supplementary Fig. 62	Continuous fetal monitoring using the UPatch in Participant #27	98
90	Supplementary Fig. 63	Continuous fetal monitoring using the UPatch in Participant #28	99
91	Supplementary Fig. 64	Continuous fetal monitoring using the UPatch in Participant #29	100
92	Supplementary Fig. 65	Continuous fetal monitoring using the UPatch in Participant #30	101

93	Supplementary Fig. 66	Continuous fetal monitoring using the UPatch in Participant #31	102
94	Supplementary Fig. 67	Continuous fetal monitoring using the UPatch in Participant #32	103
95	Supplementary Fig. 68	Continuous fetal monitoring using the UPatch in Participant #33	104
96	Supplementary Fig. 69	Continuous fetal monitoring using the UPatch in Participant #34	105
97	Supplementary Fig. 70	Continuous fetal monitoring using the UPatch in Participant #35	106
98	Supplementary Fig. 71	Continuous fetal monitoring using the UPatch in Participant #36	107
99	Supplementary Fig. 72	Continuous fetal monitoring using the UPatch in Participant #37	108
100	Supplementary Fig. 73	Continuous fetal monitoring using the UPatch in Participant #38	109
101	Supplementary Fig. 74	Continuous fetal monitoring using the UPatch in Participant #39	110
102	Supplementary Fig. 75	Continuous fetal monitoring using the UPatch in Participant #40	111
103	Supplementary Fig. 76	Continuous fetal monitoring using the UPatch in Participant #41	112
104	Supplementary Fig. 77	Continuous fetal monitoring using the UPatch in Participant #42	113
105	Supplementary Fig. 78	Continuous fetal monitoring using the UPatch in Participant #43	114
106	Supplementary Fig. 79	Continuous fetal monitoring using the UPatch in Participant #44	115
107	Supplementary Fig. 80	Continuous fetal monitoring using the UPatch in Participant #45	116
108	Supplementary Fig. 81	Continuous fetal monitoring using the UPatch in Participant #46	117
109	Supplementary Fig. 82	Continuous fetal monitoring using the UPatch in Participant #47	118
110	Supplementary Fig. 83	Continuous fetal monitoring using the UPatch in Participant #48	119
111	Supplementary Fig. 84	Continuous fetal monitoring using the UPatch in Participant #49	120
112	Supplementary Fig. 85	Continuous fetal monitoring using the UPatch in Participant #50	121
113	Supplementary Fig. 86	Continuous fetal monitoring using the UPatch in Participant #51	122
114	Supplementary Fig. 87	Continuous fetal monitoring using the UPatch in Participant #52	123
115	Supplementary Fig. 88	Box plots of fetal heart rate during continuous monitoring	124
116	Supplementary Fig. 89	Box plots of pulsatility index during continuous monitoring.....	125
117	Supplementary Fig. 90	Box plots of systolic-to-diastolic ratio during continuous monitoring	126
118	Supplementary Fig. 91	Box plots of resistance index during continuous monitoring.....	127
119	Supplementary Fig. 92	Scatterplot of pulsatility index against FHR	128
120	Supplementary Fig. 93	Gestational trends in FHR and pulsatility index.....	129
121	Supplementary Fig. 94	Gestational trends in systolic-to-diastolic ratio and resistance index..	130
122	Supplementary Fig. 95	Risk stratification in systolic-to-diastolic ratio and resistance index ..	131
123	Supplementary Fig. 96	Predictive modeling using logistic regression	132
124	Supplementary Video 1	Real-time tracking.....	133
125	References.....		134

126

127

128 **Supplementary Discussion 1: Continuous prenatal monitoring**

129 The primary goal of antepartum fetal surveillance (also referred to as prenatal monitoring) is to
130 prevent irreversible fetal injury or stillbirth¹. Current methods, including cardiotocography², fetal
131 movement³, and ultrasound-based assessments⁴, are performed intermittently and seek to detect
132 subacute uteroplacental insufficiency^{1,5}. These methods focus on monitoring the gradual changes
133 in fetal health, allowing healthcare providers to intervene before any permanent damage occurs.
134 However, the intermittent nature of these assessments means that they may miss sudden, acute
135 events that can lead to fetal compromise.

136 Many stillbirths are suspected to result from acute events, such as umbilical cord accidents,
137 placental abruption, and premature rupture of the membrane⁵. These acute events cannot be
138 predicted by the current intermittent approaches. Umbilical cord accidents, including cord
139 compression, nuchal cord (where the cord is wrapped around the baby's neck), and prolapsed cord
140 (where the cord slips into the birth canal ahead of the baby), can lead to a rapid decrease in the
141 fetal oxygen supply⁶. Placental abruption is a serious pregnancy complication in which the
142 placenta partially or completely detaches from the inner wall of the uterus⁷. This detachment can
143 disrupt the supply of oxygen and nutrients to the fetus and cause severe internal bleeding in the
144 uterus⁷. Premature rupture of the membrane (also known as amniotic sac) can lead to infections
145 and preterm labor, posing high risks to both the mother and fetus⁸.

146 Continuous prenatal monitoring can detect both subacute and acute fetal compromise. It has the
147 potential to identify signs of sudden fetal distress as they occur, allowing for timely interventions
148 that could prevent stillbirth and other severe outcomes.

149

150 **Supplementary Discussion 2: Wearable fetal monitors**

151 Numerous wearable devices have emerged to extract fetal signals in combination with other
152 maternal sensors (Supplementary Fig. 1)⁹⁻¹¹. Fetal monitoring technologies vary considerably in
153 terms of sensing modality, number and configuration of sensors, spatial resolution, and clinical
154 application. These wearable devices can continuously detect fetal heart rate, electrocardiogram,
155 oximetry, and movements. Here, we provide a summary of state-of-the-art technologies,
156 highlighting general limitations. Additional technical details for these technologies can be found
157 in the cited references.

158 First, wearable fetal heart rate monitors, such as HeraBEAT (HeraMED)¹² and Moyo fetal heart
159 rate monitor (Moyo)¹³, have been introduced to address the limitations of handheld devices, such
160 as Sonoline B (Sonoline)¹⁴, SD1 (Edan)¹⁵, and Newman (Babybeat)¹⁶ that only offer intermittent
161 measurements. These devices utilize ultrasound and operate in continuous wave Doppler mode,
162 leveraging two ultrasound transducers for transceiving⁹. Although Doppler signals are intended to
163 originate from the movements of fetal heart valves, any movements are translated into signals⁹.
164 The absence of spatial resolution of the continuous wave Doppler mode is a crucial limitation
165 because it results in the mixing of different signals. Additionally, during advanced gestation, the
166 increased frequency of uterine contractions can influence fetal heart rate¹⁷. Consequently, the
167 measured fetal heart rate may not be accurate, and therefore, monitoring fetal heart rate alone does
168 not adequately reflect the physiological changes within the uterus.

169 To better understand how uterine contractions influence fetal heart rate, wearable
170 cardiocography can simultaneously monitor these two signals. Traditional wearable
171 cardiocography, such as Corometrics 250cx (GE Healthcare)¹⁸, Avalon FM50 (Philips)¹⁹, and
172 Sense4baby (Advanced Maternity Innovations)²⁰, relies on continuous wave Doppler for fetal
173 heart rate and a tocodynamometer for uterine contractions (Supplementary Fig. 1). Due to their
174 large form factor, these devices necessitate belts for optimal sensor placement and wired
175 connections to external hardware for power and signal transfer. Such fixations impose constraints
176 on the maternal abdomen, making them less feasible for prolonged use. Additionally, the
177 mechanical mismatch between the bulky devices and the maternal skin is prone to signal loss and
178 motion artifacts.

179 Minimally invasive methods, such as fetal scalp electrodes and intrauterine pressure catheters,
180 provide more direct measurements of fetal heart rate and uterine contractions, enhancing signal
181 integrity under critical conditions¹⁷. Accurate monitoring becomes essential in high-risk
182 pregnancies to enable prompt interventions because fetal and maternal movements can disrupt
183 cardiocography signals²¹. Additionally, amniotic sac rupture may reduce fluid levels, hindering
184 ultrasound transmission¹⁷. Scalp electrode provides direct fetal heart rate tracings by inserting
185 spiral wires into the fetal head. Intrauterine pressure catheters quantify the pressure intensity of the
186 uterine contraction, while tocodynamometers only monitor the contraction frequency and
187 duration²². However, the use of scalp electrodes and intrauterine catheters is restricted to labor
188 monitoring¹⁷. In addition, scalp electrodes may lead to complications such as scalp trauma¹⁷, while
189 intrauterine pressure catheters may cause infections and uterine rupture²².

190 More recently developed devices have focused on miniaturized and flexible wearable
191 cardiocography, such as ANNE (Sibel Health)²³ and Farus wearable ultrasound and
192 tocodynamometer (Farus)²⁴, which minimize the mechanical mismatch between the device and the
193 maternal skin (Supplementary Fig. 1). These devices integrate power, signal processors, and
194 wireless connections into the device casing, eliminating the need for securing belts. This
195 advancement largely improves portability and user-friendliness in wearable cardiocography.

196 Second, wearable electrocardiogram devices employ biopotential electrodes, such as AN24
197 (Monica Healthcare, now Novii by GE Healthcare)^{25,26}, Avalon beltless fetal monitoring solution
198 (Philips)²⁷, Invu (Nuvo)²⁸, Meridian M110 (MindChild Medical)²⁹, Bloomlife electrophysiological
199 monitor (Bloomlife)³⁰, Nemo fetal monitoring system (Nemo Healthcare)³¹, and Femom lite
200 (Biorithm)³². Maternal electrocardiograms ($\sim 200 \mu\text{V}$) often interfere with weak fetal
201 electrocardiograms ($\sim 3 \mu\text{V}$)²⁵. Additionally, movement and positional changes of the fetus cause
202 fluctuations in electrical impedance, further compromising signal integrity²⁵. To overcome the low
203 signal amplitude of fetal electrocardiograms, various systems utilize an array of electrodes on the
204 maternal abdomen with advanced signal decomposition algorithms to isolate the subtle fetal from
205 the maternal electrocardiograms. The AN24 uses a five-electrode configuration: one as a common
206 ground and the remaining four placed in upper, lower, right lateral, and left lateral positions,
207 achieving 85% reliability in estimating fetal heart rate (Supplementary Fig. 1)²⁶. The Meridian
208 M110 (MindChild Medical) uses 32 electrodes distributed across the maternal abdomen and has
209 demonstrated 89.9% reliability³³. While the increased electrode density enhances spatial resolution
210 to handle fetal movement and signal interference, the modest improvement in reliability suggests
211 that increasing the electrode count adds complexity to circuitry and signal processing but offers
212 diminishing marginal benefits.

213 Third, wearable fetal oximetry devices, such as Lumerah (Raydiant Oximetry)³⁴ and Storz
214 intrapartum fetal monitoring (Storz Technologies)³⁵, have been proposed to measure fetal blood
215 oxygen levels. However, light penetration through the various tissue layers poses immense
216 challenges, especially with signal interference from maternal signals and motion artifacts³⁶. For
217 example, while the initial placement of a wearable oximetry device can be optimized, fetal
218 movements may cause signal loss. Consequently, reliably measuring blood oxygen levels in
219 human fetuses has not yet been demonstrated.

220 Finally, wearable fetal movement devices are based on accelerometers (Supplementary Fig. 1)³⁷⁻
221 ⁴². Accelerometers can capture various signals, including both fetal and maternal movements,
222 which are often irregular³⁸. Additionally, when the position of the fetus changes, the signal
223 amplitude of different fetal movements also changes⁴². Therefore, it is challenging to distinguish
224 which signals are fetal movements. To improve signal quality, the integration of acoustic sensors
225 with accelerometers has been explored^{41,42}. These devices are currently in the proof-of-concept
226 phase, with belts and sleeves employed to secure the accelerometers, signal processing units, and
227 batteries.

228

229 **Supplementary Discussion 3: Implications and limitations of cardiotocography**

230 Cardiotocography measures fetal heart rate and uterine contractions⁹. Changes in baseline,
231 variability, and transient accelerations and decelerations of the fetal heart rate are due to the fetal
232 central nervous system's responses to various environmental changes¹⁷.

233 Fetal heart rate and heart rate variability serve as important indicators of fetal well-being^{9,17,43}.
234 These parameters reflect the physiological responses of the fetus under varying conditions,
235 particularly the oxygenation state. Thus, monitoring these parameters has been widely used for
236 identifying conditions arising from deprived oxygen levels, such as impending asphyxia during
237 labor⁴⁴.

238 Typically, the fetal heart rate lies within the range of 120–160 beats per minute (bpm), with the
239 baseline declining with advanced gestation⁹. Deviations from this range include bradycardia,
240 defined as a baseline below 120 bpm, and tachycardia, characterized as a baseline exceeding 160
241 bpm⁴³. Variability is categorized as absent, minimal (1 to 5 bpm), moderate (5 to 25 bpm), or
242 marked (>25 bpm)⁴³. Moderate and marked variabilities are often regarded as normal physiological
243 responses as the sympathetic and parasympathetic nervous systems adjust the fetal heart rate based
244 on dynamic in-utero conditions⁴³. Absent or minimal variabilities may indicate hypoxia but are
245 not always reliable as they may also be associated with other factors such as fetal sleep cycle⁹, and
246 thus need further evaluation⁴³.

247 Acceleration (transient increase in the fetal heart rate) suggests optimal fetal well-being¹⁷. Such
248 elevation is often associated with fetal movements or external stimuli. Importantly, regular
249 occurrences of accelerations are a reassuring sign, indicating that the fetus is well-oxygenated and
250 the nervous system is responsive to its movements and external stimuli¹⁷.

251 Uterine contractions are used in monitoring the onset of active labor as the uterus and cervix
252 prepare for labor²². The tocodynamometer measures the frequency and duration of uterine
253 contractions by placing a pressure transducer on the maternal abdomen to sense and record changes
254 in tension as the uterus contracts²².

255 The uterus, composed of smooth muscles, is capable of progressive stretching¹⁷. In the antepartum
256 period, two primary types of contractions are observed¹⁷. First, sporadic and weak contractions of
257 short duration occur in a localized area in the uterus. These contractions often occur in early stages
258 of pregnancy¹⁷. Second, Braxton Hicks contractions, which are more intense, may take place
259 irregularly, approximately once per hour at around 30-week of gestation, increasing up to every 5
260 to 10 min at term¹⁷. More frequent and regular contractions signal the onset of labor, leading to
261 cervical dilation¹⁷. During labor, uterine contraction monitoring is used to detect labor
262 abnormalities. For example, hypocontractile or hypercontractile uterine activity can lead to
263 prolonged labor or uterine tachysystole, respectively, posing risks to fetal health¹⁷.

264 By using cardiotocography during labor, the timing between fetal heart rate and uterine contraction
265 has been associated with fetal health¹⁷. The fetal heart rate response to uterine contractions can
266 indicate how well the fetus is coping with external stress¹⁷. Specifically, these patterns are
267 categorized into three distinct types (i.e., early, late, and variable decelerations), each defined
268 based on the temporal relationship between fetal heart rate and uterine contractions⁴³.

269 Early deceleration is characterized by a concurrent decline in fetal heart rate with the onset of
270 uterine contraction⁴³. This phenomenon is a result of pressure exerted on the fetal head during
271 contraction, which in turn alters cerebral blood flow¹⁷. Then, the central nervous system is
272 stimulated, prompting a deceleration in fetal heart rate. As the contraction amplifies, the fetal heart
273 rate continues to decelerate. Finally, as contraction subsides, the fetal heart rate returns to the
274 baseline. Early deceleration demonstrates the adaptive capabilities of the fetal central nervous
275 system and is not indicative of fetal distress⁴³.

276 Late deceleration is characterized by a subsequent decline in fetal heart rate following the onset of
277 uterine contraction⁴³. Specifically, the nadir of the fetal heart rate is observed post-peak contraction.
278 This deceleration process is commonly attributed to transient fetal hypoxia due to placental
279 insufficiency¹⁷. In scenarios where placental function is sub-optimal, diminished blood flow during
280 contractions may result in reduced oxygenation from the placenta to the fetus¹⁷. In response to the
281 low oxygenation state, the fetal central nervous system decelerates the heart rate. As contraction
282 ends, the fetal heart rate begins to recover and reverts to its baseline heart rate.

283 Variable deceleration is characterized by the unpredictable onset of fetal heart rate relative to the
284 timing of uterine contractions⁴³. These decelerations exhibit an abrupt onset and decline without a
285 consistent relationship to the contraction phase. The predominant factor for variable decelerations
286 is umbilical cord compression, leading to a transient decrease in blood flow between the fetus and
287 the placenta¹⁷. This hemodynamic alteration elicits a temporary deceleration in fetal heart rate. As
288 the umbilical cord blood flow returns to normal, the fetal heart rate returns back to the baseline.

289 While cardiotocography is useful, monitoring merely the fetal heart rate and uterine contraction
290 comes with inherent challenges and has led to misdiagnosis^{9,45}. Consequently, cardiotocography
291 cannot serve as a stand-alone diagnostic tool and requires additional sensors for a more
292 comprehensive and accurate assessment of fetal well-being.

293 First, cardiotocography interprets fetal well-being based on the central nervous system's response
294 to alterations in blood flow^{9,17}. Thus, the reliability of these measurements is constrained by the
295 complexity of the underlying biological processes. This means that these measurements indirectly
296 reflect fetal well-being, serving more as a potential consequence rather than a direct cause of the
297 fetal health.

298 Second, alterations in fetal heart rate are one of the many central nervous responses. Others include
299 systemic vasoconstriction and vasodilation of the intricate cardiovascular system⁴⁶. In severe cases,
300 the brain-sparing effect may be activated, resulting in the dilation of cerebral vessels to enhance
301 brain perfusion, while vessels in other areas are constricted⁴⁶.

302 Third, the intrinsic variability in fetal heart rate presents challenges in deciphering the significance
303 of specific patterns⁹. Determining the threshold for clinical intervention requires distinguishing
304 between transient benign changes and those that are indicative of sustained fetal compromise. For
305 instance, growth-restricted fetuses can sometimes exhibit a normal fetal heart rate range¹⁷ and
306 variability², while fetuses with bradycardia can be found to be well-oxygenated post-delivery⁴⁵.
307 Such data can precipitate unnecessary interventions, including Cesarean sections or operative
308 vaginal deliveries, thereby exposing both the mother and the fetus to additional risks, including
309 potential postnatal complications⁹.

310 Consequently, cardiotocography has a false-positive rate of up to ~50% (ref. ⁹), leading to
311 unnecessary interventions and preterm birth^{2,47}. While cardiotocography is a valuable source of
312 information, findings must be integrated within a broader clinical context, limiting the
313 effectiveness of cardiotocography as a stand-alone diagnostic approach.

314

315 **Supplementary Discussion 4: Blood flow monitoring with ultrasonography**

316 Ultrasonography is an invaluable tool in contemporary obstetrics due to its safety and diagnostic
317 effectiveness⁴⁸⁻⁵¹. Unlike fetal heart rate monitoring, which measures the response of the fetal
318 central nervous system to alterations in blood flow (Supplementary Discussion 3), spectral Doppler
319 ultrasound provides a direct quantitative measurement of the fetal and placental blood flow^{1,52}.

320 First, prenatal diagnostic options are notably limited compared to those available postnatally.
321 Postnatal diagnostics utilize direct observations (such as skin paleness, scarring, and coughing),
322 pain symptoms, and various measurements (such as blood pressure, body temperature, and oxygen
323 saturation). In comparison, prenatal assessments are based on maternal perceptions and ultrasound-
324 based measurements^{3,53}. Additionally, while postnatal diagnoses often use blood pressure
325 measurements as a standard indicator of cardiovascular well-being, prenatal monitoring heavily
326 relies on ultrasound-based blood flow assessments⁴⁸.

327 Second, blood flow is generally stable in healthy fetuses⁵⁴. The intrinsic variability in fetal heart
328 rate caused immense challenges for accurate diagnosis with cardiotocography (Supplementary
329 Discussion 3). Parameters such as umbilical artery blood flow exhibit minimal variations even
330 during maternal physical exercise⁵⁵. The relative stability of blood flow suggests that alterations
331 are indicative of hypoxia or other vulnerable states in the fetus⁵⁵.

332 Third, fetal hypoxia is a primary cause of adverse prenatal and perinatal outcomes, including
333 intrauterine growth restrictions^{49,50}, stillbirths⁵⁶, and hypoxic-ischemic encephalopathy⁵⁷, which
334 may result in cerebral palsy⁵⁸ and permanent disability⁵². Spectral Doppler is an essential tool to
335 diagnose hypoxic fetuses and aids in distinguishing pathological from healthy conditions⁵⁹⁻⁶². For
336 example, fetal biometry, while instrumental in detecting small for gestational age fetuses, does not
337 unequivocally differentiate intrauterine growth restriction from small yet healthy fetuses⁶¹.
338 Umbilical artery Doppler signals effectively differentiate the two cases. Intrauterine growth
339 restriction is often associated with abnormal blood flow patterns (such as absent or reversed end

340 diastolic flow), while small but healthy fetuses are characterized by normal blood flow patterns
341 (forward end diastolic flow)^{49,50}.

342 Fourth, third-trimester pregnancy is often the most vulnerable when the fetal demand for oxygen
343 and nutrients reaches its peak and there is a higher tendency for cord accidents (Supplementary
344 Discussion 1)⁶³. With prolonged distress, fetal asphyxia is the final common pathway leading to
345 stillbirth⁶⁴. Thus, blood flow assessment can guide the timing of delivery complicated by fetal
346 hypoxia^{49,51}. Profound compromise in blood flow may necessitate earlier delivery to prevent
347 irreversible organ damage or stillbirth. During such critical states, the brain-sparing effect, a
348 cerebral autoregulation mechanism to continuously supply sufficient oxygen to the brain, may be
349 activated by the vasodilation of cerebral vessels and vasoconstriction of other vessels^{46,65}. The
350 surveillance of fetal blood flow allows for the optimization of the timing of delivery, balancing the
351 risks of prematurity against the risks of hypoxia⁴⁹.

352 Despite the importance of continuous blood flow monitoring, current clinical protocols only
353 provide intermittent ultrasound-based measurements in high-risk pregnancies^{49,50}. This
354 intermittent approach may overlook emergent complications or severe fetal distress, potentially
355 increasing the risk of stillbirth. Continuous blood flow monitoring via spectral Doppler can provide
356 real-time information about fetal well-being, enable clinicians to make informed decisions, and
357 eventually reduce the likelihood of complications associated with undiagnosed fetal distress^{48,50,52}.

358

359 **Supplementary Discussion 5: Clinically relevant vessels for monitoring**

360 In fetal ultrasonography, three indices derived from spectral Doppler waveforms are used to assess
361 fetal well-being based on reported reference ranges^{66,67}.

362 The systolic-to-diastolic ratio (*S/D ratio*) is defined as:

$$363 \quad S/D \text{ ratio} = \frac{PSV}{EDV} \quad (1)$$

364 where *PSV* is the peak systolic velocity and *EDV* is the end diastolic velocity.

365 The pulsatility index (*PI*) is defined as:

$$366 \quad PI = \frac{PSV - EDV}{MFV} \quad (2)$$

367 where *MFV* is the mean flow velocity.

368 The resistance index (*RI*) is defined as:

$$369 \quad RI = \frac{PSV - EDV}{PSV} \quad (3)$$

370 Routine hospital examinations of spectral Doppler indices are conducted in three major vessels:
371 umbilical artery, umbilical vein, and middle cerebral artery⁶⁰.

372 The umbilical cord is a helical free-floating tube composed of two arteries and one vein. The
373 umbilical arteries transport deoxygenated blood from the fetus to the placenta⁵⁰. The spectral
374 Doppler signal exhibits low resistance and continuous forward flow throughout systole and
375 diastole in a healthy fetus⁵⁰. Additionally, resistance decreases (i.e., increasing end diastolic

376 velocity) from the fetal insertion point to the placental insertion point along the length of the
377 umbilical cord, because the branching of the umbilical artery at the placental end results in a larger
378 cumulative cross-sectional area and greater compliance of the vessels^{49,50}. In healthy pregnancy,
379 the *S/D ratio*, *PI*, and *RI* decrease with gestational progression⁵⁰. As a reference, the median
380 *S/D ratio* diminishes from 3.23 at 24-week to 2.68 at 32-week and 2.19 at 40-week gestation; the
381 median *PI* diminishes from 1.10 at 24-week to 0.96 at 32-week and 0.79 at 40-week gestation; and
382 the median *RI* diminishes from 0.69 at 24-week to 0.63 at 32-week and 0.55 at 40-week gestation⁶⁸.
383 However, a substantial increase in these Doppler indices or the critical finding of absent or
384 reversed end diastolic flow can signify fetal growth restriction^{49,50}.

385 The umbilical vein delivers oxygenated blood from the placenta to the fetus, typically showing
386 continuous and non-pulsatile flow⁵⁰. Fetal breathing is commonly observed in the umbilical venous
387 flow in the third trimester due to changes in intrathoracic pressure⁵⁰. On the other hand, pulsatile
388 umbilical vein waveforms, which reflect the pulsatility of the fetal heart rate, can indicate a
389 detrimental defect in fetal circulation, especially in the fetal heart and placental function^{49,50}. A
390 compromised fetal heart can cause back pressure through the fetal right ventricle, right atrium,
391 ductus venosus, and into the umbilical vein⁵⁰. Placental insufficiency can also alter the normal
392 pressure gradient in the umbilical vein⁵⁰.

393 The middle cerebral artery is a major branch of the circle of Willis, carrying oxygenated blood for
394 the fetal cerebral circulation⁴⁹. Similar to the umbilical artery waveform, the middle cerebral artery
395 spectral Doppler shows pulsatile forward flow throughout the cardiac cycle under normal
396 conditions⁵⁰. Two abnormalities can be monitored. First, the brain-sparing reflex is a physiological
397 response to compensate for hypoxic or nutrient-deficient conditions⁴⁹. Blood flow redistributes to
398 prioritize the brain for survival and development⁴⁹. This is characterized by increased end diastolic
399 velocity in the spectral Doppler of the middle cerebral artery, which is reflected by a low *PI*⁴⁹.
400 Clinically, the cerebroplacental ratio (*CPR*), defined as the *PI* ratio of the middle cerebral artery
401 to the umbilical artery, serves as an index to gauge the adequacy of fetal brain perfusion relative
402 to placental blood flow⁵⁰. The median *CPR* is 1.37 at 20-week, 2.34 at 30-week, and 1.80 at 40-
403 week gestation⁴⁶. Second, fetal anemia is characterized by decreased circulating red blood cells in
404 the fetus⁵¹. An increased *PSV* in the middle cerebral artery, exceeding 1.5 times the median at a
405 particular gestational age, is indicative of fetal anemia⁵¹. The median *PSV* is 25.5 cm/s at 20-week,
406 40.5 cm/s at 30-week, and 64.4 cm/s at 40-week gestation⁶⁹.

407

408 **Supplementary Discussion 6: Novelty of the UPatch**

409 The UPatch enables continuous fetal blood flow monitoring, which is essential for high-risk
410 pregnancies.

411 A key limitation of current ultrasound-based fetal blood flow assessments is the need for a trained
412 sonographer to manually place the sample gate, making continuous monitoring impractical⁷⁰. The
413 autonomous vessel tracking algorithm demonstrated in this work eliminates this limitation,
414 enabling continuous measurements even during fetal movement. This advancement is particularly
415 valuable in low-resource settings, where access to skilled sonographers is often limited or
416 unavailable⁷¹.

417 Previous wearable ultrasound patches developed for cardiac⁷² and vascular⁷³ imaging employed
418 relatively small apertures at 12.8 mm and 12 mm, respectively, which were sufficient for imaging
419 large cardiac structures and adult vessels at relatively shallow depths. In contrast, the UPatch is
420 designed to image substantially deeper and smaller fetal vessels. To accommodate these
421 requirements, the UPatch aperture was increased to 25.6 mm, representing more than a twofold
422 increase and enabling much enhanced sensitivity and penetration for deep fetal imaging (Extended
423 Data Fig. 1).

424 The previous design did not incorporate elevational focusing, relying instead on unfocused
425 elevational beam profiles⁷². In contrast, the UPatch integrates an acoustic lens that enhances
426 elevational focusing, reducing the elevational focal beamwidth by 25% and shifting the elevational
427 focal depth from 14 cm to 10 cm. This design enables more balanced elevational resolution across
428 the ~20 cm imaging depth of a typical womb⁷⁴.

429 Conventional dicing strategies in the previous designs limited the achievable kerf width to 0.1–0.2
430 mm, constraining element density and thereby limiting signal-to-noise ratio⁷². In contrast, the use
431 of super multipass dicing approach reduced the kerf width to 0.05 mm, increasing element width
432 by >50% and improving signal-to-noise ratio while maintaining a minimal level of crosstalk
433 between adjacent elements.

434 Electromagnetic shielding in prior designs used two isolated electrode layers of liquid metal⁷² or
435 copper mesh⁷³, which provided two-dimensional shielding but could not block electromagnetic
436 interference from entering through the edges of the two electrodes⁷⁵. In contrast, the UPatch was
437 designed with a soft Faraday cage that was made of copper mesh and stitching vertical interconnect
438 accesses. The soft Faraday cage connects the edges of the two electrodes using stitching vertical
439 interconnect accesses. This design enables a three-dimensional soft Faraday cage, providing more
440 effective electromagnetic shielding than prior planar approaches and improving signal integrity
441 across various conditions encountered during wearable operation.

442

443 **Supplementary Discussion 7: Transducer dicing**

444 Transducer dicing is a critical fabrication step in ultrasound array design. There are two primary
445 dicing methods that are utilized: laser-based and blade-based dicing.

446 For transducer dicing using a laser, a key challenge is the thickness of the entire material stack.
447 The UPatch is composed of PZT-5H 1–3 composite and conductive epoxy backing layer (Von
448 Roll 3022 E–Solder, EIS) with a total thickness of ~1 mm. First, while laser dicing can effectively
449 cut through PZT, it is limited to thin material stacks (e.g., 0.262 mm⁷⁶, 0.08 mm⁷⁷, and 0.045 mm⁷⁸).
450 As a result, laser dicing is feasible for selectively dicing the PZT layer only or for high-frequency
451 applications where the entire material stack is very thin. However, it is impractical for achieving
452 precise dicing of the 1 mm-thick material stack used in this study. Second, a key limitation of laser
453 dicing is the heat generated during processing⁷⁷, which evaporates Pb to reduce its concentration
454 and possibly induces a metastable pyrochlore phase, leading to a complete loss of piezoelectric
455 properties⁷⁹. Annealing and repolarization are required to restore piezoelectric properties,
456 introducing additional processing steps.

457 Dicing ultrasound transducers typically utilizes blades with diamond grits embedded in
458 electroplated nickel binders⁸⁰. As the blade rotates, the diamond grits abrade the transducers. The

459 sharp edges of the diamond grits mechanically chip away microscopic fragments of the
460 transducers⁸⁰. However, dicing thick material stacks with conventional mechanical dicing
461 techniques remains challenging. To address this, additional preparation steps are often required to
462 separately process the PZT and backing layer^{81,82}. A common approach involves interposers,
463 which are 3D-printed with the target pitch⁸³. The backing layer is molded within the interposers,
464 which separate individual channels. The PZT is then placed on top of the backing-interposer
465 structure with careful alignment. Finally, the PZT is diced with the desired pitch. This method
466 requires each material stack layer to be separately prepared, aligned, and assembled, introducing
467 multiple fabrication steps that increase complexity, processing time, and the likelihood of errors.

468 Optimal dicing outcomes depend on two dicing blade parameters. First, the size of the grits,
469 composed of synthetic diamonds, influences the chipping mechanism during dicing⁸⁰. Larger grit
470 particles are more robustly anchored within the nickel binders, offering slower degradation rates.
471 In contrast, smaller grit sizes are more advantageous for decreasing the amount of force on the
472 transducer. This translates to finer dicing because it minimizes surface chipping and diminishes
473 blade vibrations, resulting in a more precise cut. Second, the blade thickness determines the
474 transducer kerf⁸⁰. While a smaller thickness is preferable for achieving higher precision in
475 transducer dicing, it increases the potential for blade vibration, which in extreme cases may lead
476 to blade failure.

477 While utilizing smaller grit size and blade thickness is more advantageous for finer dicing, it
478 introduces processing complexities. The conventional dicing strategy utilizes a full depth cut,
479 wherein the entire transducer thickness (e.g., 1 mm in this study) is diced with a single pass
480 (Supplementary Fig. 2)⁸⁴. This strategy often induces substantial blade vibration due to the long
481 contact edge between the blade and the transducer, which means that a large force is exerted on
482 the blade, causing it to vibrate and potentially leading to blade breakage⁸⁰. To minimize such
483 vibration, a feed speed of 0.1 mm/s was typically utilized, extending the entire cutting process to
484 ~15 h. Despite the low feed speed, this technique frequently caused thin blades to break. Thus, a
485 larger blade thickness was required.

486 To address these challenges, in this study, we employed a super multipass dicing strategy, which
487 dices each transducer element in incremental steps of 50 μm depth over a series of 20 rounds to
488 achieve the full 1 mm depth (Supplementary Fig. 2). By reducing the depth of cut in each pass,
489 this approach decreases the contact edge between the dicing blade and the transducer⁸⁰. A shorter
490 contact edge means that less force is exerted on the blade, which in turn reduces blade vibration
491 and minimizes the risk of chipping the transducer (Supplementary Fig. 2). Therefore, the super
492 multipass technique enables the use of thinner blades with smaller grit sizes, which generate
493 transducers with narrower kerf without blade breakage. With such optimized processing, the
494 transducer dicing can be performed at 10 mm/s, decreasing the total processing time to ~3 h
495 (Supplementary Fig. 2).

496 The conventional method produced a 0.12 mm kerf, while the super multipass strategy produced
497 transducers with a 0.05 mm kerf (Supplementary Figs 3 and 4). This preserved more active
498 piezoelectric elements, improving the signal-to-noise ratio by 7.2 dB (Fig. 1b). Additionally,
499 because the transducers were still fully diced, the crosstalk between individual channels was
500 similar to that of the transducers diced with the conventional method (Supplementary Figs 3 and
501 4). The super multipass dicing method provides a one-step solution using a standard dicing

502 machine, eliminating the need for complex, multi-step fabrication while maintaining high dicing
503 precision.

504

505 **Supplementary Discussion 8: Acoustic lens**

506 Ultrasound wave propagation is characterized by attenuation-induced energy loss (such as
507 absorption, scattering, and reflection), resulting in a decreased signal-to-noise ratio as imaging
508 depth increases⁸⁵.

509 The UPatch has an elevational length of 12 mm, providing a natural elevational focal depth of ~14
510 cm (Supplementary Fig. 7). Reducing the elevational length can reduce the natural focal depth, but
511 this strategy compromises the acoustic energy output⁸⁵. To ensure sufficient acoustic energy output
512 while achieving optimal focal depth, we designed and fabricated an acoustic lens.

513 The acoustic lens focuses the ultrasound beam in the elevational dimension and concentrates
514 energy into the lateral-axial imaging plane, thereby enhancing the signal-to-noise ratio⁸⁵. A two-
515 dimensional image in the lateral-axial plane assumes reconstruction from a thin slice but is actually
516 from a thick slab due to the elevational beamwidth⁸⁵. A large elevational beamwidth captures
517 signals from both tissues and red blood cells for Doppler calculation, which compromises the
518 signal-to-noise ratio^{85,86}. The acoustic lens reduces signals from regions outside the area of interest
519 and enhances the signal-to-noise ratio⁸⁷. Therefore, in this study, we used an acoustic lens to focus
520 the beam in the elevational direction, which reduces signals from regions outside the area of
521 interest and enhances the signal-to-noise ratio⁸⁷.

522 The lens design is based on Snell's law:

$$523 \frac{\sin \theta_1}{\sin \theta_2} = \frac{v_2}{v_1} \quad (4)$$

524 where θ_1 is the incidence angle, θ_2 is the refraction angle, v_1 is the ultrasound wave velocity in
525 the incident medium, and v_2 is the velocity in the refracted medium (Supplementary Fig. 5)⁸⁸.

526 Given a known speed of sound in the loading medium (such as biological tissues to be imaged),
527 the acoustic lens modulates the ultrasound beam's shape depending on its speed of sound. Speed
528 of sound is determined by the lens material. Rubbers are widely used due to their low acoustic
529 impedance and simple fabrication process. The acoustic impedance of rubbers closely aligns with
530 that of biological tissues (~1.68 MRayl), facilitating efficient ultrasound transmission into the
531 tissue⁸⁹. Additionally, rubber's low adhesion to metals enables facile molding from precisely
532 machined metal molds⁹⁰. Despite the relatively high acoustic attenuation of rubbers, the energy
533 loss is minimal in imaging applications due to the small thickness of the lens.

534 The side of the lens tightly bonded to the transducer is flat, leading to an incidence angle of 90°,
535 thereby eliminating refraction at the transducer/lens interface. The other side, which contacts the
536 loading medium, is the interface where the refraction occurs. Given rubbers' lower speed of sound
537 than water, simulations indicate that a convex lens with a constant radius effectively focuses the
538 acoustic beam. The lens radius can be calculated as:

$$539 R_{lens} = F * |n - 1| \quad (5)$$

540 where F is the focal depth and R_{lens} is the lens radius. n is given by:

541
$$n = \frac{C_{medium}}{C_{lens}} \quad (6)$$

542 where C_{medium} is the speed of sound in the loading medium, and C_{lens} is the speed of sound in the
543 lens⁹¹.

544 We measured the acoustic properties of two silicone rubbers typically used in wearable ultrasound,
545 Ecoflex and polydimethylsiloxane, using transmitters with broad bandwidths: P4-1 (ATL) for 1–
546 4 MHz and L11-5 (Philips) for 5–10 MHz. The speeds of sound were 1007 m/s and 957 m/s,
547 respectively (Supplementary Fig. 5). Despite Ecoflex exhibiting a slightly higher speed of sound,
548 indicating a smaller lens radius and thicker lens, the difference between the two rubbers is
549 negligible. Ecoflex has a lower attenuation coefficient than polydimethylsiloxane in the 1–10 MHz
550 frequency range (Supplementary Fig. 5)⁹²⁻⁹⁵. Thus, we chose Ecoflex as the lens material. With a
551 depth of interest of ~10 cm and an average speed of sound in tissue of 1540 m/s, we derived the
552 lens radius to be 53 mm based on equations (5) and (6).

553 A three-dimensional model and its corresponding mold were designed in SolidWorks according
554 to the transducer's dimensions (Supplementary Fig. 6). The designed mold was precisely machined
555 using computer numerical control machining. Then, the lens was fabricated by casting and curing
556 Ecoflex within the mold (Supplementary Fig. 6). The lens was then bonded to the transducer using
557 Ecoflex to minimize the interfacial acoustic impedance mismatch.

558 We scanned the elevational-axial acoustic field to evaluate the lens' elevational beam focusing
559 performance. Using the acoustic lens, the focal depth of the UPatch moved from 14 cm to 10 cm,
560 which balanced the elevational resolution throughout the entire 20 cm depth of a typical womb
561 (Fig. 1c and Supplementary Fig. 7). Additionally, the elevational beamwidth decreased from 6.0
562 mm to 4.5 mm at the focal point, improving the signal-to-noise ratio (Supplementary Fig. 7). While
563 the acoustic lens enhances the signal amplitude at the focal region, it can also introduce minor
564 attenuation due to the added lens material, which elongates the acoustic path and causes additional
565 acoustic interfaces with impedance mismatch. These competing effects can offset each other. As
566 a result, despite the more confined beam profile, the peak amplitude remains comparable at the
567 focal point with and without the acoustic lens due to the attenuation introduced by the lens
568 (Supplementary Fig. 7).

569 Beam steering controls lateral positioning in the XZ plane, while the acoustic lens enhances
570 elevational beam focusing in the YZ plane to improve signal quality. The acoustic lens focusing
571 remains beneficial even when the beam is steered off-axis in the XZ plane. When steered from -
572 7.5° to 7.5°, the angle range of the duplex imaging algorithm used in this work, the elevational
573 beamwidth is consistent at ~4.5 mm and ~6.0 mm for with and without the acoustic lens,
574 respectively (Supplementary Fig. 8). The improved beam confinement leads to higher contrast and
575 better vessel visualization, ensuring more reliable blood flow measurements.

576

577 **Supplementary Discussion 9: Soft Faraday cage**

578 The UPatch is vulnerable to electromagnetic interference due to its operational frequency within
579 the radiofrequency spectrum. These interferences primarily originate from two sources: external
580 electronic devices and contact with the human body.

581 External electronic devices (e.g., smartphones, Wi-Fi routers, and medical equipment) emit
582 electromagnetic signals to the surrounding environment, coupling to the UPatch⁹⁶. The in-band
583 electromagnetic noise at 2.5 MHz is unlikely to couple into the UPatch through the air due to its
584 long wavelength (120 m). However, these electronic devices also emit electromagnetic signals at
585 frequencies different from ultrasound signals, which can still contribute to in-band interference
586 through several mechanisms. First, external electromagnetic signals can couple with the UPatch
587 due to its physical dimensions being comparable to the wavelength. For example, Wi-Fi signals
588 operate at 2.4 GHz, which corresponds to a wavelength of ~12.5 cm. This wavelength is
589 comparable to the size and geometry of the UPatch, allowing electromagnetic interference to occur.
590 Second, intermodulation of various external electromagnetic signals can cause down conversion
591 to in-band interference⁹⁷. Multiple electromagnetic signals can undergo nonlinear mixing within
592 the backend system, generating new frequency components through intermodulation⁹⁷. These
593 newly generated signals can span a broad range of frequencies, including those overlapping with
594 ultrasound signals, potentially degrading signal quality and affecting system performance. Third,
595 ground loops can allow external electromagnetic signals to couple into the system, generating low-
596 frequency interference⁹⁸. In a single-ended configuration, ground loops can behave like coils,
597 introducing parasitic inductance that enables inductive coupling with external electromagnetic
598 fields, further exacerbating interference⁹⁹.

599 Direct contact with the human body transmits noise to the UPatch due to its biopotentials and
600 antenna effects. Biopotentials (such as electrocardiogram and electromyogram) generated from the
601 human body can also be modulated by external electromagnetic signals, resulting in noises near
602 the ultrasound frequency band^{100,101}. The antenna effects are a phenomenon where the human body
603 inadvertently acts as an antenna that couples electromagnetic waves in the air¹⁰².

604 Ultrasound signals collected from deep tissues are intrinsically weak⁸⁵; thus, these electromagnetic
605 interferences can degrade signal and image quality. Consequently, devising effective screening
606 strategies is imperative for the UPatch to image the fetus and acquire high-fidelity spectral Doppler
607 signals from fetal vessels.

608 Various methods can reduce electromagnetic noise. First, analog and digital filters (such as low-
609 pass, high-pass, and band-pass filters) are commonly used to attenuate noise outside the frequency
610 band of interest¹⁰³. The backend system (Vantage 256, Verasonics) incorporates these filters,
611 effectively eliminating outside-band noise (such as biopotentials) which are typically below 10
612 kHz¹⁰⁴. However, due to the wideband nature of electromagnetic noise in the air, filters alone are
613 insufficient for lowering the noise floor of in-band signals. Second, specialized circuits can reduce
614 thermal noise (caused by irregular movement of electrons inside electronic components due to
615 ambient temperature) coupled to ultrasound signals during the filtering, amplification, and
616 digitization processes¹⁰³. However, this method increases the footprint, making the UPatch less
617 wearable. Third, ground shielding the entire surroundings of the UPatch can reduce the noise floor
618 by directly blocking the noise.

619 Electromagnetic interference is ubiquitous and omnidirectional, and the most effective shielding
620 approach is a Faraday cage to prevent unwanted coupling from various sources¹⁰³. These three-
621 dimensional shields redistribute the charges across the cage surface, thereby neutralizing both
622 static and dynamic electrical fields¹⁰³. Metals are often used to construct the cage due to their high
623 conductivity for the charges to move freely and quickly for effective redistribution¹⁰³. A key design
624 guideline to develop a soft Faraday cage is based on fundamental wave propagation theory. The

625 effectiveness of a Faraday cage in blocking electromagnetic signals depends on the spacing
626 between stretchable traces, which is governed by:

$$627 \quad L < \frac{c}{10f\sqrt{\epsilon_r}} \quad (7)$$

628 where L is the spacing between adjacent net traces, c is the speed of light, f is the maximum
629 frequency of the blocked signals, and ϵ_r is the relative permittivity¹⁰⁵.

630 We designed a soft Faraday cage to shield the UPatch from electromagnetic noise. The previous
631 design incorporated two isolated copper electrode layers⁷³, which provided two-dimensional
632 shielding but could not block electromagnetic interference from entering through the edges of the
633 two electrodes⁷⁵. In contrast, the UPatch was designed with a soft Faraday cage that was made of
634 laser-ablated polyimide/copper laminates and vertical interconnect accesses. The soft Faraday cage
635 connects the edges of the two electrodes using stitching vertical interconnect accesses. The
636 transducers were placed between the mesh ground electrode and electromagnetic shielding
637 electrode (Supplementary Fig. 9). Most of the body noise coupled to the UPatch will be shunted
638 to the mesh ground electrode close to the skin. Various electromagnetic frequency signals can
639 undergo intermodulation, generating spurious low-frequency signals that may overlap with the
640 ultrasound frequency band, leading to interference⁹⁸. The added electromagnetic shielding layer to
641 the top of the signal electrodes can potentially shield noise from the air. The closely patterned
642 electrical connections prevent electromagnetic interference from entering the UPatch from the
643 edges, providing three-dimensional shielding in all directions (Supplementary Fig. 10). The
644 maximum spacing between adjacent net traces was 0.9 mm, which can effectively block
645 electromagnetic waves up to 20 GHz, covering all frequency bands used in common electronic
646 devices¹⁰³.

647 We analyzed the power spectral density, which quantitatively measures the effectiveness of the
648 soft Faraday cage¹⁰⁶. In radiofrequency electronics (such as cellular transceivers, Bluetooth, and
649 Wi-Fi), dBm/Hz is the standard unit in power spectral density plot because the signal power in
650 these systems is typically in the milliwatt range¹⁰⁷. However, from a general signal processing
651 perspective, dB/Hz is a more appropriate unit for describing spectral density in relative terms¹⁰⁸.
652 The baseline noise level was also referenced to 1 W, ensuring consistency in the relative power
653 representation.

654 We evaluated baseline noise levels of the backend system, UPatch without the soft Faraday cage,
655 and UPatch with the soft Faraday cage. The baseline noise levels of the backend system were
656 measured in two conditions: input termination at 50 Ω and open circuit. The input termination at
657 50 Ω matches the system's impedance and minimizes electromagnetic interference, while the open
658 circuit captures the system's overall susceptibility to environmental noise. The baseline noise
659 levels under 50 Ω input termination and open circuit were negligibly similar (Fig. 1d). This
660 observation indicates that the noise is primarily contributed by the system itself rather than by
661 external sources. Therefore, the measured baseline noise level can be considered a reliable
662 representation of the system's intrinsic noise, regardless of the termination condition¹⁰⁹. The noise
663 level of the UPatch with the soft Faraday cage closely mirrored the baseline noise level of the
664 backend system, which is mainly composed of thermal noise (Fig. 1d). In the absence of the soft
665 Faraday cage, the noise floor increased by 11.7 dB/Hz at 2.5 MHz, the center frequency of the
666 UPatch.

667 We also performed measurements under both phantom and in vivo conditions (Supplementary
668 Figs 11–13). Noise levels were characterized using the probability density function, which
669 captures the distribution of instantaneous signal amplitudes over time¹¹⁰. Broader distributions
670 indicate greater variability due to environmental or physiological noise, making it suitable for
671 statistically quantifying noise¹¹⁰. Phantom measurements revealed the UPatch’s susceptibility to
672 ambient electromagnetic noise, while in vivo measurements demonstrated additional susceptibility
673 to physiological noise. The soft Faraday cage effectively attenuated environmental interference
674 from nearby electronic devices (Supplementary Fig. 11) and reduced noise contributions from both
675 environmental and physiological sources, resulting in improved signal fidelity (Supplementary Fig.
676 12). As a result, duplex imaging with the soft Faraday cage showed enhanced image quality and
677 reduced noise in both phantom and in vivo settings (Supplementary Fig. 13).

678 The soft Faraday cage provided shielding against electromagnetic noise while conforming to the
679 skin. Thus, this shielding strategy can be effectively adapted to enhance electromagnetic
680 compatibility and reduce noise in soft electronics.

681

682 **Supplementary Discussion 10: Umbilical cord phantom**

683 Commercially available fetal phantoms primarily support structural B-mode imaging¹¹¹. To the
684 best of our knowledge, no commercially available phantoms accurately replicate the complex flow
685 dynamics and anatomical variability of the umbilical cord and fetus.

686 To further validate the UPatch’s ability to detect the umbilical cord in varying orientations, we
687 developed an umbilical cord phantom that replicated the anatomical complexity of the intertwined
688 arteries and veins in the cord. The phantom design incorporated two helically wrapped arteries
689 (diameter ~3 mm) around a vein (diameter ~6 mm) to simulate the intertwined vascular geometry
690 observed in vivo (Supplementary Fig. 18)¹¹². We used deionized water as the surrounding medium,
691 reflecting the high water content (~98%) of amniotic fluid to replicate the in vivo acoustic
692 environment (Supplementary Fig. 18)¹¹³.

693 Commercially available silicone tubing (Metaland) does not accurately mimic the acoustic
694 impedance of soft tissue (~1.65 MRayl)⁸⁵. Its substantially lower impedance (~1.07 MRayl) results
695 in pronounced mismatch at fluid–structure interfaces, producing strong reflection during
696 insonation across multiple vascular boundaries of the umbilical cord (Supplementary Fig. 18)¹¹⁴.
697 To address this limitation, we selected Elastic 50A resin (Formlabs), which has acoustic impedance
698 (~1.66 MRayl) that closely aligns with the acoustic impedance of soft tissue (Supplementary Fig.
699 18)^{115,116}. Using the Elastic 50A resin, high-resolution stereolithographic printing enabled precise
700 and repeatable fabrication of the complex intertwined geometry of the umbilical cord
701 (Supplementary Fig. 19).

702 We conducted duplex imaging of the umbilical cord phantom across a range of vessel orientations
703 to mimic real-world dynamics caused by fetal and maternal movements (Extended Data Fig. 2).
704 These experiments demonstrated that the UPatch could reliably acquire the umbilical vessel flow
705 signals despite dynamic anatomical orientation changes in the in-utero environment.

706

707 **Supplementary Discussion 11: Acoustic exposure safety parameters**

708 The UPatch was activated at 30 V with a pulse repetition frequency (*PRF*) of 3000 Hz, which were
709 the highest values used in this study.

710 Using power P from a radiation force balance or a hydrophone (Supplementary Figs 23 and 24),
711 spatial average temporal average intensity (I_{SATA}) can be calculated by:

$$712 \quad I_{SATA} = \frac{P}{A} \quad (8)$$

713 where A is the area of the aperture (306.6 mm² in this study)¹¹⁷. This equation is valid for operation
714 with an unfocused wave, making it applicable to brightness and color-flow modes in this study¹¹⁷.

715 After waveform deconvolution using the data from calibrating the hydrophone sensitivity
716 (Supplementary Fig. 23), the hydrophone measurements calculated the derated pressure as:

$$717 \quad p_{\alpha}(z) = p(z)10^{\left(\frac{\alpha z f_{awf}}{20dB}\right)} \quad (9)$$

718 where α is the attenuation coefficient (conservatively assumed to be 0.3 dB·cm⁻¹·MHz⁻¹)¹¹⁷, z is
719 the distance from the UPatch along the beam axis to the plane containing the point of interest, and
720 f_{awf} is the acoustic working frequency. Then, the derated pulse pressure squared integral can be
721 calculated as:

$$722 \quad ppsi_{\alpha}(z) = \int p_{\alpha}^2(z, t) dt \quad (10)$$

723 where measurements are based on the maximum value of $ppsi_{\alpha}(z)$ between the break-point depth
724 z_{bp} and focal depth¹¹⁸. And z_{bp} is defined as:

$$725 \quad z_{bp} = 1.5 \times D_{eq} \quad (11)$$

726 where D_{eq} is the equivalent aperture diameter and is defined as:

$$727 \quad D_{eq} = \sqrt{\frac{4}{\pi} A} \quad (12)$$

728 Thus, z_{bp} is estimated to be 29.64 mm.

729 The derated pulse intensity integral is calculated by:

$$730 \quad pii_{\alpha}(z) = \frac{1}{\rho c} ppsi_{\alpha}(z) \quad (13)$$

731 where ρ is the density of water (997 kg·m⁻³) and c is the speed of sound in water (1480 m·s⁻¹)⁸⁵.
732 Therefore, the derated spatial peak pulse average intensity is defined as:

$$733 \quad I_{SPPA,\alpha}(z) = \frac{1}{t_d(z)} pii_{\alpha}(z) \quad (14)$$

734 where $t_d(z)$ is the pulse duration, which is 1.25 multiplied by the interval between the time when
735 the time integral of the square of the instantaneous acoustic pressure reaches 10% and 90% of its
736 final value^{119,120}.

737 The derated spatial peak temporal average intensity can be calculated as:

$$738 \quad I_{SPTA,\alpha}(z) = PRF \text{ } p_{r,\alpha}(z) \quad (15)$$

739 The mechanical index (*MI*) describes the relative probability of eliciting micromechanical bio-
740 effects, such as those associated with cavitation-induced damage^{117,121}, and is defined as:

$$741 \quad MI = \frac{p_{r,\alpha}(z_{MI})}{\sqrt{f_{awf}}} \quad (16)$$

742 where $p_{r,\alpha}$ represents the derated peak rarefactional pressure in MPa, measured along the beam
743 axis at depth z_{MI} where $p_{r,\alpha}(z)$ is maximum, and f_{awf} is in MHz.

744 The thermal index (*TI*) is an index of the estimated temperature rise in tissues and is defined as:

$$745 \quad TI = \frac{\text{Acoustic power output}}{\text{Acoustic power output needed to produce } 1^\circ\text{C rise}} \quad (17)$$

746 *TI* estimates temperature rise, postulating that the attenuation within tissue is homogeneous with
747 an attenuation coefficient of $0.3 \text{ dB}\cdot\text{cm}^{-1}\text{MHz}^{-1}$, which is lower than the attenuation coefficient of
748 most soft tissues¹²². Depending on the tissues in the scanning plane, *TI* is divided into three types:
749 soft tissue *TI* (*TIS*), bone *TI* (*TIB*), and cranium *TI* (*TIC*)^{118,122}.

750 First, the *TIS* is the maximum of the calculated values from equations (18) and (19):

$$751 \quad TIS_{as,ns} = \frac{P_{1\times 1} \cdot f_{awf}}{210 \text{ mW MHz}} \quad (18)$$

752 where $TIS_{as,ns}$ is the *TIS* at surface (non-scanning), $P_{1\times 1}$ is the bounded-square output power
753 over a 1 cm^2 area.

$$754 \quad TIS_{bs,ns} = \min \left[\frac{P_\alpha(z_{s,ns}) \times f_{awf}}{210 \text{ mW MHz}}, \frac{I_{SPTA,\alpha}(z_{s,ns}) \times f_{awf}}{210 \text{ mW cm}^{-2} \text{ MHz}} \right] \quad (19)$$

755 where $TIS_{bs,ns}$ is the *TIS* below surface (non-scanning), $P_\alpha(z_{s,ns})$ is the derated output power at
756 depth $z_{s,ns}$, and $I_{SPTA,\alpha}(z_{s,ns})$ is the derated spatial peak temporal average intensity at depth $z_{s,ns}$.

757 The derated power can be calculated as:

$$758 \quad P_\alpha(z_{s,ns}) = P(z_{s,ns}) 10^{\left(-\frac{\alpha z f_{awf}}{10 \text{ dB}}\right)} \quad (20)$$

759 where depth $z_{s,ns}$ is defined as:

$$760 \quad z_{s,ns} = \text{depth of } \max \left\{ \min \left[I_{SPTA,\alpha}(z) \times 1 \text{ cm}^2, P_\alpha(z) \right] \right\} \quad (21)$$

761 The *TIB* is calculated as:

$$762 \quad TIB = \min \left[\sqrt{\frac{P_\alpha(z_{b,ns}) \times I_{SPTA,\alpha}(z_{b,ns})}{50 \text{ mW cm}^{-1}}}, \frac{P_\alpha(z_{b,ns})}{4.4 \text{ mW}} \right] \quad (22)$$

763 where depth $z_{b,ns}$ is defined as:

764
$$z_{b,ns} = \text{depth of max}\{P_{\alpha}(z) \times I_{SPTA,\alpha}(z)\} \quad (23)$$

765 The *TIC* can be calculated by:

766
$$TIC = \frac{P/D_{eq}}{40 \text{ mW cm}^{-1}} \quad (24)$$

767 For duplex imaging, each *TI* based on B-mode and color Doppler modes was calculated separately
 768 and summed. The *TI* for Spectral Doppler mode was calculated for each focusing depth, and the
 769 highest value was reported.

770

771 **Supplementary Discussion 12: Thermal safety of the UPatch**

772 Safety guidelines for obstetric ultrasound are provided by the American Institute of Ultrasound in
 773 Medicine (AIUM)¹²³, British Medical Ultrasound Society (BMUS)¹²⁴, and Food and Drug
 774 Administration (FDA)¹¹⁷. The UPatch is an ultrasound device that may expose the mother and
 775 fetus to various safety hazards. Therefore, the device must be characterized accurately to meet the
 776 recommendations of the regulatory bodies.

777 The FDA has different recommendations for Track 1 and Track 3 devices (Track 2 is not available
 778 due to historical reasons)¹¹⁷. The UPatch was characterized to meet the recommendations for both
 779 Track 1 and Track 3 devices to ensure rigorous thermal safety evaluation.

780 The FDA Track 1 recommendations provide maximum values for the I_{SATA} , $I_{SPPA,\alpha}$, $I_{SPTA,\alpha}$, and
 781 *MI* for fetal applications. These recommended maximum values are $I_{SATA} < 20 \text{ mW/cm}^2$, $I_{SPPA,\alpha}$
 782 $< 190 \text{ W/cm}^2$, $I_{SPTA,\alpha} < 94 \text{ mW/cm}^2$, and $MI < 1.9$ (ref. ¹¹⁷). The I_{SATA} of the UPatch (0.72
 783 mW/cm^2) is substantially lower than the recommended maximum value and the Corometrics
 784 250CX Series (GE Healthcare)¹⁸ fetal heart rate monitor, which is reported to be $< 5 \text{ mW/cm}^2$
 785 (Supplementary Fig. 24). For $I_{SPPA,\alpha}$, the measured values from the hydrophone were 4.51 W/cm^2
 786 for duplex imaging and 16.42 W/cm^2 for spectral Doppler. Additionally, the $I_{SPTA,\alpha}$ values were
 787 19.86 mW/cm^2 for duplex imaging and 58.5 mW/cm^2 for spectral Doppler. The *MI* was 0.20 for
 788 duplex imaging and 0.37 for spectral Doppler (Fig. 1f). The UPatch operates well below the FDA
 789 Track 1 recommended maximum values.

790 The FDA Track 3 recommendations require device manufacturers to display *MI* and *TI* values
 791 according to the Output Display Standard in IEC 60601-2-37 (ref. ^{117,125}). *MI* and *TI* values are
 792 displayed in real time to ensure that clinicians adhere to the “as low as reasonably achievable”
 793 principle, minimizing patient exposure to ultrasound energy – although evidence suggests these
 794 are rarely checked in practice¹²⁶. While there is no specific recommendation from the FDA¹¹⁷ for
 795 the maximum *TI*, an explanation is requested for *TI* over six. The AIUM¹²³ and BMUS¹²⁴ set
 796 recommendations for maximum dwell time based on *TI* values. According to these guidelines, the
 797 recommended dwell time for obstetric scanning is set as: no dwell time limit for $TI \leq 0.7$,
 798 maximum dwell time $< 60 \text{ min}$ for $0.7 < TI \leq 1.0$, maximum dwell time $< 30 \text{ min}$ for $1.0 < TI \leq$
 799 1.5 , maximum dwell time $< 15 \text{ min}$ for $1.5 < TI \leq 2.0$, maximum dwell time $< 4 \text{ min}$ for $2.0 < TI$
 800 ≤ 2.5 , maximum dwell time $< 1 \text{ min}$ for $2.5 < TI \leq 3.0$, and scanning with $TI > 3.0$ is not
 801 recommended for obstetric uses.

802 The maximum increase in the surface temperature of the UPatch in air was measured to be 0.53 °C
803 (Supplementary Fig. 22). The device maintained a stable surface temperature well below safety
804 thresholds, supporting its viability for extended clinical use. Using measurements from a radiation
805 force balance or a hydrophone, we calculated the highest *TI* values for duplex imaging and spectral
806 Doppler. For duplex imaging, the *TIS* was 0.02, *TIB* was 0.05, and *TIC* was 0.05 (Fig. 1f). For
807 spectral Doppler, the *TIS* was 0.10, *TIB* was 0.38, and *TIC* was 0.17 (Fig. 1f). All of these values
808 were < 0.7, suggesting no dwell time limit for the UPatch according to AIUM and BMUS
809 recommendations^{123,124}. For obstetric imaging, the *TIS* is most relevant thermal index up to 10
810 weeks from the last menstrual period or a crown-rump length of about 33–34 mm, and *TIB* is the
811 most relevant thereafter¹²³.

812 In summary, the UPatch adheres to recommendations by the FDA Track 1 and Track 3 (ref. ¹¹⁷),
813 AIUM¹²³, and BMUS¹²⁴. Additionally, we strictly followed the as low as reasonably achievable
814 principle to minimize ultrasound wave exposure to the fetus and the mother¹¹⁷.

815

816 **Supplementary Discussion 13: Beamforming of the UPatch on the abdomen**

817 Beamforming is traditionally performed using a fixed array configuration. Thus, the UPatch image
818 reconstruction assumes that the 64 channels are on a static surface. However, the curvature of the
819 pregnant woman's abdomen differs from person to person and varies at different locations of the
820 abdomen, introducing phase aberration to the beamforming of the UPatch¹²⁷. This curvature for
821 the third trimester typically has a radius ranging from 14 cm to 18 cm^{128,129}.

822 To mitigate this problem, phase aberration was corrected for a curvature radius of 16 cm,
823 accommodating the typical abdominal geometry (Supplementary Fig. 25). The aberration
824 correction was applied in both transmission and reception, which adjusted the time delay profile
825 of the ultrasound waves to ensure accurate image reconstruction. The delay-and-sum beamformer
826 used the same curvature profile for consistent aberration correction during reception. With this
827 phase aberration correction, the UPatch could provide high-quality images even with varying
828 maternal abdominal curvatures (Extended Data Fig. 3 and Supplementary Figs 27 and 28).
829 Additionally, while the curved shape of the maternal abdomen focuses the ultrasound beam, we
830 compensated for the bending radius by beamforming, so unwanted focusing was largely alleviated.

831

832 **Supplementary Discussion 14: Vessel tracking algorithms**

833 Traditional methods require clinicians to manually maneuver the handheld clinical ultrasound
834 device and select the appropriate sample gate on the duplex image for spectral Doppler analysis of
835 fetal vessels (Supplementary Fig. 31)⁵³. This approach can only provide intermittent measurements
836 and faces challenges during dynamic physiological changes (e.g., fetal and maternal movements,
837 respiratory processes, and uterine contractions)^{48,51}. These changes can alter the locations of fetal
838 vessels and sample gates^{130,131}. For example, the umbilical cord can rotate and orient in various
839 directions⁵³. Such movements can displace the sample gate initially placed on the umbilical artery
840 to other tissues (Fig 3c). Thus, strategies are needed to adaptively adjust the sample gate to the
841 moving vessel.

842 Efforts to address this challenge remain in early stages of development. One approach involved
843 developing a vessel tracking algorithm that detects the vessel wall using A-mode¹³². However, this
844 algorithm cannot differentiate between various vessel types (such as the umbilical arteries and vein)
845 or vessel orientations (such as the transverse and longitudinal planes). In a separate study,
846 computer vision was used to estimate the ultrasound Doppler angle for automatic angle correction.
847 Yet this method still requires a clinician to initially identify the vessel of interest¹³³. Furthermore,
848 a machine learning model applied to M-mode images successfully detected the vessel diameter but
849 was limited to the transverse view of the vessel¹³⁴.

850 Image segmentation offers a promising alternative for vessel detection because different vessel
851 types and orientations provide distinct features. Thus, commercial devices have recently
852 implemented image segmentation-based strategies. The Arietta 65 (Fujifilm) claims to automate
853 sample gate selection for mitral valve in the apical four-chamber view¹³⁵ and received FDA
854 clearance in November 2020 (ref. ¹³⁶), but the automated sample gate feature¹³⁵ was not included
855 in its regulatory submission. The Acuson Origin (Siemens) received FDA clearance in October
856 2023 (ref. ¹³⁷). This artificial intelligence system places sample gates for 12 cardiac views,
857 supporting up to 4 anatomical locations with a total of 42 sample gate placements^{137,138}. The
858 automated sample gate feature in Kosmos (cart-based ultrasound system; EchoNous) and Kosmos
859 Mobile (wireless ultrasound system; EchoNous) was introduced in September 2024 (ref. ¹³⁹⁻¹⁴¹)
860 but has not received FDA clearance¹⁴². An artificial intelligence system was proposed to provide
861 sample gate selection for apical four-chamber view, specifically for the left ventricular outflow
862 tract, mitral valve, pulmonary valve, and tricuspid valve¹⁴⁰.

863 These developments reflect exciting progress in echocardiography. However, there remains no
864 commercially available solution for automated sample gate selection in fetal ultrasound. Unlike
865 cardiac imaging, which benefits from anatomical landmarks that are changing periodically, fetal
866 imaging must contend with continuously shifting anatomy due to fetal and maternal movements.
867 The intertwined vascular geometry of the umbilical cord, comprising two arteries helically
868 wrapped around a central vein, results in dynamic variation in depth, orientation, and position
869 (Extended Data Fig. 2). Additionally, these existing commercial probes must be held by humans
870 or robotic arms, making them impractical for continuous monitoring.

871 The image segmentation in this study utilizes color Doppler signals in the duplex image. This
872 method effectively differentiates the umbilical artery from the umbilical vein by identifying
873 differences in the flow direction and pulsatility (Fig. 3a). It enables dynamic tracking and adaptive
874 sample gate selection in response to changing vessel geometry and motion, representing a
875 substantial advance over existing cardiac-focused approaches and addressing an unmet need in
876 continuous fetal blood flow monitoring. Additionally, we optimized the computational load by
877 reducing the number of frames analyzed by the tracking algorithm. The UPatch is self-adhering
878 and integrates autonomous vessel tracking specifically designed for fetal ultrasound, enabling
879 prolonged monitoring without the need for a sonographer or a robotic arm. This method facilitates
880 autonomous monitoring during physiological changes, thereby enhancing the reliability and
881 effectiveness for fetal monitoring.

882

883 **Supplementary Discussion 15: Working principles of vessel tracking algorithm**

884 The tracking algorithm leverages pulsatility characteristics encoded in the color Doppler signal to
885 quantitatively differentiate the vessels.

886 Each pixel in the frame is assigned a color intensity value ranging from 1 to 128 (Extended Data
887 Fig. 6). Values from 1 to 64 represent flow away from the UPatch using cool hues, where lower
888 color intensity values correspond to cyan (higher velocity), and higher values correspond to dark
889 blue (lower velocity). Values from 65 to 128 represent flow toward the UPatch using warm hues,
890 where lower color intensity values correspond to dark red (lower velocity), and higher values
891 correspond to yellow (higher velocity).

892 Based on this numerically assigned pixel color intensity, the inter-frame color difference compares
893 the color intensity of each pixel among consecutive frames. A high inter-frame color difference
894 reflects greater temporal variation in flow velocity, characteristic of arterial pulsatility. In contrast,
895 low variation corresponds to steadier flow typically observed in veins. Thus, the algorithm
896 evaluated the inter-frame color difference to obtain pixels designated for the umbilical artery or
897 vein. We implemented a threshold for the inter-frame color difference across each vessel region.
898 Regions exceeding this threshold are classified as arteries, while those below are identified as veins.

899 Binary segmentation maps were generated, followed by morphological opening and closing to
900 remove granular noise and smooth region boundaries. Opening removes small, isolated artifacts,
901 while closing fills gaps and connects nearby regions^{143,144}. These two steps improve segmentation
902 quality by preserving large, coherent vessel structure. Among the identified regions, the one with
903 the largest pixel area is designated as the primary region because larger regions offer more stable
904 signals, are less affected by noise, and align with the selection norm typically used by sonographers
905 in clinical practice (Supplementary Fig. 33). This approach effectively suppresses sparse, spatially
906 dispersed noise while retaining the dominant vascular structure. Finally, we computed the
907 geometric centroid of the selected primary region to define the sample gate location
908 (Supplementary Fig. 34). The centroid, calculated as the mean x and y coordinates of all pixels
909 within the segmented region, ensures a spatially robust placement of the sample gate.

910

911 **Supplementary Discussion 16: Umbilical vein tracking**

912 Most clinical applications of fetal Doppler focus on the umbilical artery^{48,51,67}. Therefore, this
913 study optimized the tracking algorithm specifically for the detection of the umbilical artery (Fig.
914 3a).

915 Nevertheless, this tracking algorithm can also be adapted to detect the umbilical vein. The
916 umbilical vein transports oxygenated blood from the placenta to the fetus, ensuring it receives
917 essential oxygen and nutrients for its growth and development (Supplementary Discussion 5)¹⁴⁵.
918 Thus, monitoring the umbilical vein is likely to provide direct insights into fetal oxygenation.

919 While the umbilical arteries and vein are intertwined, their color Doppler signals are typically
920 opposite due to their opposite flow directions (Extended Data Fig. 3). Thus, if the color Doppler
921 signal of the arteries is red (indicating flow towards the UPatch), the signal of the vein will be blue
922 (indicating flow away from the UPatch), or vice versa. Additionally, the umbilical vein is typically

923 non-pulsatile because the placenta acts as a blood reservoir (Supplementary Discussion 5)⁴⁸.
924 Therefore, when the tracking algorithm calculates the variance in color Doppler pixel intensity
925 over several consecutive frames, it can identify the umbilical vein as the non-pulsatile region (Fig.
926 3a). A similar segmentation method can then be applied to identify the primary region and its
927 spatial centroid of the umbilical vein for sample gating (Fig. 3a). This adaptation allows the
928 tracking algorithm to be utilized for continuous umbilical vein tracking and blood flow monitoring.

929

930 **Supplementary Discussion 17: Response time during image segmentation**

931 Due to limitations in the computational power of the backend system, the autonomous tracking
932 algorithm cannot simultaneously perform duplex imaging, tracking, and spectral Doppler
933 recording. Thus, the algorithm sequentially reconstructs a duplex image, tracks the umbilical artery
934 to obtain a sample gate, and records spectral Doppler signals (Fig. 3a). In such cases, fetal
935 movement may affect the performance of the image segmentation algorithm. Fast movements can
936 particularly cause the initially registered sample gate to shift away from the target vessel before
937 the next round of image segmentation begins.

938 To address this issue, we integrated a standard deviation threshold at the end of the image
939 segmentation sequence. This ensures that when the algorithm detects fast cord movements, it does
940 not provide a sample gate until the movement is slowed down. The algorithm computes the x and
941 y coordinates of tracked points across consecutive frames. A threshold based on the standard
942 deviation of these coordinate changes was applied to identify and exclude tracked points with
943 abrupt displacements, which may occur during rapid fetal movements. This approach reduces the
944 likelihood of erroneous sampling and ensures reliable tracking performance during continuous
945 monitoring of dynamic conditions. Consequently, sample gates were applied only to vessels that
946 have no or slow movements (Supplementary Video 1).

947 A typical uninterrupted period of observations is ~ 5 s. Fetal and maternal movements are the
948 dominant factors affecting continuity, and we did not observe dependence on gestational age or
949 pathology grouping. A minimum uninterrupted duration of ~ 2 s (corresponding to >5 fetal cardiac
950 cycles) is required to localize and stably track the umbilical artery in duplex imaging for spectral
951 Doppler acquisition. During continuous monitoring sessions, duplex mode vessel tracking
952 occurred in intermittent segments of variable duration (typically several seconds), reflecting
953 ongoing fetal and maternal motion, while still allowing recurrent spectral Doppler acquisition
954 whenever motion was sufficiently slow (Supplementary Video 1).

955 Despite this improvement, the method still has limitations. First, the autonomous tracking
956 algorithm cannot detect movements after spectral Doppler signals have been acquired. Second,
957 waiting until the vessel stops moving quickly to apply a sample gate leads to variability in the
958 response time. Third, the algorithm cannot acquire spectral Doppler during vessel movement.

959 To mitigate these issues, three solutions are proposed. First, an additional algorithm can be
960 developed to identify signal loss in the spectral Doppler based on its luminosity¹³⁴. This would
961 detect fast movements, enabling the algorithm to identify when the signal is lost and switch back
962 to duplex imaging for further tracking. Currently, we minimized this issue by acquiring 3 s of
963 spectral Doppler prior to switching back to duplex imaging (Fig. 3c and Supplementary Video 1).

964 This approach ensures that spectral Doppler signals are acquired for a short duration, minimizing
965 the impact of movement.

966 Second, image segmentation-based machine learning models can directly generate a sample gate
967 from a single image¹⁴⁶. The current tracking algorithm requires multiple frames to calculate the
968 sample gate, resulting in variability in response time (Supplementary Video 1). To solve this
969 problem, machine learning models, trained on annotated datasets, allow individual images to
970 generate a sample gate. This approach minimizes variability in response time and tracks the target
971 vessel during movement.

972 Third, integrating a more advanced graphics processing unit in the backend system can
973 substantially enhance the beamforming framework¹⁴⁷. Recent advances in graphics processing
974 units enable a much larger number of parallel executing cores, facilitating faster computation and
975 allowing simultaneous duplex imaging and spectral Doppler acquisition¹⁴⁸. This approach allows
976 spectral Doppler acquisition even during movement, thereby improving overall efficiency and
977 response time.

978

979 **Supplementary Discussion 18: Evaluation of the autonomous tracking algorithm**

980 The vessel tracking algorithm is based on conventional image processing techniques, which do not
981 require cross-validation. Machine learning or artificial intelligence-based models require a labeled
982 training dataset to learn features and a separate testing dataset to evaluate performance. Our
983 approach applies deterministic operations directly to the input data and does not involve model
984 training. There is no differentiation between training and testing datasets. Therefore, cross-
985 validation procedures, which are essential for evaluating generalizability in trained models, are not
986 applicable in this context.

987 The autonomous tracking algorithm in this study was evaluated using three methods to test its
988 accuracy and reliability across different scenarios. In fetal ultrasound, manual sample gating by
989 experienced sonographers remains the clinical gold standard for assessing signal quality and
990 tracking accuracy¹⁴⁹. The evaluation method we employed aligns with established clinical
991 standards and other studies in the literature^{137,150}. Additionally, in contrast to these cited
992 studies^{137,150}, which employed only a single validation method, our approach was comprehensively
993 validated using three independent methods. In the FDA-cleared Acuson Origin (Siemens) system,
994 the autonomous sample gate placement underwent validation using only 168 images as part of its
995 FDA clearance process¹³⁷. The validation accuracy evaluated by three sonographers was defined
996 as “no adjustment or only minor adjustment needs to be made by the user”¹³⁷. In the peer-reviewed
997 study, accuracy of a deep learning-based sample gating was validated using a method similar to
998 our first validation method¹⁵⁰. To the best of our knowledge, these reported works were the only
999 studies that demonstrate tracking algorithm validation for ultrasound imaging.

1000 The first two methods were based on pre-collected images, allowing direct comparison against
1001 sonographers. In the first method, a double-blind setup was used where both the tracking algorithm
1002 and the sonographer selected optimal tracking points in the same images collected using the
1003 UPatch. The differences between these points were then measured in axial and lateral dimensions,
1004 providing a quantifiable metric of the algorithm’s accuracy.

1005 In the second method, three sonographers visually assessed the accuracy of the tracking algorithm.
1006 They categorized the tracked points into three levels: “Optimal” for points suitable for acquiring
1007 high-quality spectral Doppler signals, “Sub-optimal” for points that might yield low quality signals,
1008 and “Non-diagnostic” for points incapable of providing usable Doppler signals. However, these
1009 evaluations did not account for the actual spectral Doppler signals that could be acquired from the
1010 tracked points.

1011 Thus, a third method was employed to quantify the differences between the systolic-to-diastolic
1012 ratios of the actual spectral Doppler signals collected from the points of the autonomous tracking
1013 algorithm and those selected by a sonographer, providing a more practical assessment of the
1014 algorithm’s performance.

1015 This three-step evaluation process provided a robust framework for optimizing the tracking
1016 algorithm. By incorporating offline sonographer comparisons of the sample gates and practical
1017 online assessments of spectral Doppler accuracy, the study ensured the algorithm was finely tuned
1018 for clinical uses.

1019 We also performed a retrospective comparison with two widely used deep learning models: U-
1020 Net¹⁵¹ and ConvLSTM¹⁵² (Supplementary Fig. 35). Both deep learning models were trained and
1021 evaluated using a dataset containing 1,000 duplex images acquired with the UPatch. The dataset
1022 was split into independent training and validation sets, and training was continued until
1023 convergence of the validation loss to ensure optimal model performance without overfitting.

1024 Tracking accuracy was assessed by three independent sonographers. The tracking algorithm in this
1025 work achieved a tracking accuracy of 93.1%, the U-Net model achieved 92.2%, and the
1026 ConvLSTM model achieved 96.7%. Computational efficiency was evaluated by measuring per-
1027 frame processing time on the backend system (Vantage 256, Verasonics). The tracking algorithm
1028 in this work required 0.0698 ± 0.0083 s per frame, the U-Net model required 0.719 ± 0.0436 s,
1029 and the ConvLSTM model required 0.7439 ± 0.0535 s. While the accuracy of the three methods
1030 is similar, the tracking algorithm developed in this work achieves more than a tenfold reduction in
1031 processing time, enabling real-time image processing.

1032

1033 **Supplementary Discussion 19: Ultrasound sample gate**

1034 Accurately delineating the sample gate within the duplex image is crucial¹⁵³. Ideally, the sample
1035 gate should cover the entire vessel diameter to ensure accurate measurement of the complete
1036 hemodynamic profile⁴⁸. However, clinicians commonly position a 2 mm sample gate at the
1037 vessel’s center to record the spectral Doppler signals (Supplementary Fig. 31)⁵⁰. There are two
1038 practical reasons.

1039 First, the 2 mm size ensures that the vessel does not shift away from the sample gate during
1040 measurements⁴⁸. The umbilical arteries are closely intertwined with the umbilical vein,
1041 necessitating a clear distinction between them. This sample gate size is typically smaller than most
1042 fetal vessels in the third trimester, allowing assessment of the target vessel even during small vessel
1043 movements⁵³.

1044 Second, Doppler indices derived from the vessel’s center are negligibly different from those
1045 derived from the entire vessel diameter. Blood flow within vessels typically exhibits a parabolic

1046 profile (laminar flow), with red blood cells traveling at varying velocities⁸⁵. This velocity gradient
1047 is characterized by the highest velocities at the vessel's center and the lowest velocities near the
1048 vascular wall due to viscous drag⁸⁵. Doppler indices, such as the systolic-to-diastolic ratio,
1049 pulsatility index, and resistance index, are derived from the peak systolic velocity, end diastolic
1050 velocity, and mean flow velocity extracted from the spectral waveform envelope^{48,51}. The peak
1051 systolic velocity, end diastolic velocity, and mean flow velocity extracted from the spectral
1052 waveform envelope of the entire vessel diameter are negligibly different from those extracted from
1053 the spectral waveform envelope of the vessel center. Thus, these Doppler indices are not affected
1054 much when the sample gate is positioned at the vessel's center.

1055 Because of such practical considerations, this study utilized the standard sample gate size of 2 mm.

1056

1057 **Supplementary Discussion 20: Continuous monitoring of the umbilical artery**

1058 Doppler indices vary along the umbilical artery, with blood flow resistance highest at the fetal
1059 abdominal cord insertion, intermediate at the free-loop cord, and lowest at the placental cord
1060 insertion⁴⁹. Thus, it is important to sample spectral Doppler consistently at the same site of the
1061 umbilical artery throughout the duration of continuous monitoring⁶⁰.

1062 Continuous monitoring of the umbilical cord at the fetal abdominal insertion site presents practical
1063 difficulties, particularly in advanced gestation⁴⁹. First, the fetus can move or rotate in the uterus,
1064 causing the umbilical cord at the fetal abdominal insertion site to move out of the sonographic
1065 window. Second, the site may be obscured by fetal lower limbs or oligohydramnios, a condition
1066 characterized by low amniotic fluid levels that limit the acoustic window⁴⁹.

1067 Sampling a fixed position of the free-loop cord also has disadvantages. First, the umbilical cord
1068 can extend an average length of 64 cm, making it challenging to sample consistently at the same
1069 position during continuous monitoring¹⁵⁴. The umbilical cord is constantly displaced as it floats
1070 inside the amniotic fluid under various environmental changes, including fetal movement, fetal
1071 breathing, maternal movement, maternal breathing, and uterine contractions⁵¹.

1072 The umbilical cord at the placental cord insertion is also moving, but the placenta is fixed on the
1073 maternal uterine wall^{48,51}. Although the umbilical cord itself moves, its position at the placental
1074 cord insertion remains relatively identifiable by using the placenta as a stable anatomical reference
1075 (Extended Data Fig. 5)⁵⁰. As a result, the UPatch was positioned to insonate the umbilical cord at
1076 the placental cord insertion. In our experiments, after identifying the optimal location and
1077 orientation using a clinical device, we laminated the UPatch. Throughout various maternal and
1078 fetal movements, this consistent anatomical reference enables reliable imaging at the placental
1079 cord insertion, ensuring continuous monitoring without relocating the UPatch.

1080 We conducted a study in which the UPatch was tested across a range of common maternal postures:
1081 lying supine, lying on the right side, lying on the left side, and sitting upright (Extended Data Fig.
1082 5). In all cases, the UPatch successfully acquired the umbilical cord Doppler signals. As a result,
1083 the UPatch did not require repositioning and could maintain continuous spectral Doppler sampling
1084 at the placental cord insertion throughout the monitoring period.

1085

1086 **Supplementary Discussion 21: Ultrasound incident angle**

1087 Accurate measurements of blood flow velocities are influenced by the ultrasound incident angle,
1088 which is the angle between the ultrasound beam and the direction of blood flow¹³³. To derive
1089 accurate velocity, measuring the ultrasound incident angle is essential. Conventionally, an angle
1090 correction cursor is aligned to the flow direction within the vessel visualized in the duplex image
1091 to calculate the incident angle^{48,51}. However, this method may be inaccurate because the vessel
1092 may not lie in the incident plane⁴⁸.

1093 To circumvent the need for angle measurements and eliminate its associated inaccuracies, Doppler
1094 indices, such as the systolic-to-diastolic ratio, pulsatility index, and resistance index, are widely
1095 employed⁴⁸. These indices are angle-independent because they are normalized (Supplementary
1096 Discussion 5)⁴⁸. This allows reliable assessment of vascular resistance and blood flow
1097 characteristics that are not subject to the variances of vessel orientations. Consequently, these
1098 angle-independent indices are preferred in clinical diagnosis^{66,67}.

1099 The UPatch operates as a single-beam device using the full aperture to generate either a diverging
1100 or focused beam. Future work could enable cross-beam Doppler acquisition, where beams intersect
1101 the same vessel segment from different angles to recover the absolute flow velocity¹⁵⁵, and multi-
1102 point acquisition, where spatially separated sampling locations allow assessment of pulse wave
1103 propagation^{156,157}. These capabilities can assess absolute flow or pulse wave velocity values
1104 distributed across the fetoplacental vessels.

1105 Cross-beam Doppler enables calculation of the blood flow velocity by insonating the same
1106 vascular segment with two intersecting ultrasound beams with a defined geometric relationship¹⁵⁵.
1107 The intersecting beams are transmitted using individual transducers^{158,159} or electronically steered
1108 sub-apertures of an array^{160,161}, and each beam provides an independent measurement of Doppler
1109 frequency shift. Using these values, the blood flow velocity can be calculated as¹⁵⁵:

$$1110 \quad v = \frac{c}{2F_0} \frac{1}{\sin\delta} \sqrt{f_1^2 + f_2^2 - 2f_1f_2\cos\delta} \quad (25)$$

1111 where c is the speed of sound, F_0 is the transmit frequency, δ is the intersection angle between
1112 the two beams, and f_1 and f_2 are the Doppler frequency shifts.

1113 This calculation yields a flow velocity estimate at the beam intersection with minimal
1114 computational power. However, the measurement is highly sensitive to maternal and fetal
1115 movements, as even small displacements can cause the beam intersection to no longer coincide
1116 with the intended vessel segment. As a result, accurate cross-beam measurements require frequent
1117 realignment of the beam intersection with the moving vessel, which has limited the adoption of
1118 this technique in dynamic fetal monitoring.

1119 The vessel tracking algorithm developed in this work could provide a pathway toward cross-beam
1120 Doppler by continuously updating beam placement to maintain alignment with the target vessel
1121 during motion. This approach could enable automated estimation of absolute blood flow velocity
1122 and would be particularly advantageous for fetoplacental vessels with complex or dynamically
1123 changing orientations, such as the umbilical cord.

1124 Multi-point acquisition records pulse waveforms from two or more spatially separated points along
1125 a vessel using individual devices, enabling pulse wave velocity measurements¹⁵⁶. By recording

1126 pulse waveforms at these distinct locations, the system can measure the pulse transit time, the time
1127 for the pulse pressure wave to travel between two sites, and calculate the pulse wave velocity¹⁶²:

$$1128 \quad PWV = \frac{L}{PTT} \quad (26)$$

1129 where L is the distance between two recording sites, and PTT is the measured pulse transit time.

1130 As an indicator of vascular tone and stiffness, increased pulse wave velocity in fetoplacental
1131 vessels reflects compromised placental perfusion and impaired oxygen and nutrient transfer, which
1132 are associated with fetal growth restriction and adverse perinatal outcomes. However, accurate
1133 measurement of the path length between recording sites is challenging in fetal vessels due to depth,
1134 curvature, and continuous motion, leading to uncertainty in pulse wave velocity estimation.

1135 Phase aberration correction in the UPatch beamforming enables accurate image reconstruction
1136 across varying maternal abdominal curvatures, preserving geometric fidelity. This allows accurate
1137 length estimation of deep fetoplacental vessels, after which two beams can be targeted at proximal
1138 and distal vessel locations to acquire synchronized pulse waveforms. Combining the measured
1139 pulse transit time with the accurately estimated vessel path length enables the precise calculation
1140 of pulse wave velocity.

1141

1142 **Supplementary Discussion 22: Abnormality in a pre-eclamptic participant**

1143 We continuously monitored 52 participants across a range of gestational ages in third trimester
1144 and clinical conditions to evaluate the UPatch's ability to capture hemodynamic changes. One pre-
1145 eclamptic participant exhibited markedly abnormal patterns in her Doppler indices. To highlight
1146 the diagnostic value of continuous monitoring of blood flow, we present a comparative analysis
1147 between a healthy participant at 32 weeks 6 days and the pre-eclamptic one at 28 weeks 3 days
1148 gestational age.

1149 The average fetal heart rate was 149.5 bpm for the healthy and 143.3 bpm for the pre-eclamptic
1150 participants (Fig. 4b). Both were within the normal range of 120–160 bpm (Supplementary
1151 Discussion 3)^{17,43}. In addition, their fetal heart rate variabilities were 20.3 bpm and 21.5 bpm,
1152 respectively, characterized as moderate variability, indicating healthy fetuses (Supplementary
1153 Discussion 3)^{17,43}. Thus, cardiocography devices could not detect the compromised fetal health
1154 of the pre-eclamptic participant.

1155 Notable differences were observed in the resistance index, pulsatility index, and systolic-to-
1156 diastolic ratio between the two participants. The healthy participant had an average resistance
1157 index of 0.62, pulsatility index of 1.04, and systolic-to-diastolic ratio of 2.61 (Fig. 4b and
1158 Supplementary Fig. 36). In contrast, the pre-eclamptic participant had an average resistance index
1159 of 0.85, pulsatility index of 2.04, and systolic-to-diastolic ratio of 5.11 (Fig. 4b and Supplementary
1160 Fig. 37).

1161 For the healthy participant's gestational age, the 50th percentile values are 0.63 for resistance index,
1162 0.96 for pulsatility index, and 2.68 for systolic-to-diastolic ratio⁶⁸. For the pre-eclamptic
1163 participant's gestational age, the 50th percentile values are 0.66 for resistance index, 1.03 for
1164 pulsatility index, and 2.93 for systolic-to-diastolic ratio⁶⁸. The healthy participant's values were

1165 near the 50th percentile, whereas the pre-eclamptic participant's values were markedly higher,
1166 indicating poor blood flow exchange between the fetus and placenta.

1167 Following the detection of abnormal umbilical artery blood flow in the pre-eclamptic participant
1168 using the UPatch, the research activities were halted. The mother underwent intensive monitoring
1169 with clinically validated devices, and the baby was delivered 4 days later, at 203 days of gestation,
1170 via Cesarean section. The UPatch detected abnormalities that conventional cardiocography
1171 failed to identify, leading to a timely intervention that saved the fetus. The newborn is thriving,
1172 demonstrating the real-world clinical value of this technology.

1173

1174 **Supplementary Discussion 23: Clinical importance of continuous monitoring of blood flow**

1175 Continuous monitoring of blood flow using the UPatch enables clinically meaningful assessment
1176 of fetal well-being throughout pregnancy.

1177 First, in current obstetric practice, cardiocography is used to continuously monitor fetal heart
1178 rate, particularly for inpatients. When prolonged fetal heart rate decelerations or abnormal patterns
1179 are observed, Doppler ultrasound is typically employed by sonographers to assess umbilical blood
1180 flow⁵⁹. This two-step process is time-consuming and labor-intensive, which may delay or miss the
1181 optimal timing to detect fetal complications, reflecting a technological gap. The UPatch addresses
1182 this gap by providing continuous monitoring of both fetal heart rate and umbilical blood flow in a
1183 single system without the need for a sonographer.

1184 Second, the UPatch enables baseline measurement of umbilical blood flow and differentiate
1185 normal from abnormal physiological fluctuations. Normal fluctuations can temporarily alter
1186 spectral Doppler waveforms. When captured by intermittent scans, such altered values do not
1187 reflect true pathology and may raise false positive concerns or trigger unnecessary clinical
1188 interventions (Supplementary Figs 36–87)¹⁶³. This limitation of intermittent scans reduces
1189 reliability in dynamic and complicated clinical settings, often requiring serial measurements over
1190 several days. The UPatch addresses this limitation by providing a continuous data stream of
1191 umbilical blood flow, allowing clinicians to distinguish sustained compromise from transient, self-
1192 resolving physiological fluctuations, which supports more reliable, real-time clinical decision-
1193 making.

1194 Third, unlike fetal heart rate, which requires complex time-series analysis, Doppler indices offer
1195 clinically validated measurements of fetal hemodynamics^{9,164}. Fetal heart rate interpretation relies
1196 on pattern recognition to assess baseline, variability, accelerations, and decelerations over a long
1197 period of time, because isolated values are insufficient to reveal fetal well-being⁹. However, these
1198 time-series features show poor correlation with gestational trends and perinatal risks^{2,9,165}. In
1199 contrast, the three Doppler indices used in this study are well-established parameters heavily used
1200 in hospitals to assess placental and fetal vascular resistance^{66-68,166,167}. Doppler indices have well-
1201 defined reference ranges, exhibit consistent gestational trends, and stratify risk groups with great
1202 sensitivity^{59,67,68}. Continuous monitoring with the UPatch enables real-time acquisition of these
1203 indices without the need for time-series analysis (Fig. 4e–i and Supplementary Figs 93–95).

1204 Fourth, the UPatch provides continuous, actionable information that supports more precise risk
1205 management of the trade-off between preterm delivery (delivery before 37 weeks) and stillbirth
1206 than cardiocography¹⁶⁸. Before 37 weeks, clinicians aim to avoid delivery unless fetal

1207 compromise is evident. In a pre-eclamptic patient (28 weeks 3 days gestational age) in this study,
1208 the UPatch identified umbilical flow abnormalities that were not evident on conventional
1209 cardiotocography, prompting an intervention that saved a baby (Fig. 4a–d).

1210

1211 **Supplementary Discussion 24: Data processing**

1212 Data preprocessing and processing were performed locally on the backend system (Vantage 256,
1213 Verasonics), which is a research-grade ultrasound platform widely used for real-time data
1214 acquisition^{169,170}. Data preprocessing is the initial step, including down-sampling and denoising,
1215 which are applied to the raw radiofrequency signals. Then, data processing, including
1216 beamforming to generate duplex images, autonomous tracking to identify the sample gate, and
1217 spectral Doppler estimation to extract velocity waveforms, is implemented for real-time data
1218 acquisition.

1219 By directly transferring raw radiofrequency signals to the backend system, this protocol ensured
1220 minimal latency with negligible delay. Privacy was maintained because all participant data were
1221 transmitted by a flexible cable and remained within the local processing station, eliminating
1222 security concerns associated with wireless transmission or cloud-based storage. Additionally, the
1223 study was approved by the Institutional Review Board, ensuring compliance with privacy
1224 regulations. Computational requirements were sufficiently managed by the backend system, which
1225 was specifically designed to handle high-throughput ultrasound data processing¹⁷⁰.

1226 To optimize storage, the system prioritizes clinically actionable data and discard unnecessary high-
1227 volume raw imaging. Specifically, instead of storing full duplex images and spectral Doppler
1228 waveforms, the system extracts and saves Doppler indices (such as resistance index, pulsatility
1229 index, and systolic-to-diastolic ratio) and fetal heart rate, which are one-dimensional and require
1230 minimal storage. This approach ensures storage efficiency while providing essential information
1231 for clinical decision-making.

1232

1233 **Supplementary Discussion 25: Predictive modeling**

1234 To assess the feasibility of risk classification using UPatch measurement features, we performed
1235 pilot predictive modeling using participant-level mean Doppler indices and fetal heart rate
1236 (Supplementary Fig. 96)¹⁷¹. While limited sample sizes within individual perinatal condition
1237 groups may constrain predictive performance, we piloted implementing logistic regression to
1238 evaluate whether mean fetal heart rate, pulsatility index, systolic-to-diastolic ratio, and resistance
1239 index could distinguish perinatal risk conditions¹⁷².

1240 Receiver operating characteristic (ROC) analyses were used to evaluate the ability of a predictive
1241 measurement to quantify discriminative performance among different health outcomes¹⁷³. The x-
1242 axis shows the false positive rate (1 – specificity; specificity quantifies the proportion of true
1243 negatives correctly identified), and the y-axis shows the true positive rate (sensitivity; sensitivity
1244 measures the proportion of true positives correctly identified). Each point on the curve represents
1245 the performance of the classifier at a different decision threshold, which is the cutoff to convert a
1246 predicted probability into a perinatal risk condition. The area under the ROC curve (AUROC)
1247 provides a single summary metric of discriminative performance: a value of 0.5 corresponds to

1248 chance-level performance (no predictive ability), whereas values closer to 1.0 indicate stronger
1249 ability to distinguish perinatal risk conditions. By comparing AUROC values for fetal heart rate
1250 and Doppler indices, we can quantify how well each measurement predicts perinatal risk.

1251 For the healthy, large for gestational age, pre-eclampsia, and hypertension groups, AUROC values
1252 for Doppler indices were in the range of 0.605–0.651 compared with 0.533–0.646 for fetal heart
1253 rate, reflecting modest but systematic improvement in discrimination. For the small for gestational
1254 age group, Doppler indices achieved AUROC values in the range of 0.959–0.962, substantially
1255 exceeding the corresponding fetal heart rate AUROC of 0.511, indicating markedly stronger
1256 discriminative performance. For the diabetes group, classification performance remained near
1257 chance level for both Doppler indices and FHR with AUROC values of 0.522–0.525 and 0.562,
1258 respectively, suggesting limited separability.

1259

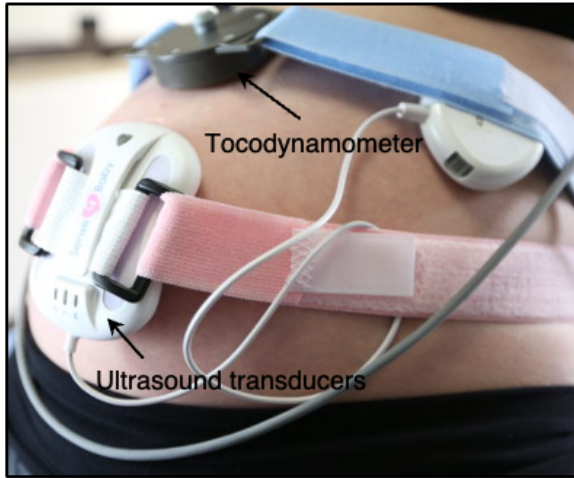
1260 **Supplementary Discussion 26: Circuit integration**

1261 The current UPatch with a wired connection for power and data is optimal for hospital monitoring.
1262 However, wireless home monitoring presents distinct clinical advantages. First, it offers a
1263 comfortable environment that can yield more precise baseline measurements of fetal blood flow,
1264 which is critical for high-risk pregnancies (such as gestational diabetes and pre-eclampsia)⁵⁴.
1265 Additionally, it can allow research into how maternal exercise influences fetal hemodynamics⁵⁵.
1266 Second, continuous home monitoring generates more extensive data over time, allowing for trend
1267 analysis and research into the mechanisms of fetal complications and stillbirth¹⁷⁴. Third, it supports
1268 regular assessments without the inconvenience and costs associated with hospital visits, crucial for
1269 those with limited access to healthcare facilities, especially in low/middle-income areas^{11,175}.

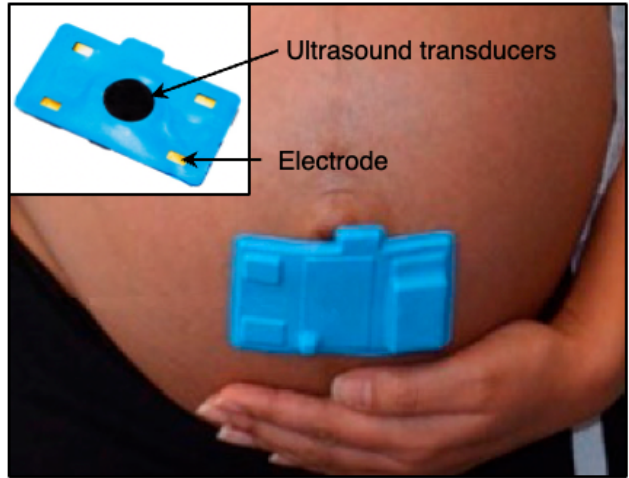
1270 A recently introduced wearable ultrasound circuit has enabled wireless home monitoring¹³⁴. This
1271 system can multiplex the signals from all 32 channels of transducer elements through a single
1272 transceiver. A Wi-Fi module transmits the received signals to a smartphone, monitoring tissue
1273 interfaces and providing critical insights during physical activities (such as biking and high-
1274 intensity training). However, its imaging capabilities are limited due to the circuit comprising only
1275 a single transceiver. First, while multiplexing can enable imaging, the transducer elements are
1276 activated sequentially. This means that there is a time delay between received signals, resulting in
1277 low image quality from moving tissue interfaces and red blood cells¹⁷⁶. Second, for color Doppler
1278 imaging, the transceiver must activate the same transducer at a high pulse repetition frequency
1279 (~3000 Hz) to assess the mean phase differences among multiple pulse echos⁸⁵. This setup, while
1280 feasible for a single transducer, results in a loss of spatial resolution and intrinsically low Doppler
1281 signal-to-noise ratio⁸⁶. Due to these limitations, this circuit is inadequate for producing high-
1282 quality ultrasound images.

1283 Multiple transceivers are needed to achieve high-quality imaging, but there are three major
1284 challenges¹⁷⁷. First, the increased power consumption from additional transceivers will necessitate
1285 more efficient power management solutions to sustain battery life¹⁷⁸. Second, heat generation
1286 poses a substantial challenge because additional circuit components will cause heat accumulation,
1287 requiring advanced thermal management strategies to ensure the device's safe use¹⁷⁷. Third,
1288 multiple transceivers will complicate the firmware design, requiring more sophisticated signal
1289 processing algorithms¹⁷⁷. Despite its challenges, the integration of multiple transceivers into
1290 wearable ultrasound circuits will enable high-quality imaging for wireless home monitoring.

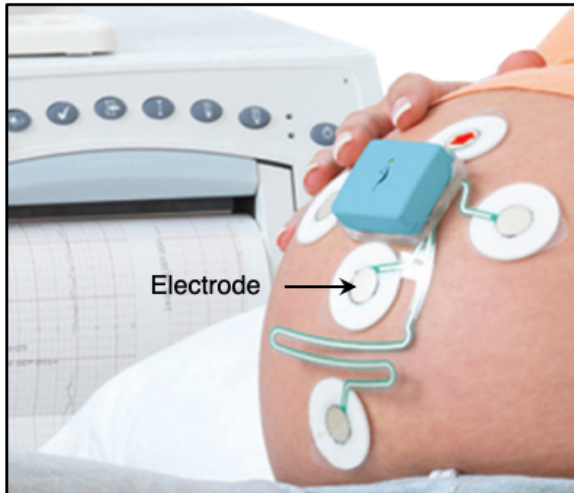
a Conventional cardiocography



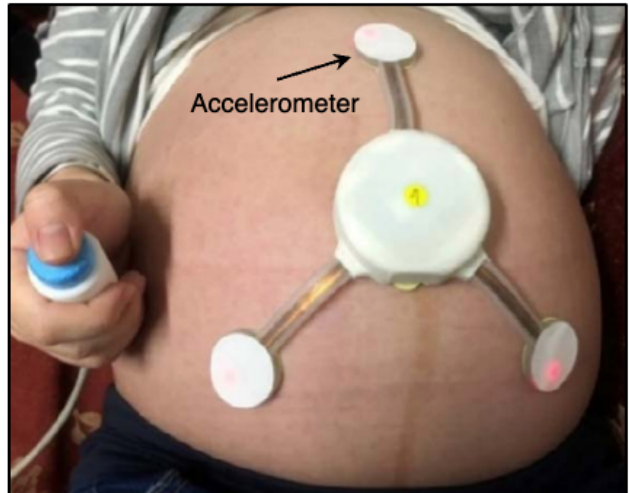
b Flexible cardiocography



c Electrocardiogram

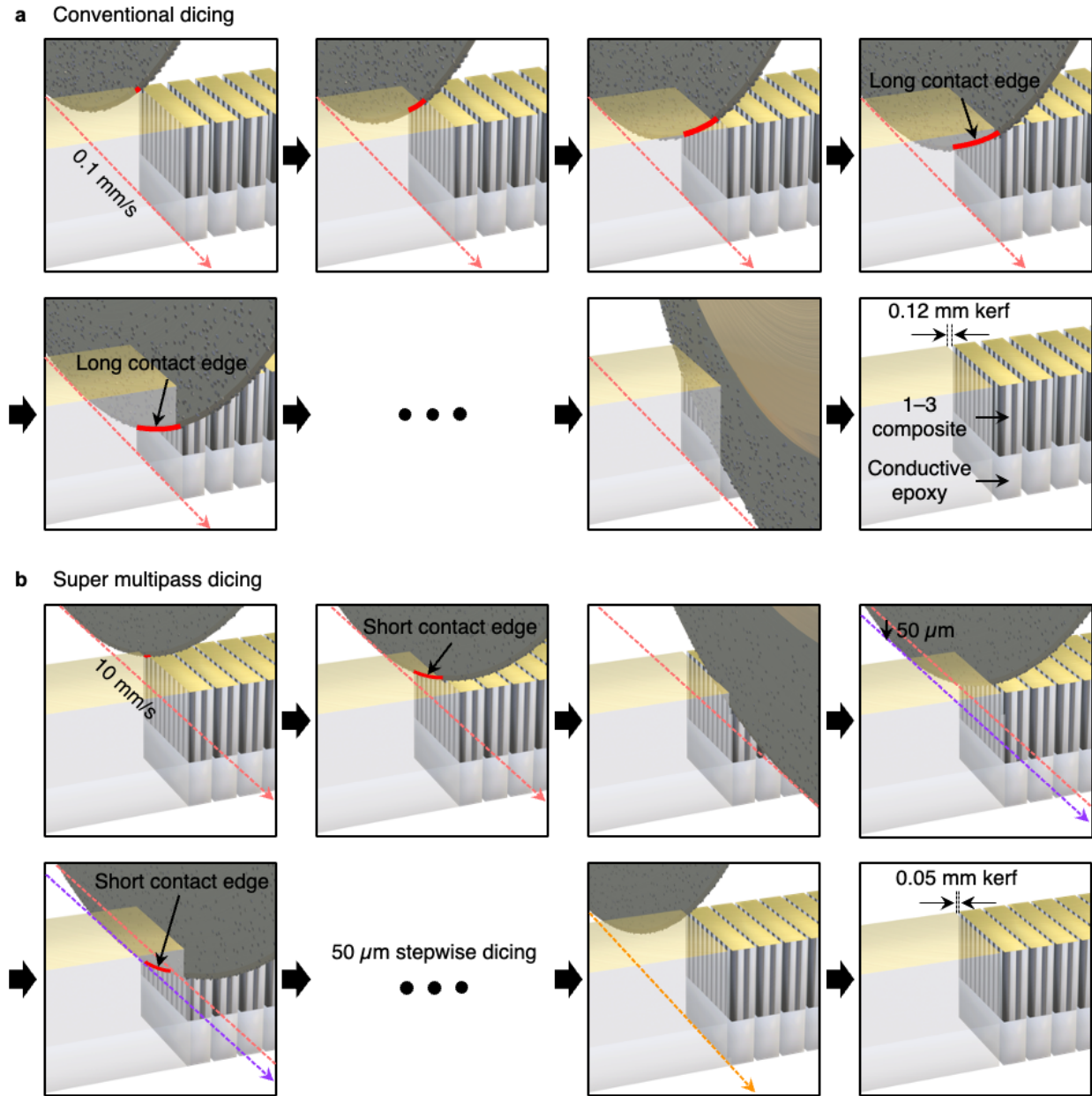


d Fetal movement monitor

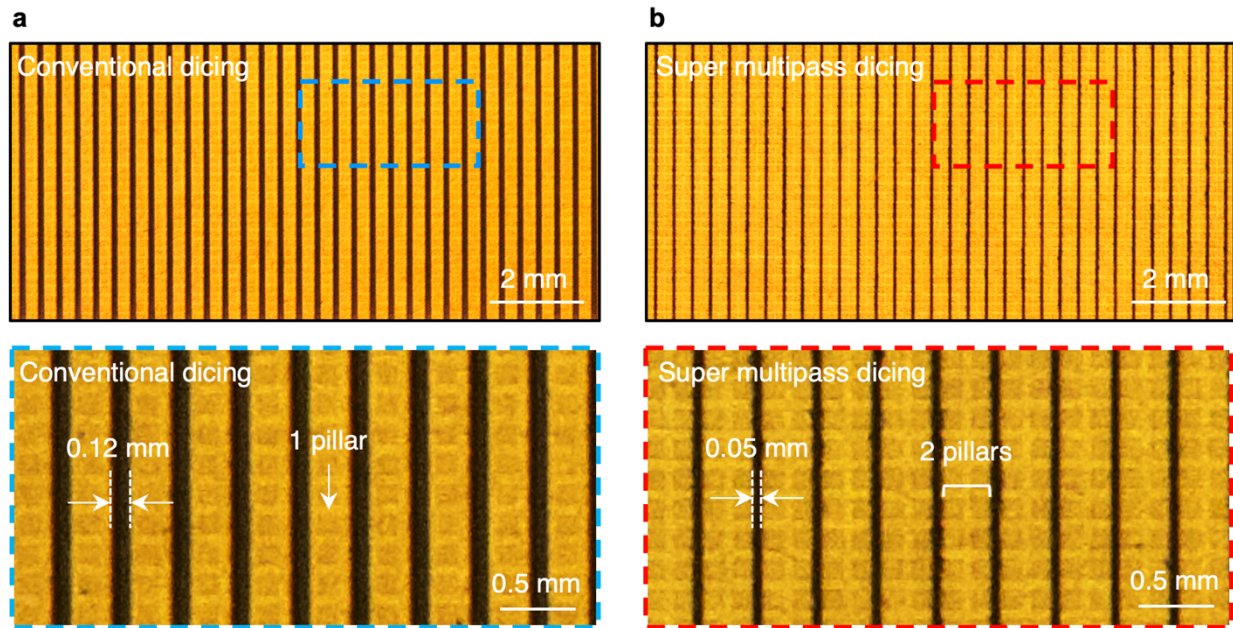


1291
1292
1293
1294
1295
1296
1297
1298
1299
1300

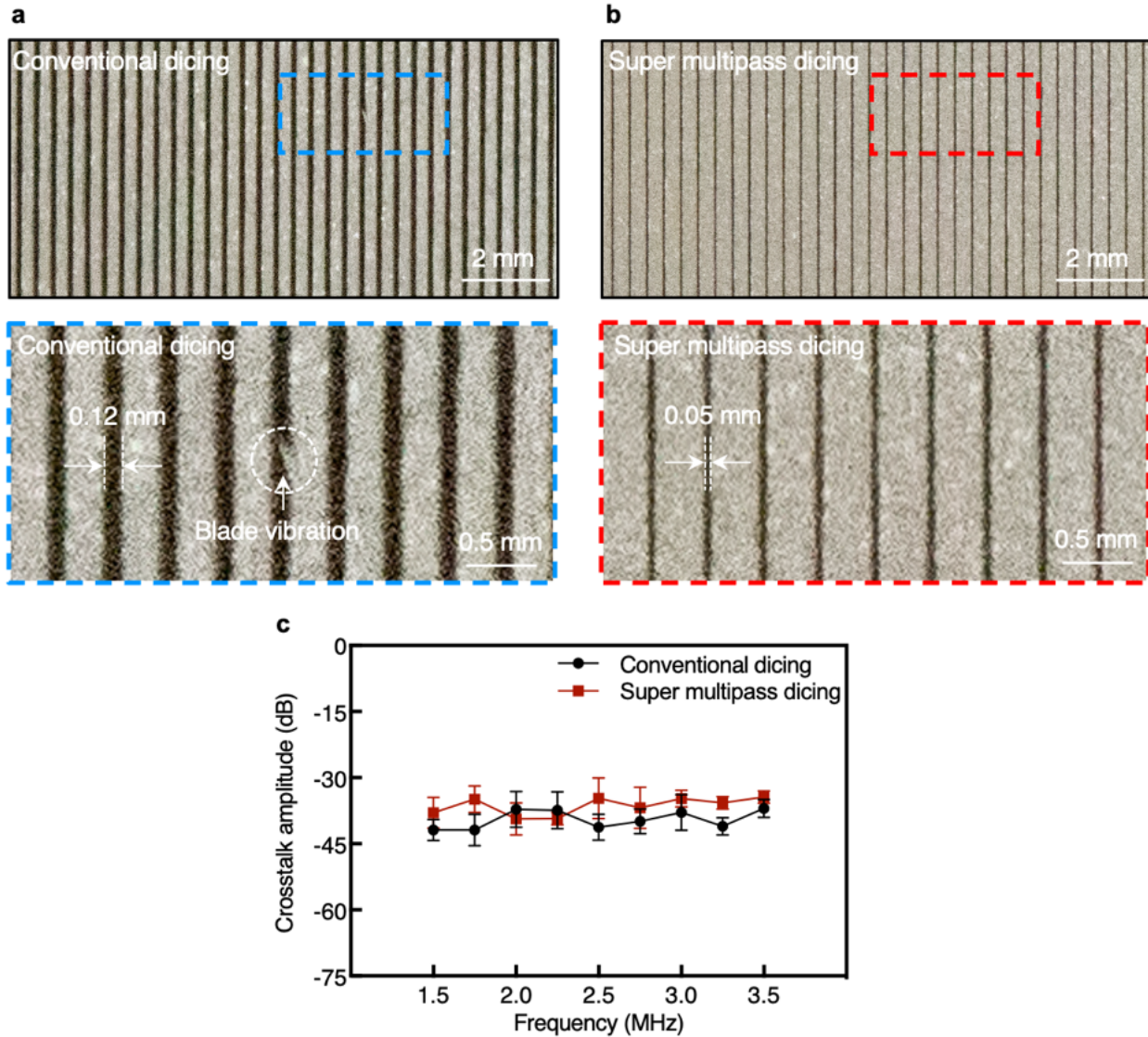
Supplementary Fig. 1 | Existing wearable fetal monitors. **a**, Conventional cardiocography comprising ultrasound transducers for fetal heart rate monitoring and a tocodynamometer for uterine contraction monitoring developed by Sense4baby^{20,179}. **b**, Flexible cardiocography using two ultrasound transducers for fetal heart rate recording and four electrodes for maternal electrocardiogram and electrohysterogram to derive uterine contraction developed by Sibel Health²³. **c**, Fetal electrocardiogram measured with five electrodes to derive fetal heart rate developed by Monica Healthcare (now GE Healthcare)^{25,180}. This configuration claims to derive fetal heart rate regardless of fetal position in the maternal abdomen. **d**, Fetal movement sensor using accelerometers³⁸.



1301
 1302 **Supplementary Fig. 2 | Dicing strategies.** **a**, Conventional dicing strategy. The blade is lowered
 1303 to the entire transducer depth of 1 mm and diced at 0.1 mm/s feed speed. This method results in a
 1304 long contact edge, producing a 0.12 mm kerf. The entire process takes ~15 h to dice a 64-channel
 1305 array with a 0.4 mm pitch for a 25.55 mm by 12 mm transducer element. **b**, Super multipass dicing
 1306 used in this study. A thinner dicing blade is used with 50 µm stepwise depth cuts. The blade is first
 1307 lowered 50 µm from the top of the transducer and diced at 10 mm/s. Then, it is subsequently
 1308 lowered to another 50 µm depth for dicing. This method results in a short contact edge. A total of
 1309 20 stepwise cuts are performed to achieve a 0.05 mm kerf for the same array size, which only takes
 1310 ~3 h.

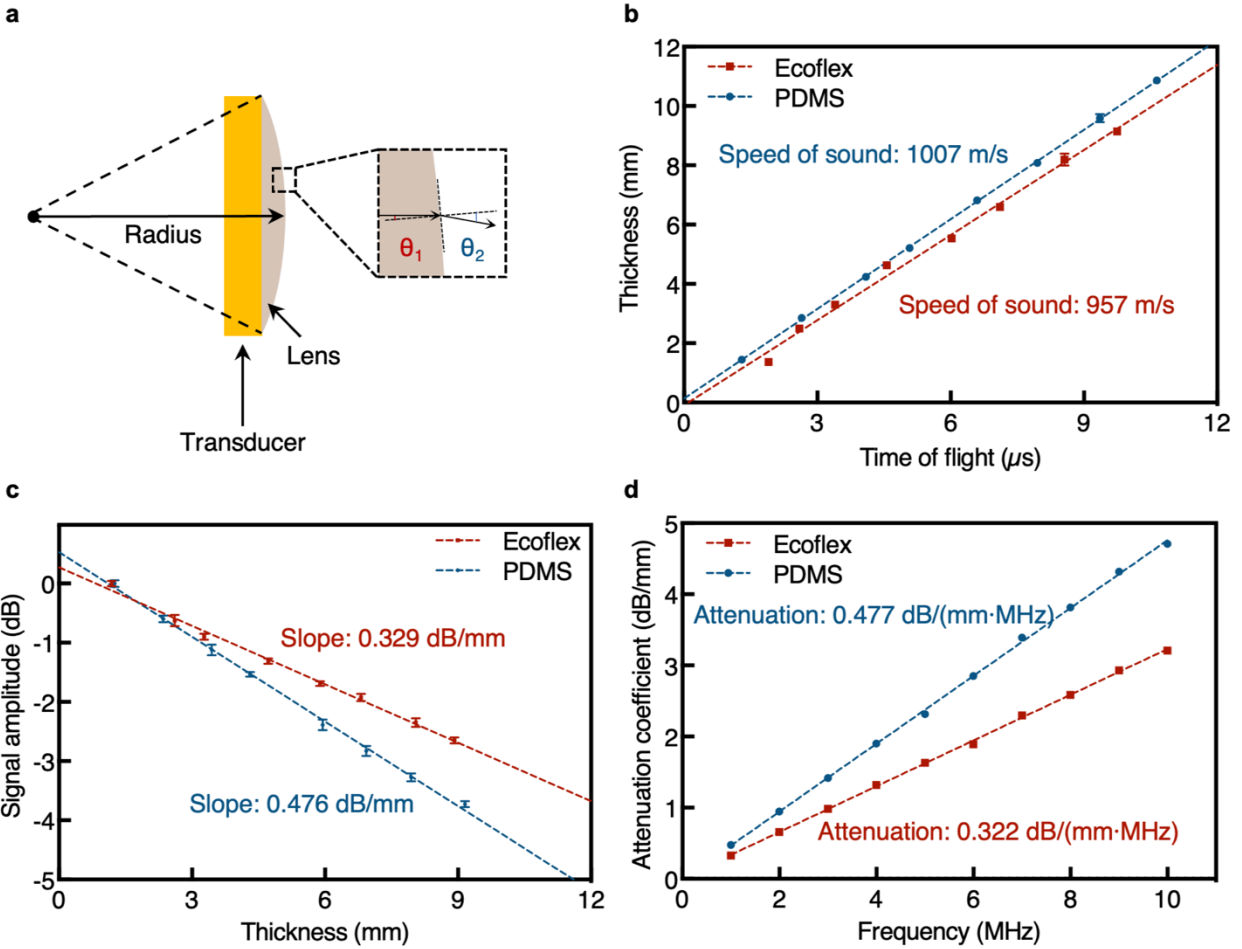


1311
 1312 **Supplementary Fig. 3 | 1–3 composite side of the transducers diced with different strategies.**
 1313 **a**, Optical images of transducers diced with the conventional strategy. The kerf is 0.12 mm and
 1314 can only accommodate one piezoelectric pillar of the 1–3 composite. **b**, Optical images of
 1315 transducers diced with the super multipass strategy. The kerf is 0.05 mm and can accommodate
 1316 two piezoelectric pillars of the 1–3 composite.



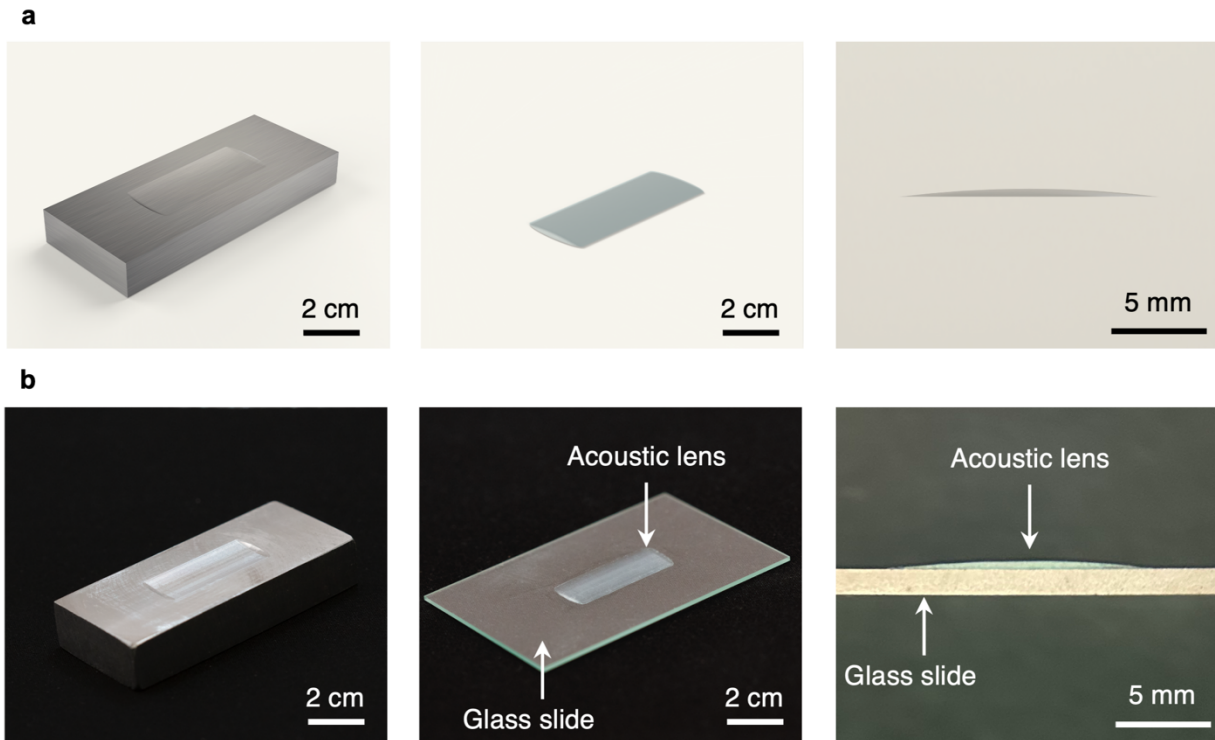
1317
 1318
 1319
 1320
 1321
 1322
 1323

Supplementary Fig. 4 | Comparison of transducers diced with different strategies. **a**, Optical images of the backing layer side of the transducer diced with the conventional strategy. The kerf is 0.12 mm and blade vibration can cause defects in the transducers. **b**, Optical images of backing layer side of the transducer diced with the super multipass strategy. The kerf is 0.05 mm. **c**, Transducers diced with both strategies demonstrate similar crosstalk amplitude. Data in **c** are presented as mean \pm standard deviations ($n = 4$).

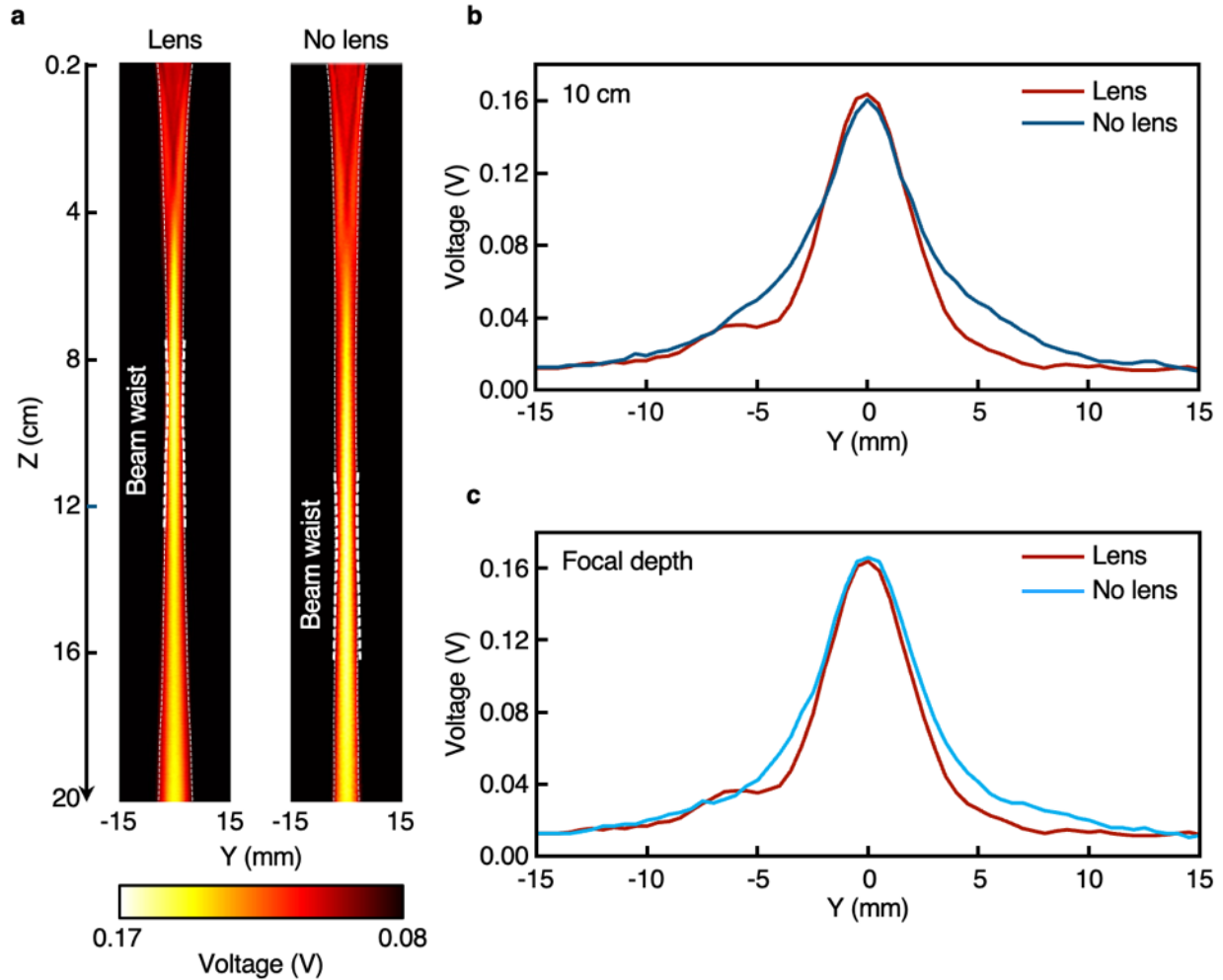


1324
1325
1326
1327
1328
1329
1330
1331
1332

Supplementary Fig. 5 | Design of the acoustic lens. **a**, Schematics of the lens. The speed of sound of the lens material is used to determine the lens radius. θ_1 and θ_2 are the incidence angle and refraction angle, respectively. **b**, Speed of sound and **c**, acoustic attenuation coefficients at 1 MHz ultrasound frequency of soft acoustic lens materials. **d**, Acoustic attenuation coefficients at 1–10 MHz ultrasound frequencies of soft acoustic lens materials. Each data point in **d** is obtained from a linear fit in **c**. Ecoflex has a lower speed of sound and attenuation coefficient than those of polydimethylsiloxane (PDMS). Data in **b** and **c** are presented as mean \pm standard deviations ($n = 4$).



1333
 1334 **Supplementary Fig. 6 | Fabrication of the acoustic lens.** **a**, Designs and **b**, optical images of the
 1335 aluminum block mold (left), the molded lens (middle), and the cross section of the lens (right).
 1336 The aluminum block mold was fabricated using computer numerical control machining. Ecoflex
 1337 was molded and cured inside the mold to produce an acoustic lens.



1338

1339

1340

1341

1342

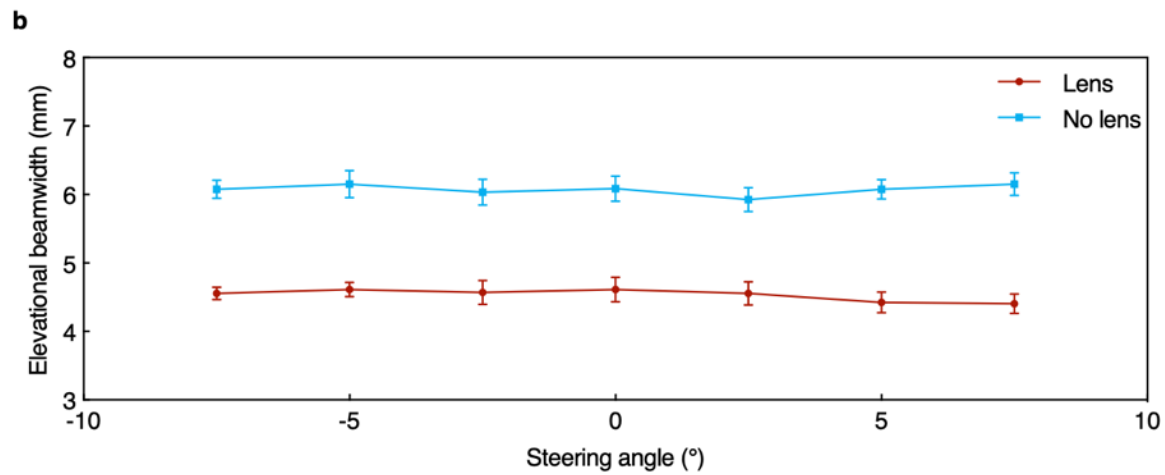
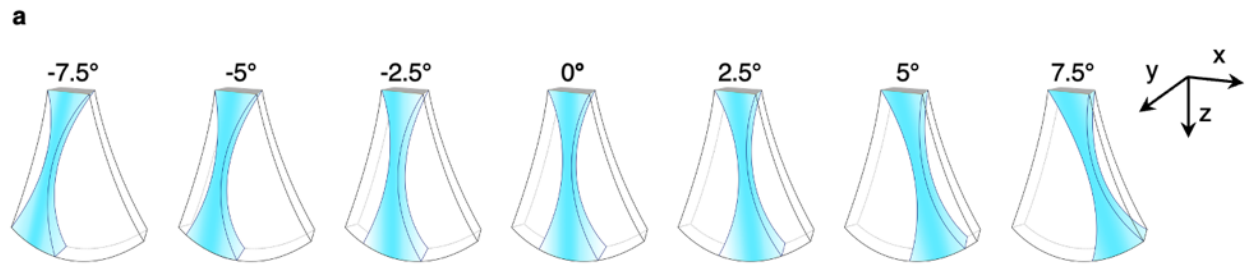
1343

1344

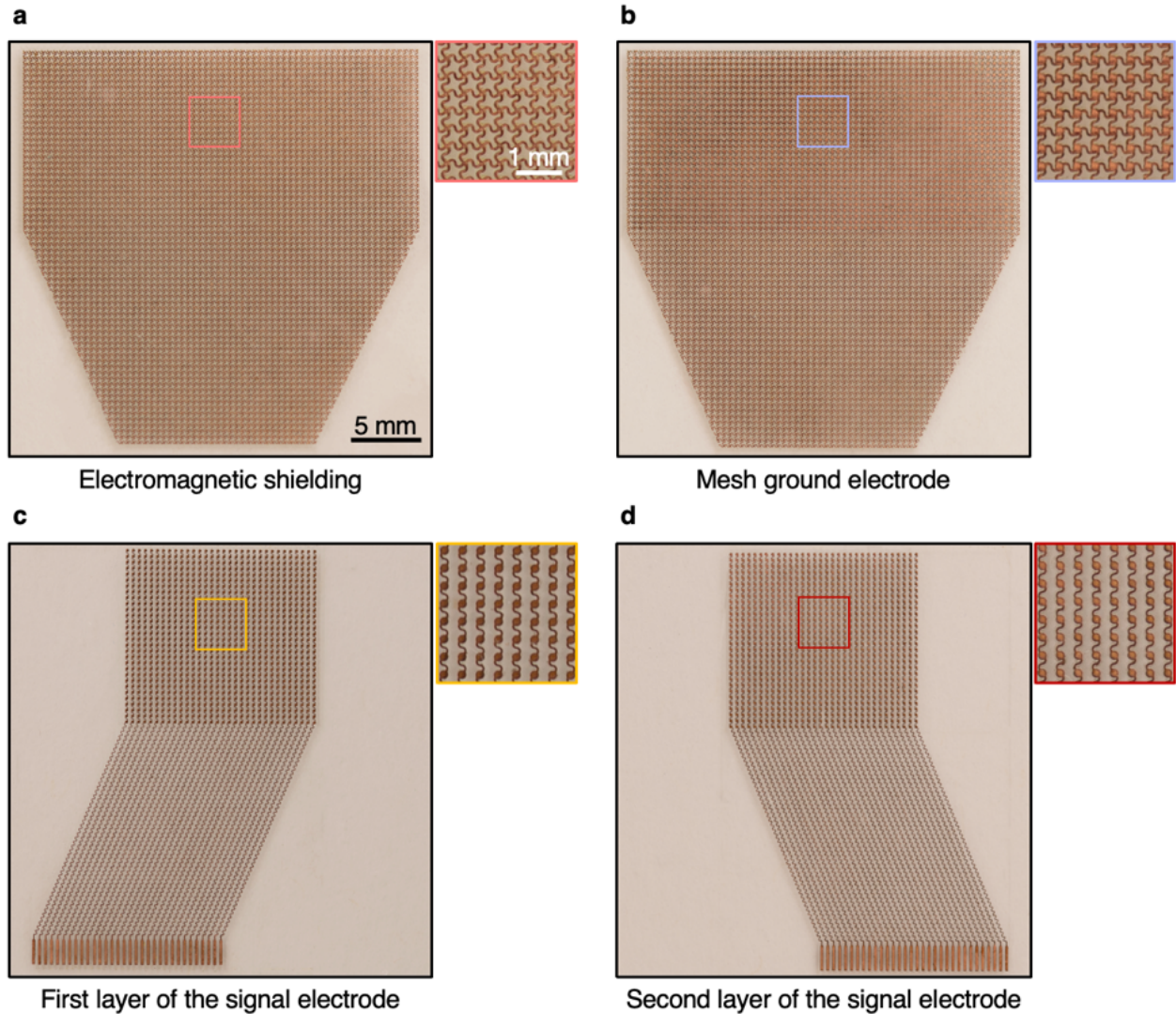
1345

1346

Supplementary Fig. 7 | Characterization of the acoustic lens. **a**, Hydrophone scanning of the acoustic fields of the UPatch with and without the lens in the YZ plane. The acoustic lens shifts the elevational focal region from ~14 cm to ~10 cm, the typical depth of interest for fetal monitoring. The images share the same color bar for hydrophone output voltage, which can be converted to acoustic pressure. Elevational beamwidth comparisons at **b**, 10 cm and **c**, focal depth with and without the acoustic lens. For **c**, the red line is the signal at 10 cm (lens) while the light blue line is the signal at 14 cm (no lens). In both **b** and **c**, the lens decreases the elevational beamwidth with negligible attenuation.

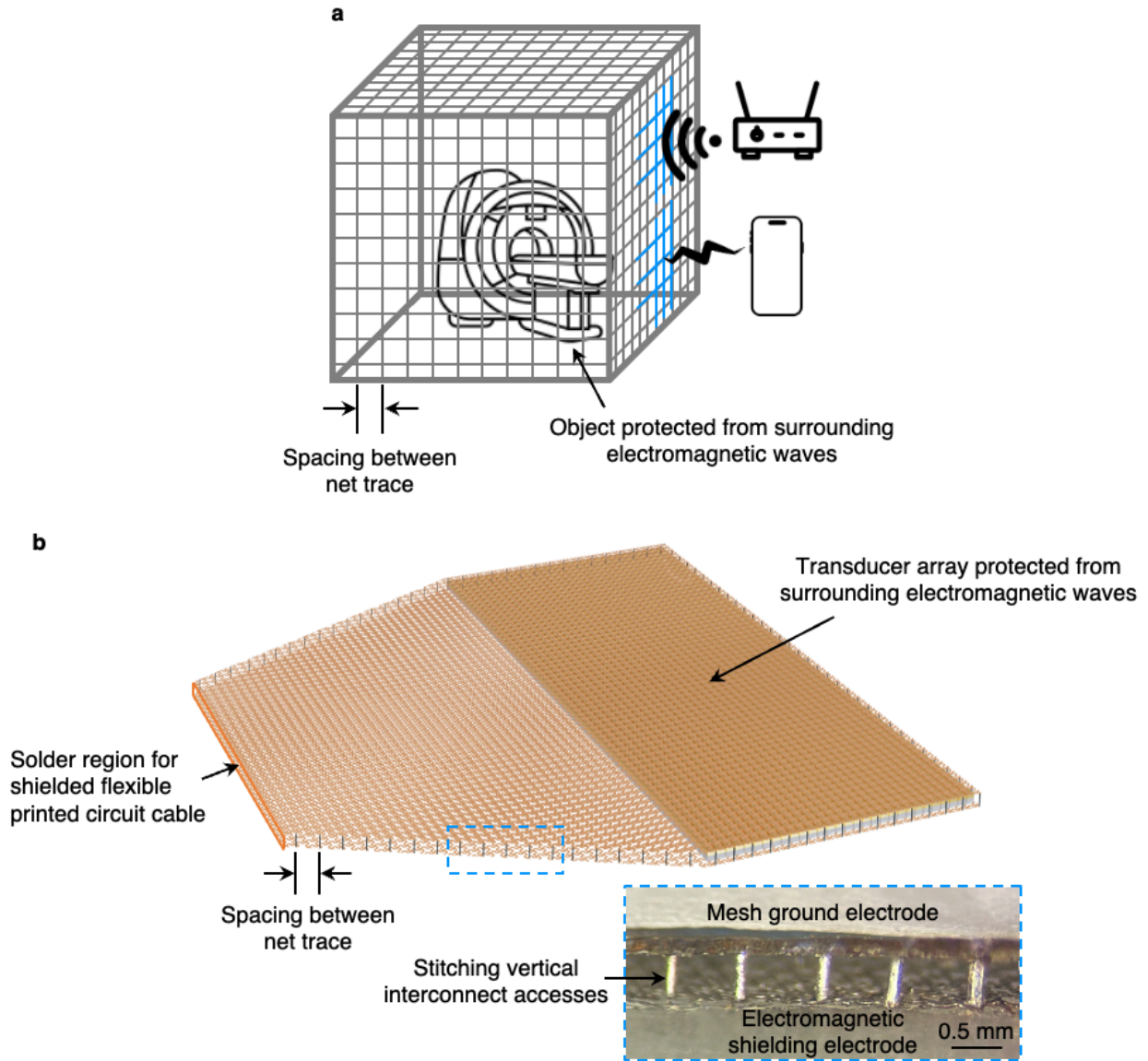


1347
 1348 **Supplementary Fig. 8 | Elevational beamwidth during beam steering.** **a**, Schematics
 1349 illustrating three-dimensional acoustic propagation during beam steering. Beam steering occurs in
 1350 the XZ plane, while the acoustic lens focuses the beam in the YZ plane. **b**, Experimental data
 1351 comparing the elevational beamwidth at different steering angles with and without the acoustic
 1352 lens. In both cases, the elevational beamwidth remains consistent across the steering range. Data
 1353 in **b** are presented as mean \pm standard deviations ($n = 4$).

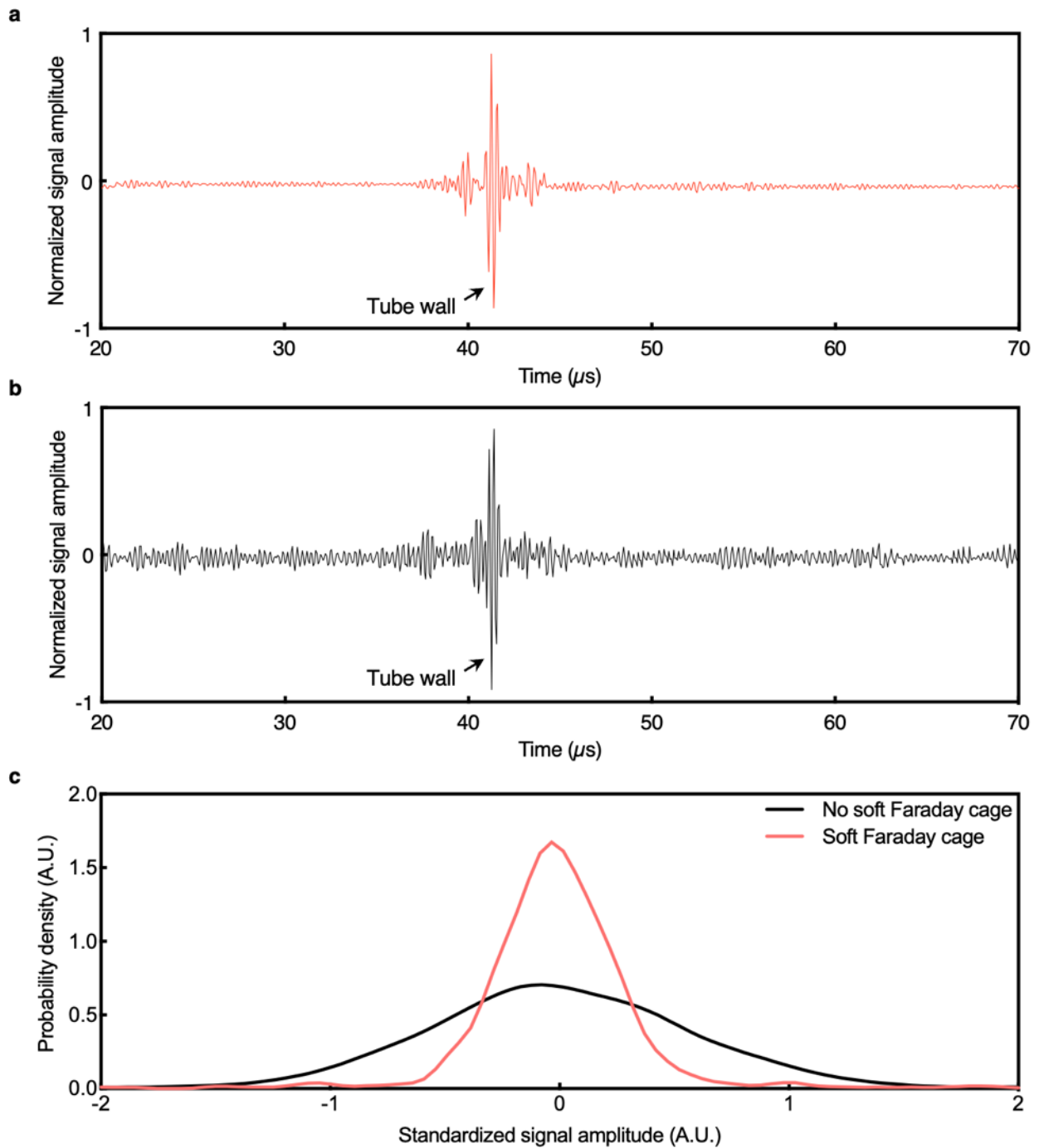


1354
1355
1356
1357
1358
1359
1360

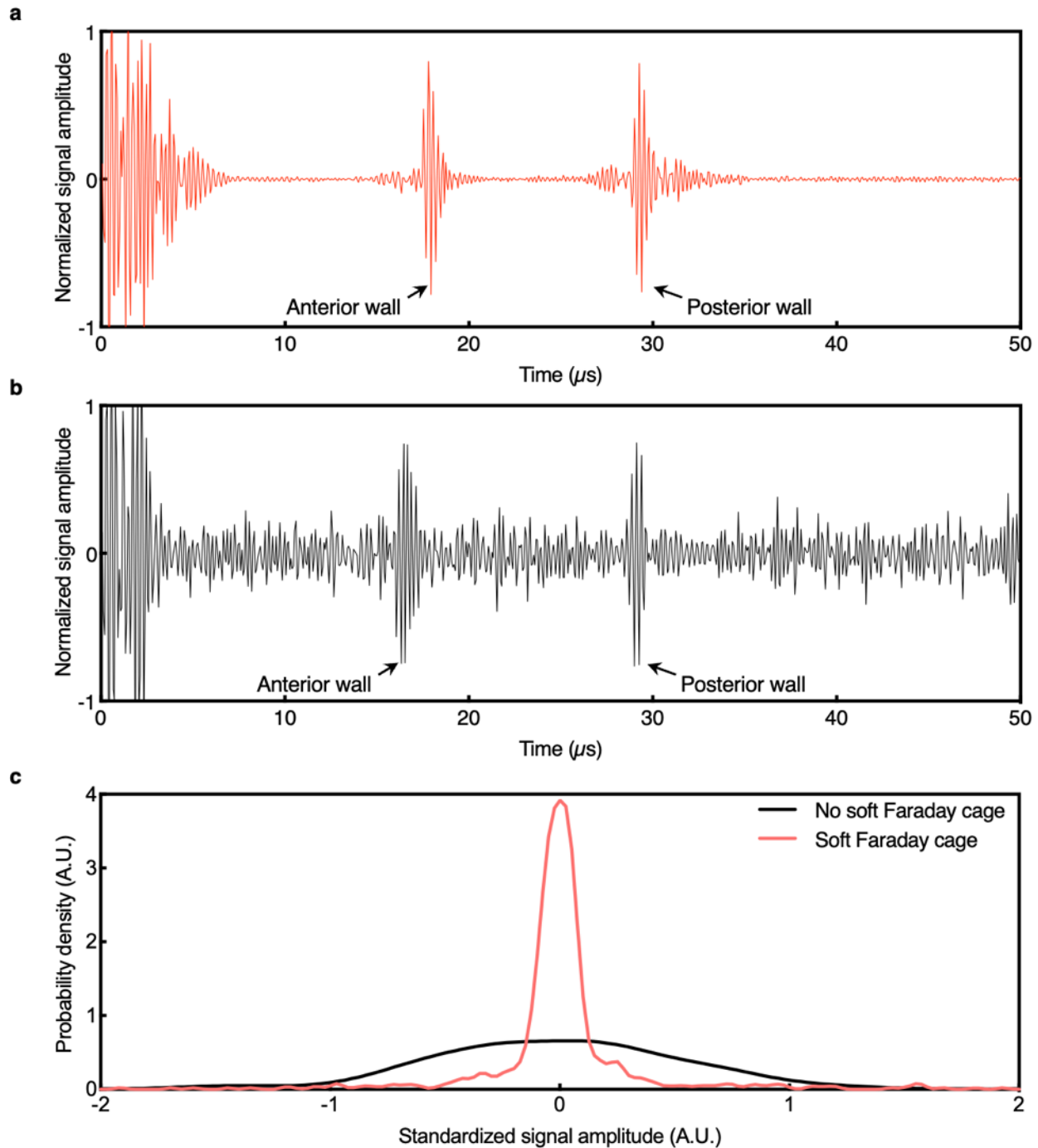
Supplementary Fig. 9 | Photographs of each layer of electrodes. **a**, Electromagnetic shielding layer. **b**, Mesh ground electrode layer. **c**, The first layer of the signal electrode. **d**, The second layer of the signal electrode. Insets are the serpentine design of each layer. The first and second layers of the signal electrodes activate 32 channels each. The electromagnetic shielding and mesh ground electrode layers minimize electromagnetic interference from the surrounding environment. The photographs and insets share the same scale bar, respectively.



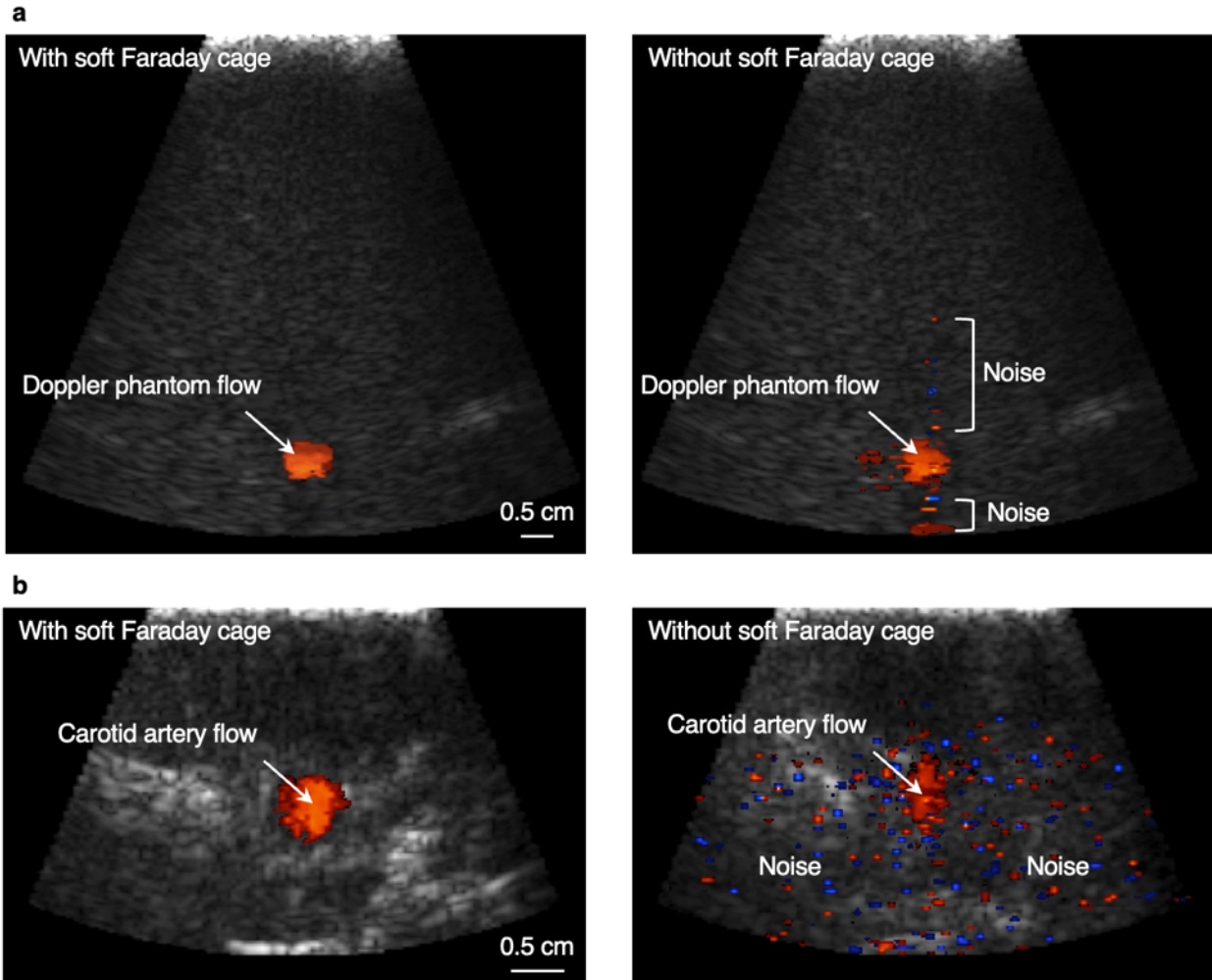
1361
 1362 **Supplementary Fig. 10 | Faraday cages.** **a**, Schematics of a Faraday cage. The Faraday cage
 1363 protects sensitive electronic equipment by absorbing electromagnetic waves from other electronic
 1364 sources (e.g., Wi-Fi routers and smartphones). The spacing between the metal traces determines
 1365 the frequency bands of the electromagnetic waves that can be blocked. **b**, Schematics of the soft
 1366 Faraday cage. Inset is a zoomed-in photograph of the stitching vertical interconnect accesses. The
 1367 electromagnetic shielding and mesh ground electrode layers are patterned with serpentine traces
 1368 and encapsulated in a soft elastomer. The stitching vertical interconnect accesses enable a three-
 1369 dimensional enclosure of the transducer, thereby providing effective isolation within the soft
 1370 Faraday cage.



1371
 1372 **Supplementary Fig. 11 | Effects of the soft Faraday cage on phantom measurements.**
 1373 Radiofrequency signals **a**, with and **b**, without the soft Faraday cage. **c**, Probability density
 1374 function comparison with and without the soft Faraday cage. The narrower distribution of
 1375 measurements with the soft Faraday cage indicates reduced susceptibility to ambient
 1376 electromagnetic noise.



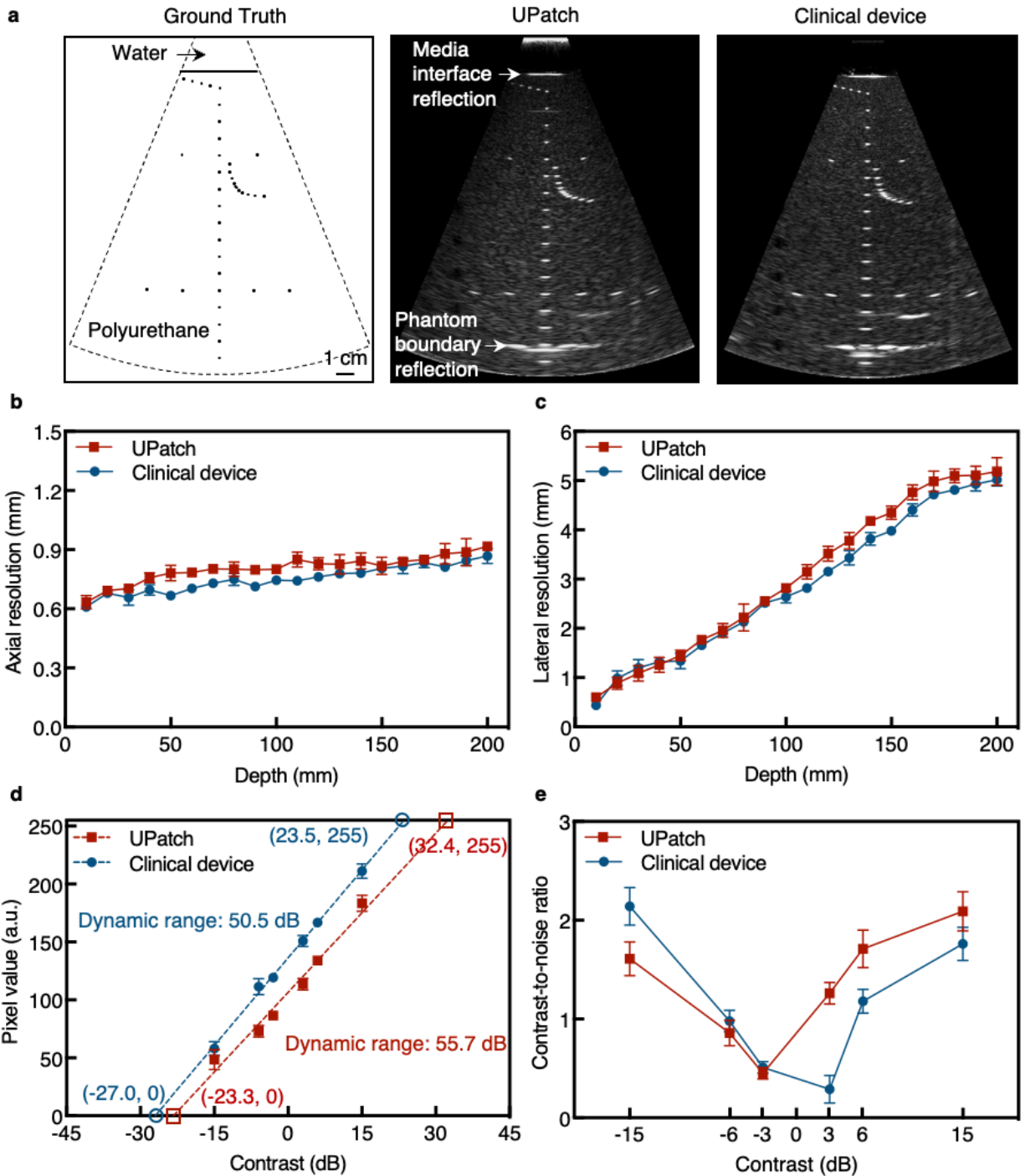
1377
 1378 **Supplementary Fig. 12 | Effects of the soft Faraday cage on adult carotid artery**
 1379 **measurements.** Radiofrequency signals **a**, with and **b**, without the soft Faraday cage. **c**,
 1380 Probability density function comparison with and without the soft Faraday cage. The narrower
 1381 distribution of measurements with the soft Faraday cage indicates reduced electromagnetic
 1382 interference, potentially from both physiological and environmental sources, enhancing in vivo
 1383 signal fidelity.



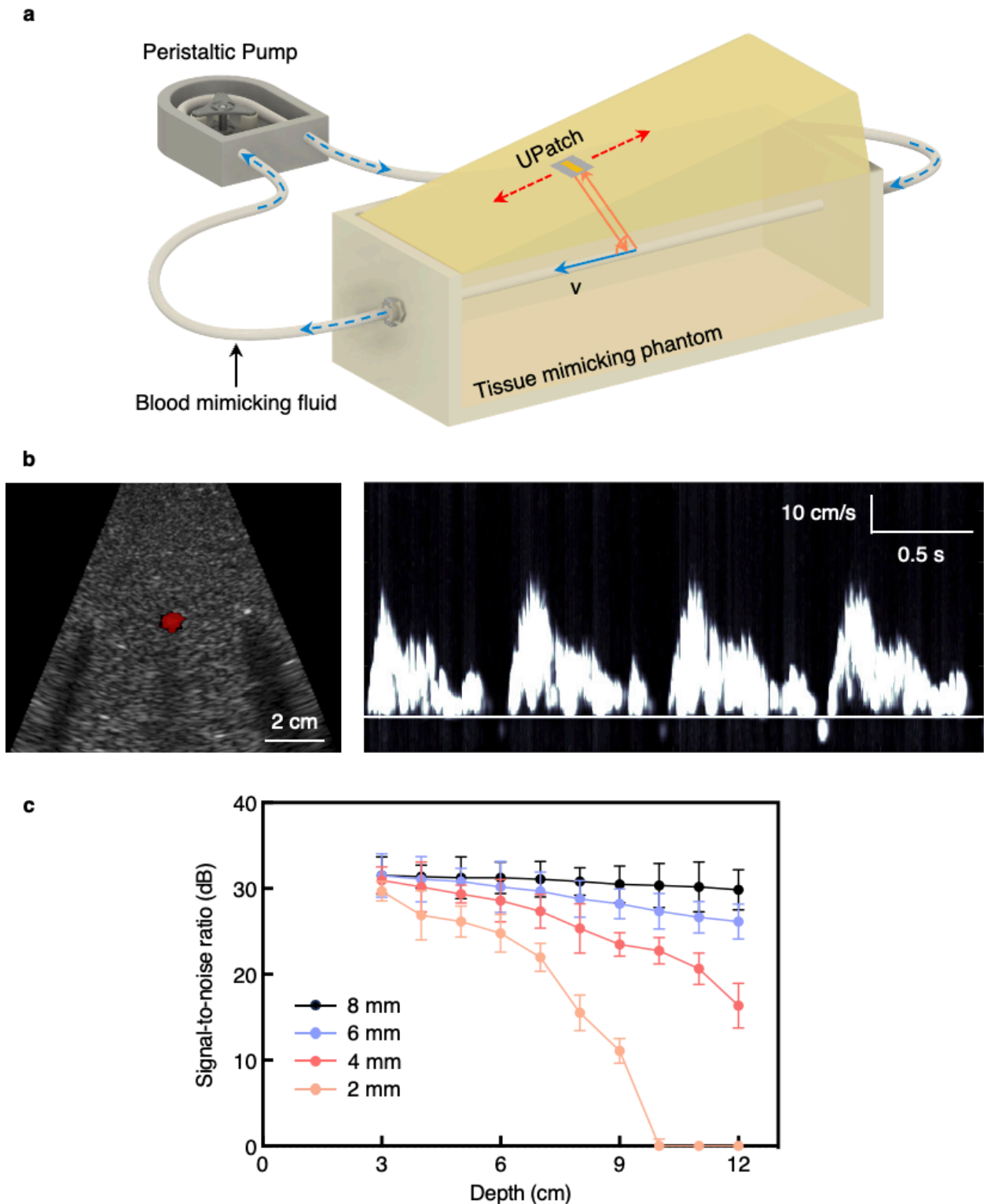
1384
 1385 **Supplementary Fig. 13 | Effects of the soft Faraday cage on noise levels in duplex imaging. a,**
 1386 Duplex images of a phantom with and without the soft Faraday cage. The images share the same
 1387 scale bar. **b,** Duplex images of the carotid artery in a healthy adult with and without the soft
 1388 Faraday cage. The images share the same scale bar. The use of the soft Faraday cage reduces noise
 1389 and improves image quality.



1390
1391 **Supplementary Fig. 14 | Photographs of the UPatch on a pregnant woman.** The UPatch is
1392 laminated on a pregnant participant in **a**, standing and **b**, sitting positions. The UPatch conforms
1393 closely to the contour of the abdominal surface, ensuring intimate contact for effective ultrasound
1394 transmission. The photographs share the same scale bar.

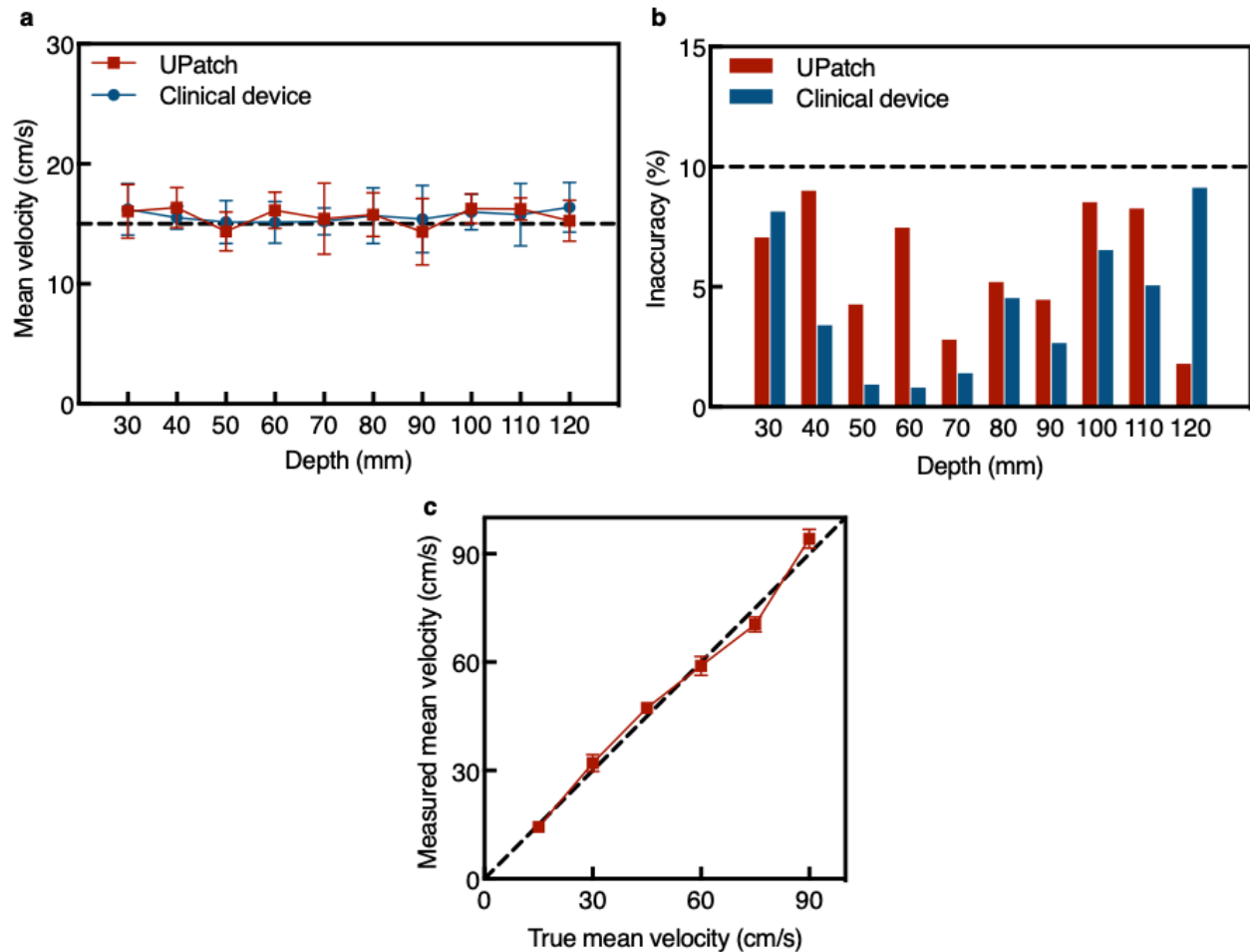


1395
 1396 **Supplementary Fig. 15 | Brightness mode characterizations.** **a**, Schematics of the phantom
 1397 (left), and brightness-mode images from the UPatch (middle) and a clinical device (P4-1, ATL)
 1398 (right). The brightness-mode image quality is comparable between the UPatch and clinical device.
 1399 The images share the same scale bar. **b**, Axial resolution from depths 10 mm to 200 mm. **c**, Lateral
 1400 resolution from depths 10 mm to 200 mm. **d**, Dynamic range calculated based on six grayscale
 1401 targets (-15 dB, -6 dB, -3 dB, +3 dB, +6 dB, and +15 dB). **e**, Contrast-to-noise ratio
 1402 calculated based on the six grayscale targets. Data in **b-e** are presented as mean \pm standard deviations ($n = 4$).

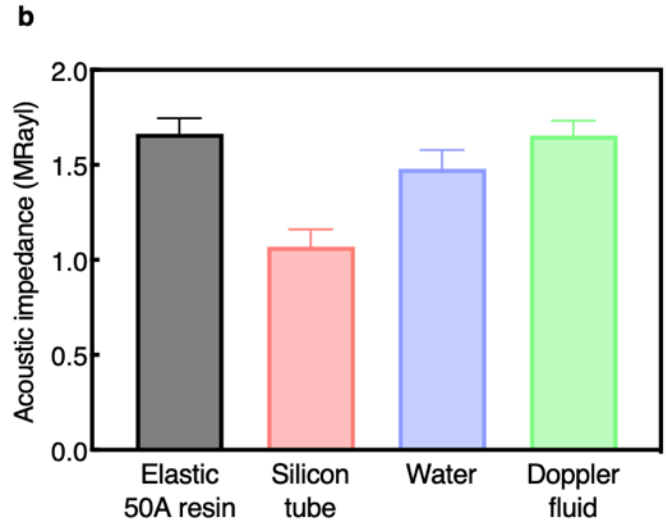
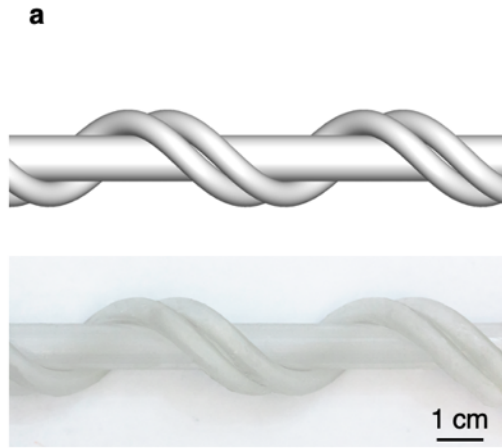


1403
 1404 **Supplementary Fig. 16 | Doppler characterizations.** **a**, Schematic setup of a commercial
 1405 Doppler phantom (CIRS ATS523A) for Doppler characterizations. Blood-mimicking fluid was
 1406 pumped into the phantom with a known Doppler angle using a peristaltic pump. The depth from
 1407 the UPatch to the phantom vessel ranges from 3 cm to 12 cm. **b**, Exemplary color-flow image (left)
 1408 and spectral Doppler signal (right) acquired from the phantom using the UPatch. **c**, Signal-to-noise

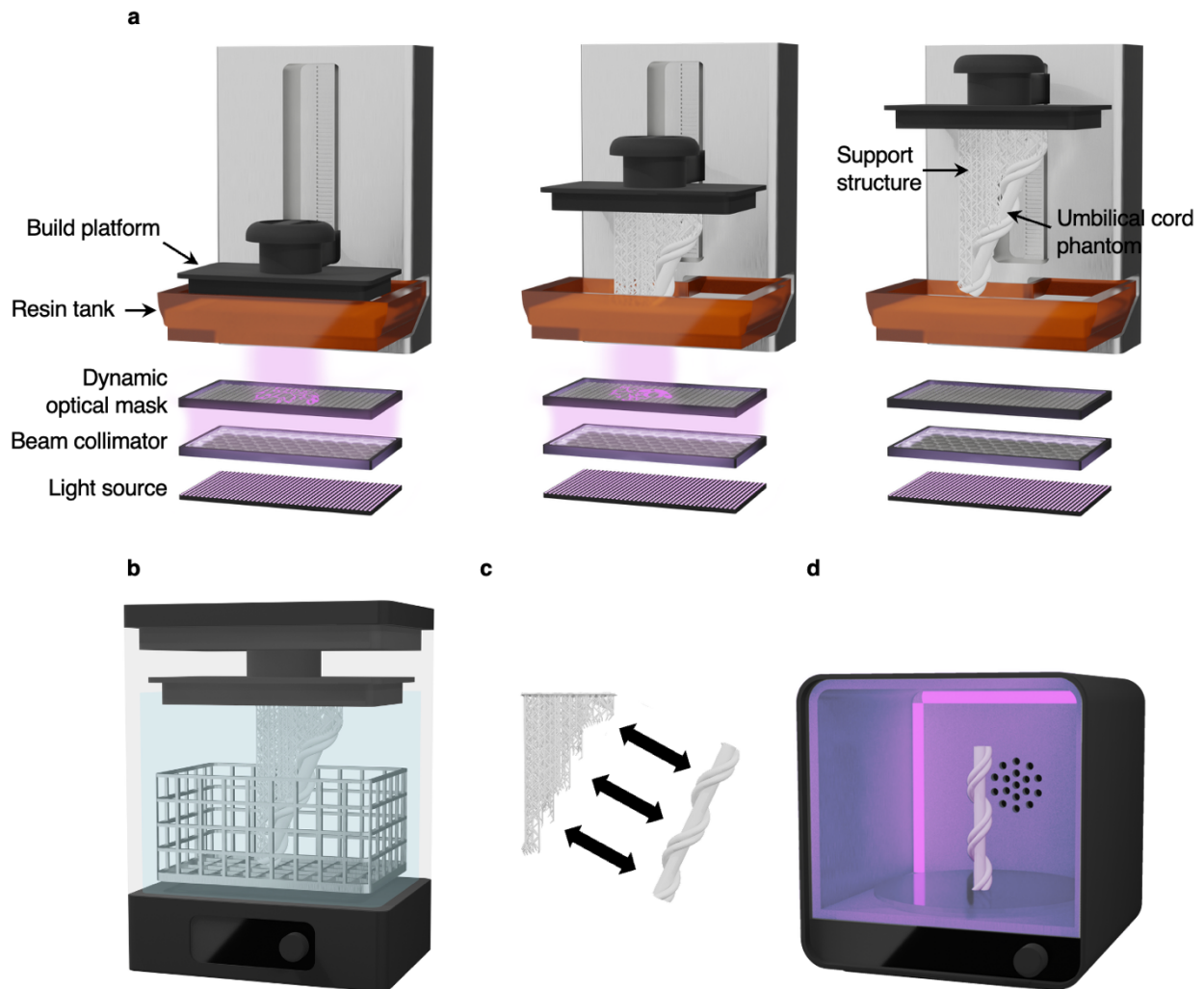
1409 ratio of color Doppler signals of the UPatch at different phantom vessel depths. The UPatch can
1410 detect the smallest phantom vessel diameter of 2 mm at a depth of 10 cm. Data in **c** are presented
1411 as mean \pm standard deviations (n = 4).



1412
 1413 **Supplementary Fig. 17 | Blood flow measurement accuracy.** **a**, Mean blood flow velocity at
 1414 each depth. The black dashed line shows the ground truth mean velocity of 15 cm/s set on the
 1415 peristaltic pump. **b**, Inaccuracy of the mean blood flow velocity as a function of depth. The dashed
 1416 line shows the inaccuracy threshold of 10% typically used in ultrasound quality assurance
 1417 protocols¹⁸¹. The two devices demonstrate similar levels of inaccuracies. **c**, Measured mean
 1418 velocities as a function of different ground truth mean velocities at a depth of 50 mm. The black
 1419 dashed line represents the linearity between the measured and ground truth velocities. Data in **a**
 1420 and **c** are presented as mean \pm standard deviations ($n = 4$).

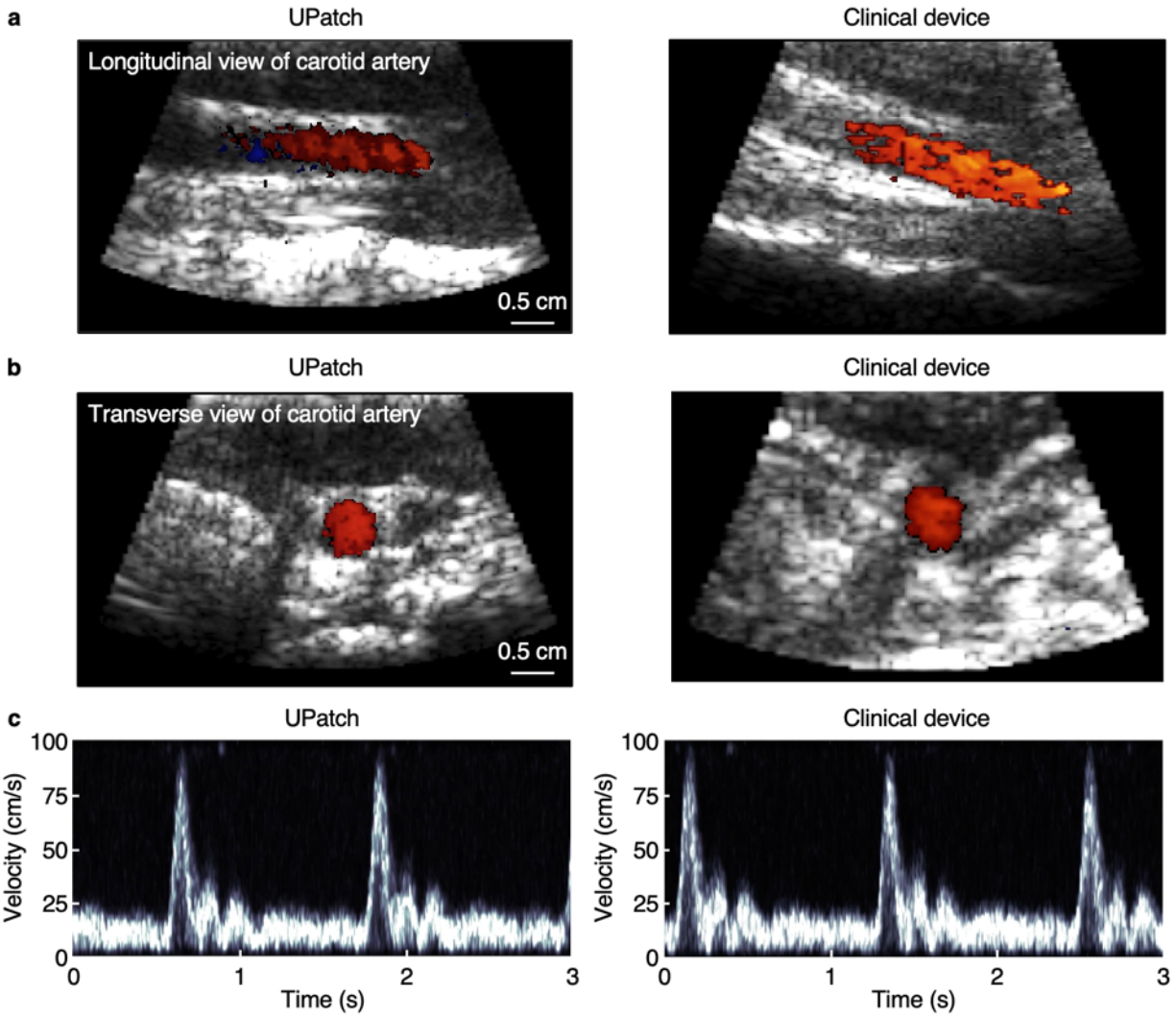


1421
 1422 **Supplementary Fig. 18 | Design of the umbilical cord phantom.** **a**, Model (top) and image of
 1423 the stereolithographically printed phantom (bottom) of the helical umbilical cord. The umbilical
 1424 cord is composed of two arteries and one vein. **b**, Acoustic impedances of different materials. The
 1425 Elastic 50A resin (Formlabs) exhibits small acoustic impedance mismatch with water and Doppler
 1426 fluid^{85,182}, minimizing acoustic reflection at fluid–structure interfaces. In contrast, the greater
 1427 mismatch of silicone tubing (Metaland) leads to substantial acoustic reflection, particularly when
 1428 insonating through multiple interfaces of the umbilical cord. Data in **b** are presented as mean \pm
 1429 standard deviations ($n = 4$).

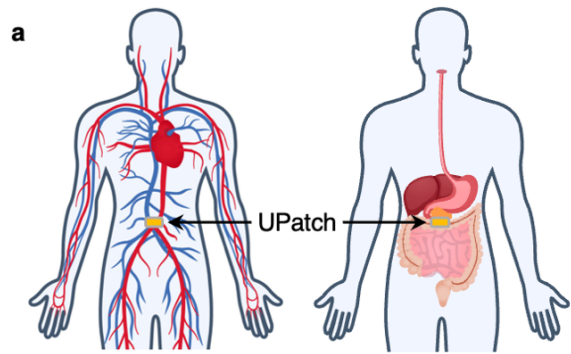


1430
 1431
 1432
 1433
 1434
 1435
 1436
 1437
 1438
 1439
 1440

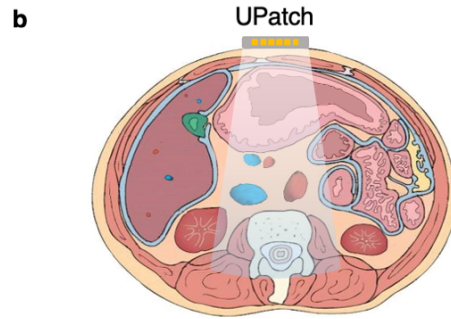
Supplementary Fig. 19 | Stereolithographic fabrication of the umbilical cord phantom. a, Schematic of the stereolithography process showing layer-by-layer photopolymerization of resin to fabricate an umbilical cord phantom. A vertically translating build platform enables sequential printing within a resin tank. A light source passes through the beam collimator to produce coherent illumination. A dynamic optical mask modulates the illumination to define each layer's geometry. A support structure is printed in parallel with the umbilical cord phantom to ensure geometric stability during stereolithography. **b,** Post-print washing process. The structure is immersed in solvent to remove uncured resin. **c,** Manual removal of support structures to isolate the umbilical cord phantom. **d,** Final polymerization step. An ultraviolet light fully cures the umbilical cord phantom to improve mechanical and chemical robustness.



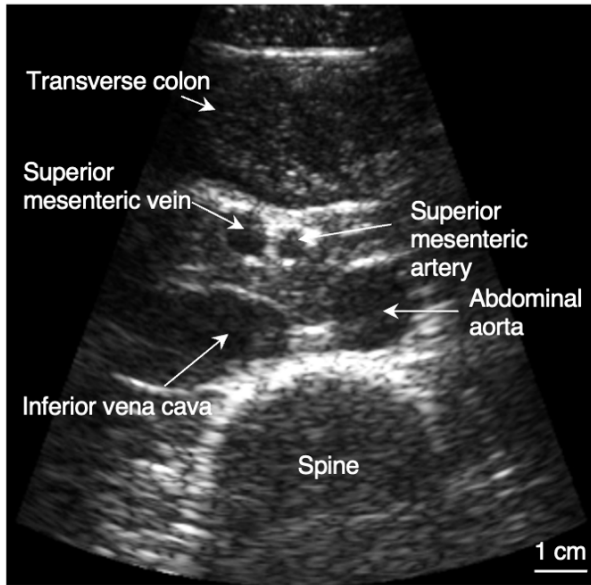
1441
 1442 **Supplementary Fig. 20 | Measurements on the carotid artery of a healthy adult.** Duplex
 1443 imaging of the carotid artery showing the **a**, longitudinal view and **b**, transverse view with the
 1444 UPatch (left) and clinical device (right). Anatomy and blood flow of the carotid artery can be
 1445 recognized from the brightness mode and color Doppler mode, respectively. The images share the
 1446 same scale bar. **c**, Blood flow measurements of the carotid artery using the spectral Doppler mode.
 1447 Blood flow spectra obtained from the UPatch (left) and clinical device (right) are comparable on
 1448 the same participant.



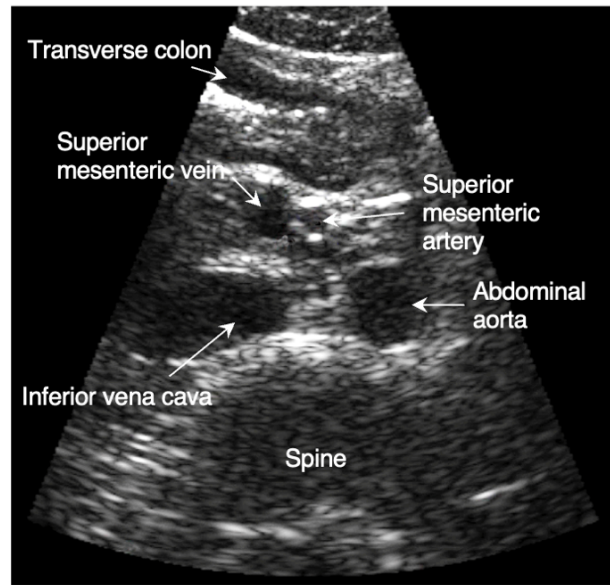
c UPatch



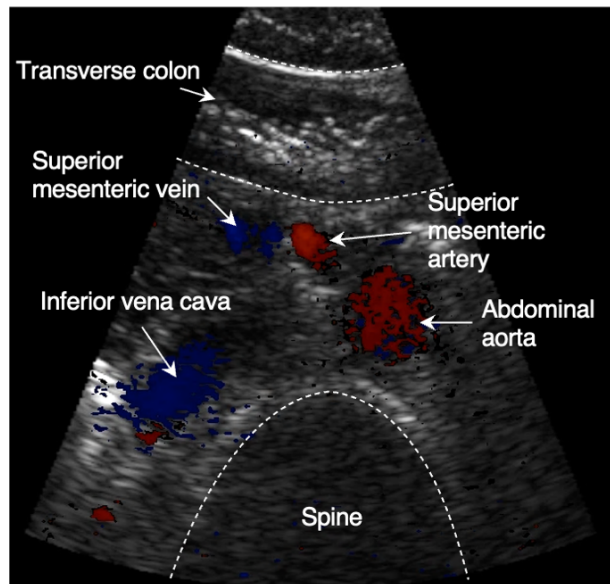
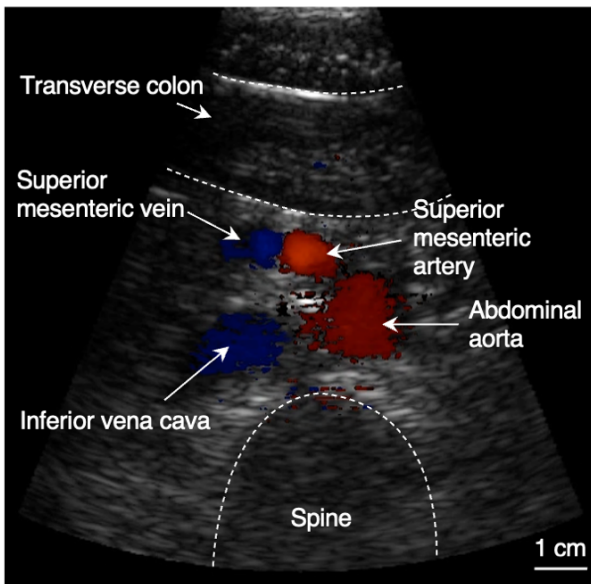
Clinical device



d UPatch



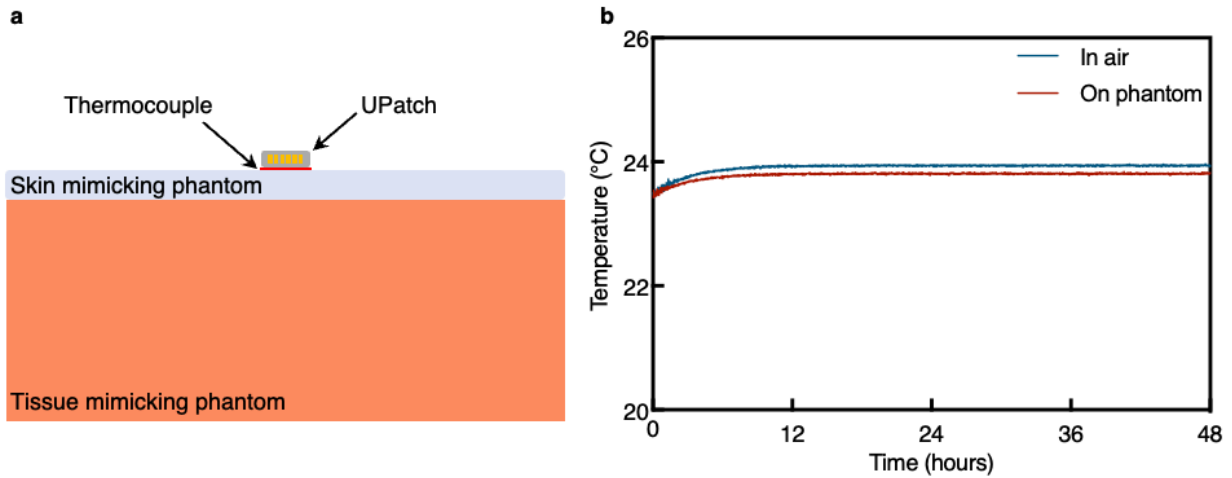
Clinical device



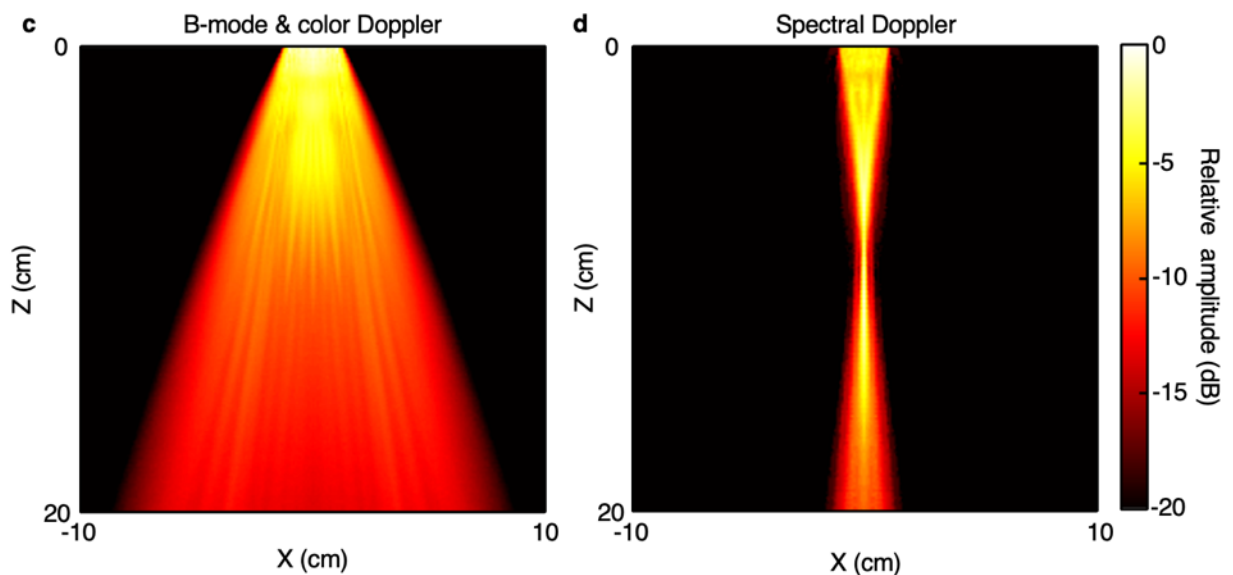
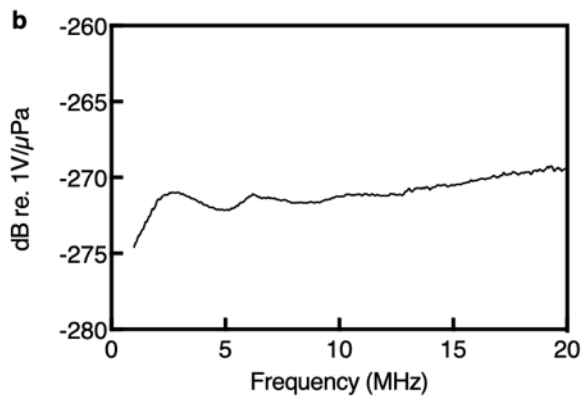
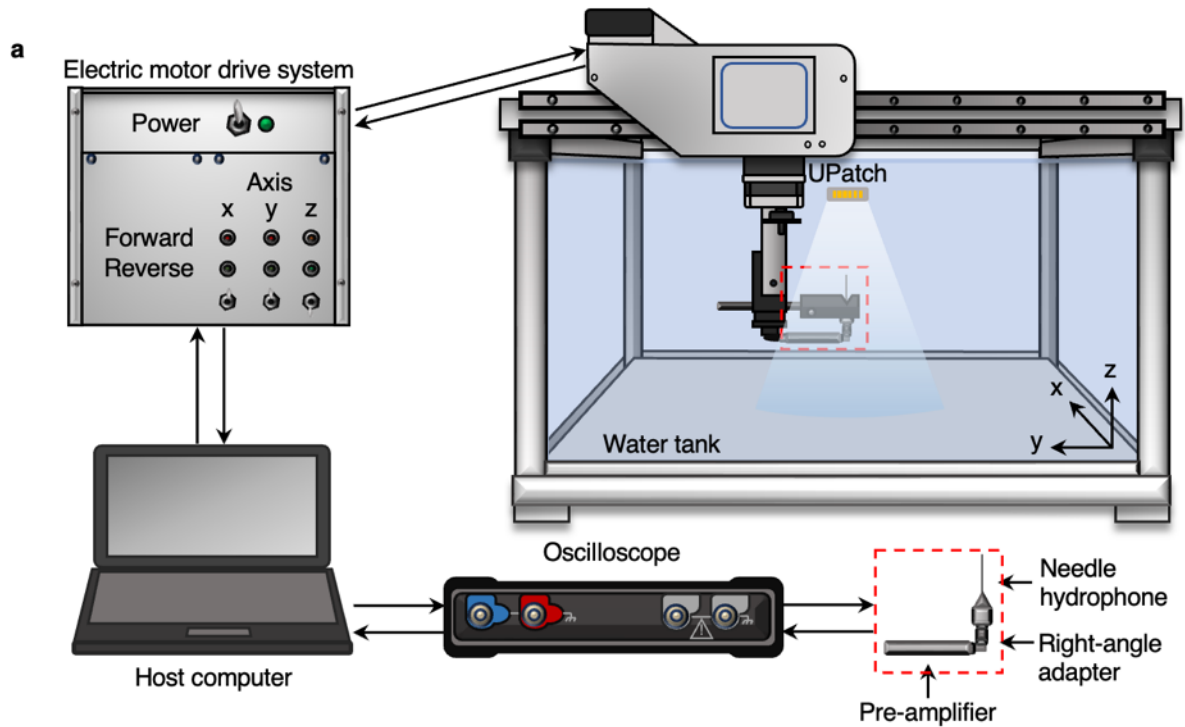
1449
1450
1451

Supplementary Fig. 21 | Measurements on the abdominal cross-section of a healthy adult. a, Schematics showing the position of the UPatch imaging the cardiovascular system (left) and

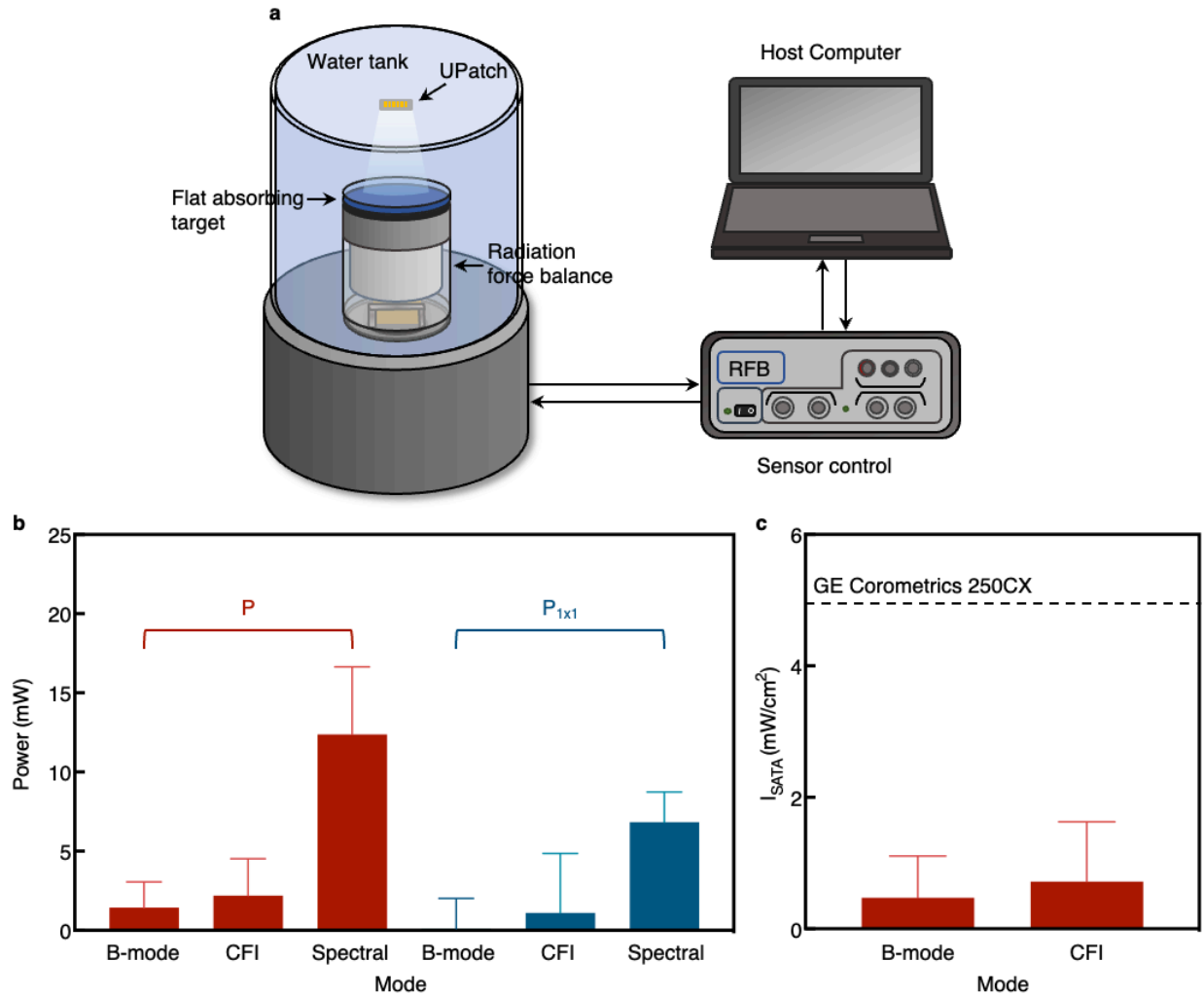
1452 digestive system (right). **b**, Schematics illustrating the transverse anatomical view of the abdomen.
1453 Transverse view of the abdominal anatomy in **c**, brightness and **d**, duplex modes. Both the UPatch
1454 and clinical device can clearly recognize the structures of the transverse colon, superior mesenteric
1455 vein, superior mesenteric artery, inferior vena cava, abdominal aorta, and spine. The images share
1456 the same scale bar.



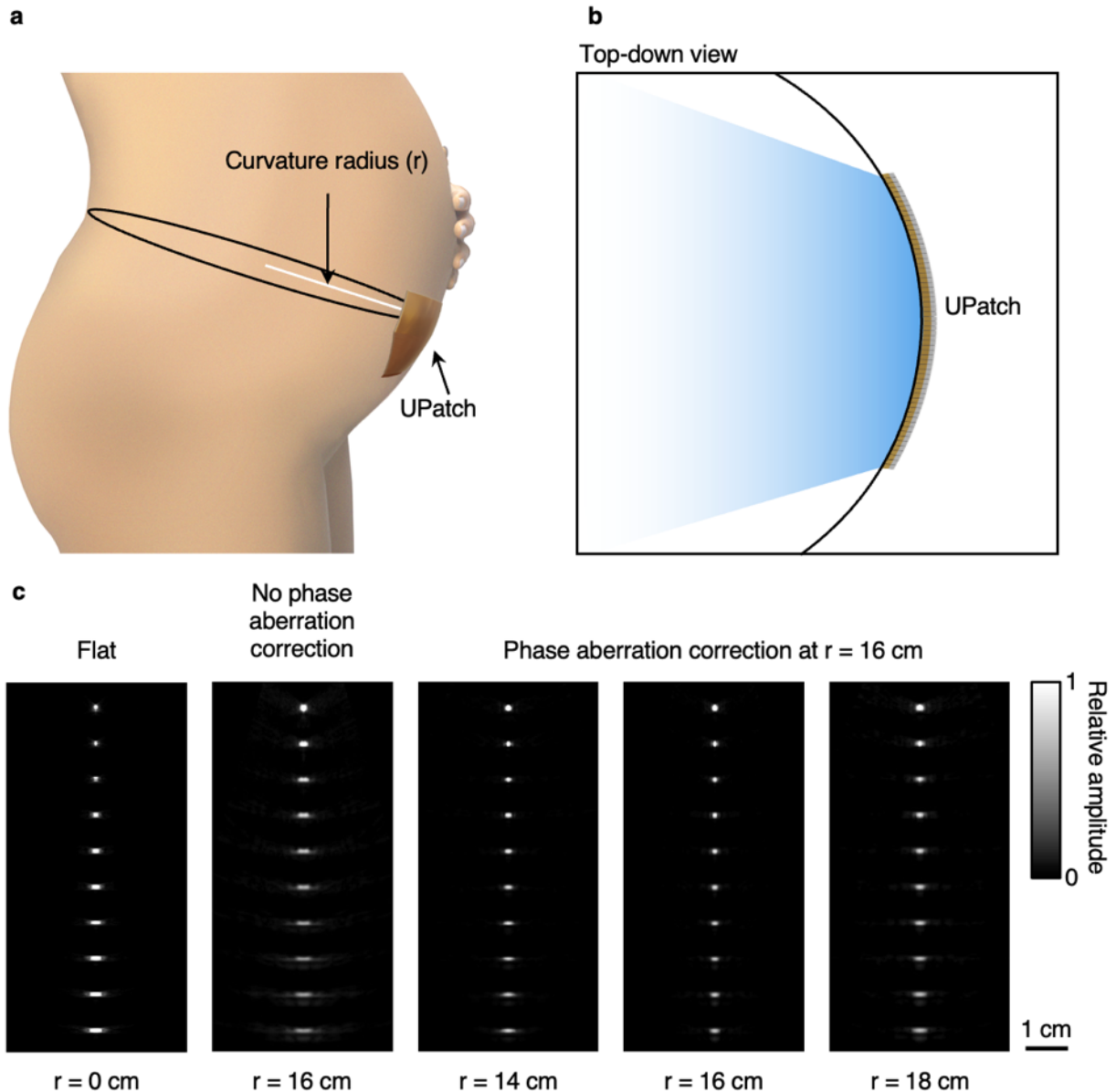
1457
 1458 **Supplementary Fig. 22 | Surface temperature characterizations.** **a**, Schematic setup for the on
 1459 phantom testing. The setup includes a skin and tissue mimic phantom (NPL, UK) with similar
 1460 acoustic and thermal properties to those of human skin and tissues. The thermocouple was placed
 1461 in between the UPatch and the skin mimic phantom during the measurement. **b**, Surface
 1462 temperature measurements on phantom and in air. The in-air test was performed by placing the
 1463 UPatch and thermocouple in still air¹⁸³. The maximum temperature increase was ~ 0.53 °C, which
 1464 was < 0.7 °C for continuous monitoring recommended by the AIUM¹²³ and BMUS¹²⁴.



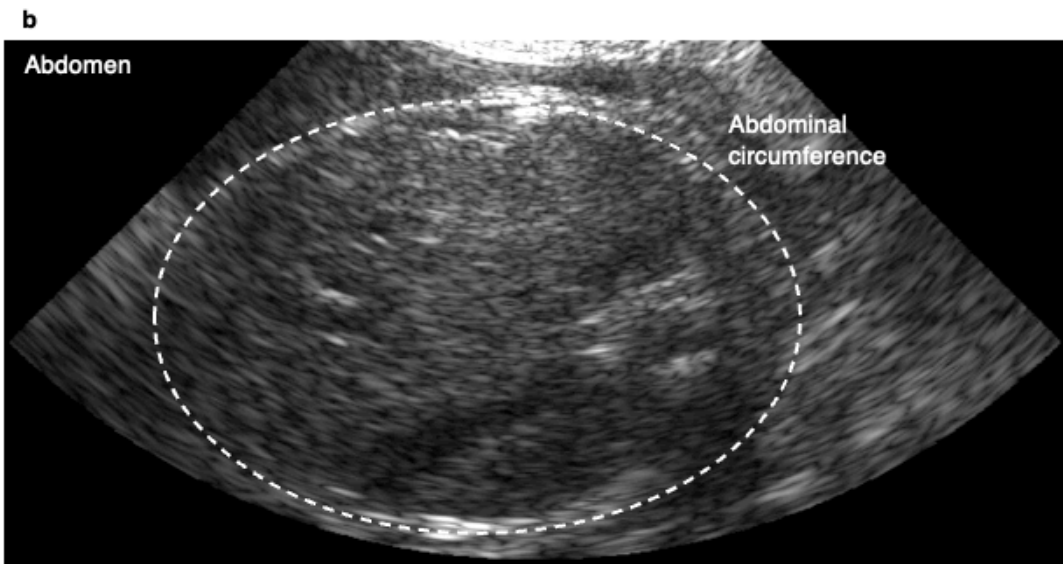
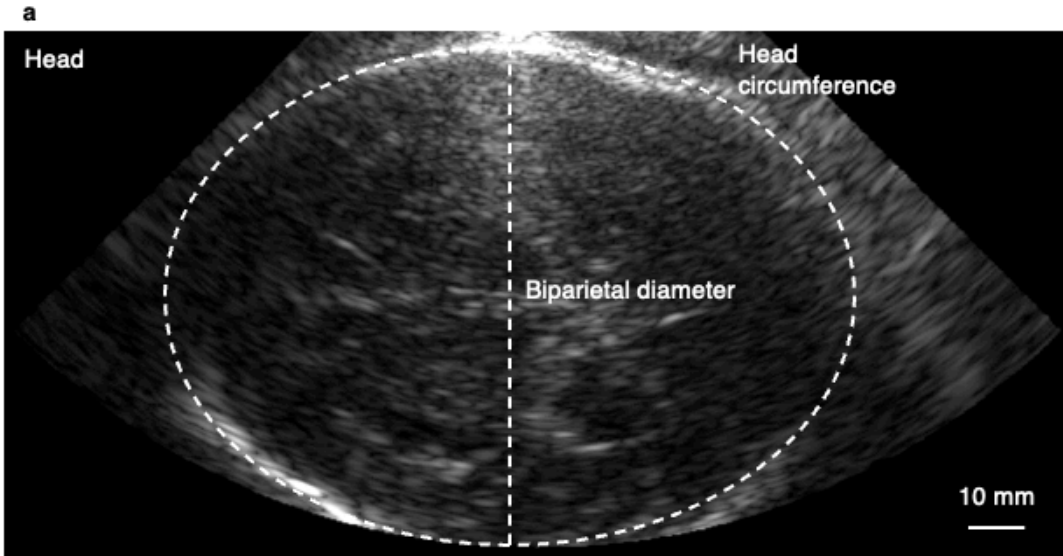
1466 **Supplementary Fig. 23 | Safety measurements with a hydrophone.** **a**, Schematic setup with a
1467 hydrophone system. Ultrasound intensity from the UPatch can be measured in a water tank. **b**,
1468 Magnitude data from calibrating the hydrophone sensitivity for accurate calculation of its acoustic
1469 properties. Acoustic field scans of **c**, a diverging beam (for brightness and color-flow modes) and
1470 **d**, a focused beam (for the spectral Doppler mode) with the UPatch in the XZ plane. The images
1471 share the same color bar.



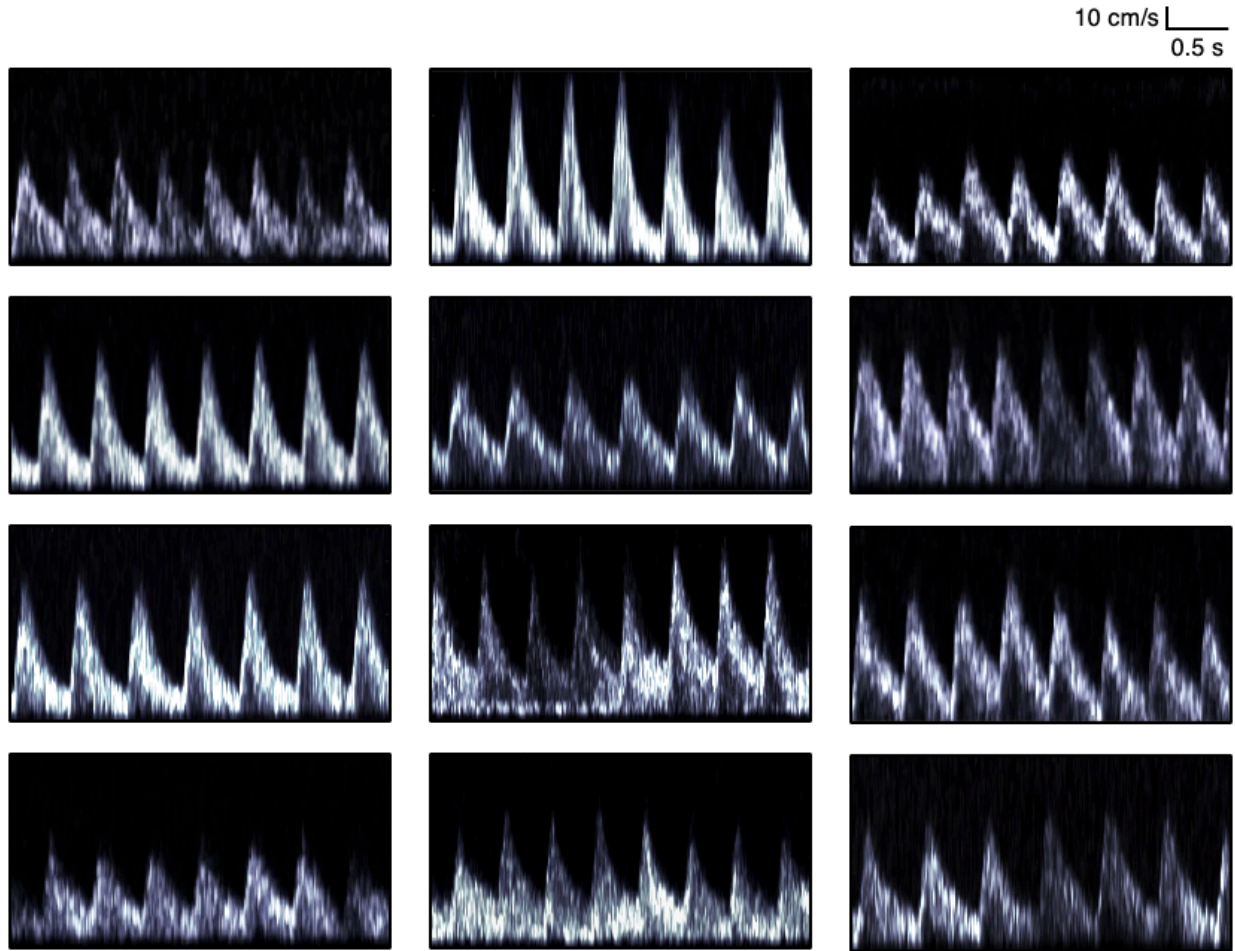
1472
 1473 **Supplementary Fig. 24 | Safety measurements with a radiation force balance.** **a**, Schematic
 1474 setup with a radiation force balance. The ultrasound beam from the UPatch is uniformly absorbed
 1475 in the flat absorbing target and the radiation force balance can accurately measure the power of the
 1476 transmitted beam. **b**, Power (P) and bounded-square output power over a one square centimeter
 1477 area ($P_{1 \times 1}$) were measured in brightness (B-mode), color-flow imaging (CFI), and spectral Doppler
 1478 modes. **c**, Spatial average temporal average intensity (I_{SATA}) derived from power (Supplementary
 1479 Discussion 11). The black dashed line represents I_{SATA} of GE Corometrics 250CX fetal heart rate
 1480 monitors¹⁸. Data in **b** and **c** are presented as mean \pm standard deviations ($n = 4$).



1481
 1482 **Supplementary Fig. 25 | Deformation of the UPatch.** **a**, Schematics of the UPatch on the
 1483 maternal abdomen. **b**, Top-down view of the UPatch on the maternal abdomen. **c**, Simulation
 1484 results of the image quality. The maternal abdominal curvatures can induce phase aberration and
 1485 affect the image quality of the UPatch. To address this, the phase aberration was corrected at a
 1486 curvature radius of 16 cm, which encompasses the typical curvature radii from 14 cm to 18 cm in
 1487 the third trimester^{128,129}. The phase aberration correction improved the image quality within this
 1488 curvature range. Simulations were performed with the Matlab Field II toolbox. The images share
 1489 the same scale bar.

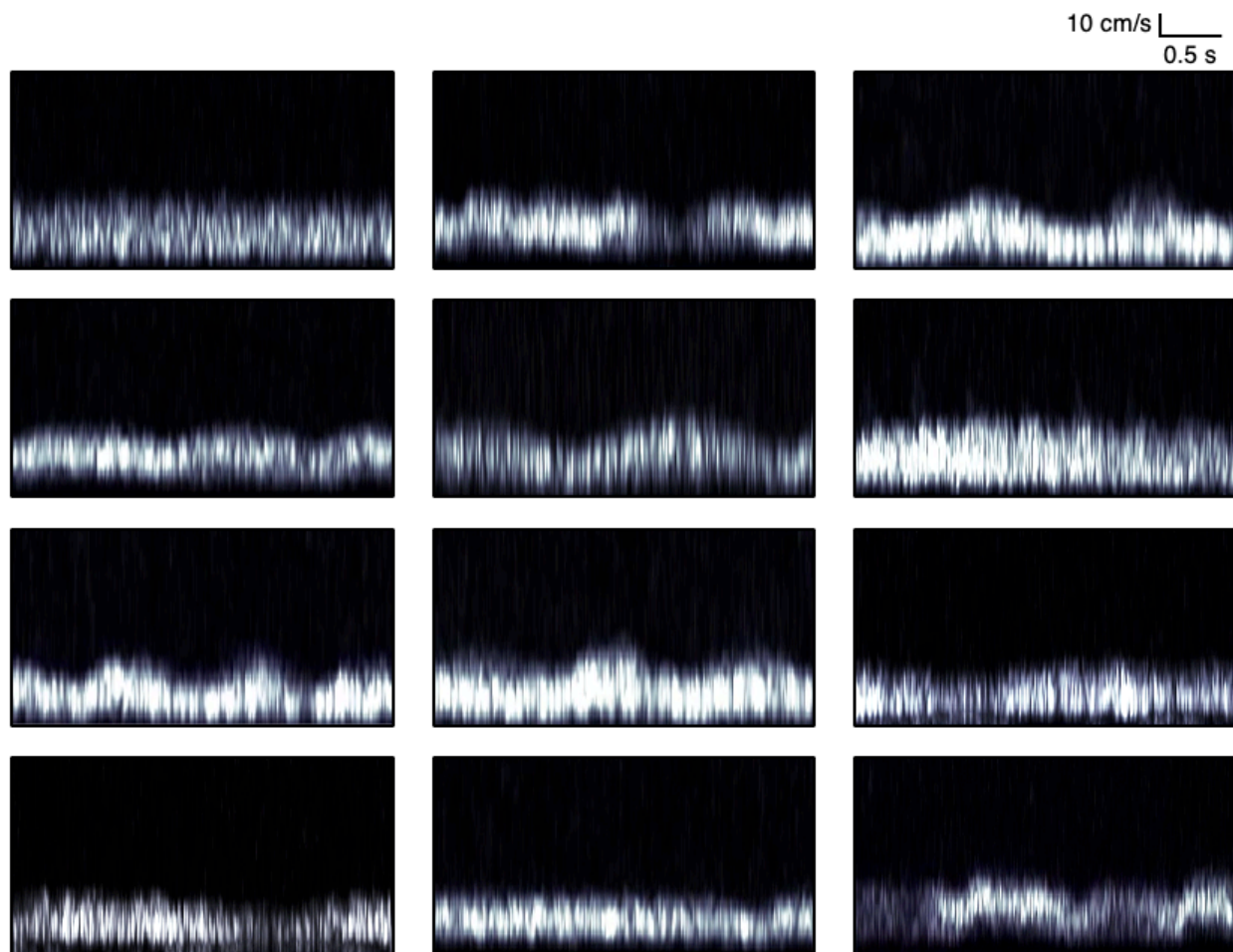


1491 **Supplementary Fig. 26 | Fetal biometry.** Brightness-mode images of a fetal **a**, head, **b**, abdomen,
1492 and **c**, femur. All images share the same scale bar. Biparietal diameter, head circumference,
1493 abdominal circumference, and femur length can be measured to calculate the estimated fetal
1494 weight using the Hadlock IV formula¹⁸⁴. For this particular fetus, its weight is calculated to be 3.56
1495 kg using the UPatch and 3.54 kg using the clinical device.

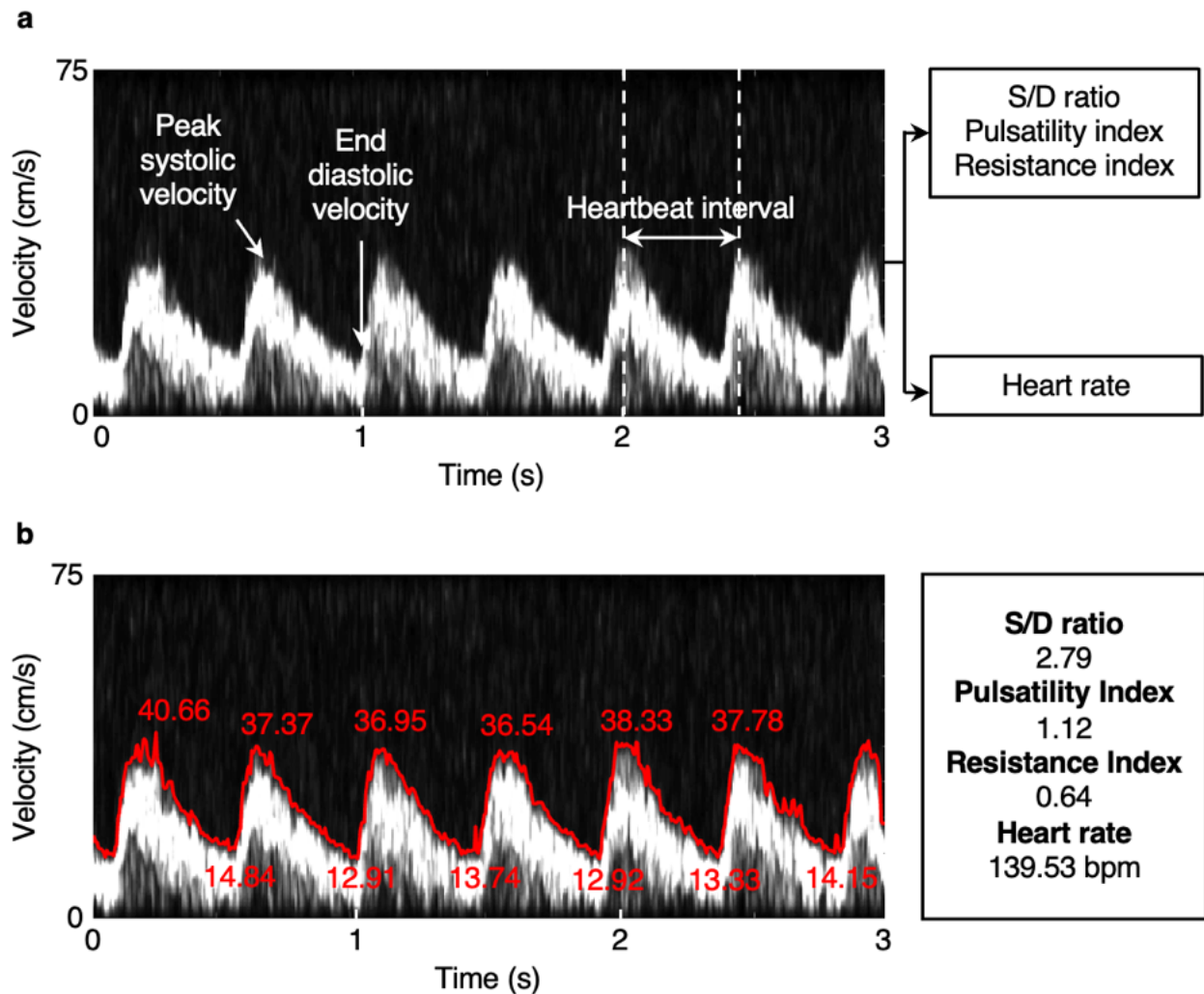


1496
1497
1498
1499
1500

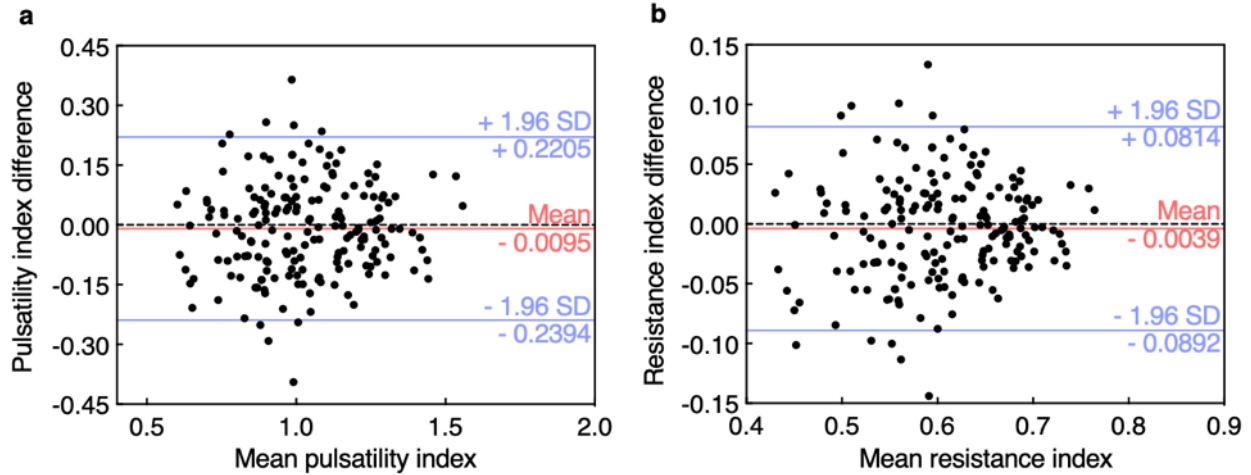
Supplementary Fig. 27 | Spectral Doppler of the umbilical artery. The UPatch can acquire spectral Doppler signals from the umbilical artery of pregnant participants. All signals were acquired by a sonographer specializing in fetal ultrasonography. All images share the same scale bars. Each panel corresponds to the same participant and ordering as in Extended Data Fig. 3.



1501
 1502 **Supplementary Fig. 28 | Spectral Doppler of the umbilical vein.** The UPatch can acquire
 1503 spectral Doppler signals from the umbilical vein of pregnant participants. All signals were acquired
 1504 by a sonographer specializing in fetal ultrasonography. All images share the same scale bars. Each
 1505 panel corresponds to the same participant and ordering as in Extended Data Fig. 3 and
 1506 Supplementary Fig. 27.

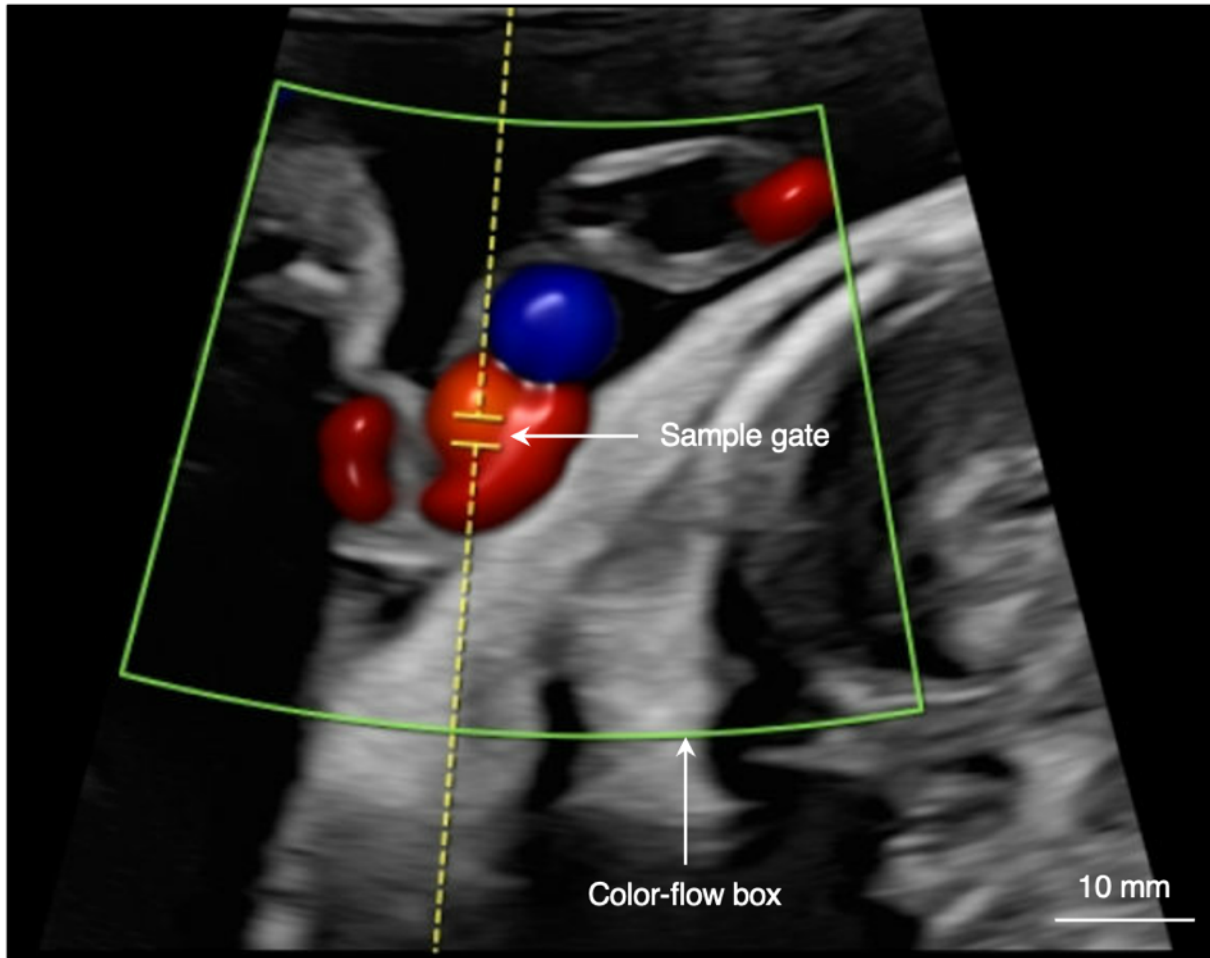


1507
 1508 **Supplementary Fig. 29 | Envelope extraction from spectral Doppler signals.** a, Spectral
 1509 Doppler signals from the fetal umbilical artery. Peak systolic velocity, end diastolic velocity, and
 1510 heartbeat intervals can be manually identified and used to derive the systolic-to-diastolic (S/D)
 1511 ratio, pulsatility index, resistance index, and heart rate. b, The envelope extraction algorithm we
 1512 developed in this study allows automated derivation of these parameters⁷³.

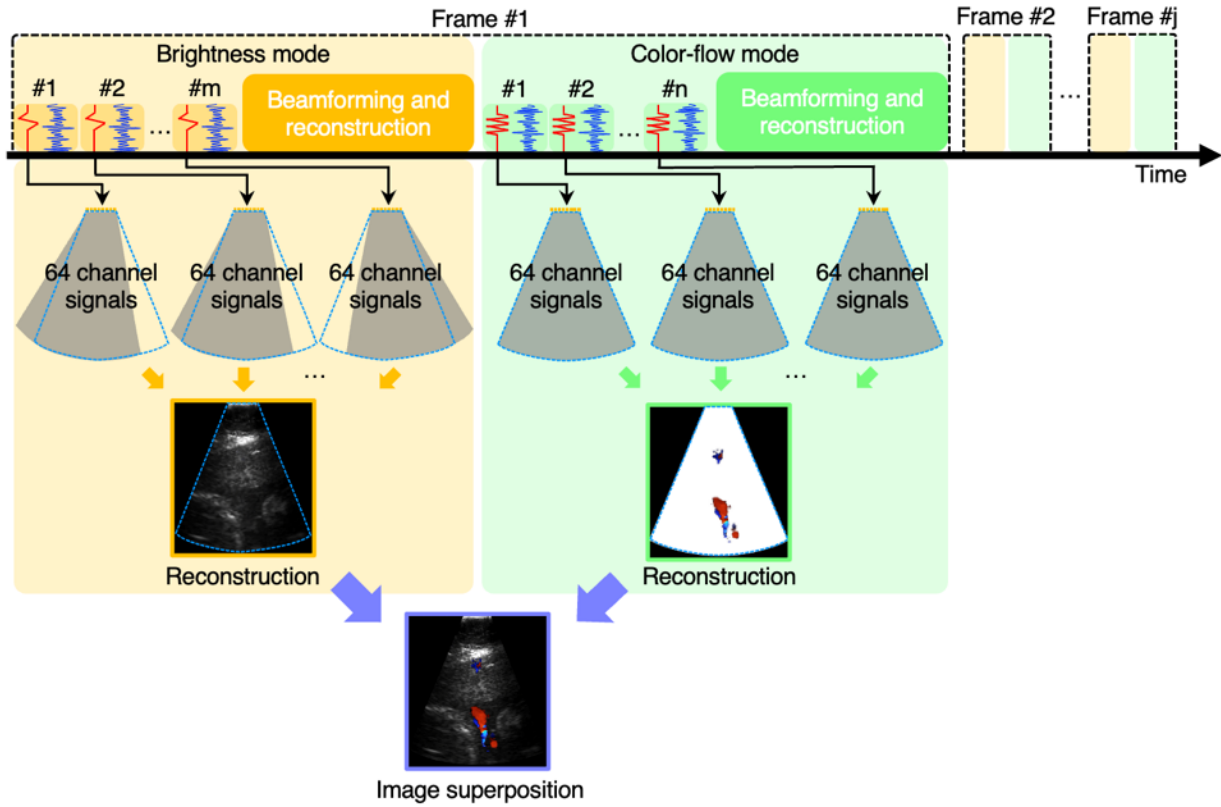


1513
 1514
 1515
 1516
 1517
 1518
 1519
 1520

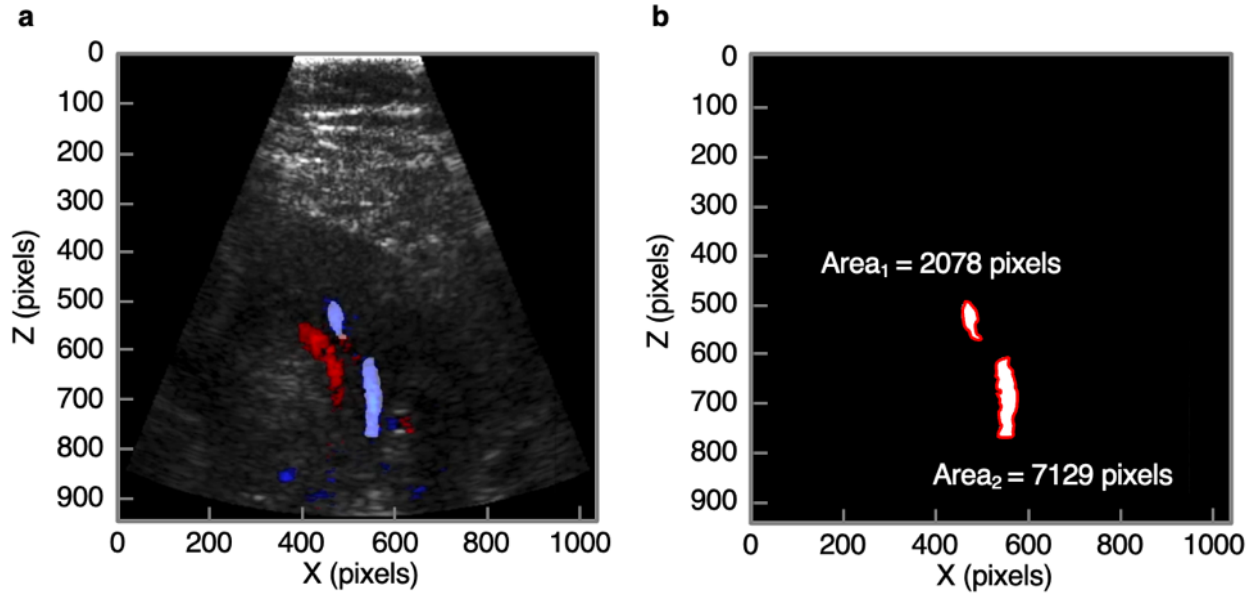
Supplementary Fig. 30 | Statistical analysis of the pulsatility index and the resistance index. Bland-Altman plots of **a**, the pulsatility index and **b**, the resistance index measured using the UPatch and a handheld clinical ultrasound device (Voluson E10, GE). Solid red lines are the mean differences between the two devices, solid blue lines are 95% limits of agreement (1.96 standard deviations above and below the mean differences), and black dashed lines are the zero difference between the two devices. Each plot has three measurement pairs by repeating three times with the same devices on the same participant for each of the 62 participants.



1521
1522 **Supplementary Fig. 31 | Imaging with a handheld clinical ultrasound device.** Duplex imaging
1523 of the umbilical cord with a handheld clinical ultrasound device (GE Voluson E10) requires
1524 maneuvering by a sonographer. First, a color-flow box (green) is manually moved to find the color-
1525 flow signals from the umbilical cord. Then, a sample gate (yellow) is chosen inside the color-flow
1526 box for spectral Doppler recording.

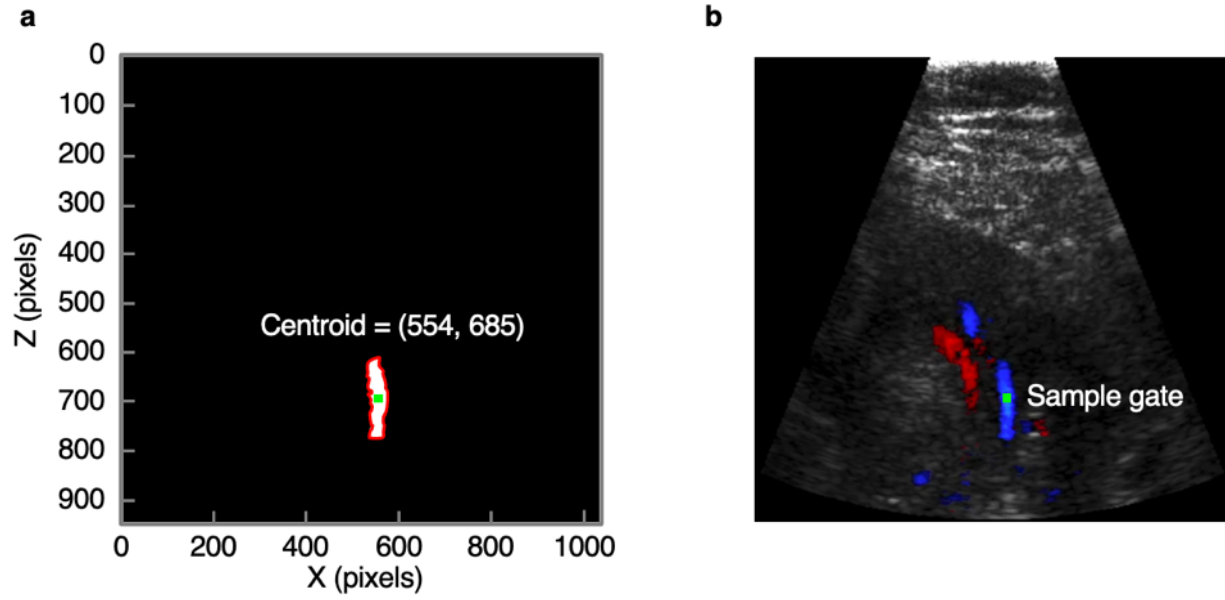


1527
 1528 **Supplementary Fig. 32 | Data acquisition processes of the UPatch.** The UPatch requires a
 1529 complex beamforming process to synthesize an image from 64 channels. Reconstructing a
 1530 brightness-mode image requires compounding radiofrequency signals from multiple steered
 1531 beams. Reconstructing a color-flow image requires estimating the mean frequency across multiple
 1532 transmitted and received beams. These two images are overlaid to form a duplex image.



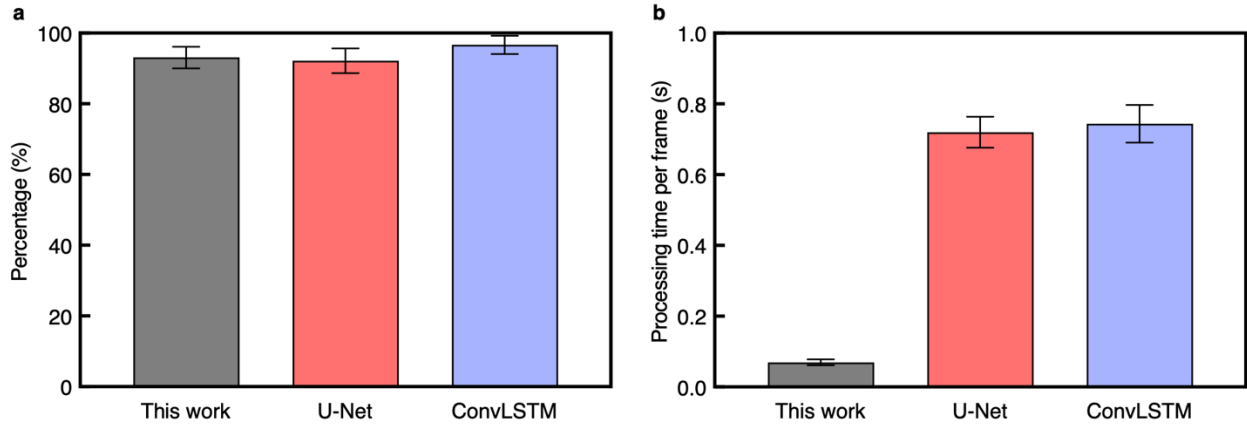
1533
 1534
 1535
 1536
 1537

Supplementary Fig. 33 | Recognition of the primary region of the umbilical artery. **a**, Duplex image with assigned pixel coordinates in the XZ plane for vessel localization. **b**, Number of pixels for each segmented arterial region. The region with the largest area ($Area_2$ in this case) was designated as the primary region.

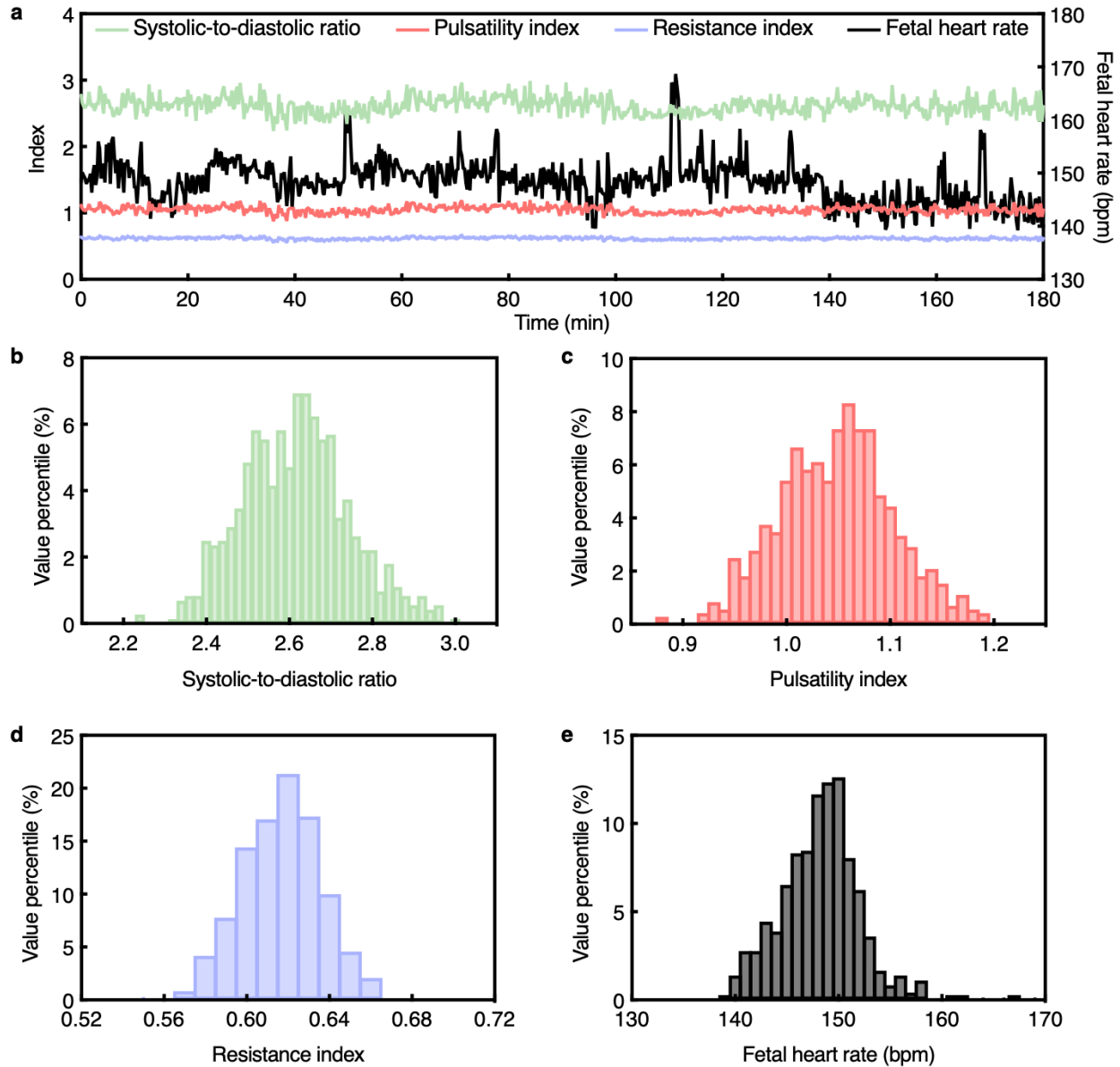


1538
1539
1540
1541
1542
1543

Supplementary Fig. 34 | Identification of the centroid for sample gate placement. **a**, Centroid calculation of the segmented primary arterial region. The centroid was computed using the geometric center of the pixel distribution. **b**, The sample gate was placed at the calculated centroid position within the duplex image. The color of the artery in the duplex image, whether toward (warm hue) or away from (cool hue) the UPatch, does not affect the centroid placement.

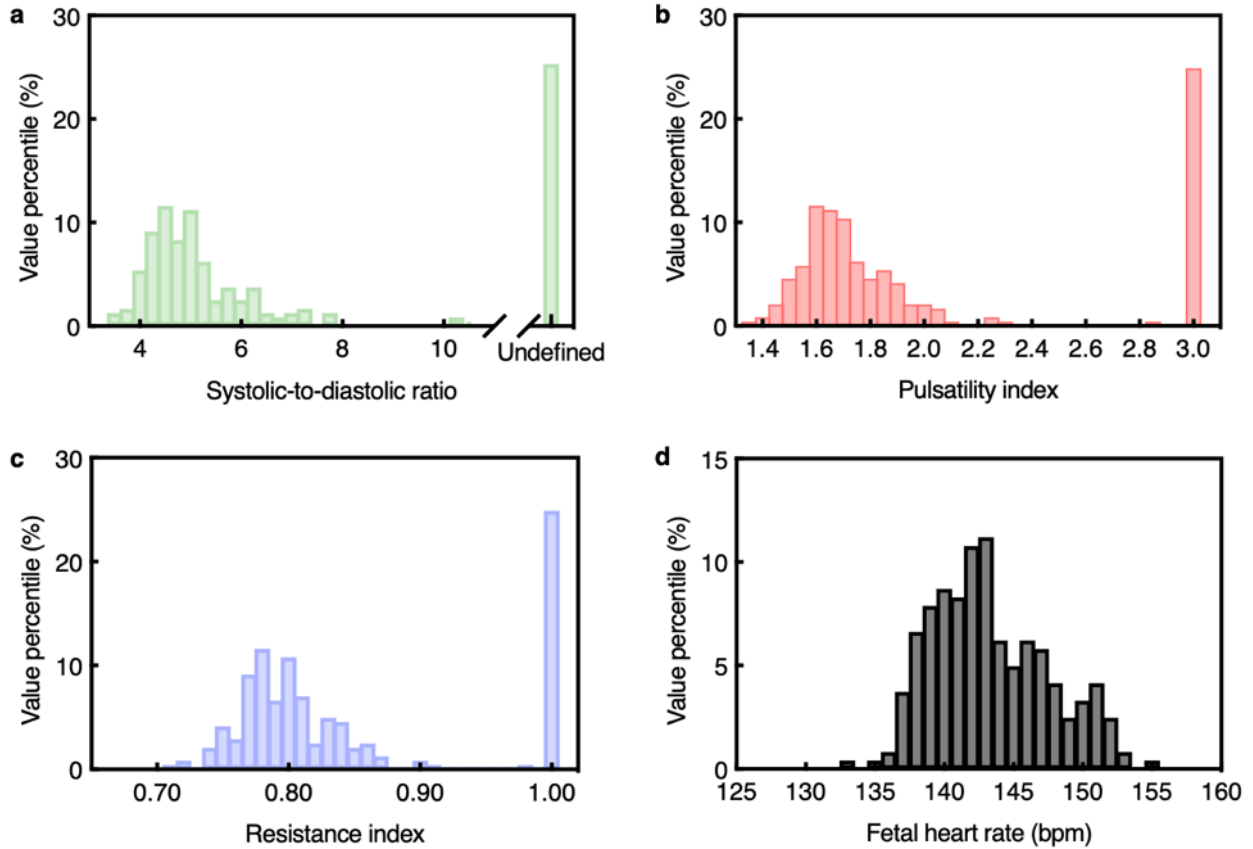


1544
 1545 **Supplementary Fig. 35 | Benchmarking the tracking algorithm against deep learning**
 1546 **methods.** **a**, Sonographer-evaluated tracking accuracy for the algorithm (“This work”), U-Net
 1547 model, and ConvLSTM model, reported as “optimal” by the sonographers. **b**, Processing time per
 1548 frame for each method. Data are presented as mean \pm standard deviations ($n = 3$ for **a** and $n = 50$
 1549 for **b**). While all three approaches achieve comparable tracking accuracy, the customized algorithm
 1550 operates at substantially lower computational cost, enabling real-time tracking during fetal
 1551 movement.
 1552

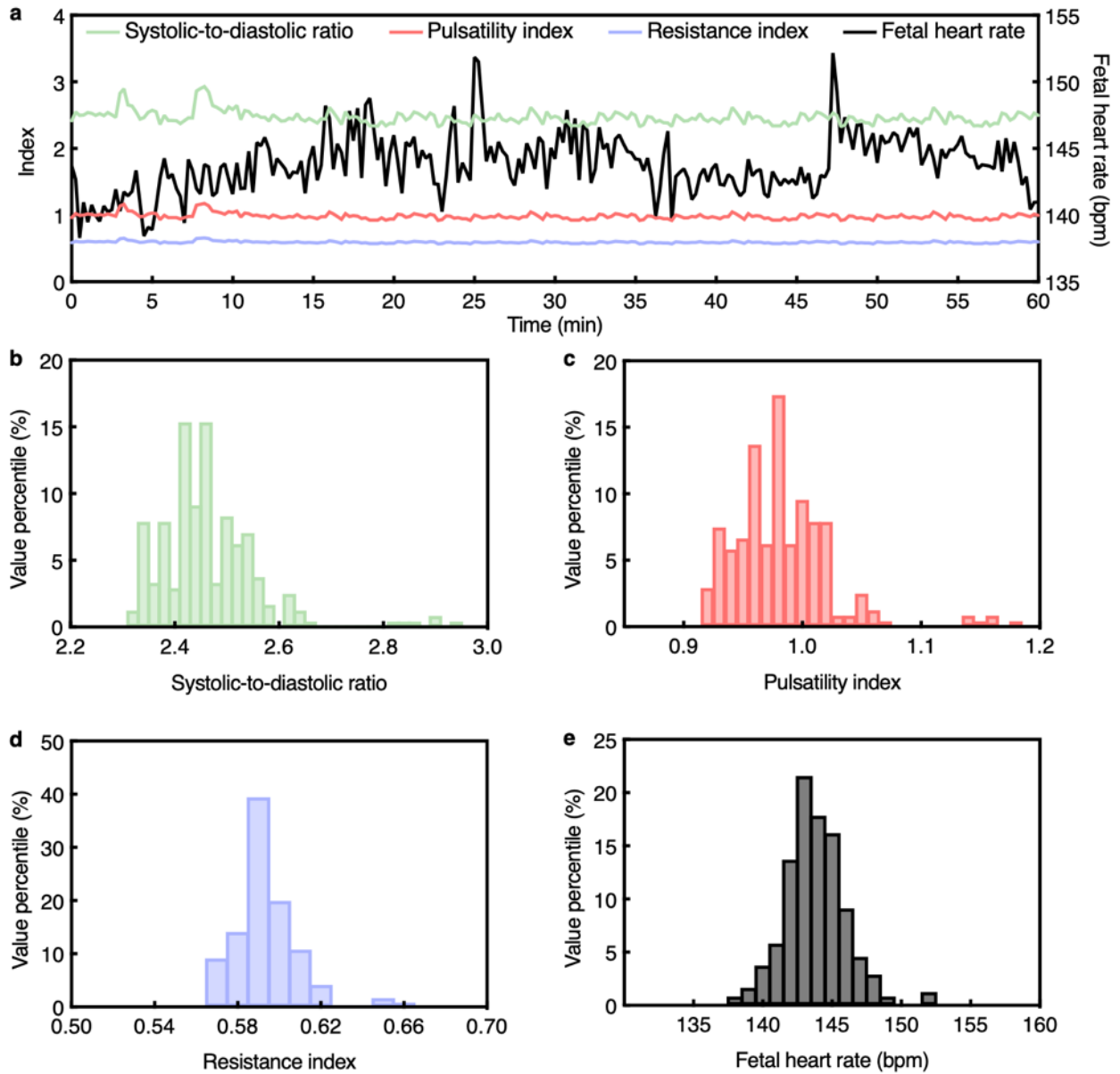


1553
 1554
 1555
 1556
 1557
 1558

Supplementary Fig. 36 | Continuous fetal monitoring using the UPatch in Participant #1. a, Time series data from the 3-h continuous monitoring session. Systolic-to-diastolic ratio, pulsatility index, and resistance index are plotted on the left y-axis, and fetal heart rate is plotted on the right y-axis. Histograms of b, systolic-to-diastolic ratio, c, pulsatility index, d, resistance index, and e, fetal heart rate over the recording period.

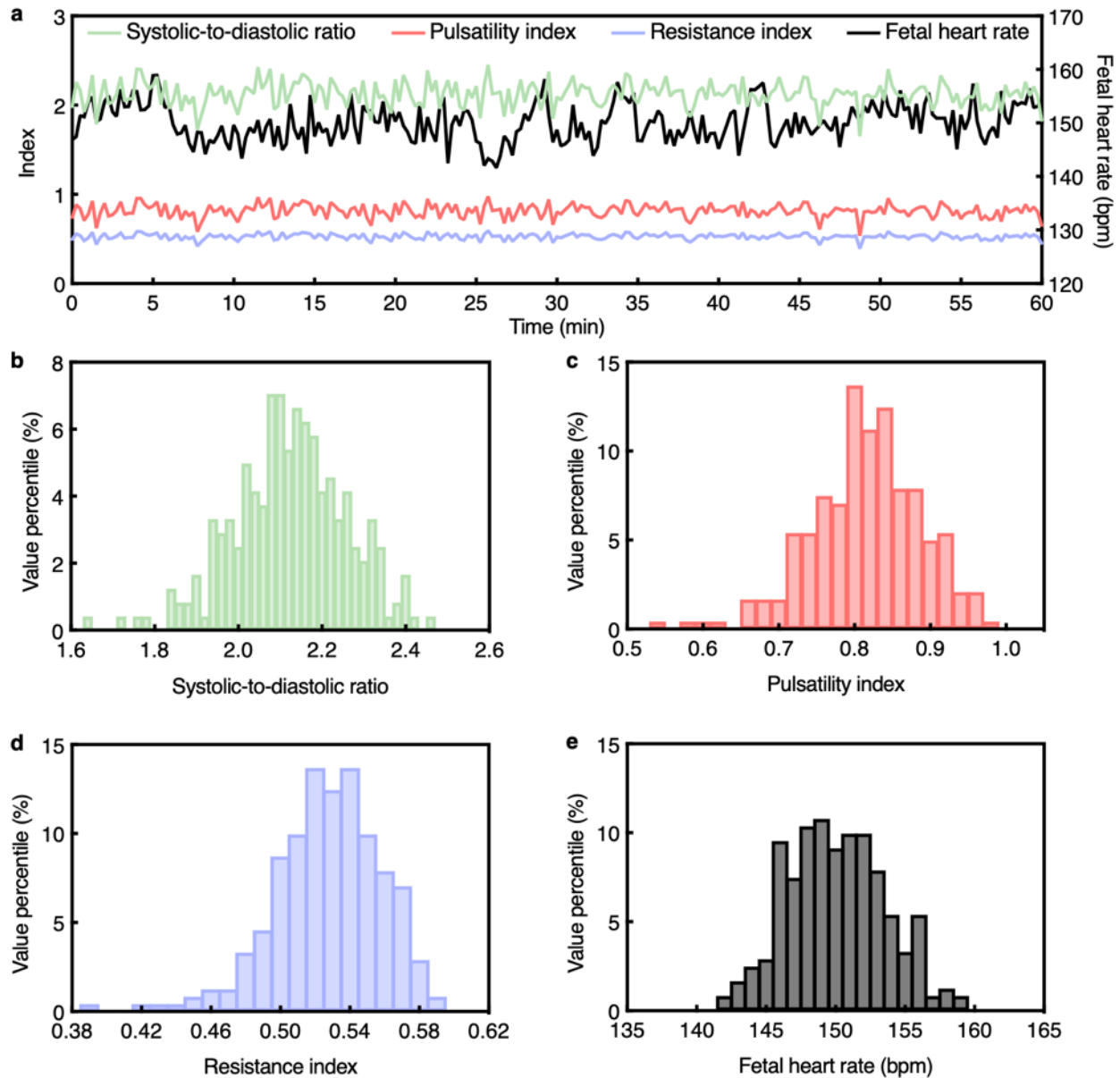


1559
 1560 **Supplementary Fig. 37 | Continuous fetal monitoring using the UPatch in Participant #2.**
 1561 Histograms of **a**, systolic-to-diastolic ratio, **b**, pulsatility index, **c**, resistance index, and **d**, fetal
 1562 heart rate over the recording period. The time series data is in Fig. 4d in the main text. The systolic-to-
 1563 diastolic ratio was not plotted in the time series due to the presence of undefined values.



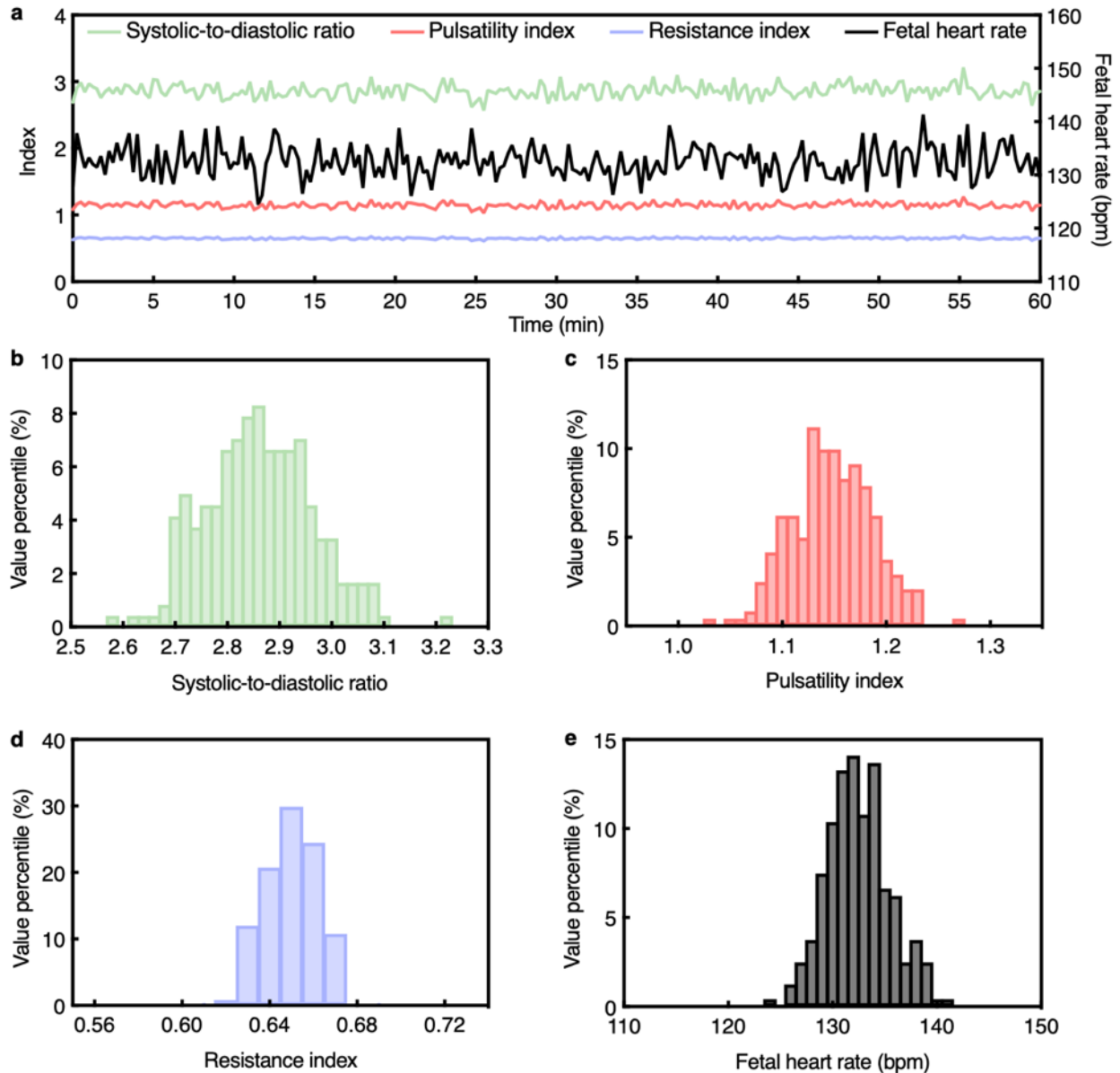
1564
 1565
 1566
 1567
 1568
 1569

Supplementary Fig. 38 | Continuous fetal monitoring using the UPatch in Participant #3. a, Time series data from the 1-h continuous monitoring session. Systolic-to-diastolic ratio, pulsatility index, and resistance index are plotted on the left y-axis, and fetal heart rate is plotted on the right y-axis. Histograms of b, systolic-to-diastolic ratio, c, pulsatility index, d, resistance index, and e, fetal heart rate over the recording period.



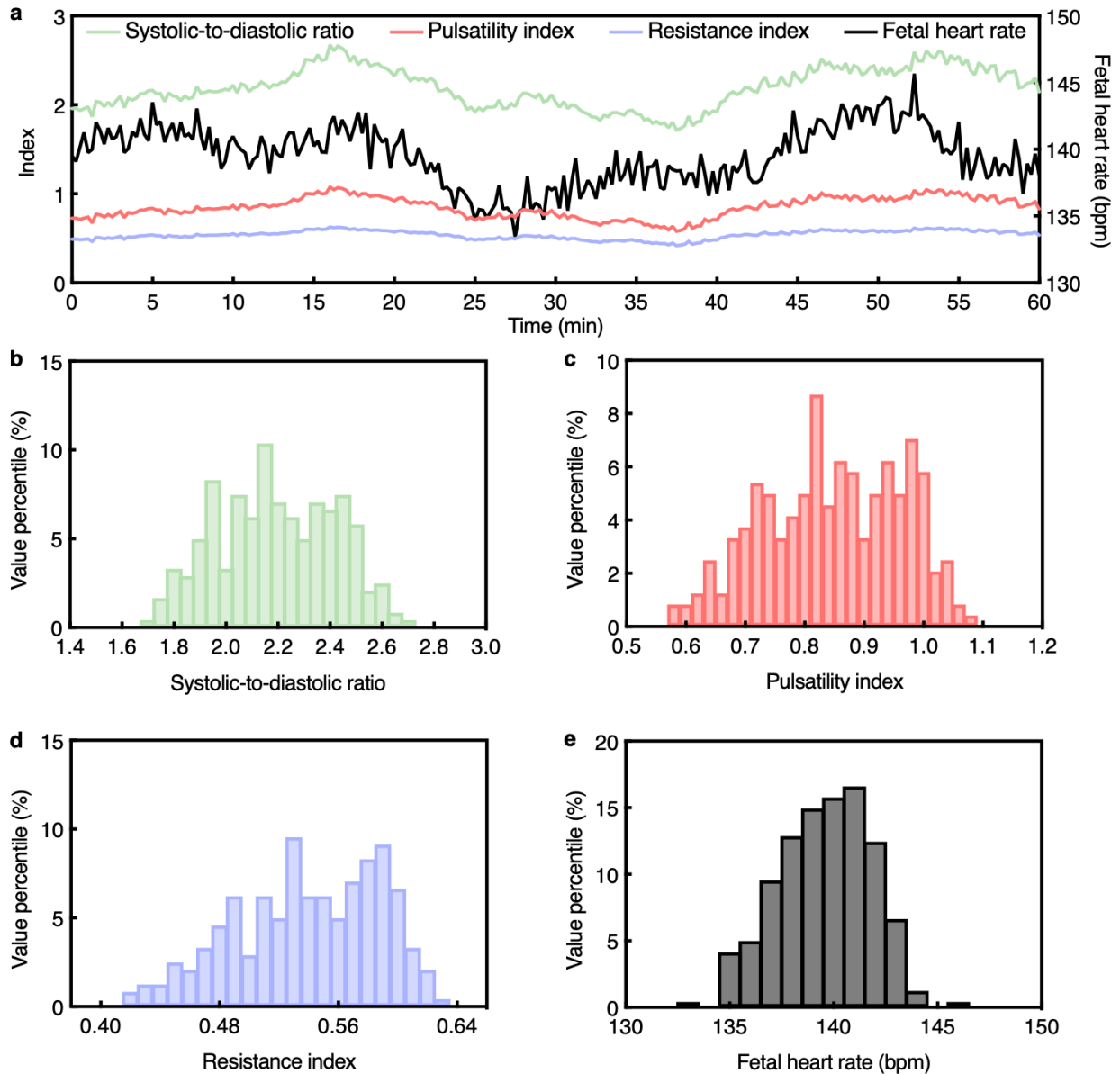
1570
1571
1572
1573
1574
1575

Supplementary Fig. 39 | Continuous fetal monitoring using the UPatch in Participant #4. **a**, Time series data from the 1-h continuous monitoring session. Systolic-to-diastolic ratio, pulsatility index, and resistance index are plotted on the left y-axis, and fetal heart rate is plotted on the right y-axis. Histograms of **b**, systolic-to-diastolic ratio, **c**, pulsatility index, **d**, resistance index, and **e**, fetal heart rate over the recording period.



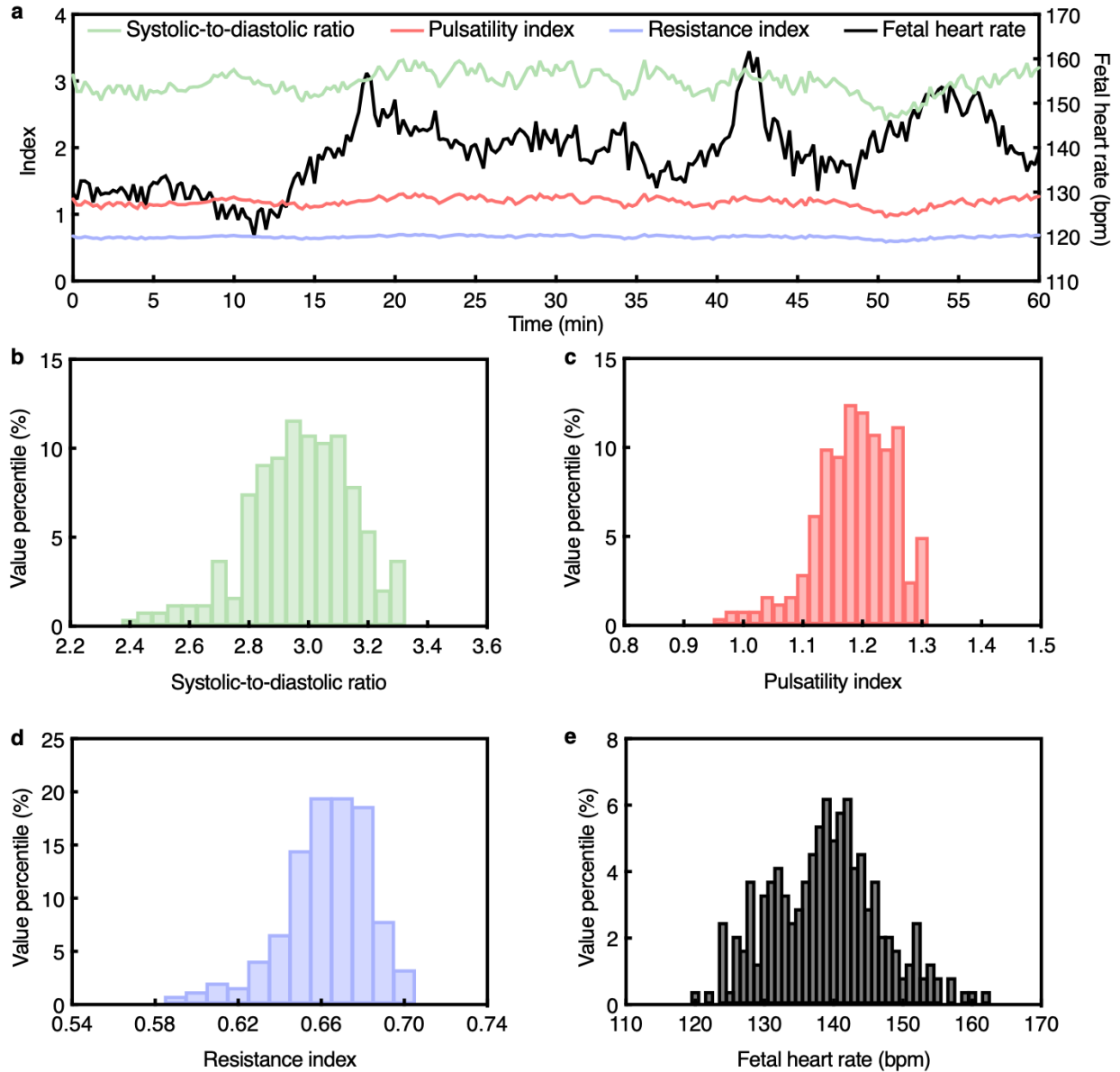
1576
 1577
 1578
 1579
 1580
 1581

Supplementary Fig. 40 | Continuous fetal monitoring using the UPatch in Participant #5. a, Time series data from the 1-h continuous monitoring session. Systolic-to-diastolic ratio, pulsatility index, and resistance index are plotted on the left y-axis, and fetal heart rate is plotted on the right y-axis. Histograms of b, systolic-to-diastolic ratio, c, pulsatility index, d, resistance index, and e, fetal heart rate over the recording period.



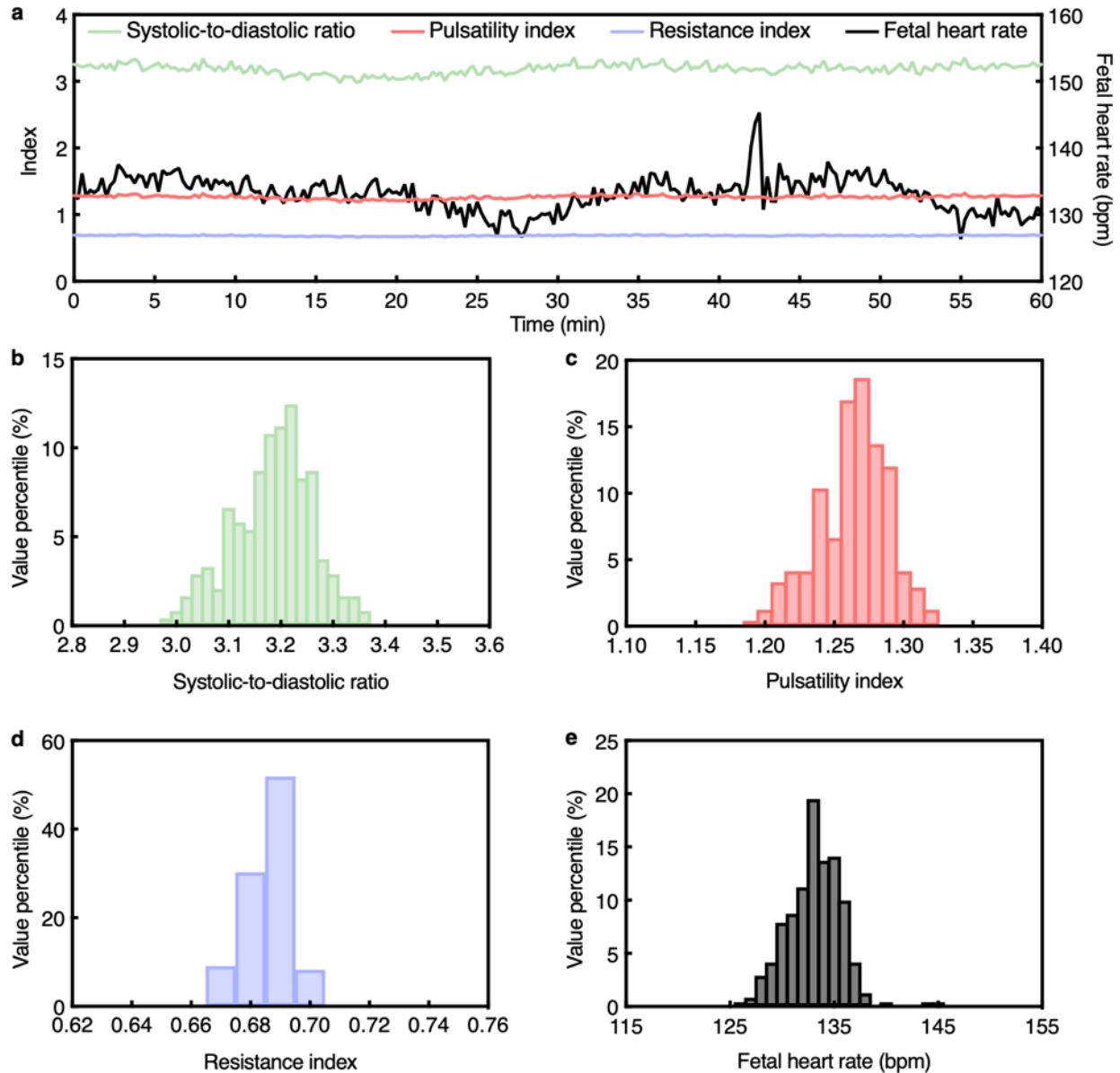
1582
 1583
 1584
 1585
 1586
 1587

Supplementary Fig. 41 | Continuous fetal monitoring using the UPatch in Participant #6. **a**, Time series data from the 1-h continuous monitoring session. Systolic-to-diastolic ratio, pulsatility index, and resistance index are plotted on the left y-axis, and fetal heart rate is plotted on the right y-axis. Histograms of **b**, systolic-to-diastolic ratio, **c**, pulsatility index, **d**, resistance index, and **e**, fetal heart rate over the recording period.



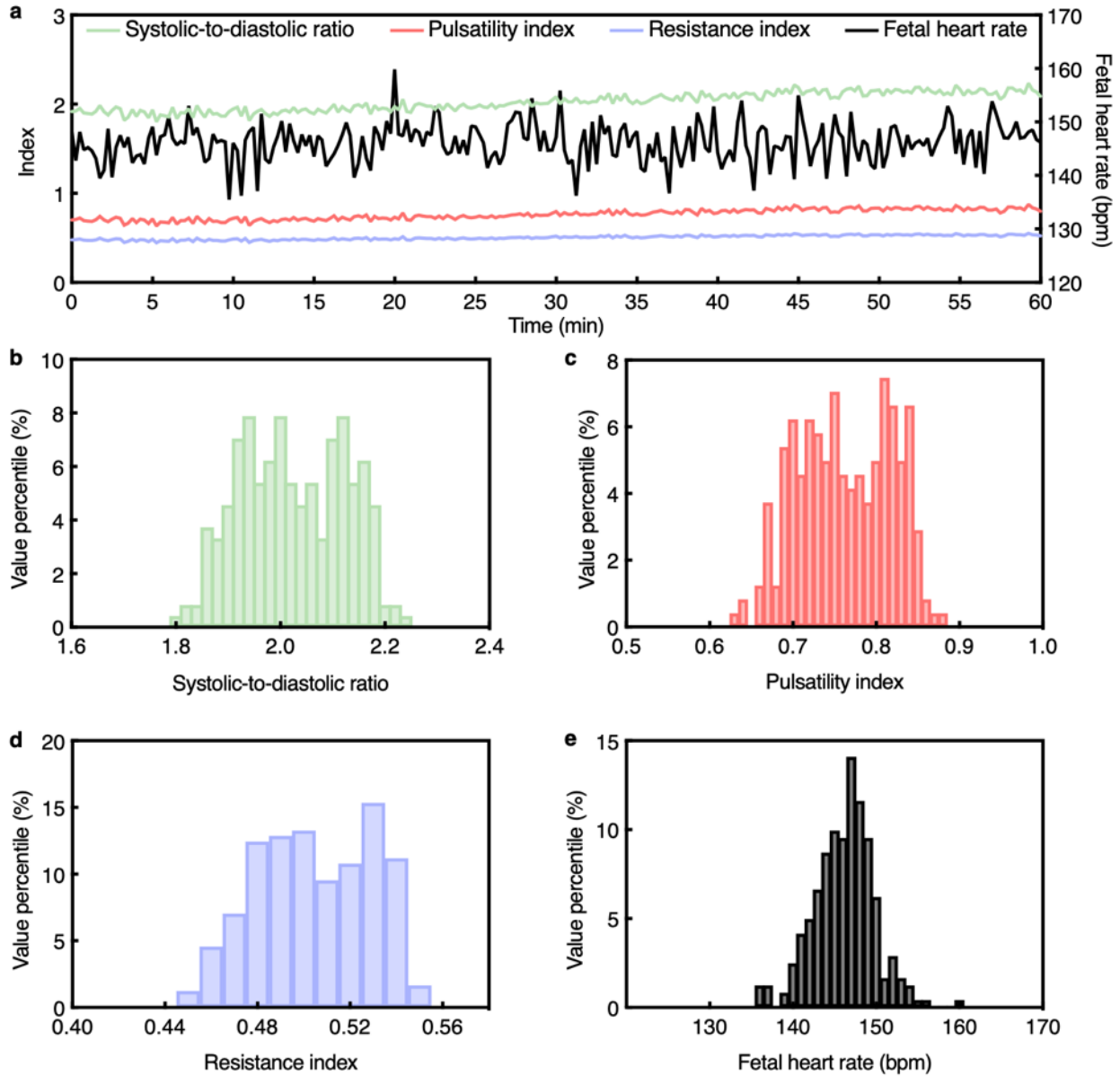
1588
 1589
 1590
 1591
 1592
 1593

Supplementary Fig. 42 | Continuous fetal monitoring using the UPatch in Participant #7. a, Time series data from the 1-h continuous monitoring session. Systolic-to-diastolic ratio, pulsatility index, and resistance index are plotted on the left y-axis, and fetal heart rate is plotted on the right y-axis. Histograms of **b**, systolic-to-diastolic ratio, **c**, pulsatility index, **d**, resistance index, and **e**, fetal heart rate over the recording period.



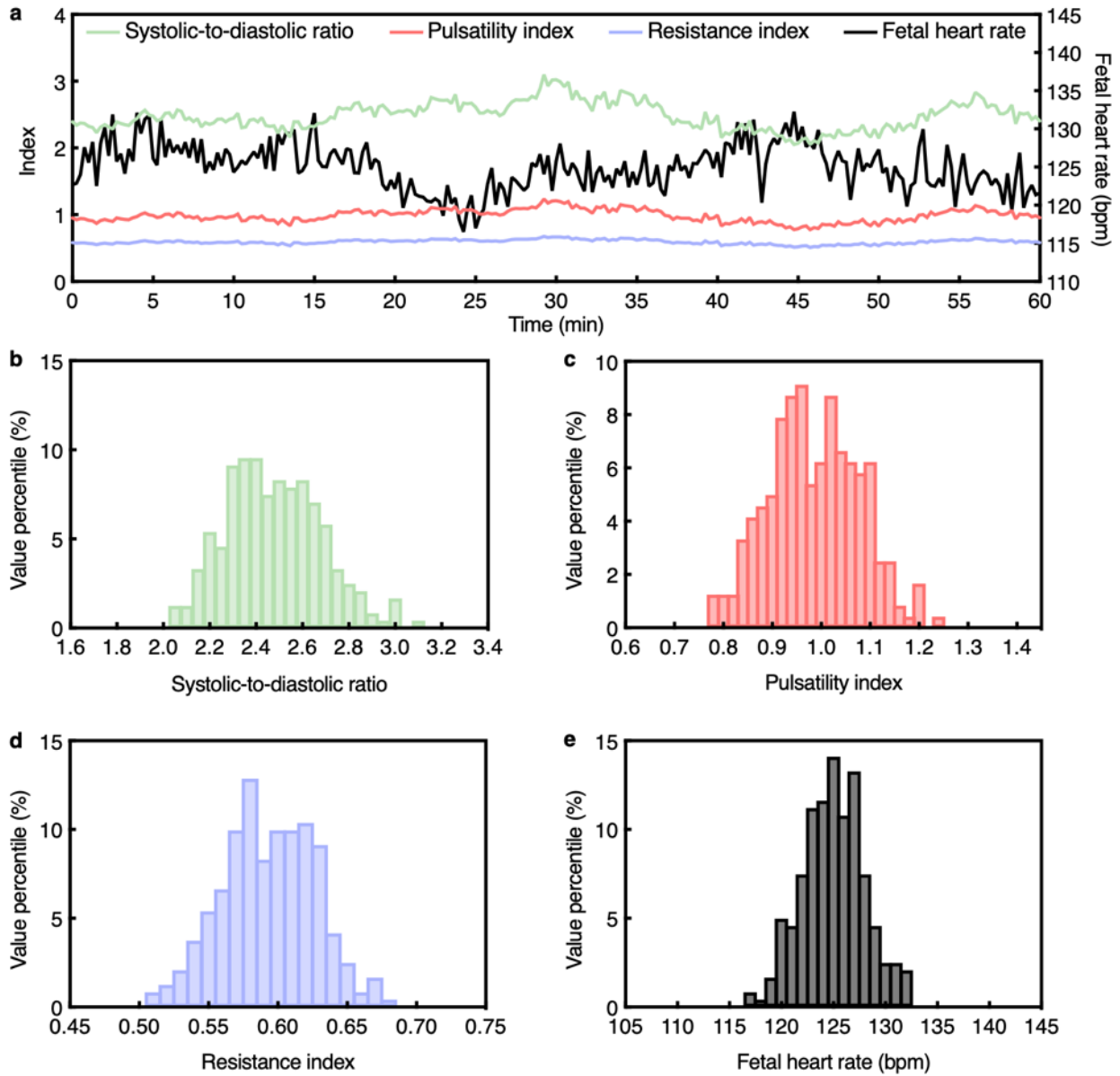
1594
 1595
 1596
 1597
 1598
 1599

Supplementary Fig. 43 | Continuous fetal monitoring using the UPatch in Participant #8. **a**, Time series data from the 1-h continuous monitoring session. Systolic-to-diastolic ratio, pulsatility index, and resistance index are plotted on the left y-axis, and fetal heart rate is plotted on the right y-axis. Histograms of **b**, systolic-to-diastolic ratio, **c**, pulsatility index, **d**, resistance index, and **e**, fetal heart rate over the recording period.



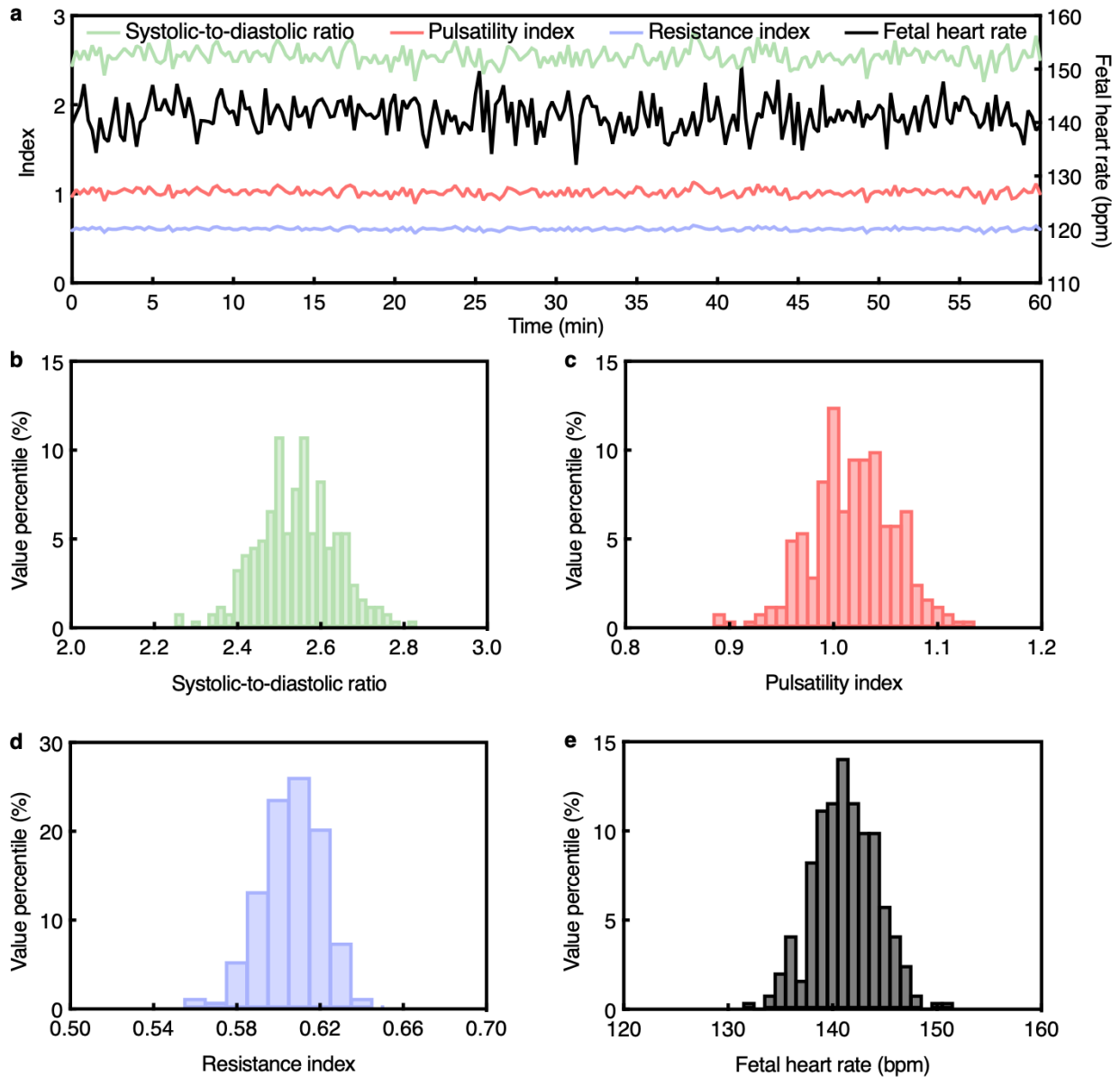
1600
 1601
 1602
 1603
 1604
 1605

Supplementary Fig. 44 | Continuous fetal monitoring using the UPatch in Participant #9. **a**, Time series data from the 1-h continuous monitoring session. Systolic-to-diastolic ratio, pulsatility index, and resistance index are plotted on the left y-axis, and fetal heart rate is plotted on the right y-axis. Histograms of **b**, systolic-to-diastolic ratio, **c**, pulsatility index, **d**, resistance index, and **e**, fetal heart rate over the recording period.



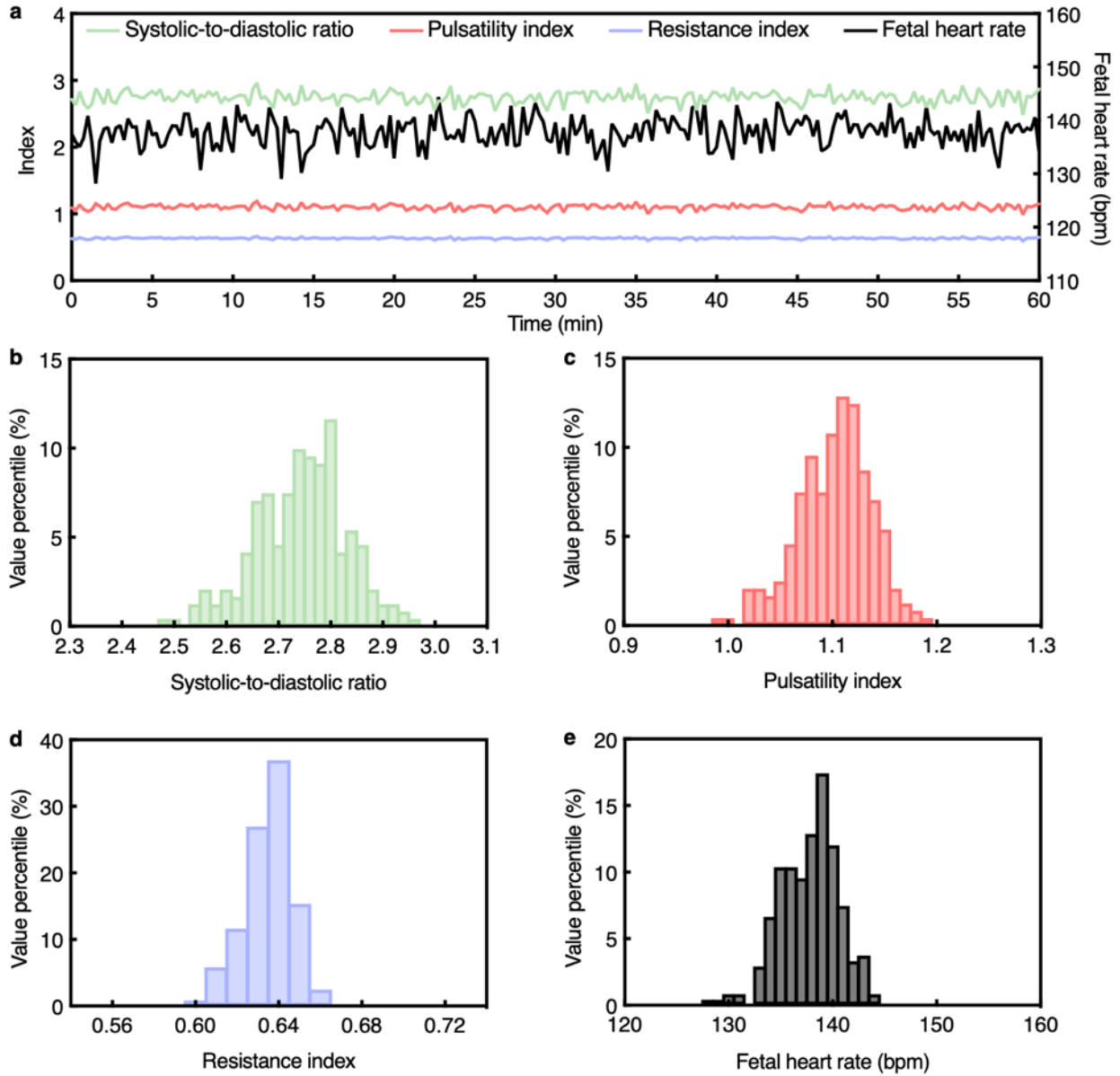
1606
 1607
 1608
 1609
 1610
 1611

Supplementary Fig. 45 | Continuous fetal monitoring using the UPatch in Participant #10. a, Time series data from the 1-h continuous monitoring session. Systolic-to-diastolic ratio, pulsatility index, and resistance index are plotted on the left y-axis, and fetal heart rate is plotted on the right y-axis. Histograms of b, systolic-to-diastolic ratio, c, pulsatility index, d, resistance index, and e, fetal heart rate over the recording period.



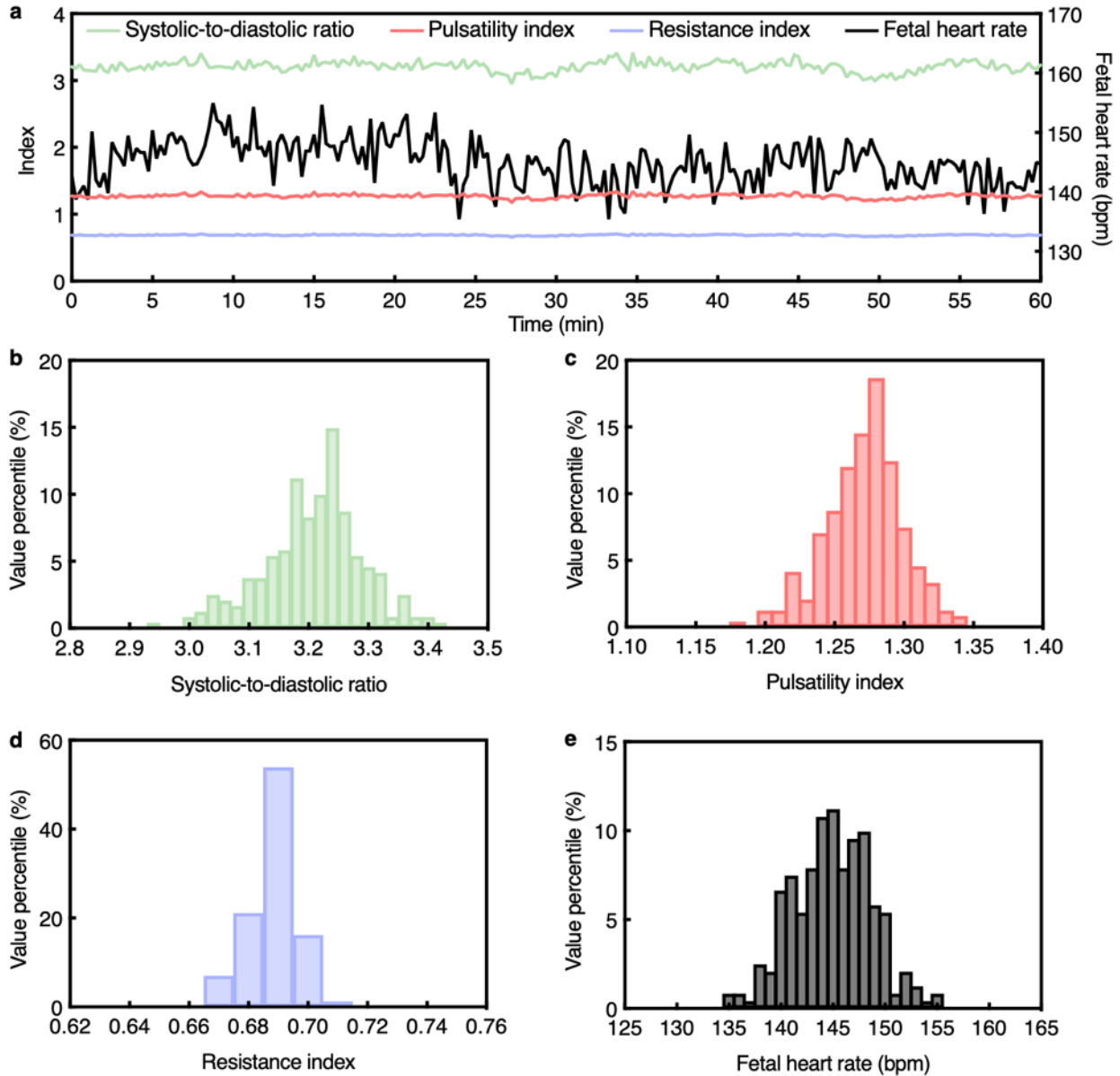
1612
 1613
 1614
 1615
 1616
 1617

Supplementary Fig. 46 | Continuous fetal monitoring using the UPatch in Participant #11. a, Time series data from the 1-h continuous monitoring session. Systolic-to-diastolic ratio, pulsatility index, and resistance index are plotted on the left y-axis, and fetal heart rate is plotted on the right y-axis. Histograms of b, systolic-to-diastolic ratio, c, pulsatility index, d, resistance index, and e, fetal heart rate over the recording period.



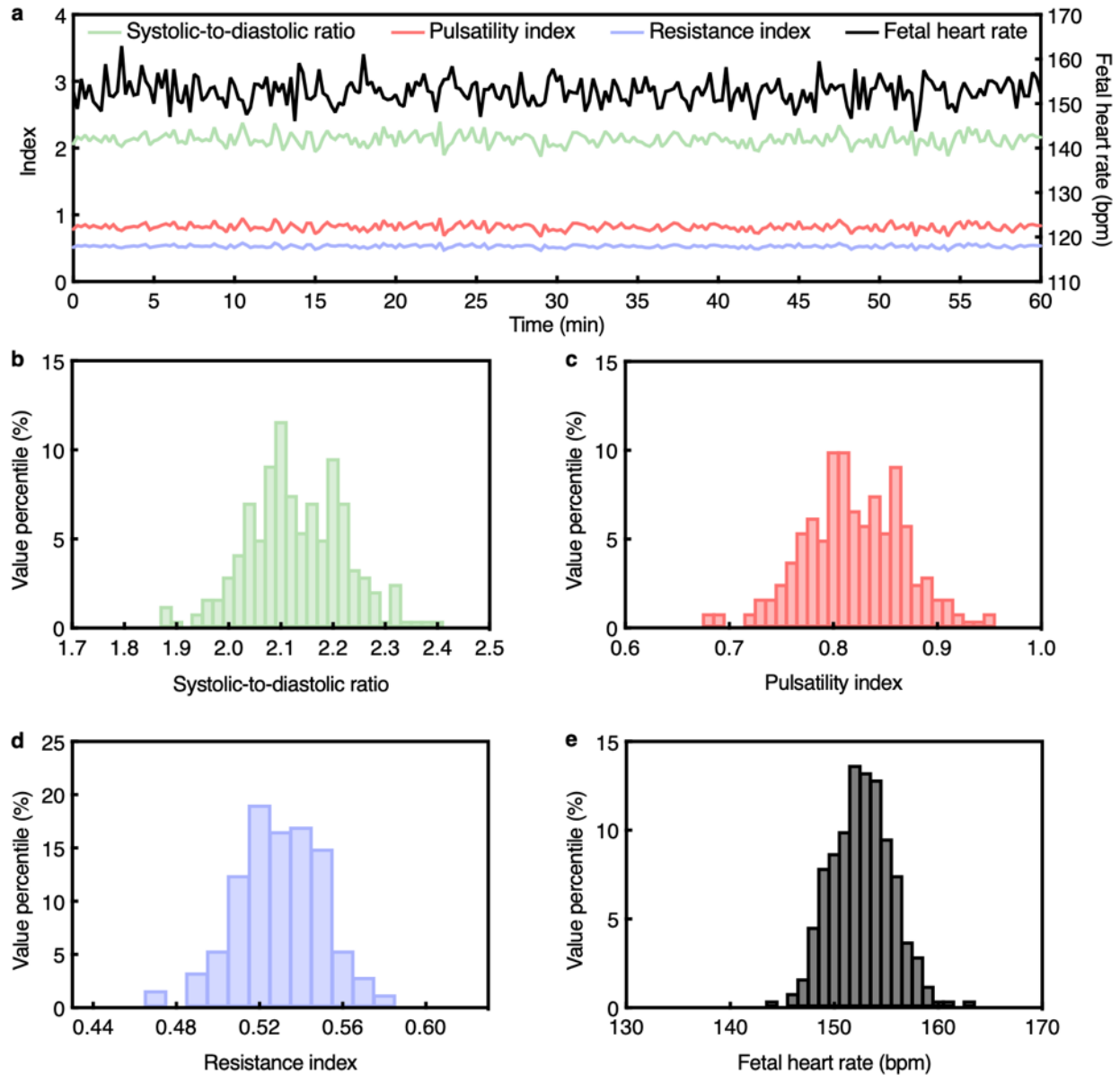
1618
 1619
 1620
 1621
 1622
 1623

Supplementary Fig. 47 | Continuous fetal monitoring using the UPatch in Participant #12. **a**, Time series data from the 1-h continuous monitoring session. Systolic-to-diastolic ratio, pulsatility index, and resistance index are plotted on the left y-axis, and fetal heart rate is plotted on the right y-axis. Histograms of **b**, systolic-to-diastolic ratio, **c**, pulsatility index, **d**, resistance index, and **e**, fetal heart rate over the recording period.



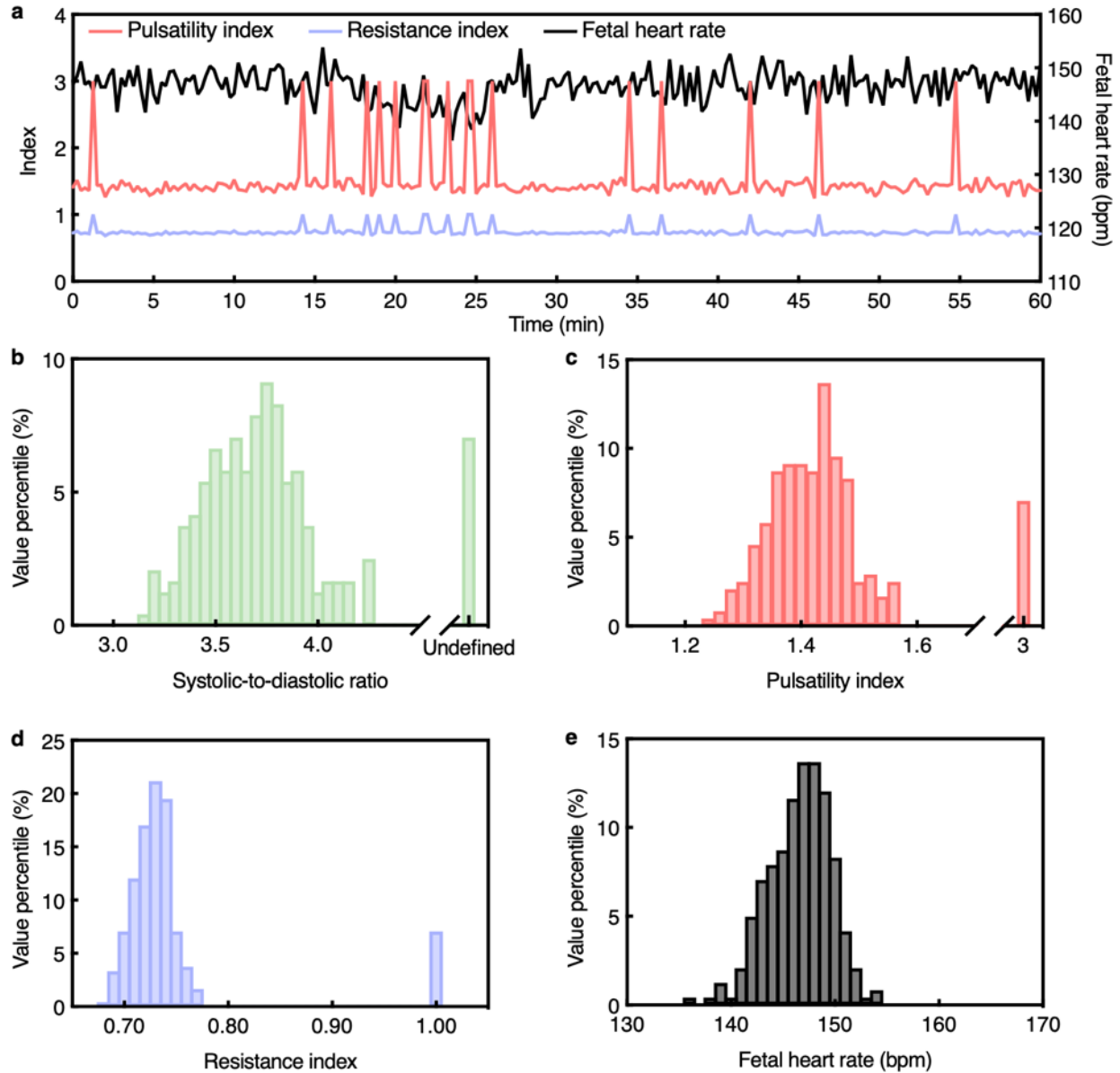
1624
 1625
 1626
 1627
 1628
 1629

Supplementary Fig. 48 | Continuous fetal monitoring using the UPatch in Participant #13. **a**, Time series data from the 1-h continuous monitoring session. Systolic-to-diastolic ratio, pulsatility index, and resistance index are plotted on the left y-axis, and fetal heart rate is plotted on the right y-axis. Histograms of **b**, systolic-to-diastolic ratio, **c**, pulsatility index, **d**, resistance index, and **e**, fetal heart rate over the recording period.



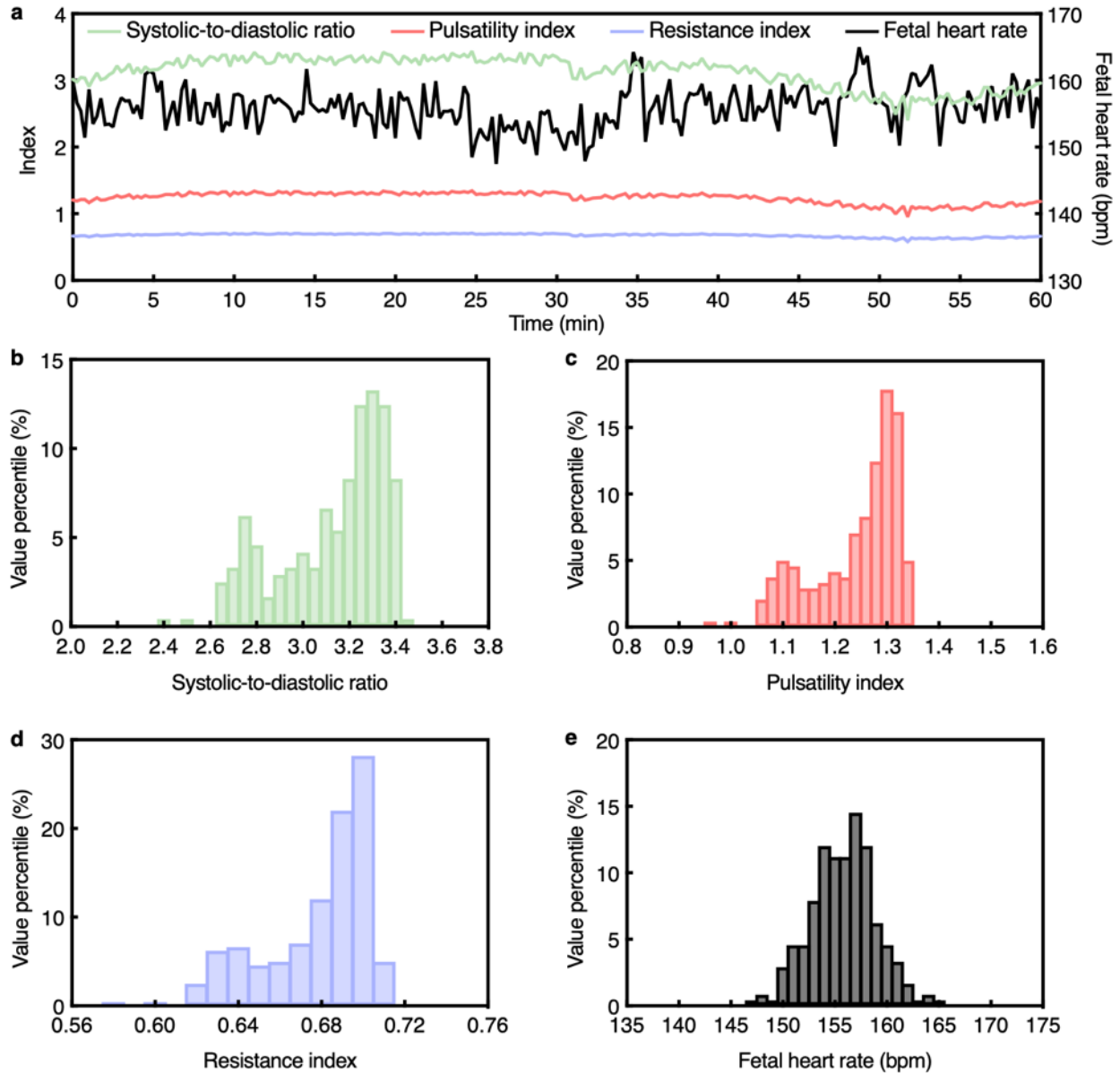
1630
 1631
 1632
 1633
 1634
 1635

Supplementary Fig. 49 | Continuous fetal monitoring using the UPatch in Participant #14. **a**, Time series data from the 1-h continuous monitoring session. Systolic-to-diastolic ratio, pulsatility index, and resistance index are plotted on the left y-axis, and fetal heart rate is plotted on the right y-axis. Histograms of **b**, systolic-to-diastolic ratio, **c**, pulsatility index, **d**, resistance index, and **e**, fetal heart rate over the recording period.



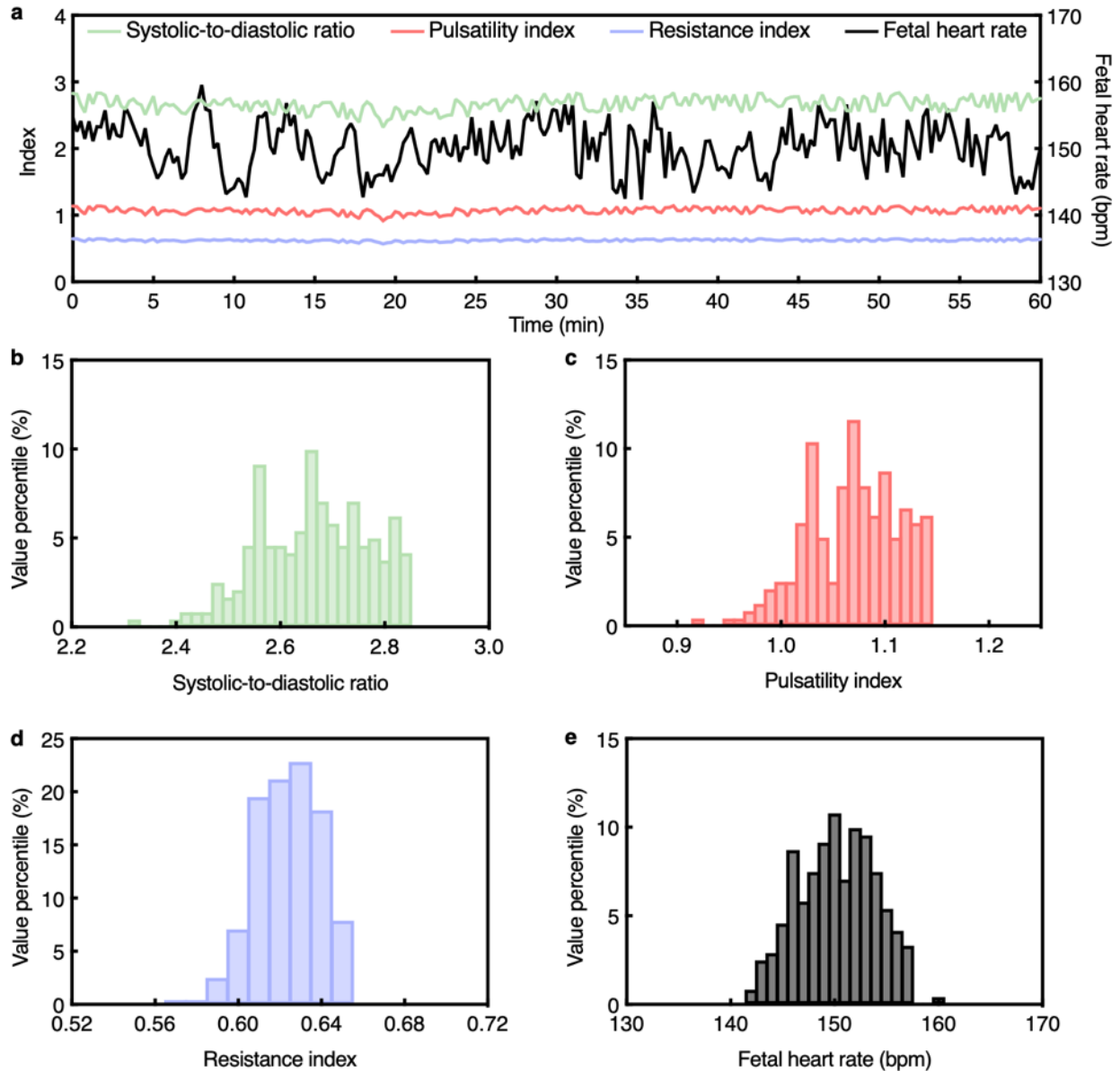
1636
 1637
 1638
 1639
 1640
 1641
 1642
 1643
 1644
 1645
 1646

Supplementary Fig. 50 | Continuous fetal monitoring using the UPatch in Participant #15. a, Time series data from the 1-h continuous monitoring session. Pulsatility index and resistance index are plotted on the left y-axis, and fetal heart rate is plotted on the right y-axis. The systolic-to-diastolic ratio was not plotted in the time series due to the presence of undefined values. The large peaks correspond to periods of absent end diastolic flow, during which the systolic-to-diastolic ratio is undefined, the pulsatility index is 3.0, and the resistance index is 1.0. Such absence of end diastolic flow is clinically relevant because it is associated with abnormal fetoplacental hemodynamics and can indicate evolving intrauterine growth restriction, whereas healthy fetuses typically maintain forward end diastolic flow^{49,50}. Histograms of **b**, systolic-to-diastolic ratio, **c**, pulsatility index, **d**, resistance index, and **e**, fetal heart rate over the recording period.

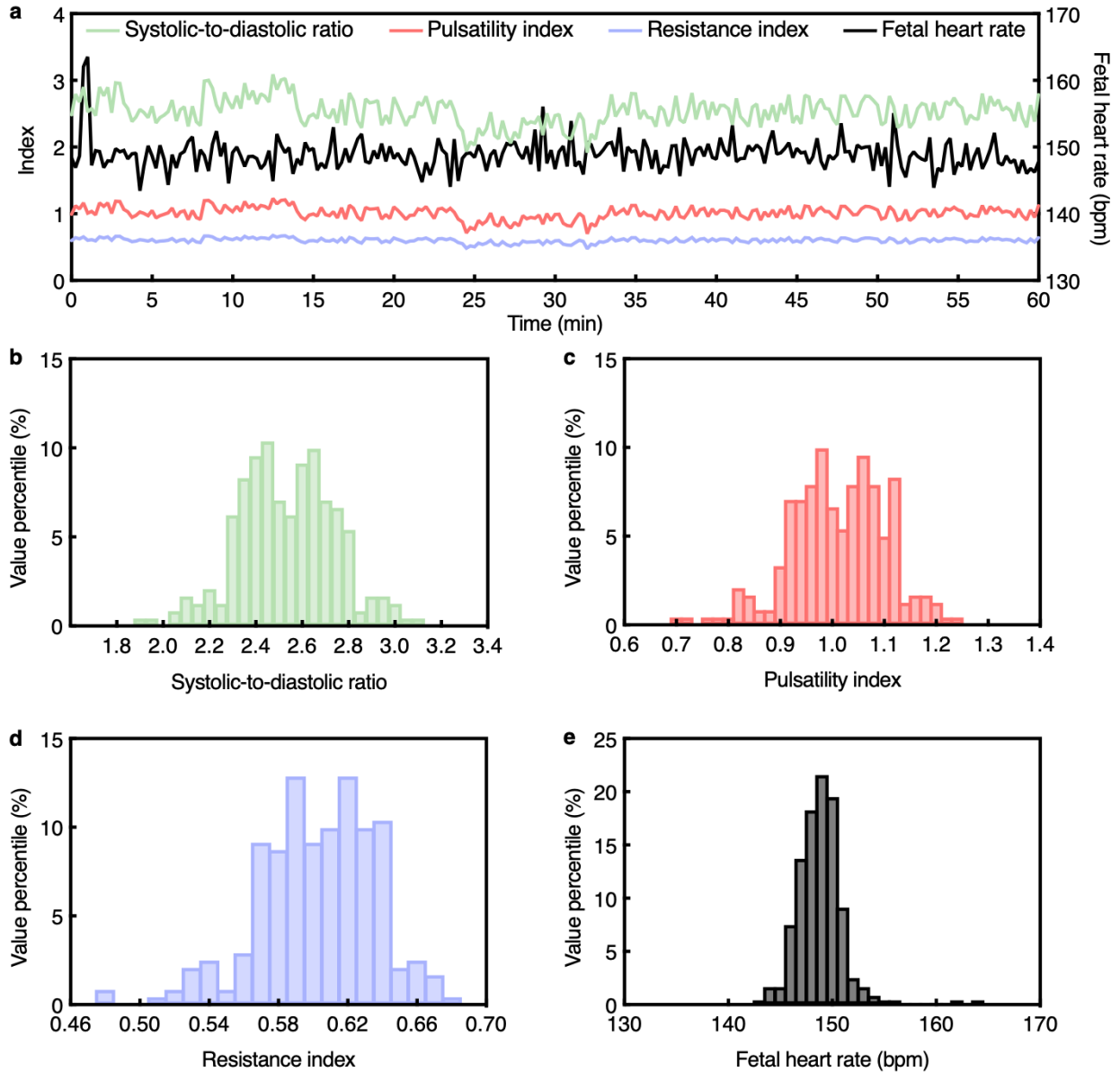


1647
 1648
 1649
 1650
 1651
 1652

Supplementary Fig. 51 | Continuous fetal monitoring using the UPatch in Participant #16. a, Time series data from the 1-h continuous monitoring session. Systolic-to-diastolic ratio, pulsatility index, and resistance index are plotted on the left y-axis, and fetal heart rate is plotted on the right y-axis. Histograms of b, systolic-to-diastolic ratio, c, pulsatility index, d, resistance index, and e, fetal heart rate over the recording period.

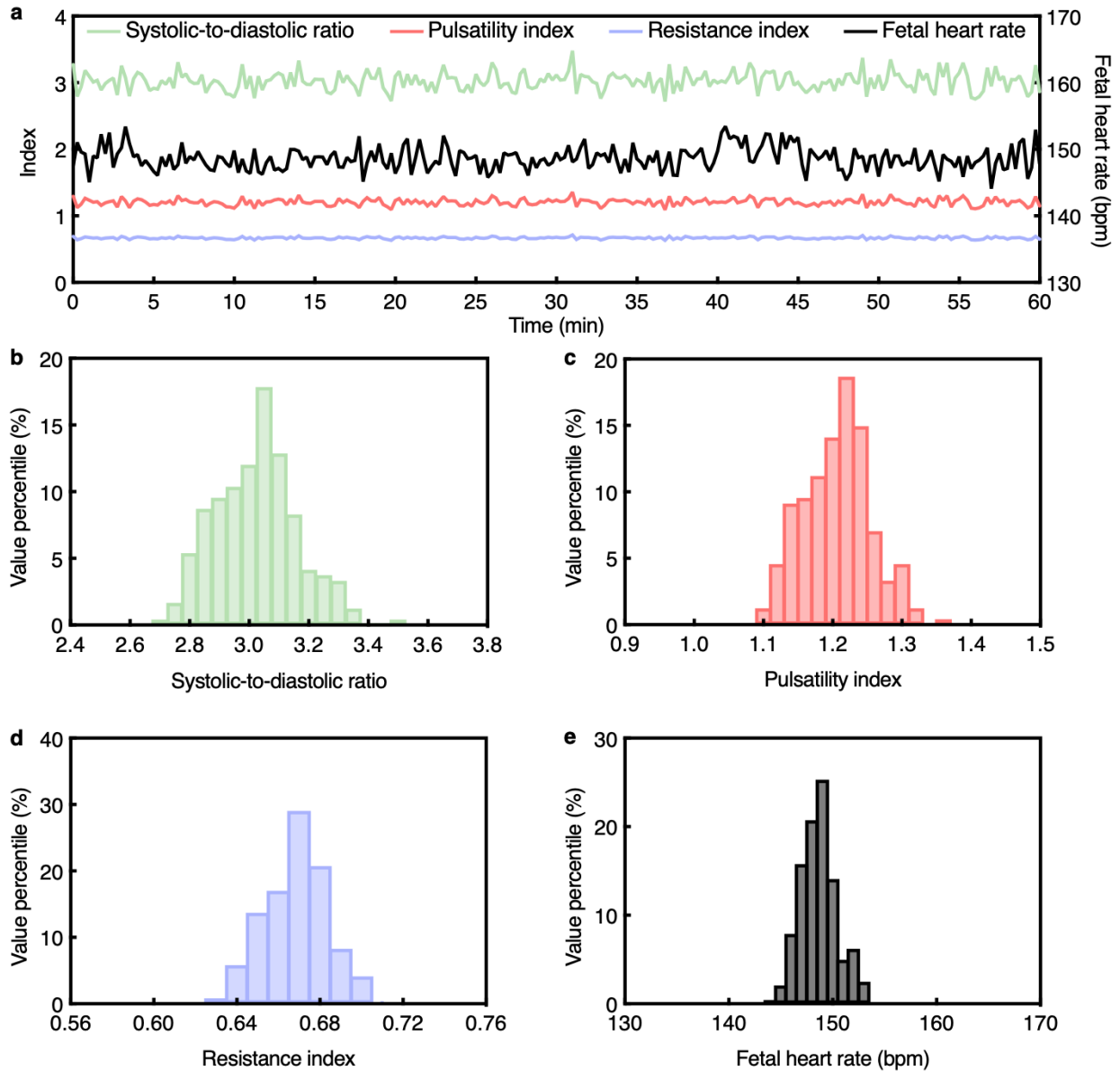


1653
 1654 **Supplementary Fig. 52 | Continuous fetal monitoring using the UPatch in Participant #17.** a,
 1655 Time series data from the 1-h continuous monitoring session. Systolic-to-diastolic ratio, pulsatility
 1656 index, and resistance index are plotted on the left y-axis, and fetal heart rate is plotted on the right
 1657 y-axis. Histograms of b, systolic-to-diastolic ratio, c, pulsatility index, d, resistance index, and e,
 1658 fetal heart rate over the recording period.



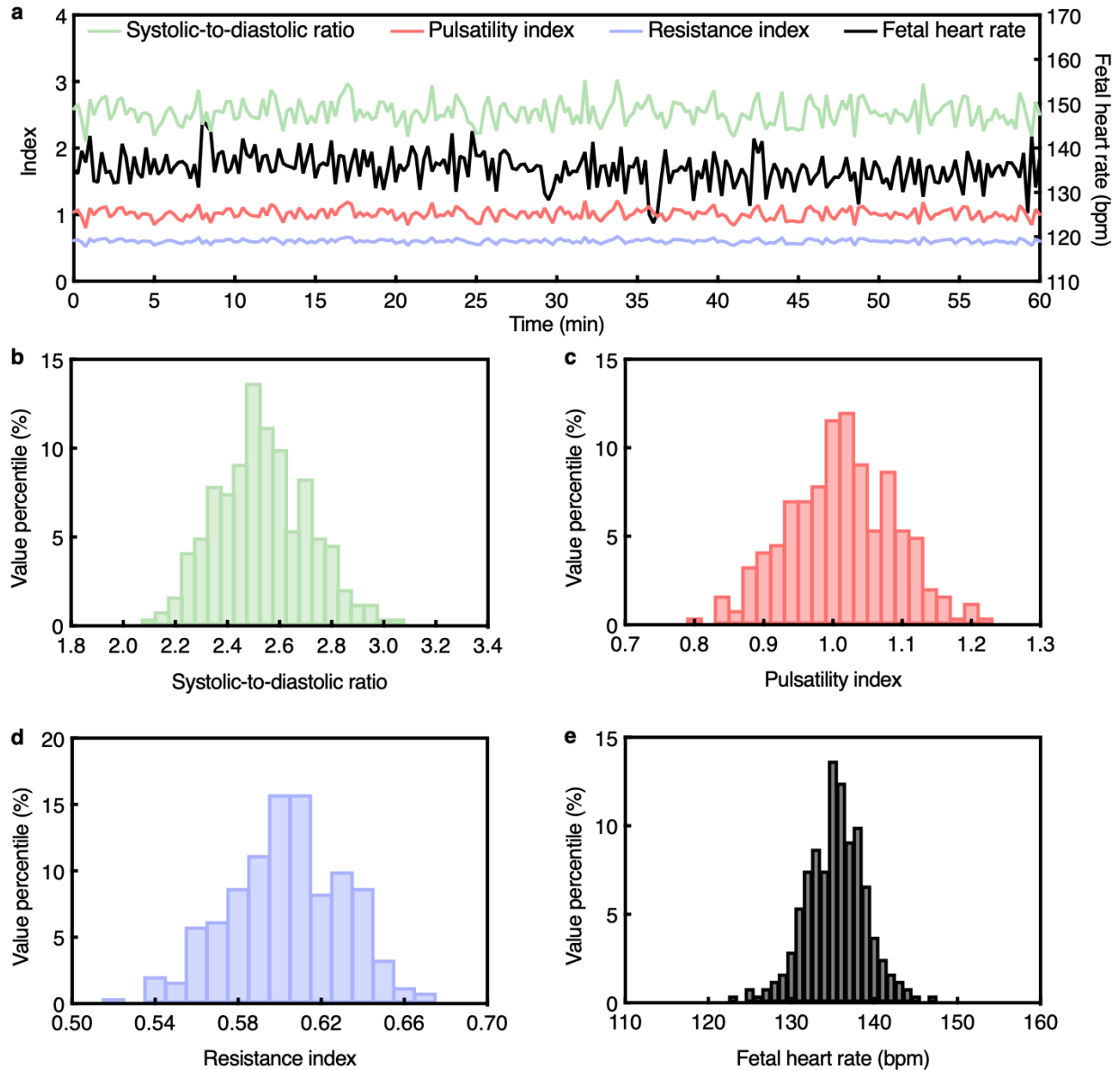
1659
 1660
 1661
 1662
 1663
 1664

Supplementary Fig. 53 | Continuous fetal monitoring using the UPatch in Participant #18. **a**, Time series data from the 1-h continuous monitoring session. Systolic-to-diastolic ratio, pulsatility index, and resistance index are plotted on the left y-axis, and fetal heart rate is plotted on the right y-axis. Histograms of **b**, systolic-to-diastolic ratio, **c**, pulsatility index, **d**, resistance index, and **e**, fetal heart rate over the recording period.



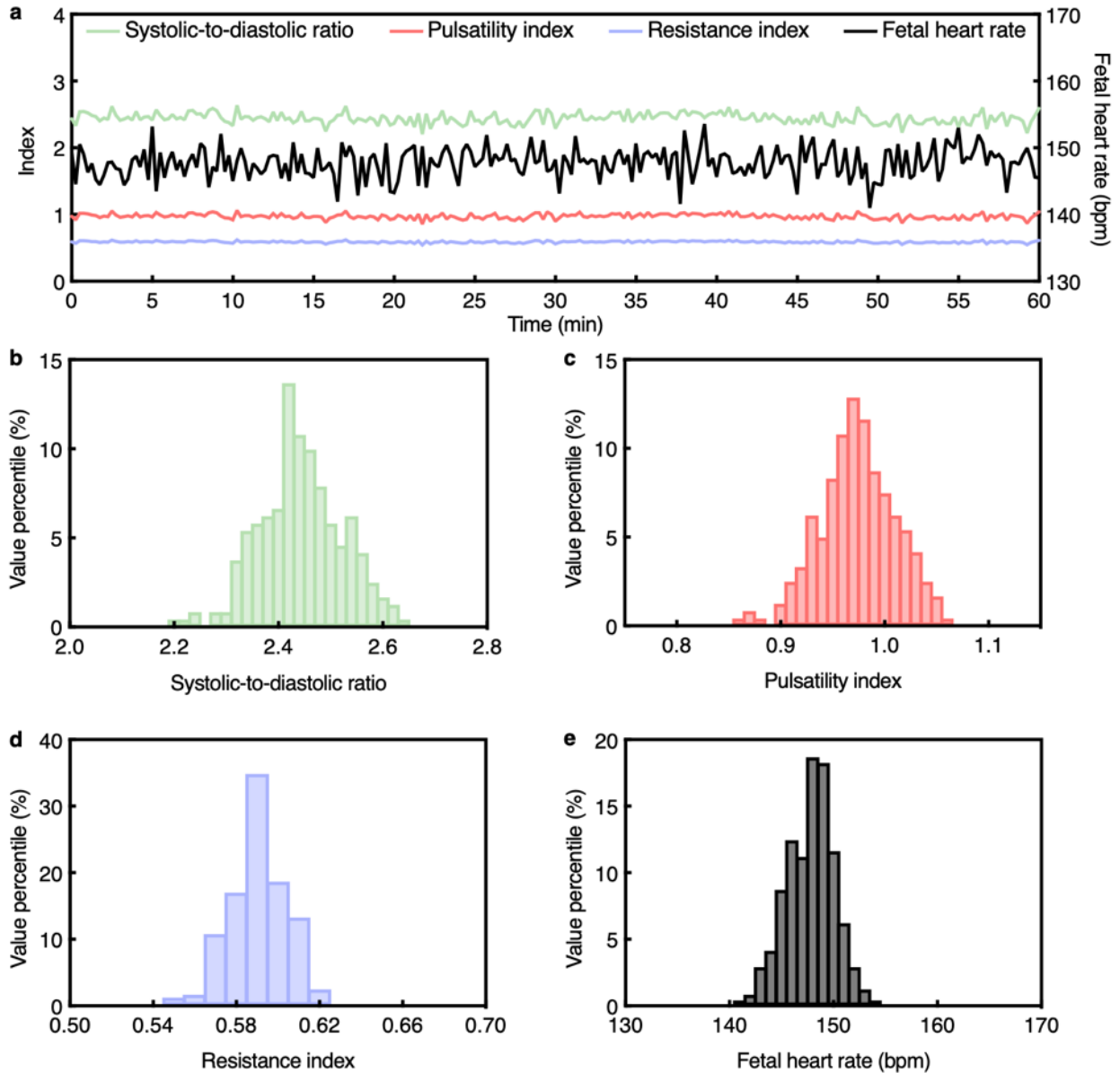
1665
 1666
 1667
 1668
 1669
 1670

Supplementary Fig. 54 | Continuous fetal monitoring using the UPatch in Participant #19. **a**, Time series data from the 1-h continuous monitoring session. Systolic-to-diastolic ratio, pulsatility index, and resistance index are plotted on the left y-axis, and fetal heart rate is plotted on the right y-axis. Histograms of **b**, systolic-to-diastolic ratio, **c**, pulsatility index, **d**, resistance index, and **e**, fetal heart rate over the recording period.



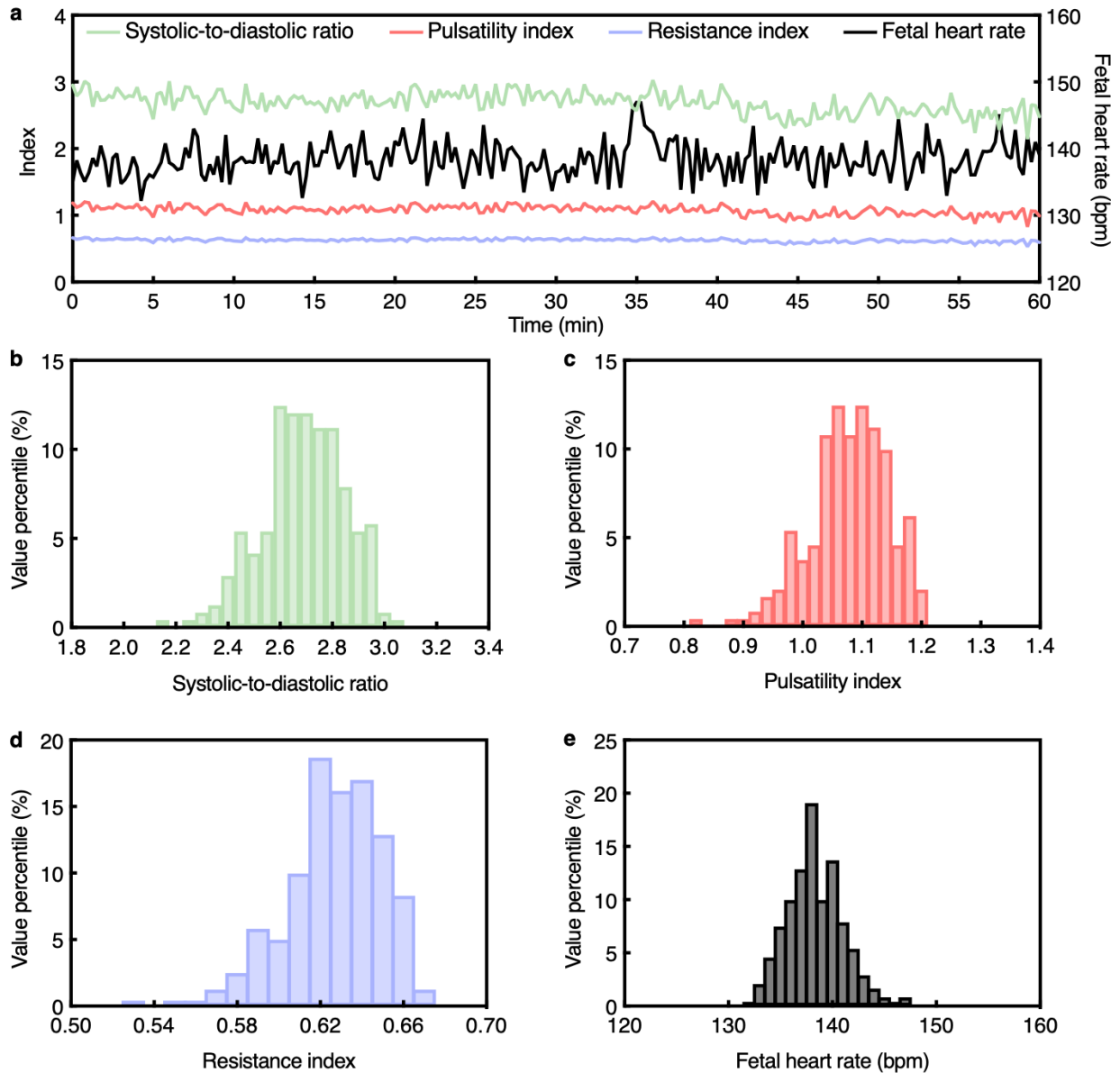
1671
 1672
 1673
 1674
 1675
 1676

Supplementary Fig. 55 | Continuous fetal monitoring using the UPatch in Participant #20. a, Time series data from the 1-h continuous monitoring session. Systolic-to-diastolic ratio, pulsatility index, and resistance index are plotted on the left y-axis, and fetal heart rate is plotted on the right y-axis. Histograms of b, systolic-to-diastolic ratio, c, pulsatility index, d, resistance index, and e, fetal heart rate over the recording period.



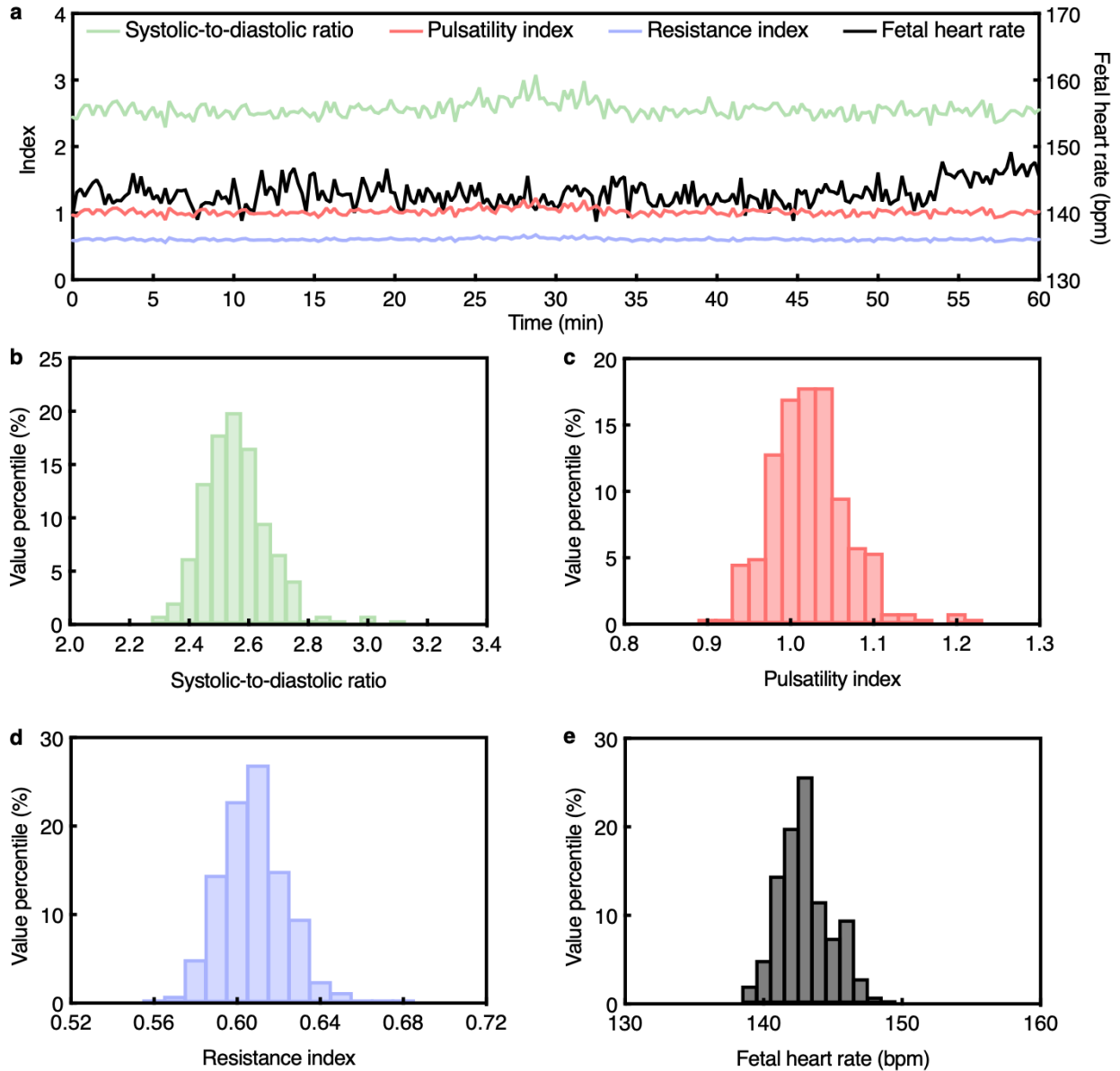
1677
 1678
 1679
 1680
 1681
 1682

Supplementary Fig. 56 | Continuous fetal monitoring using the UPatch in Participant #21. a, Time series data from the 1-h continuous monitoring session. Systolic-to-diastolic ratio, pulsatility index, and resistance index are plotted on the left y-axis, and fetal heart rate is plotted on the right y-axis. Histograms of b, systolic-to-diastolic ratio, c, pulsatility index, d, resistance index, and e, fetal heart rate over the recording period.



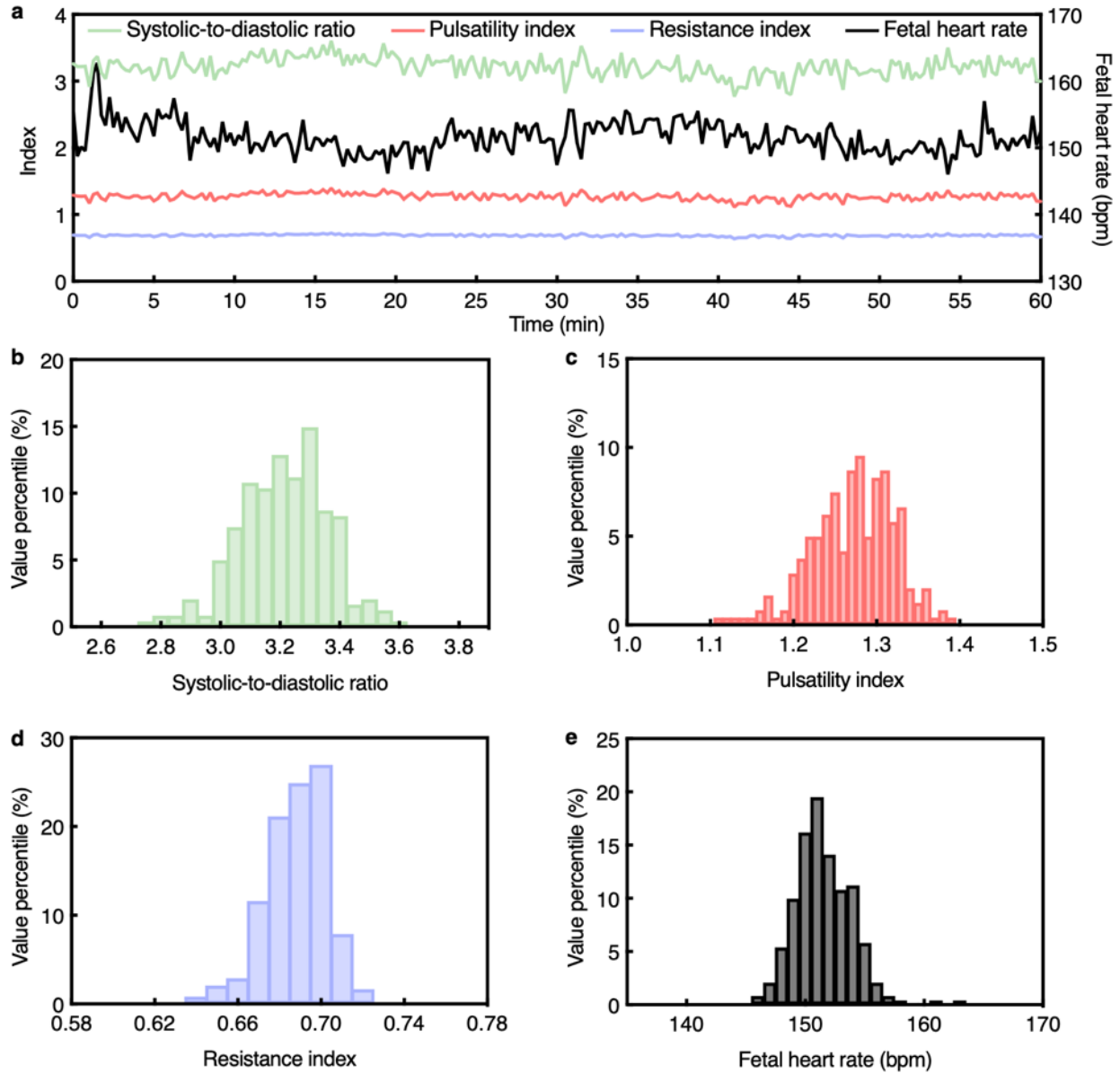
1683
 1684
 1685
 1686
 1687
 1688

Supplementary Fig. 57 | Continuous fetal monitoring using the UPatch in Participant #22. **a**, Time series data from the 1-h continuous monitoring session. Systolic-to-diastolic ratio, pulsatility index, and resistance index are plotted on the left y-axis, and fetal heart rate is plotted on the right y-axis. Histograms of **b**, systolic-to-diastolic ratio, **c**, pulsatility index, **d**, resistance index, and **e**, fetal heart rate over the recording period.



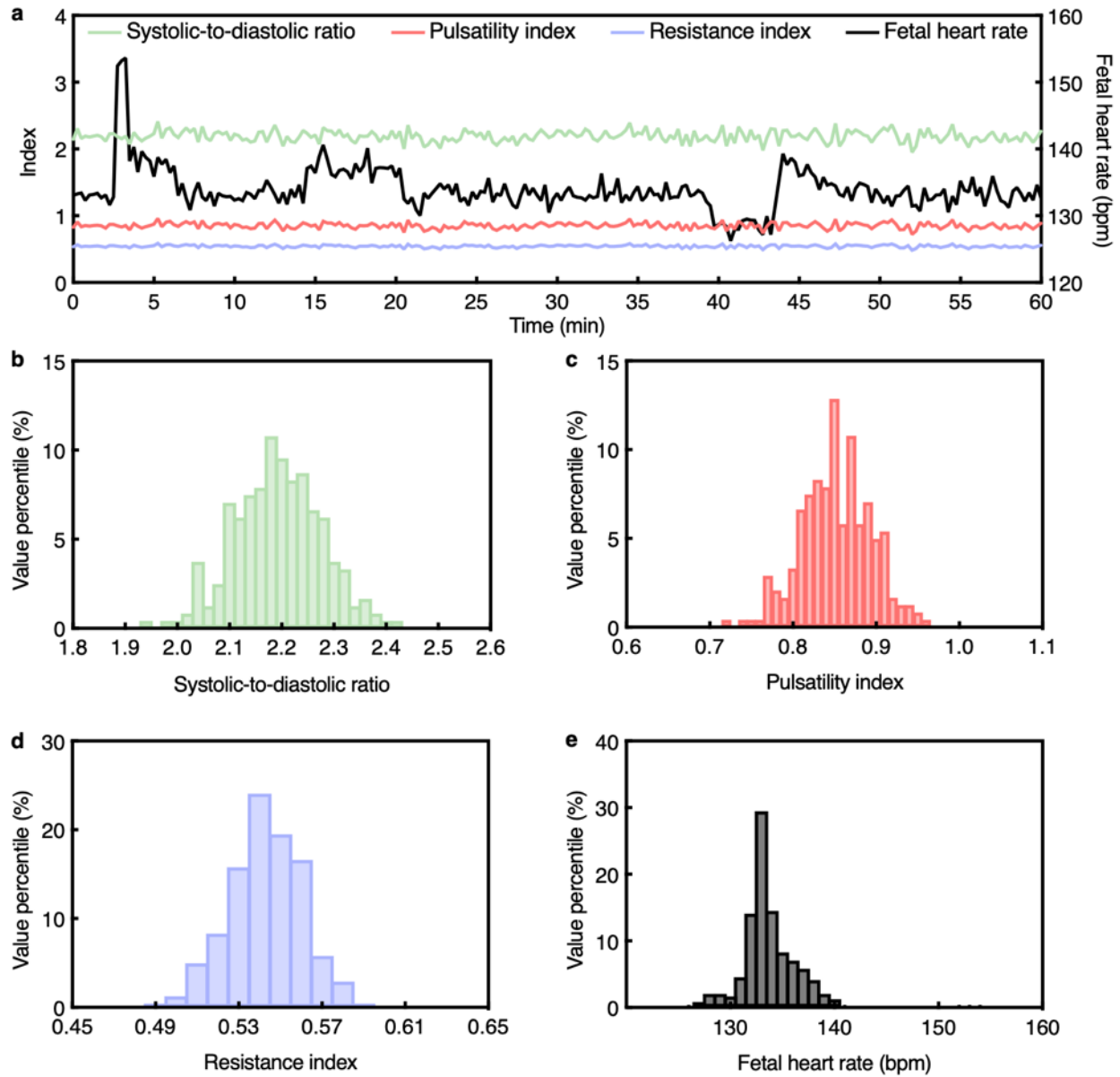
1689
 1690
 1691
 1692
 1693
 1694

Supplementary Fig. 58 | Continuous fetal monitoring using the UPatch in Participant #23. **a**, Time series data from the 1-h continuous monitoring session. Systolic-to-diastolic ratio, pulsatility index, and resistance index are plotted on the left y-axis, and fetal heart rate is plotted on the right y-axis. Histograms of **b**, systolic-to-diastolic ratio, **c**, pulsatility index, **d**, resistance index, and **e**, fetal heart rate over the recording period.

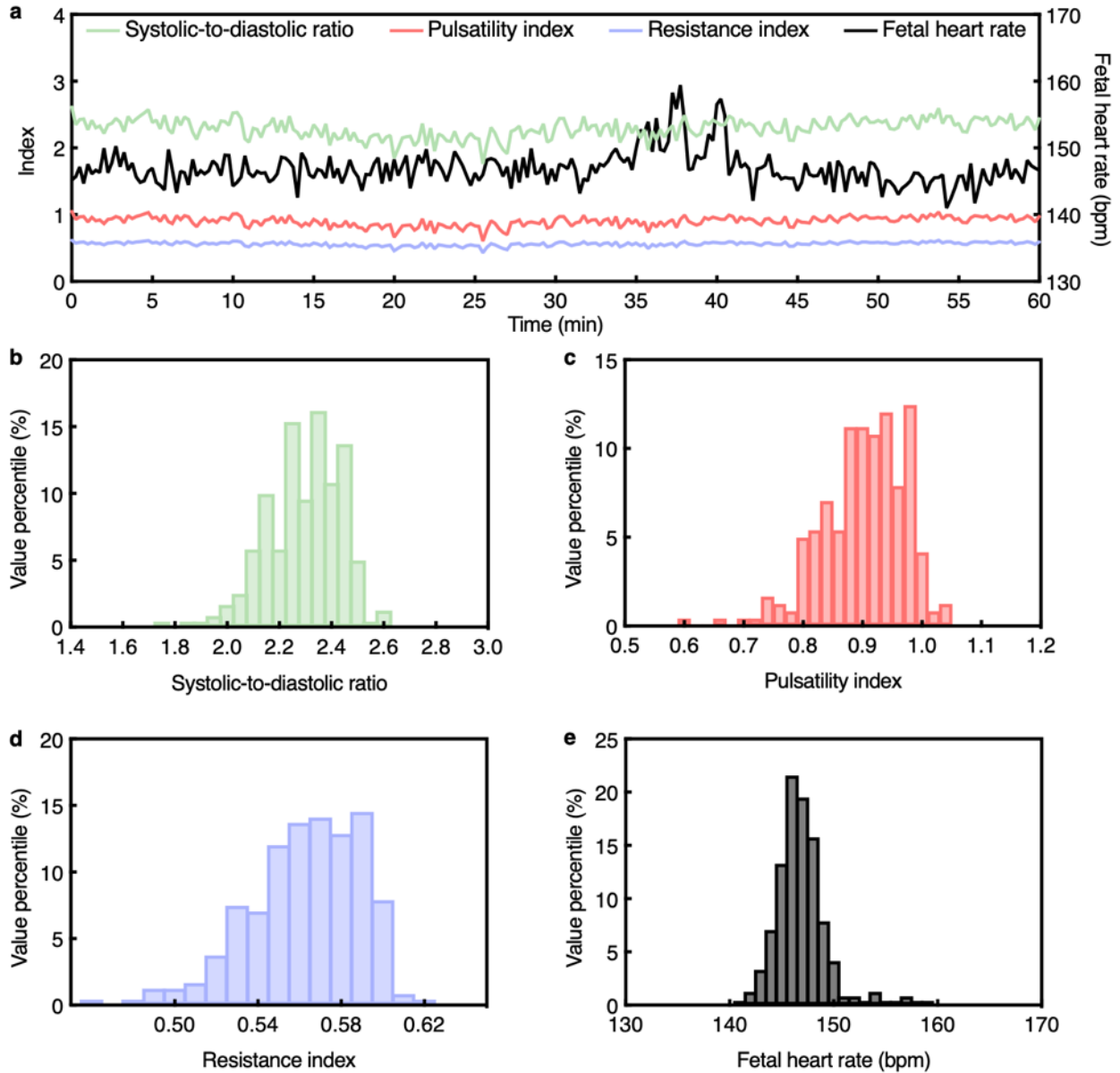


1695
 1696
 1697
 1698
 1699
 1700

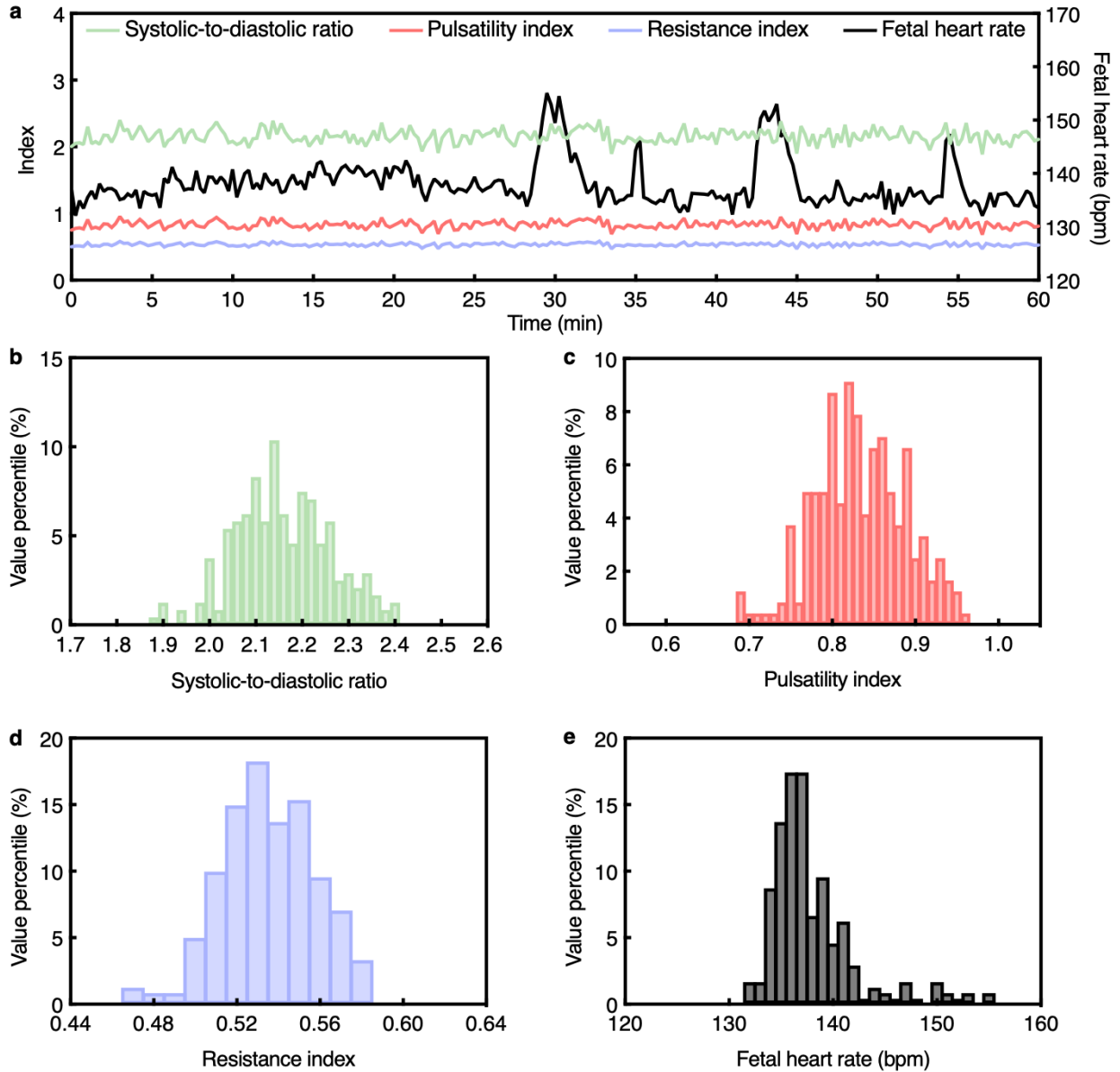
Supplementary Fig. 59 | Continuous fetal monitoring using the UPatch in Participant #24. **a**, Time series data from the 1-h continuous monitoring session. Systolic-to-diastolic ratio, pulsatility index, and resistance index are plotted on the left y-axis, and fetal heart rate is plotted on the right y-axis. Histograms of **b**, systolic-to-diastolic ratio, **c**, pulsatility index, **d**, resistance index, and **e**, fetal heart rate over the recording period.



1701
 1702 **Supplementary Fig. 60 | Continuous fetal monitoring using the UPatch in Participant #25. a,**
 1703 Time series data from the 1-h continuous monitoring session. Systolic-to-diastolic ratio, pulsatility
 1704 index, and resistance index are plotted on the left y-axis, and fetal heart rate is plotted on the right
 1705 y-axis. Histograms of **b**, systolic-to-diastolic ratio, **c**, pulsatility index, **d**, resistance index, and **e**,
 1706 fetal heart rate over the recording period.

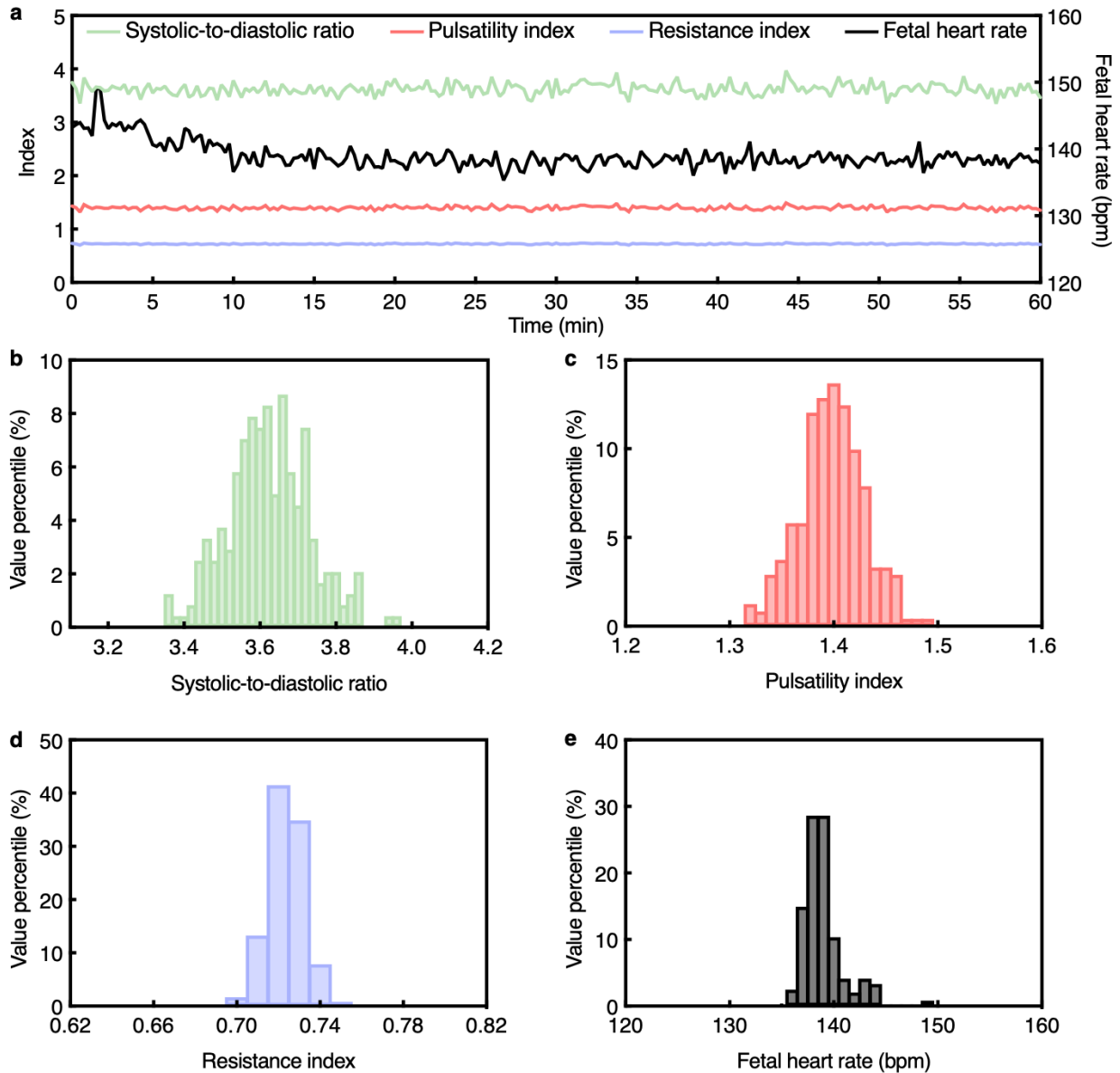


1707
 1708 **Supplementary Fig. 61 | Continuous fetal monitoring using the UPatch in Participant #26.** a,
 1709 Time series data from the 1-h continuous monitoring session. Systolic-to-diastolic ratio, pulsatility
 1710 index, and resistance index are plotted on the left y-axis, and fetal heart rate is plotted on the right
 1711 y-axis. Histograms of b, systolic-to-diastolic ratio, c, pulsatility index, d, resistance index, and e,
 1712 fetal heart rate over the recording period.



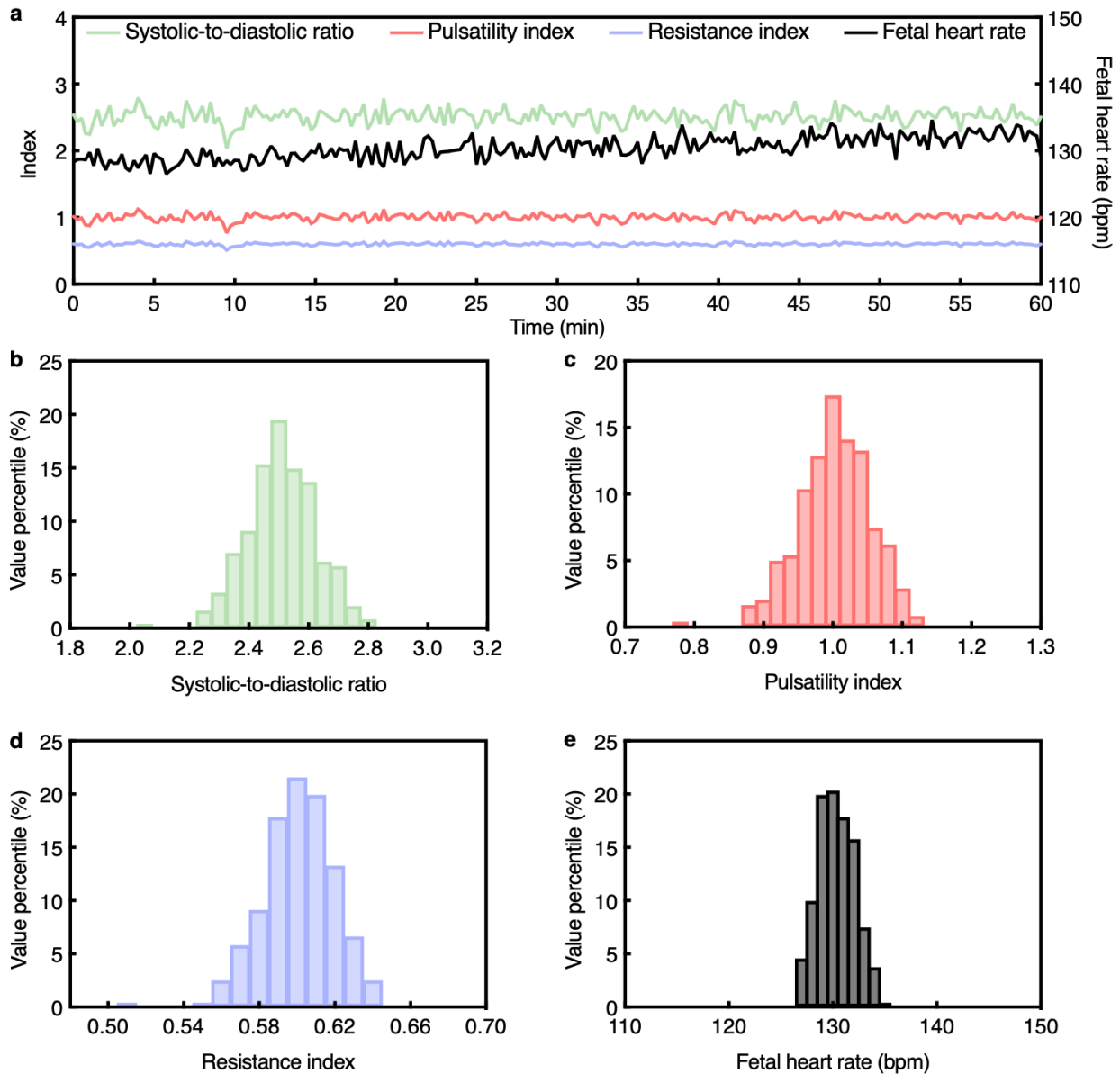
1713
 1714
 1715
 1716
 1717
 1718

Supplementary Fig. 62 | Continuous fetal monitoring using the UPatch in Participant #27. **a**, Time series data from the 1-h continuous monitoring session. Systolic-to-diastolic ratio, pulsatility index, and resistance index are plotted on the left y-axis, and fetal heart rate is plotted on the right y-axis. Histograms of **b**, systolic-to-diastolic ratio, **c**, pulsatility index, **d**, resistance index, and **e**, fetal heart rate over the recording period.



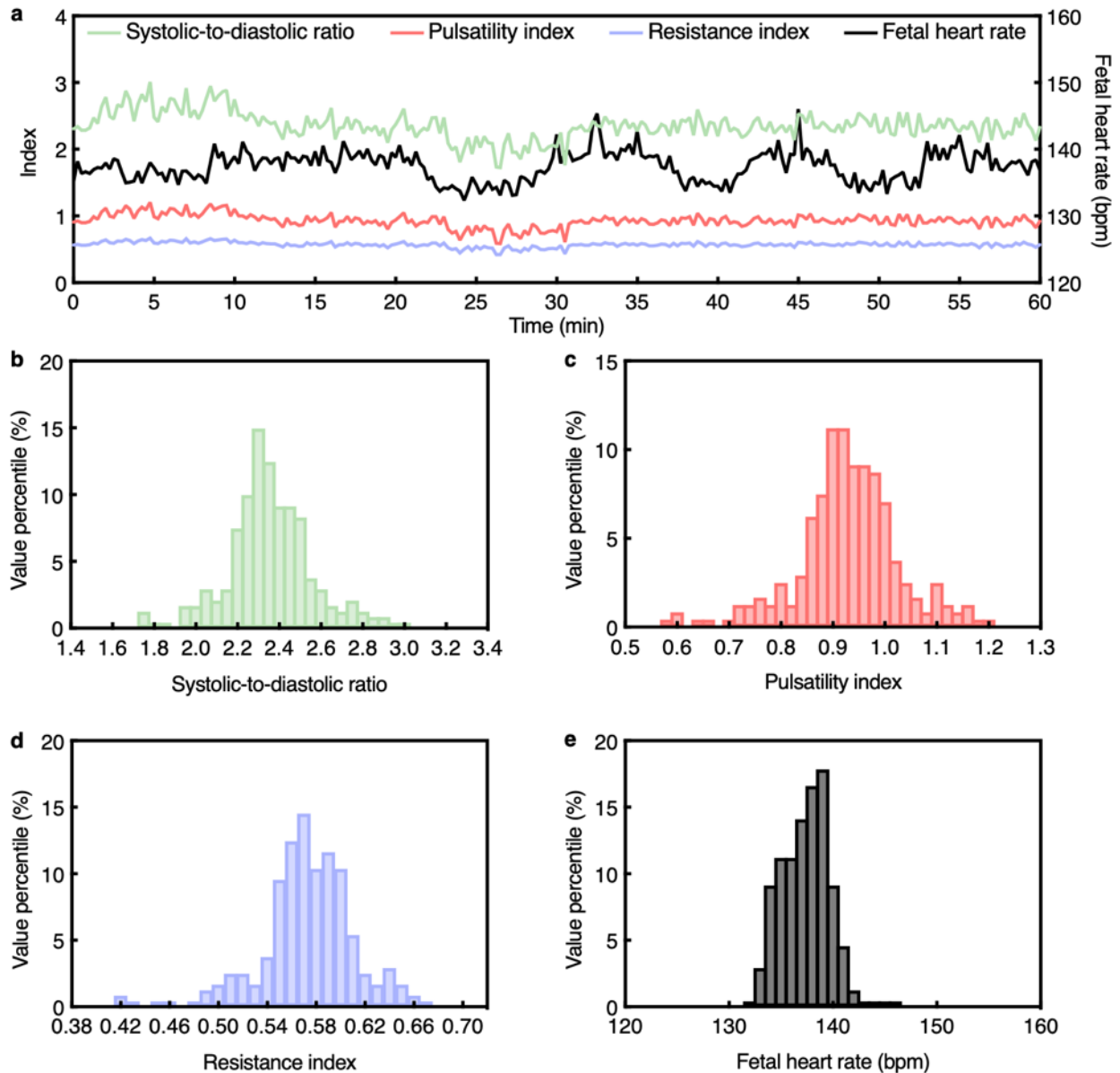
1719
 1720
 1721
 1722
 1723
 1724

Supplementary Fig. 63 | Continuous fetal monitoring using the UPatch in Participant #28. **a**, Time series data from the 1-h continuous monitoring session. Systolic-to-diastolic ratio, pulsatility index, and resistance index are plotted on the left y-axis, and fetal heart rate is plotted on the right y-axis. Histograms of **b**, systolic-to-diastolic ratio, **c**, pulsatility index, **d**, resistance index, and **e**, fetal heart rate over the recording period.



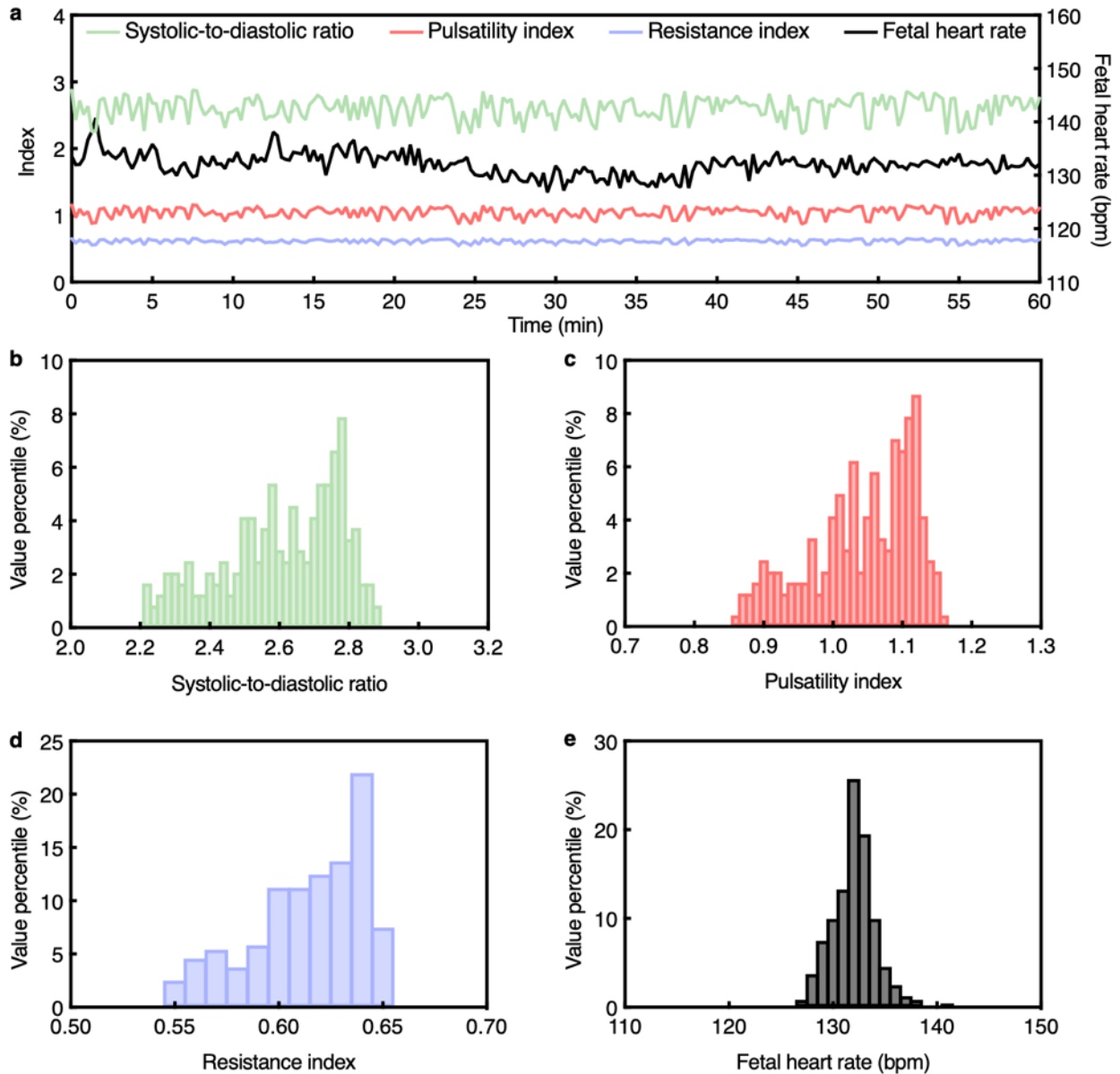
1725
 1726
 1727
 1728
 1729
 1730

Supplementary Fig. 64 | Continuous fetal monitoring using the UPatch in Participant #29. **a**, Time series data from the 1-h continuous monitoring session. Systolic-to-diastolic ratio, pulsatility index, and resistance index are plotted on the left y-axis, and fetal heart rate is plotted on the right y-axis. Histograms of **b**, systolic-to-diastolic ratio, **c**, pulsatility index, **d**, resistance index, and **e**, fetal heart rate over the recording period.



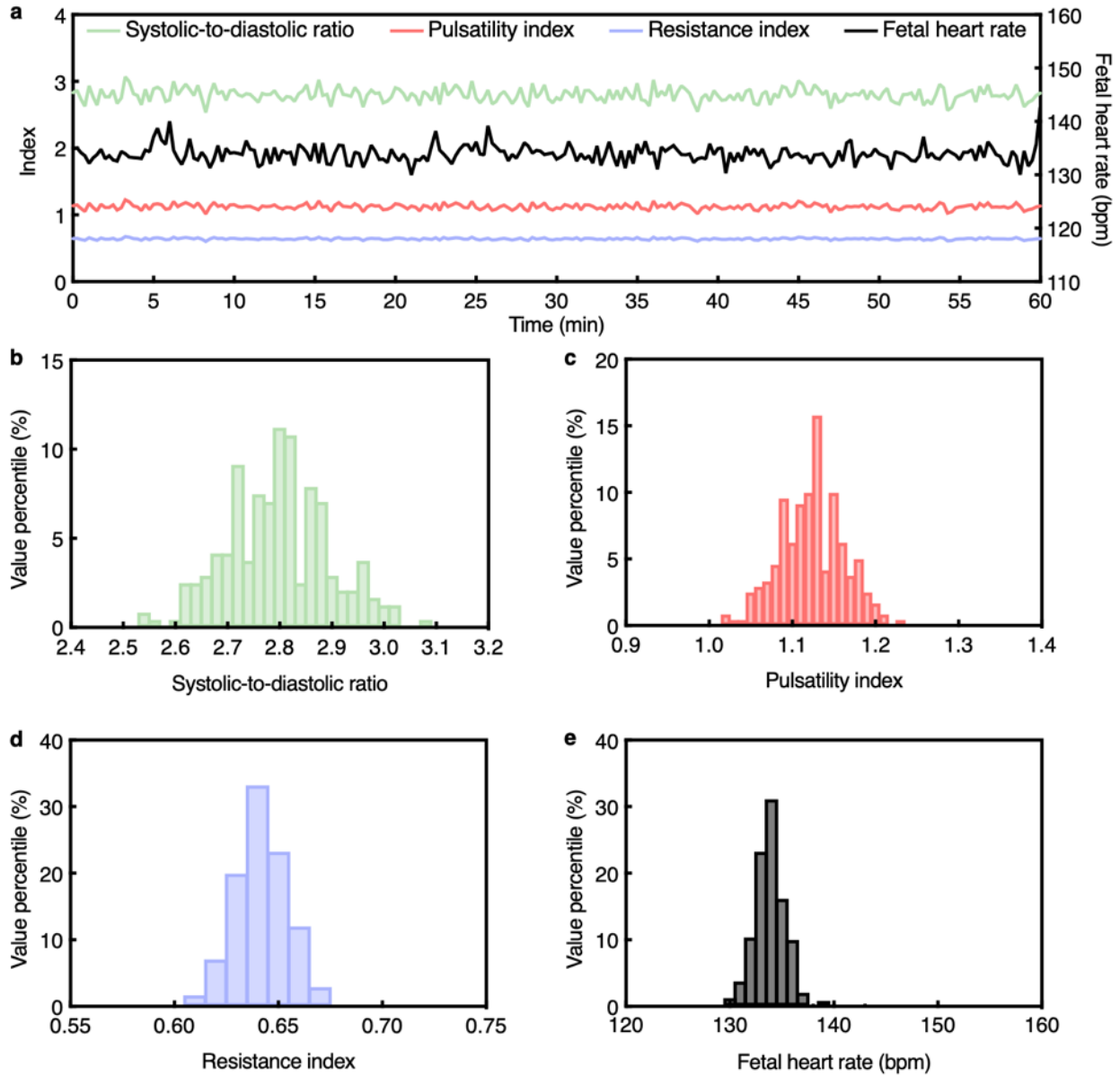
1731
 1732
 1733
 1734
 1735
 1736

Supplementary Fig. 65 | Continuous fetal monitoring using the UPatch in Participant #30. **a**, Time series data from the 1-h continuous monitoring session. Systolic-to-diastolic ratio, pulsatility index, and resistance index are plotted on the left y-axis, and fetal heart rate is plotted on the right y-axis. Histograms of **b**, systolic-to-diastolic ratio, **c**, pulsatility index, **d**, resistance index, and **e**, fetal heart rate over the recording period.



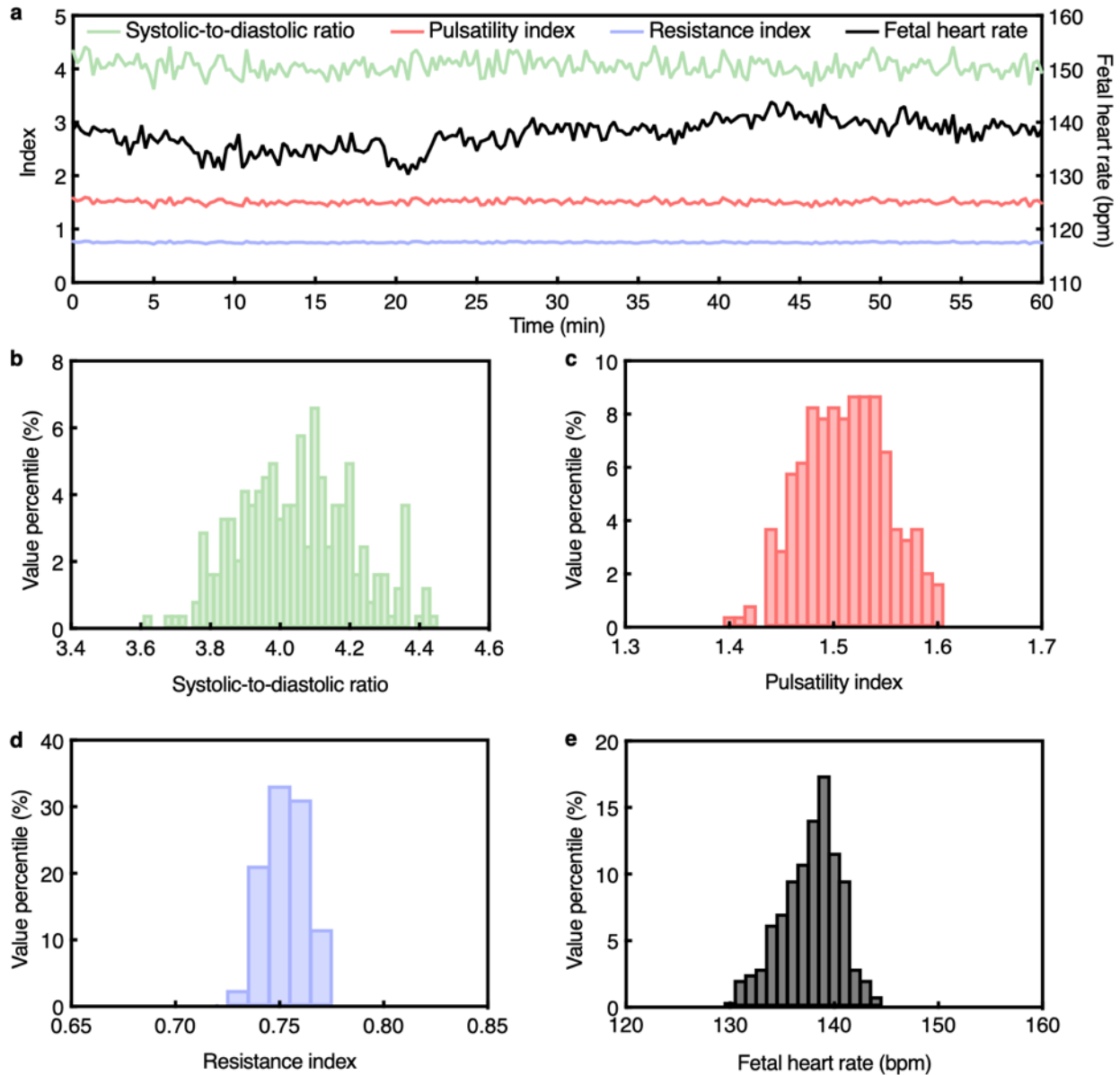
1737
 1738
 1739
 1740
 1741
 1742

Supplementary Fig. 66 | Continuous fetal monitoring using the UPatch in Participant #31. a, Time series data from the 1-h continuous monitoring session. Systolic-to-diastolic ratio, pulsatility index, and resistance index are plotted on the left y-axis, and fetal heart rate is plotted on the right y-axis. Histograms of b, systolic-to-diastolic ratio, c, pulsatility index, d, resistance index, and e, fetal heart rate over the recording period.



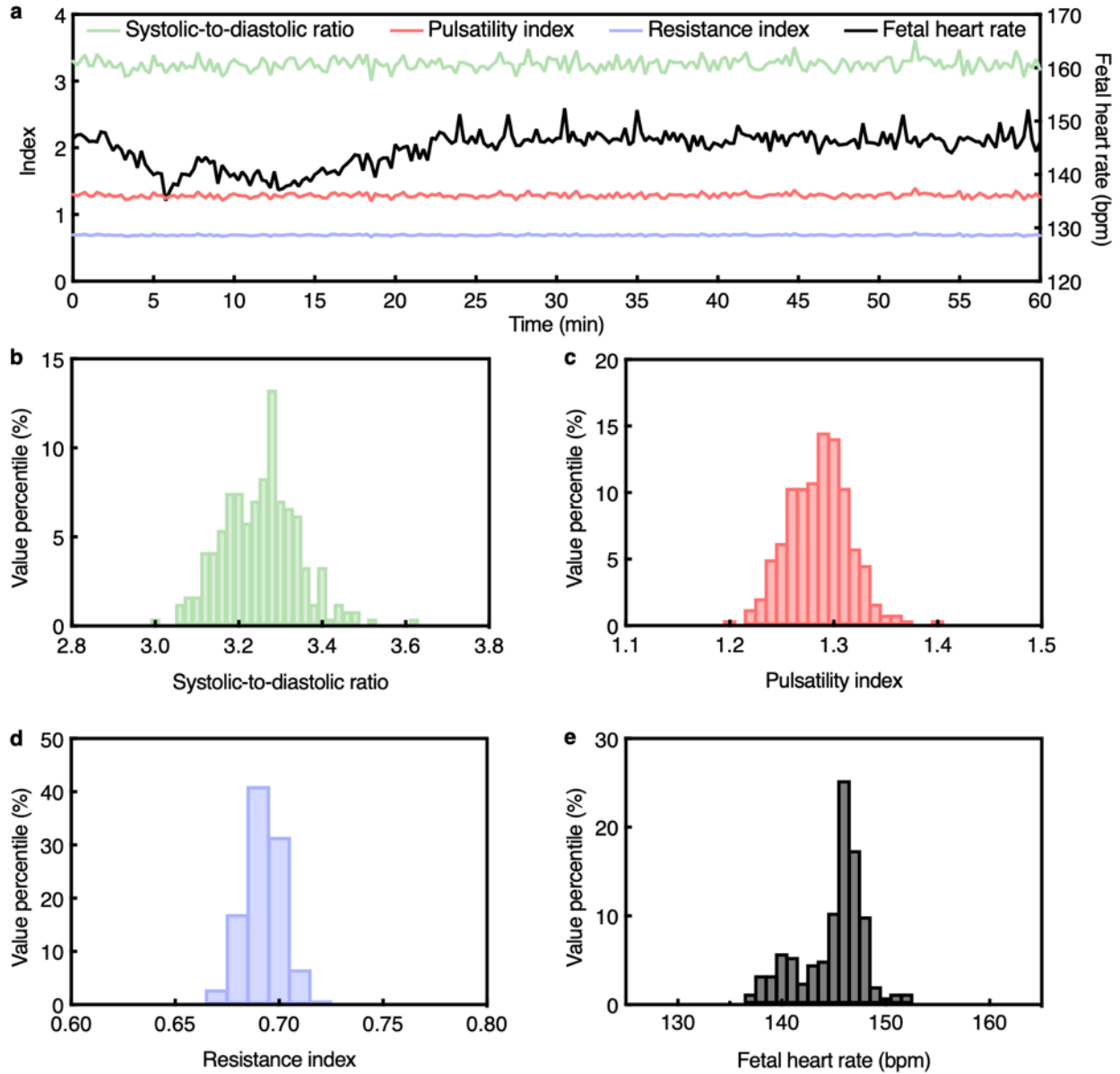
1743
 1744
 1745
 1746
 1747
 1748

Supplementary Fig. 67 | Continuous fetal monitoring using the UPatch in Participant #32. **a**, Time series data from the 1-h continuous monitoring session. Systolic-to-diastolic ratio, pulsatility index, and resistance index are plotted on the left y-axis, and fetal heart rate is plotted on the right y-axis. Histograms of **b**, systolic-to-diastolic ratio, **c**, pulsatility index, **d**, resistance index, and **e**, fetal heart rate over the recording period.



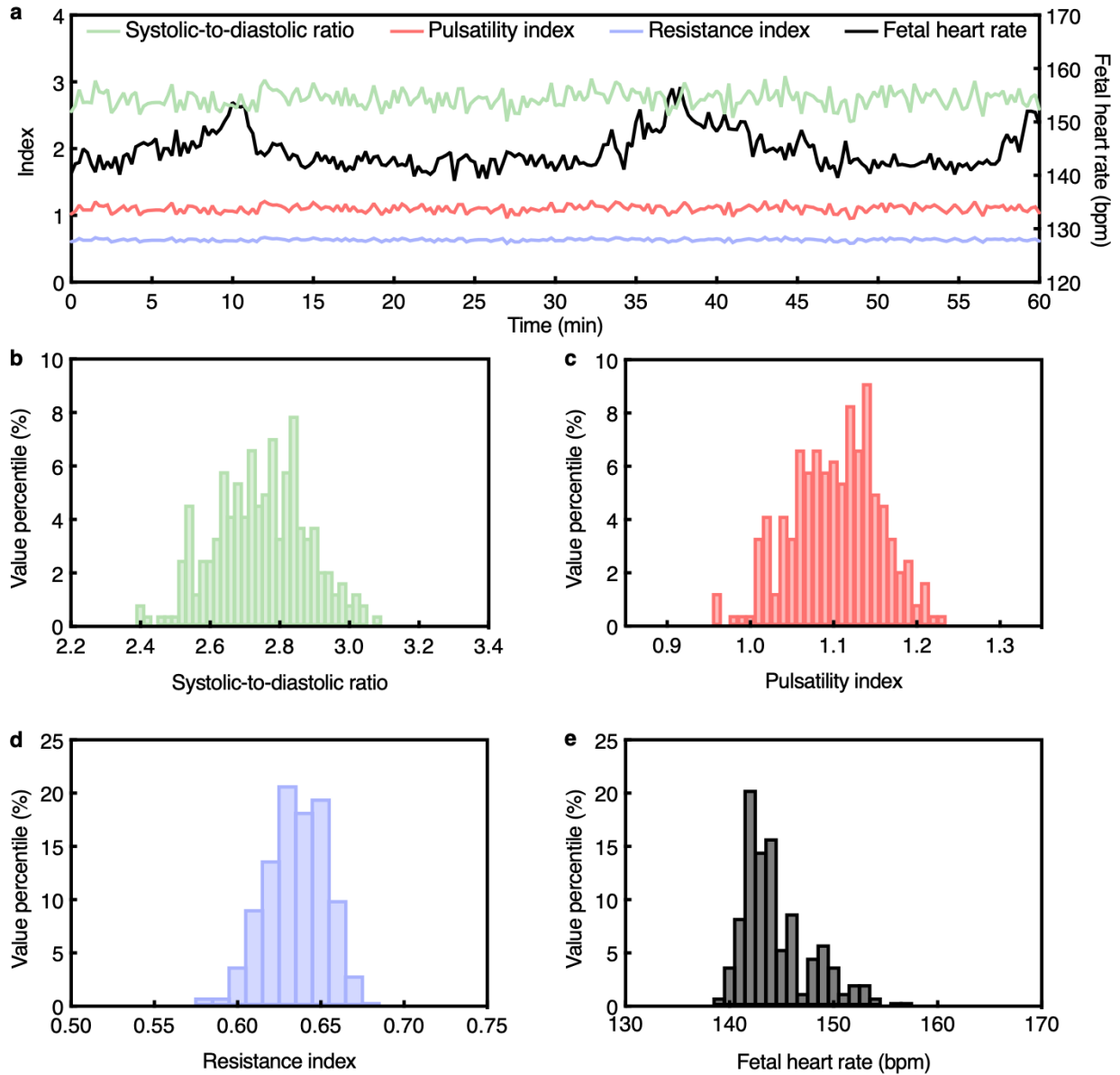
1749
 1750
 1751
 1752
 1753
 1754

Supplementary Fig. 68 | Continuous fetal monitoring using the UPatch in Participant #33. **a**, Time series data from the 1-h continuous monitoring session. Systolic-to-diastolic ratio, pulsatility index, and resistance index are plotted on the left y-axis, and fetal heart rate is plotted on the right y-axis. Histograms of **b**, systolic-to-diastolic ratio, **c**, pulsatility index, **d**, resistance index, and **e**, fetal heart rate over the recording period.



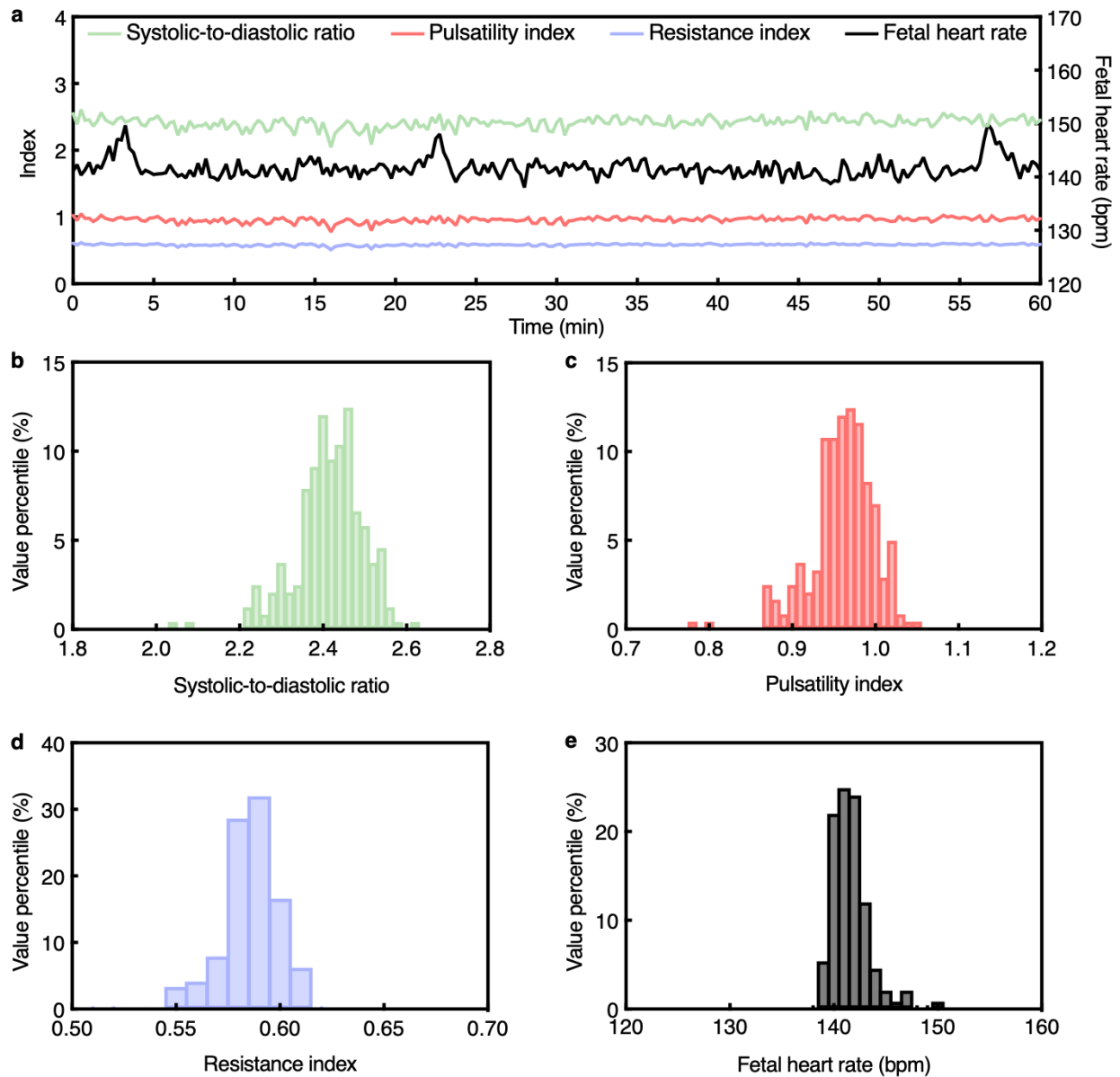
1755
 1756
 1757
 1758
 1759
 1760

Supplementary Fig. 69 | Continuous fetal monitoring using the UPatch in Participant #34. a, Time series data from the 1-h continuous monitoring session. Systolic-to-diastolic ratio, pulsatility index, and resistance index are plotted on the left y-axis, and fetal heart rate is plotted on the right y-axis. Histograms of b, systolic-to-diastolic ratio, c, pulsatility index, d, resistance index, and e, fetal heart rate over the recording period.



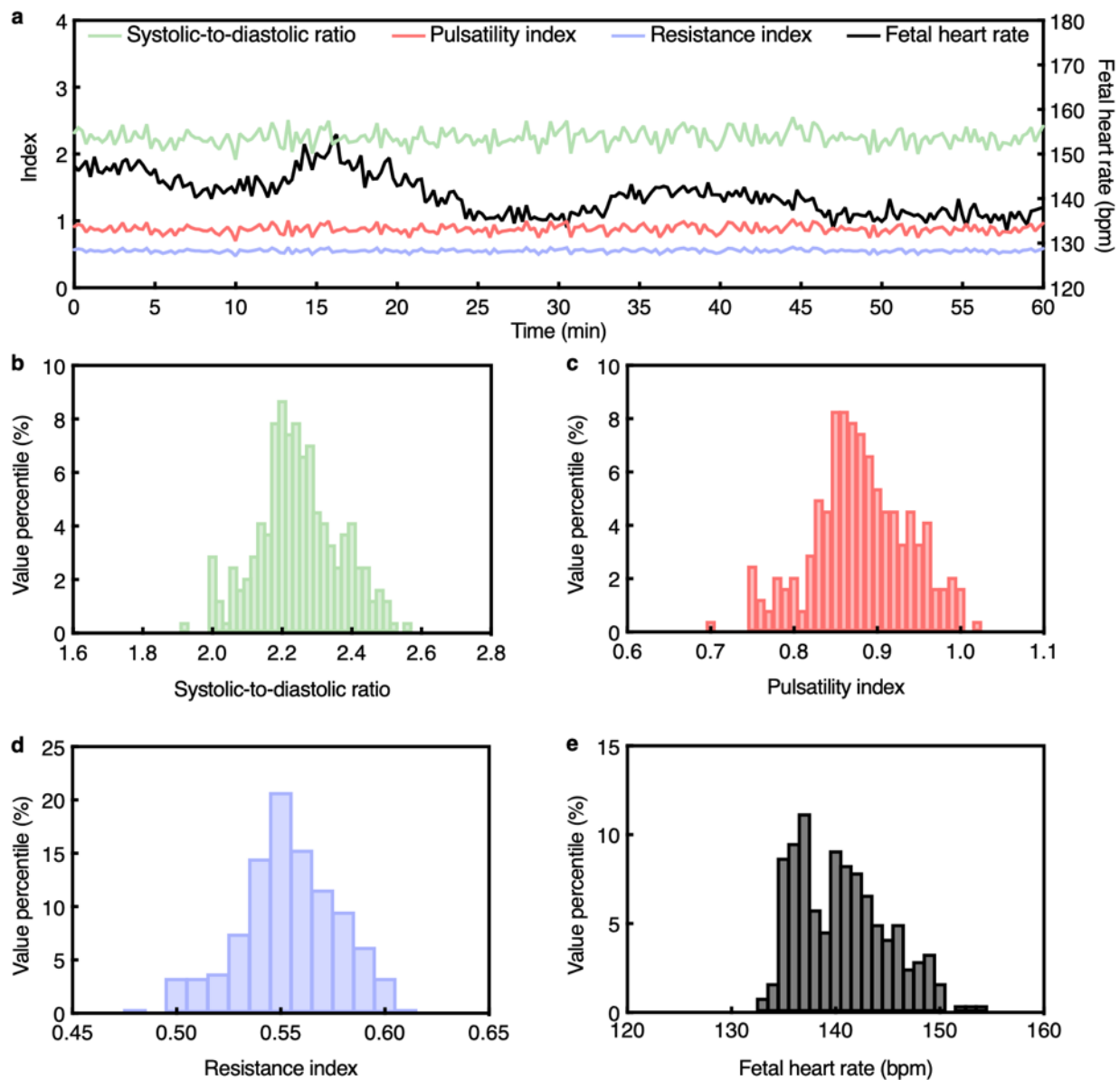
1761
 1762
 1763
 1764
 1765
 1766

Supplementary Fig. 70 | Continuous fetal monitoring using the UPatch in Participant #35. **a**, Time series data from the 1-h continuous monitoring session. Systolic-to-diastolic ratio, pulsatility index, and resistance index are plotted on the left y-axis, and fetal heart rate is plotted on the right y-axis. Histograms of **b**, systolic-to-diastolic ratio, **c**, pulsatility index, **d**, resistance index, and **e**, fetal heart rate over the recording period.



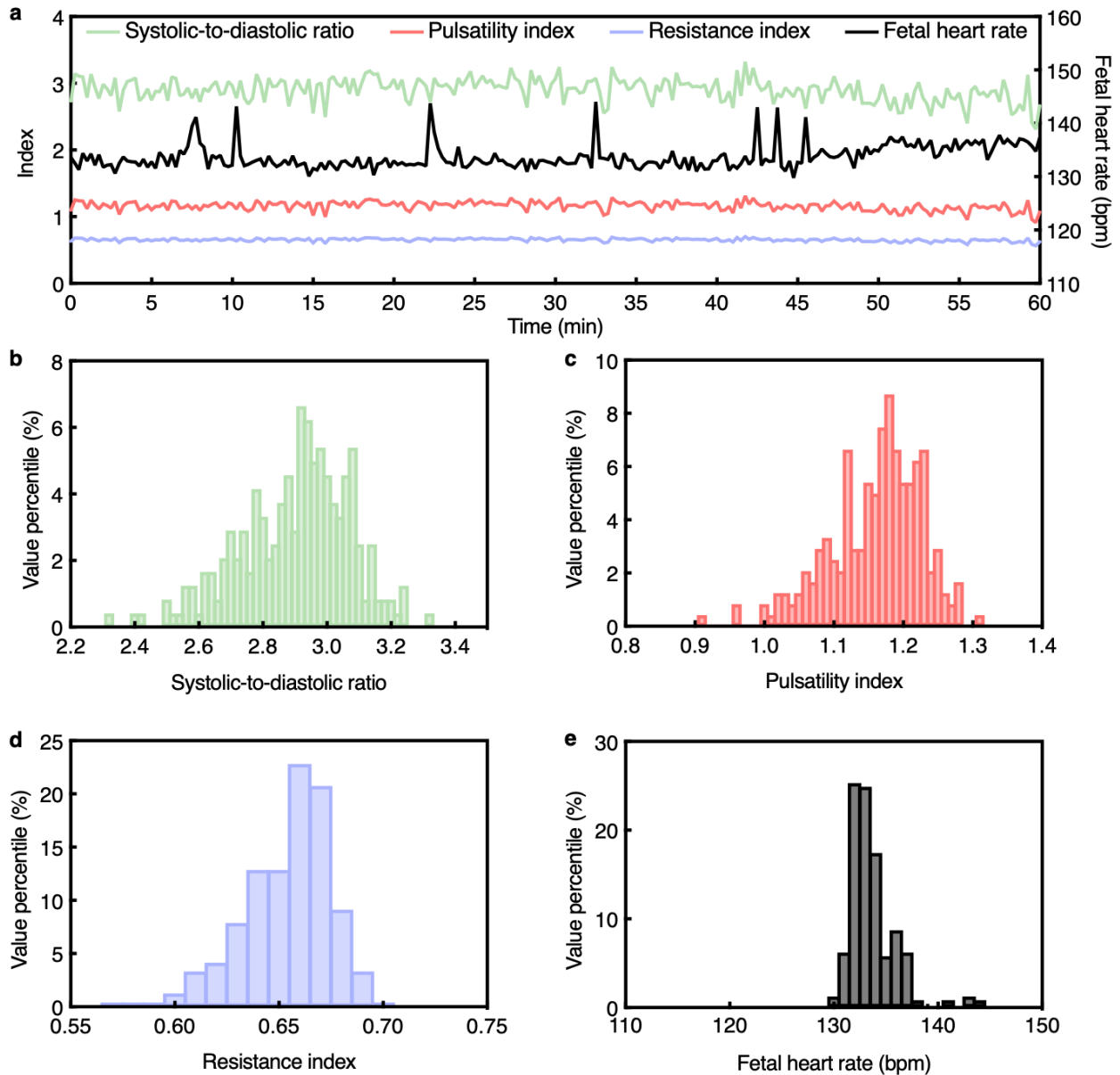
1767
 1768
 1769
 1770
 1771
 1772

Supplementary Fig. 71 | Continuous fetal monitoring using the UPatch in Participant #36. a, Time series data from the 1-h continuous monitoring session. Systolic-to-diastolic ratio, pulsatility index, and resistance index are plotted on the left y-axis, and fetal heart rate is plotted on the right y-axis. Histograms of b, systolic-to-diastolic ratio, c, pulsatility index, d, resistance index, and e, fetal heart rate over the recording period.



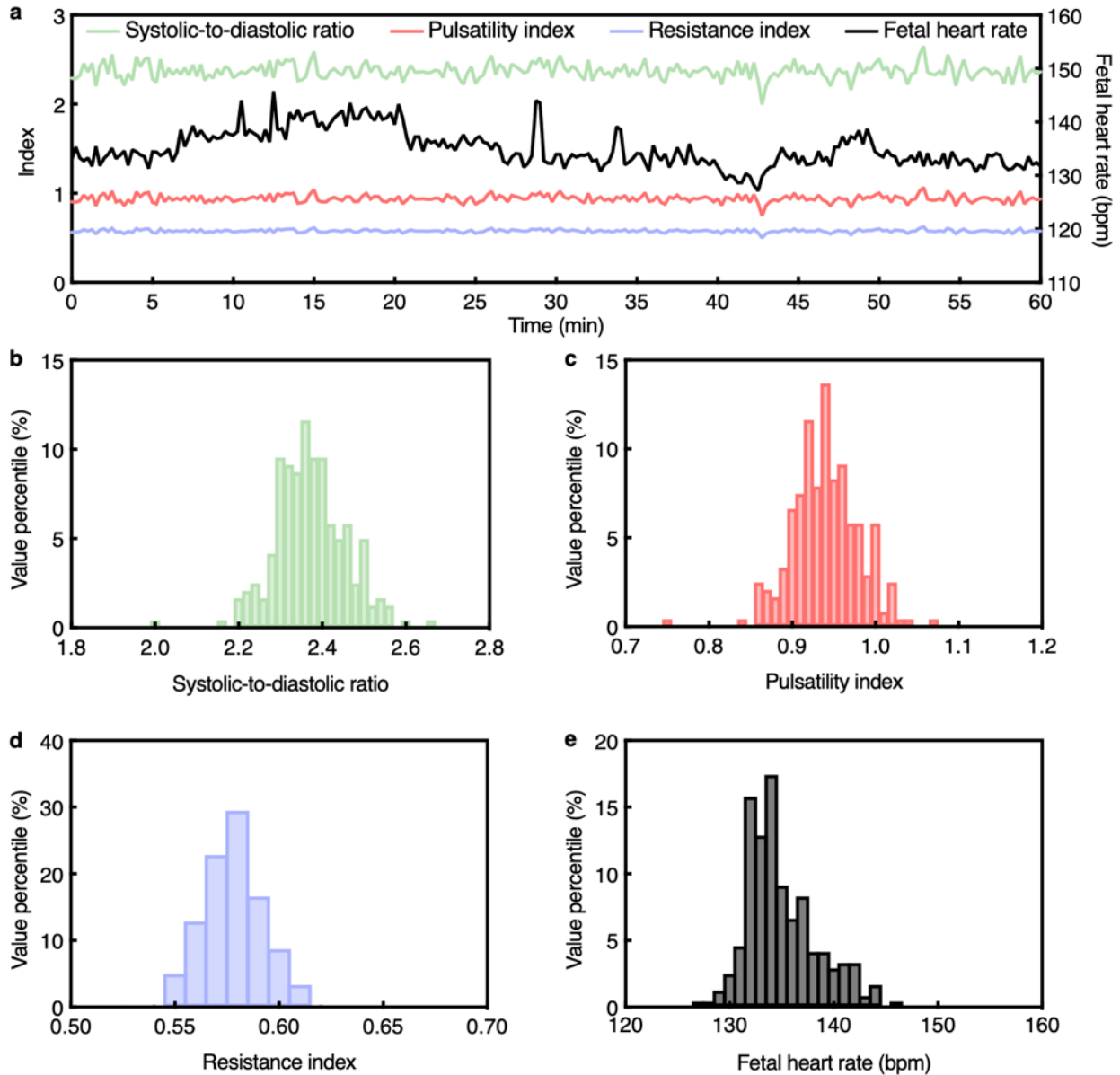
1773
 1774
 1775
 1776
 1777
 1778

Supplementary Fig. 72 | Continuous fetal monitoring using the UPatch in Participant #37. **a**, Time series data from the 1-h continuous monitoring session. Systolic-to-diastolic ratio, pulsatility index, and resistance index are plotted on the left y-axis, and fetal heart rate is plotted on the right y-axis. Histograms of **b**, systolic-to-diastolic ratio, **c**, pulsatility index, **d**, resistance index, and **e**, fetal heart rate over the recording period.



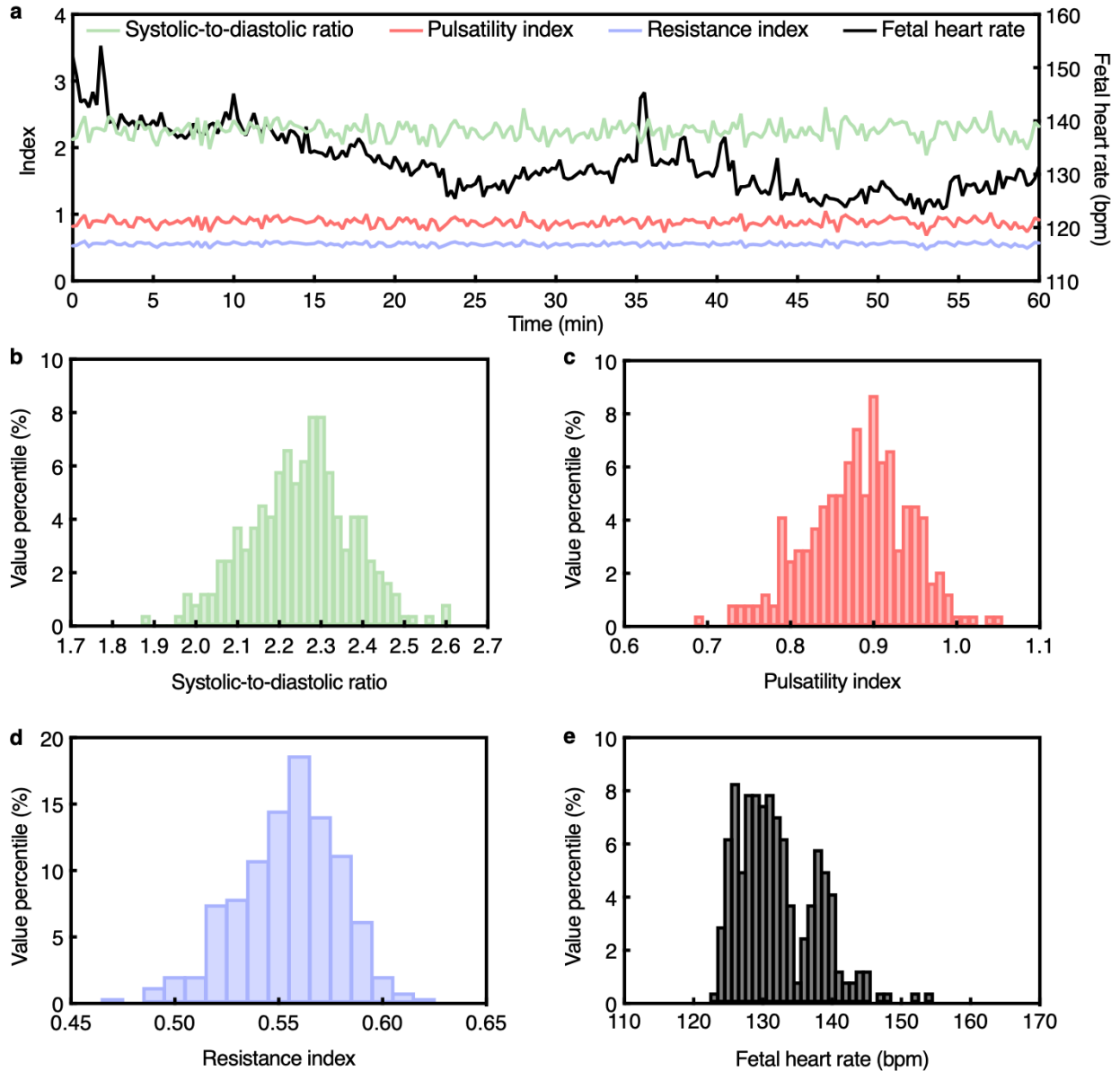
1779
 1780
 1781
 1782
 1783
 1784

Supplementary Fig. 73 | Continuous fetal monitoring using the UPatch in Participant #38. **a**, Time series data from the 1-h continuous monitoring session. Systolic-to-diastolic ratio, pulsatility index, and resistance index are plotted on the left y-axis, and fetal heart rate is plotted on the right y-axis. Histograms of **b**, systolic-to-diastolic ratio, **c**, pulsatility index, **d**, resistance index, and **e**, fetal heart rate over the recording period.



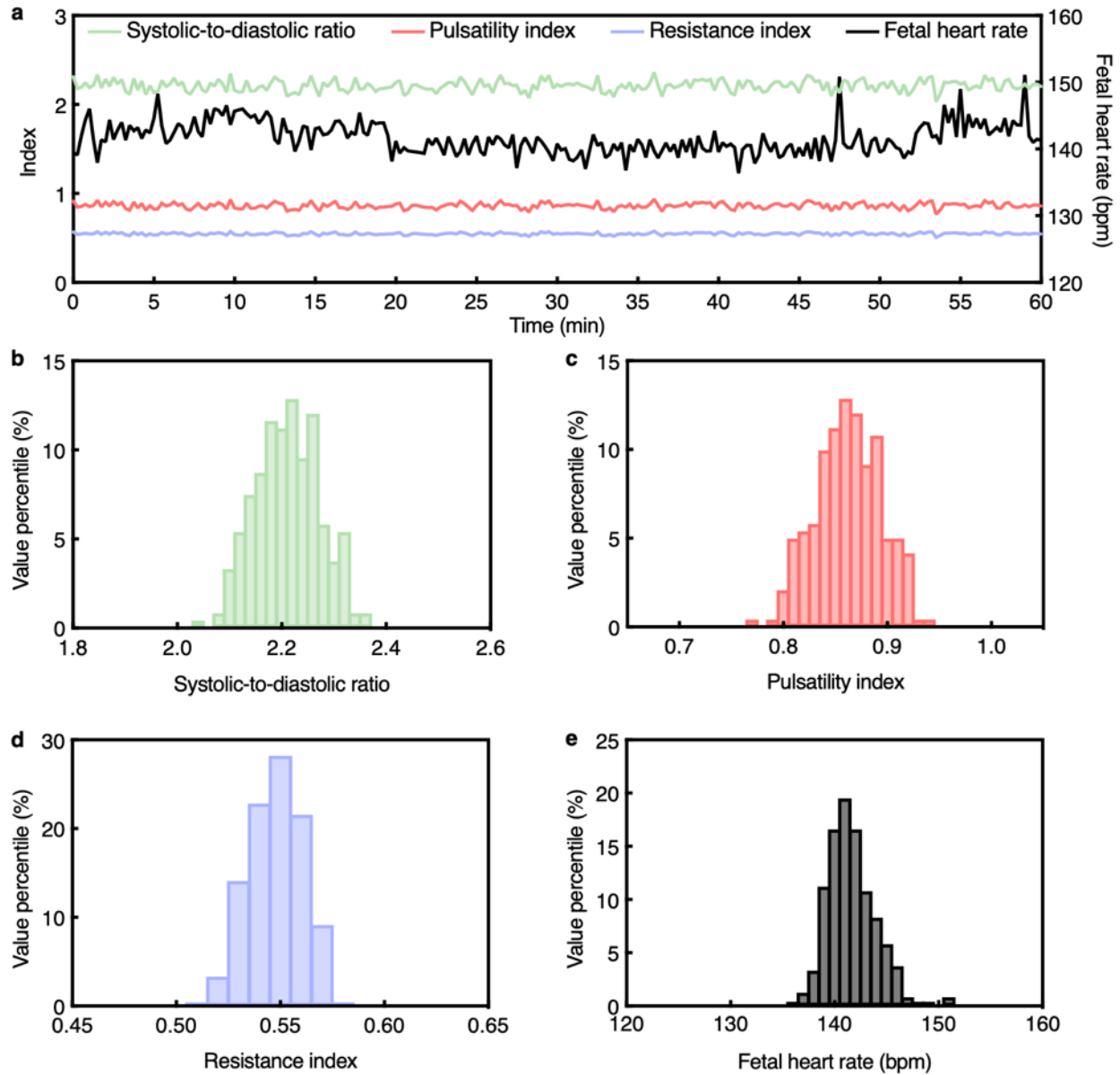
1785
 1786
 1787
 1788
 1789
 1790

Supplementary Fig. 74 | Continuous fetal monitoring using the UPatch in Participant #39. **a**, Time series data from the 1-h continuous monitoring session. Systolic-to-diastolic ratio, pulsatility index, and resistance index are plotted on the left y-axis, and fetal heart rate is plotted on the right y-axis. Histograms of **b**, systolic-to-diastolic ratio, **c**, pulsatility index, **d**, resistance index, and **e**, fetal heart rate over the recording period.



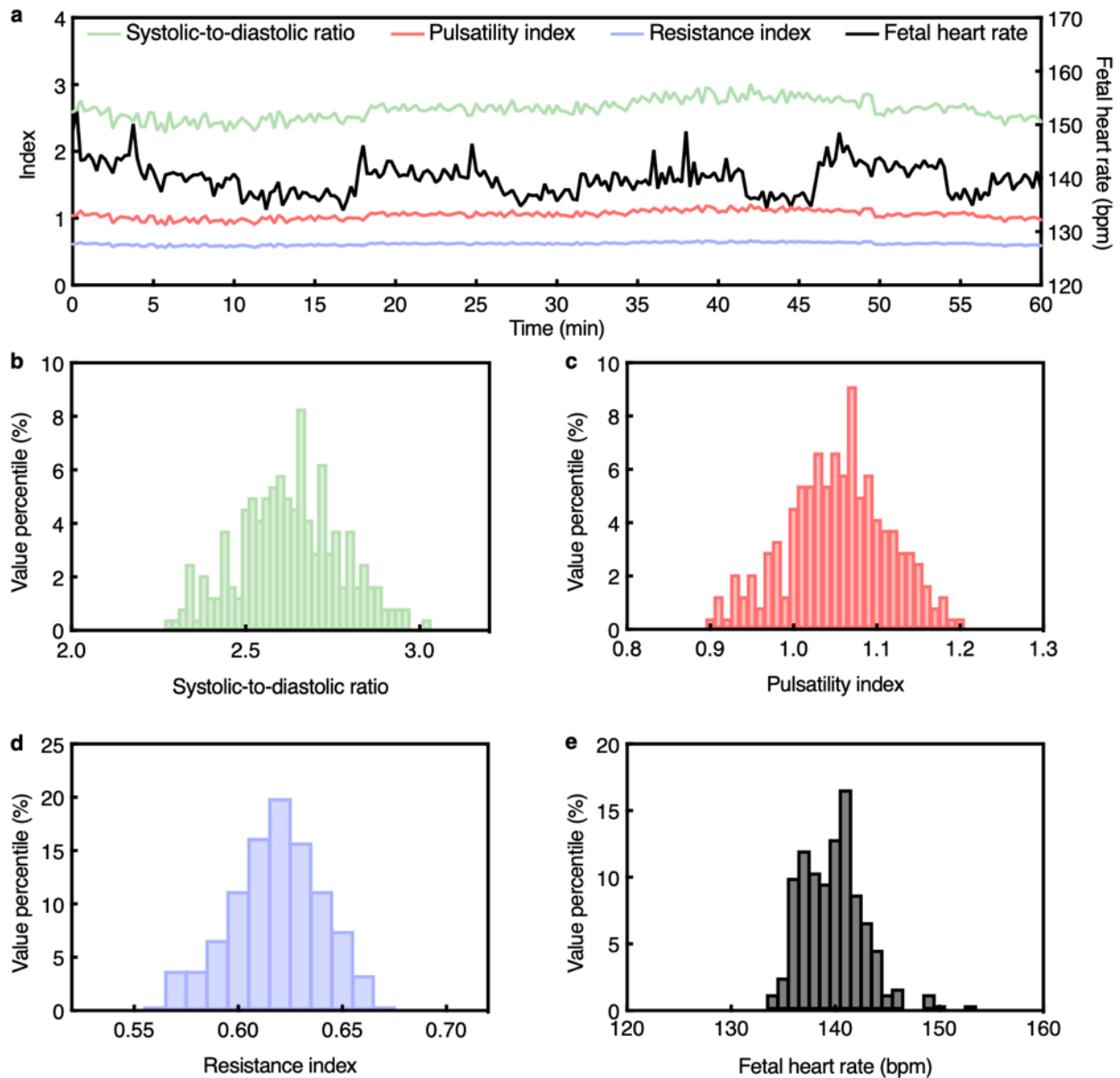
1791
 1792
 1793
 1794
 1795
 1796

Supplementary Fig. 75 | Continuous fetal monitoring using the UPatch in Participant #40. **a**, Time series data from the 1-h continuous monitoring session. Systolic-to-diastolic ratio, pulsatility index, and resistance index are plotted on the left y-axis, and fetal heart rate is plotted on the right y-axis. Histograms of **b**, systolic-to-diastolic ratio, **c**, pulsatility index, **d**, resistance index, and **e**, fetal heart rate over the recording period.

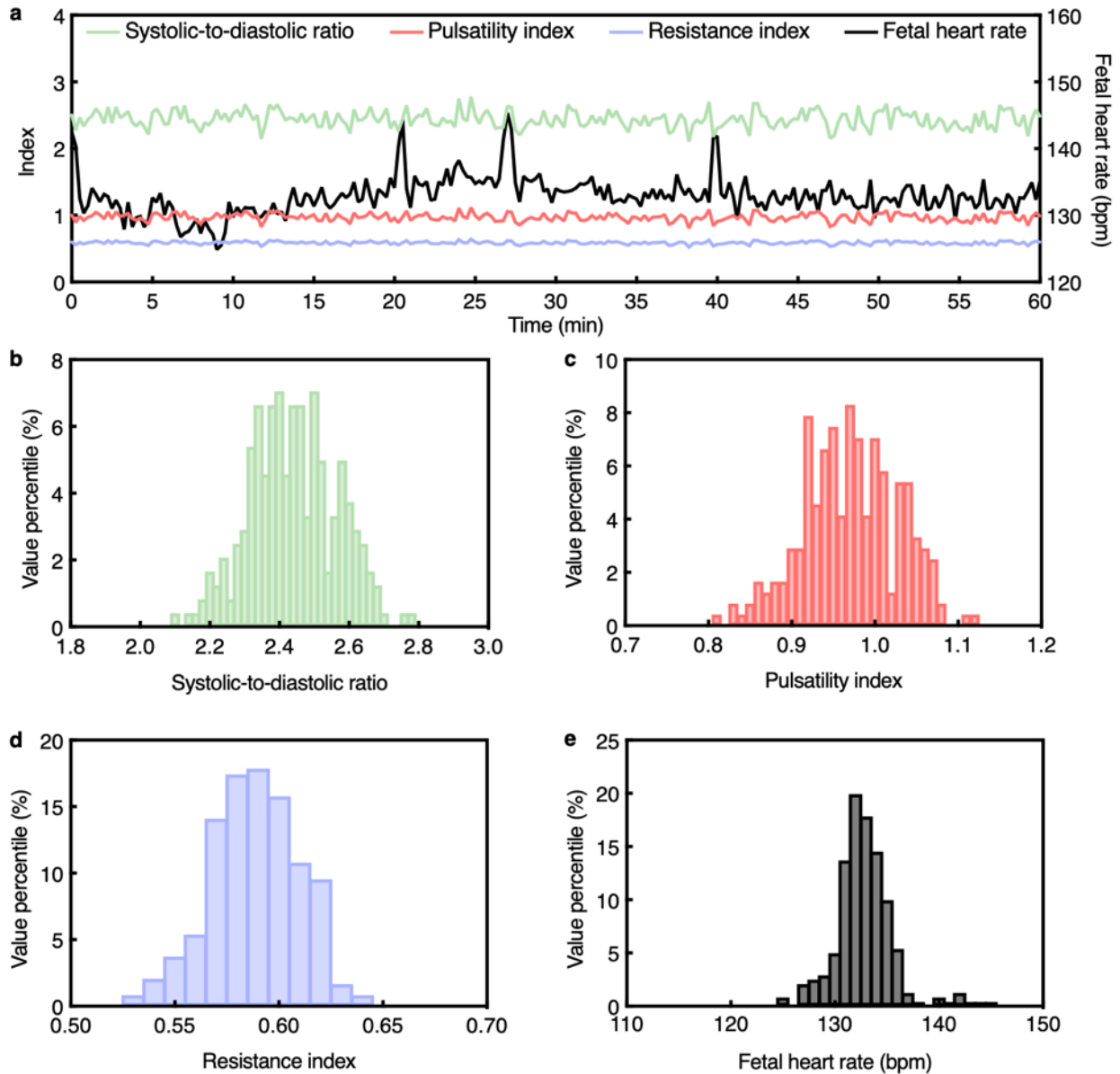


1797
 1798
 1799
 1800
 1801
 1802

Supplementary Fig. 76 | Continuous fetal monitoring using the UPatch in Participant #41. a, Time series data from the 1-h continuous monitoring session. Systolic-to-diastolic ratio, pulsatility index, and resistance index are plotted on the left y-axis, and fetal heart rate is plotted on the right y-axis. Histograms of b, systolic-to-diastolic ratio, c, pulsatility index, d, resistance index, and e, fetal heart rate over the recording period.

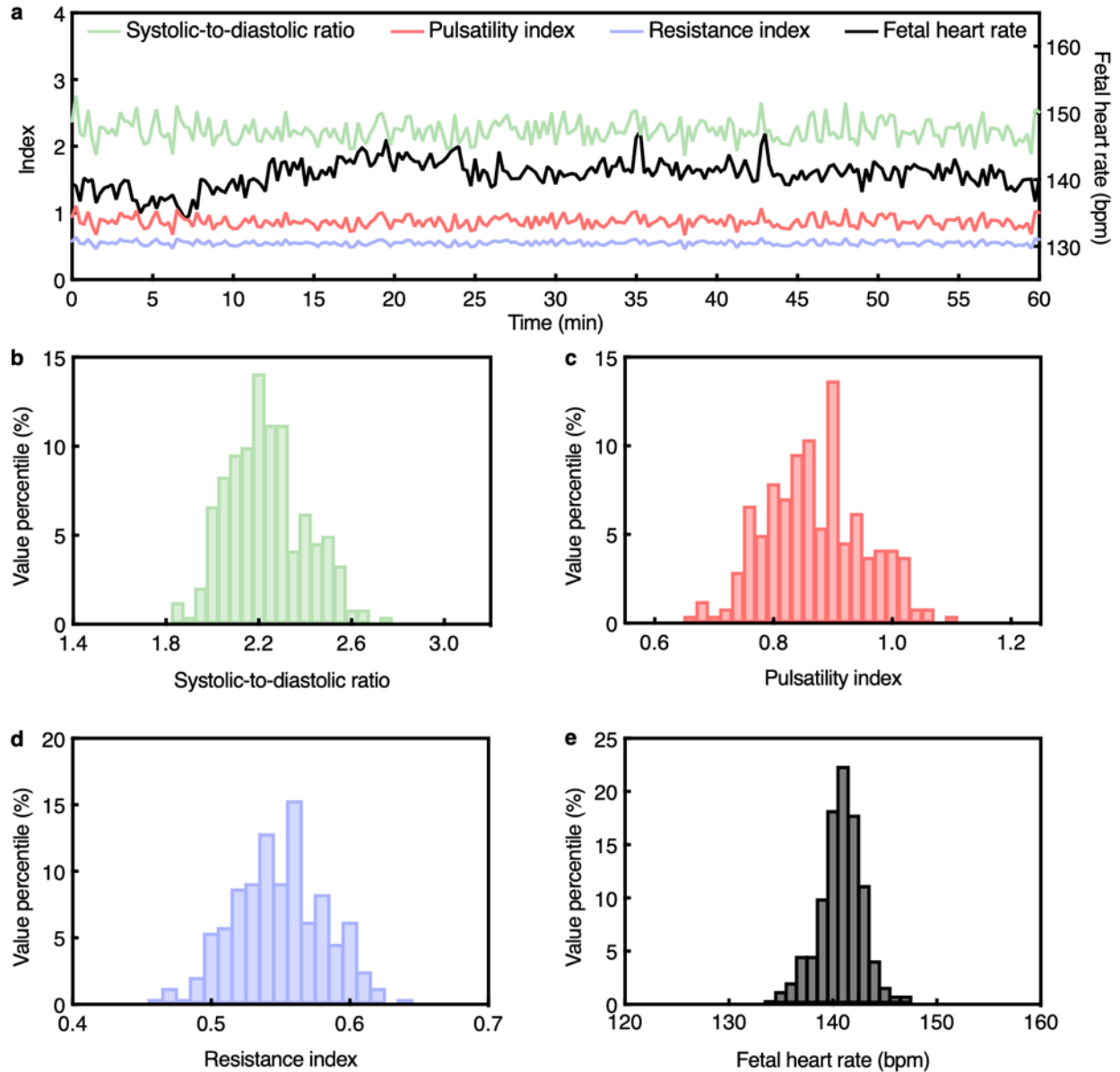


1803
 1804 **Supplementary Fig. 77 | Continuous fetal monitoring using the UPatch in Participant #42.** a,
 1805 Time series data from the 1-h continuous monitoring session. Systolic-to-diastolic ratio, pulsatility
 1806 index, and resistance index are plotted on the left y-axis, and fetal heart rate is plotted on the right
 1807 y-axis. Histograms of **b**, systolic-to-diastolic ratio, **c**, pulsatility index, **d**, resistance index, and **e**,
 1808 fetal heart rate over the recording period.



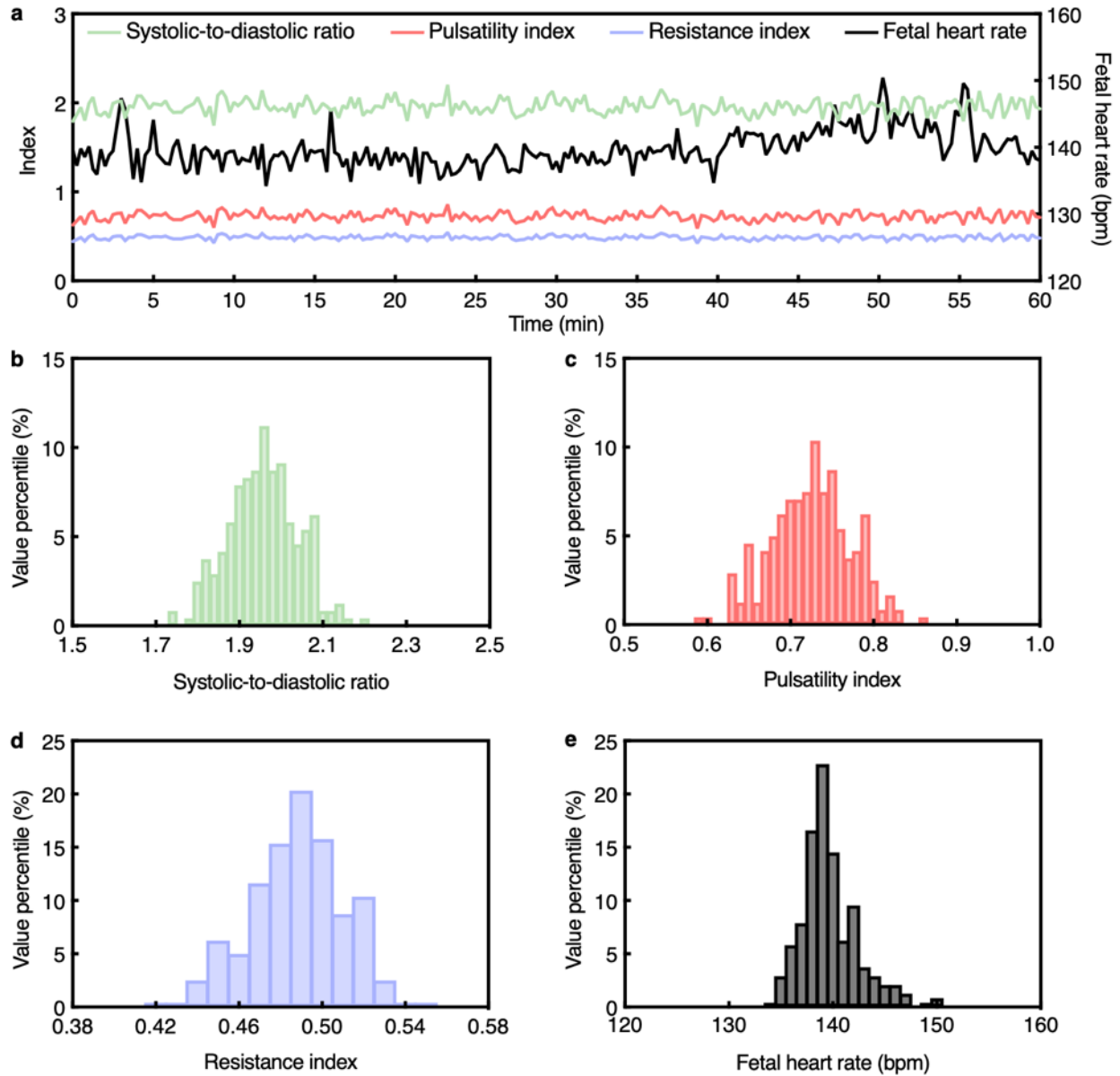
1809
 1810
 1811
 1812
 1813
 1814

Supplementary Fig. 78 | Continuous fetal monitoring using the UPatch in Participant #43. a, Time series data from the 1-h continuous monitoring session. Systolic-to-diastolic ratio, pulsatility index, and resistance index are plotted on the left y-axis, and fetal heart rate is plotted on the right y-axis. Histograms of **b**, systolic-to-diastolic ratio, **c**, pulsatility index, **d**, resistance index, and **e**, fetal heart rate over the recording period.

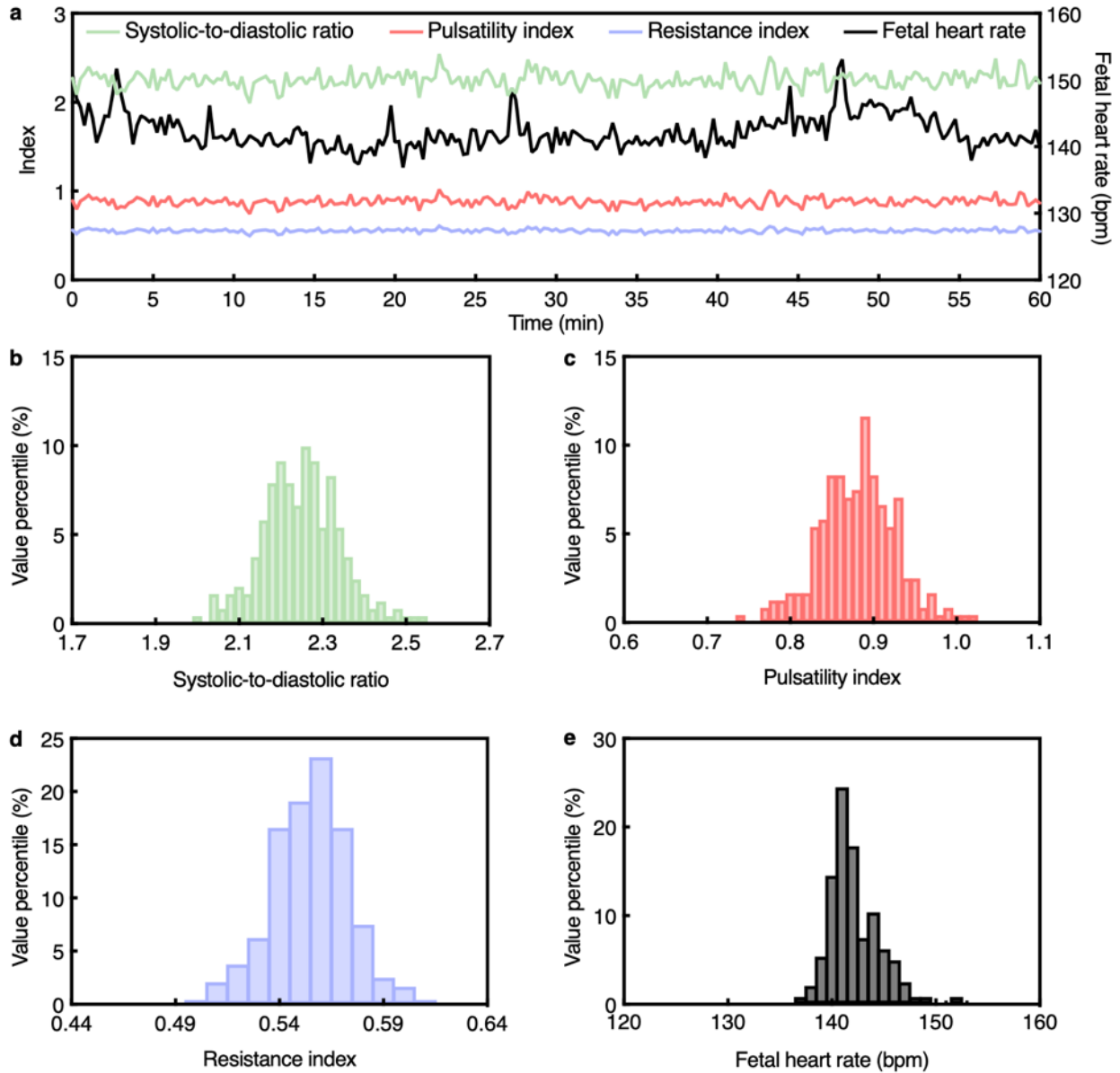


1815
 1816
 1817
 1818
 1819
 1820

Supplementary Fig. 79 | Continuous fetal monitoring using the UPatch in Participant #44. a, Time series data from the 1-h continuous monitoring session. Systolic-to-diastolic ratio, pulsatility index, and resistance index are plotted on the left y-axis, and fetal heart rate is plotted on the right y-axis. Histograms of b, systolic-to-diastolic ratio, c, pulsatility index, d, resistance index, and e, fetal heart rate over the recording period.

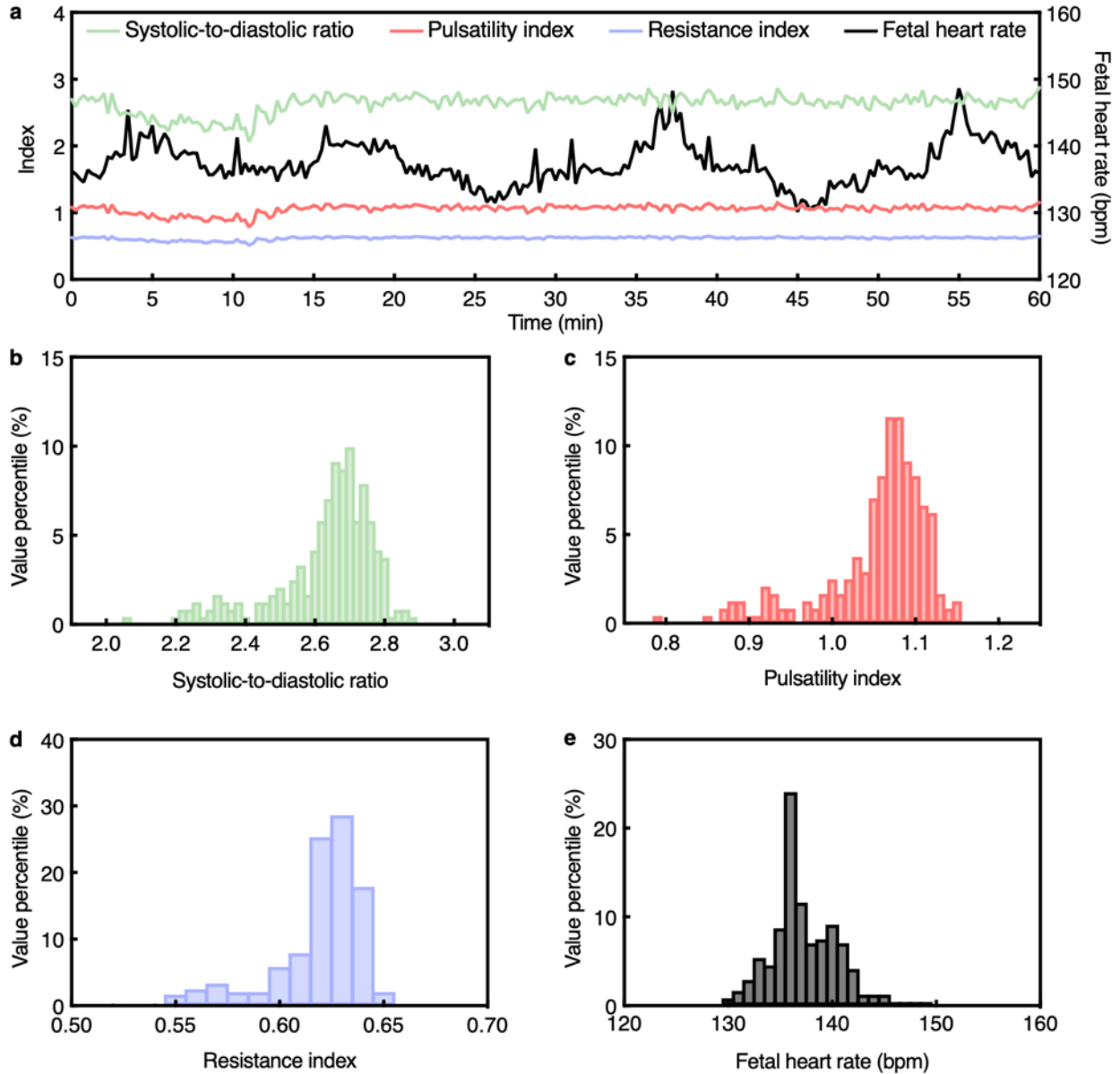


1821
 1822 **Supplementary Fig. 80 | Continuous fetal monitoring using the UPatch in Participant #45. a,**
 1823 Time series data from the 1-h continuous monitoring session. Systolic-to-diastolic ratio, pulsatility
 1824 index, and resistance index are plotted on the left y-axis, and fetal heart rate is plotted on the right
 1825 y-axis. Histograms of **b**, systolic-to-diastolic ratio, **c**, pulsatility index, **d**, resistance index, and **e**,
 1826 fetal heart rate over the recording period.



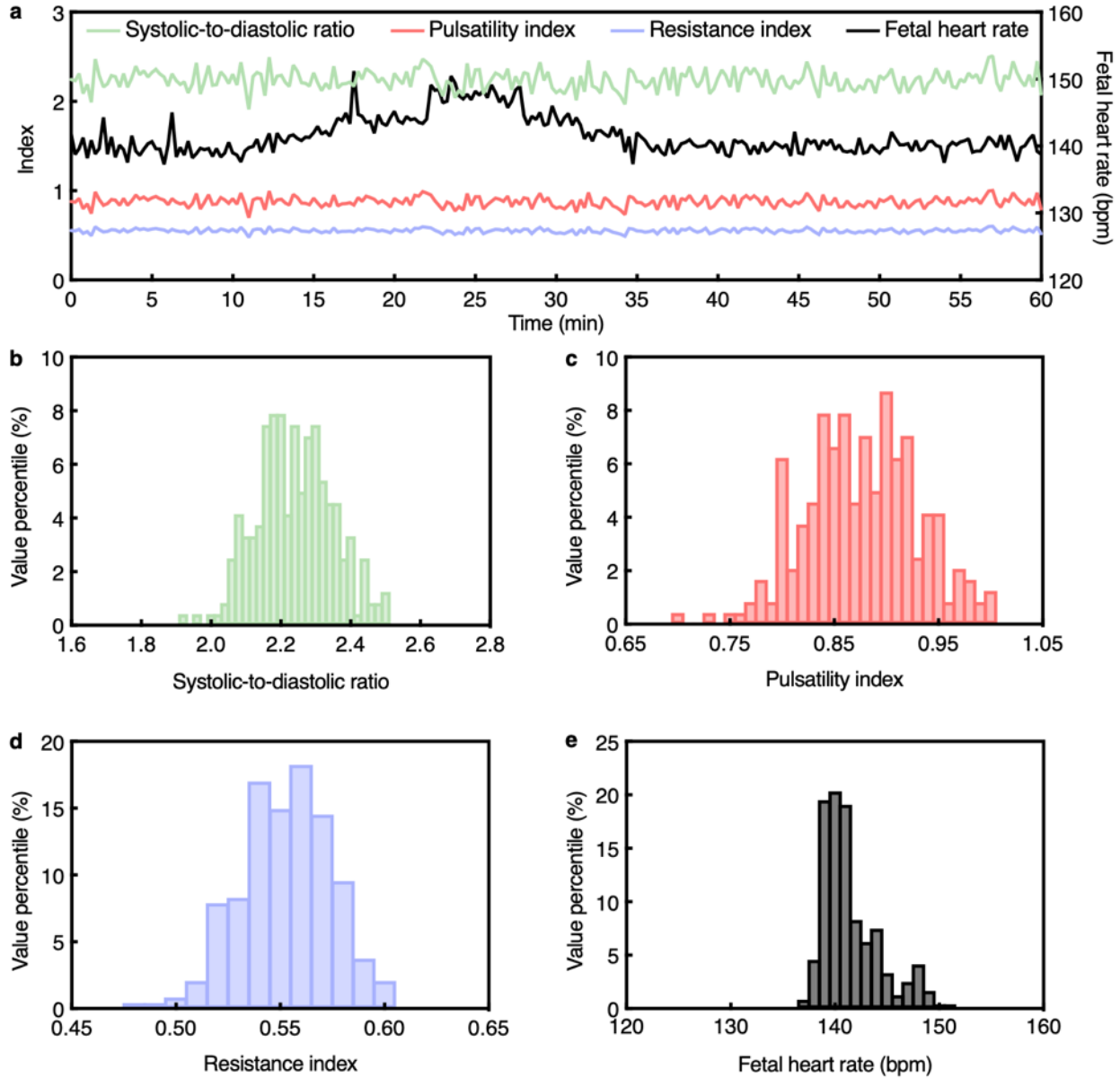
1827
 1828
 1829
 1830
 1831
 1832

Supplementary Fig. 81 | Continuous fetal monitoring using the UPatch in Participant #46. a, Time series data from the 1-h continuous monitoring session. Systolic-to-diastolic ratio, pulsatility index, and resistance index are plotted on the left y-axis, and fetal heart rate is plotted on the right y-axis. Histograms of b, systolic-to-diastolic ratio, c, pulsatility index, d, resistance index, and e, fetal heart rate over the recording period.



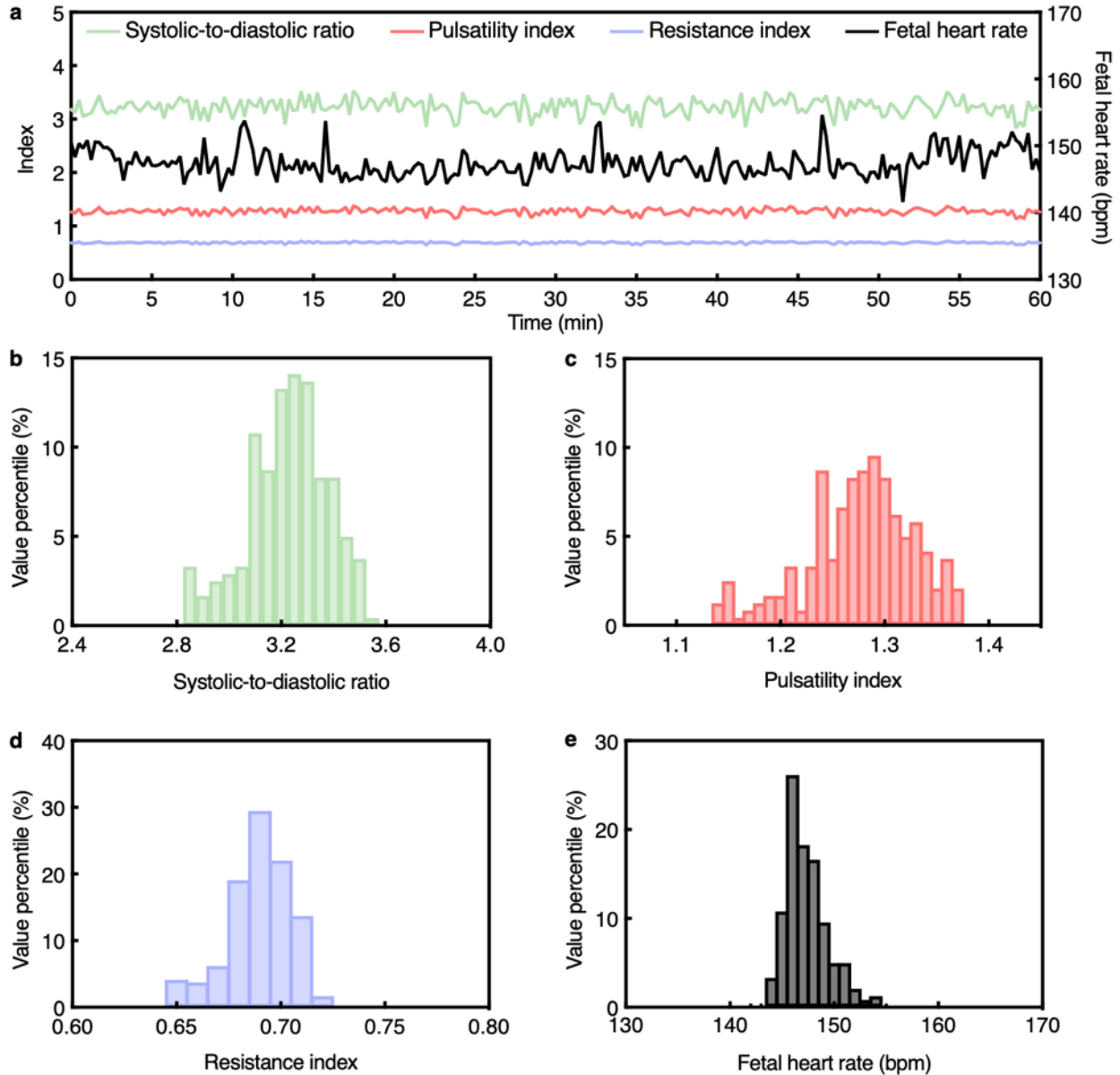
1833
 1834
 1835
 1836
 1837
 1838

Supplementary Fig. 82 | Continuous fetal monitoring using the UPatch in Participant #47. a, Time series data from the 1-h continuous monitoring session. Systolic-to-diastolic ratio, pulsatility index, and resistance index are plotted on the left y-axis, and fetal heart rate is plotted on the right y-axis. Histograms of **b**, systolic-to-diastolic ratio, **c**, pulsatility index, **d**, resistance index, and **e**, fetal heart rate over the recording period.



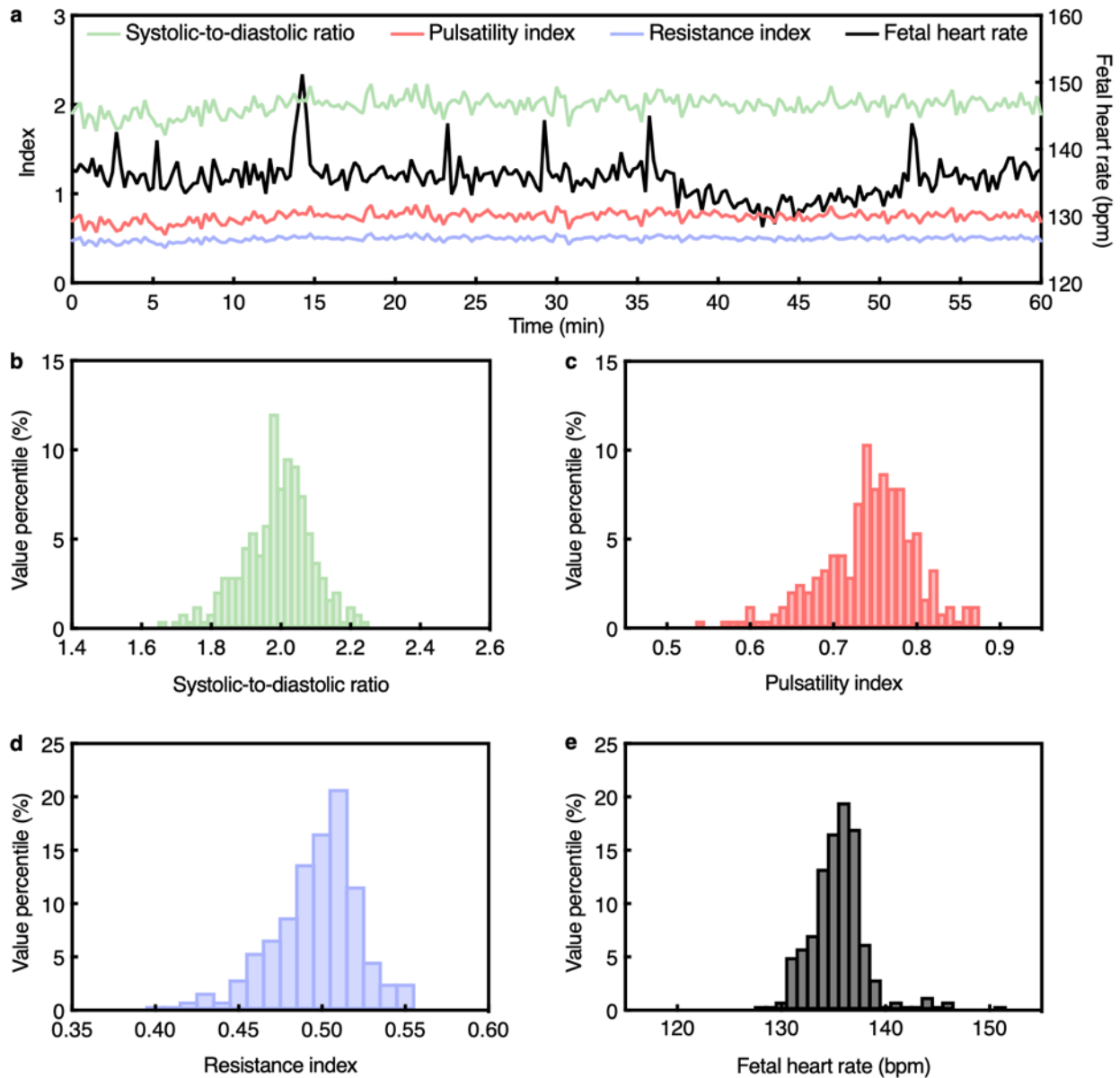
1839
 1840
 1841
 1842
 1843
 1844

Supplementary Fig. 83 | Continuous fetal monitoring using the UPatch in Participant #48. a, Time series data from the 1-h continuous monitoring session. Systolic-to-diastolic ratio, pulsatility index, and resistance index are plotted on the left y-axis, and fetal heart rate is plotted on the right y-axis. Histograms of b, systolic-to-diastolic ratio, c, pulsatility index, d, resistance index, and e, fetal heart rate over the recording period.

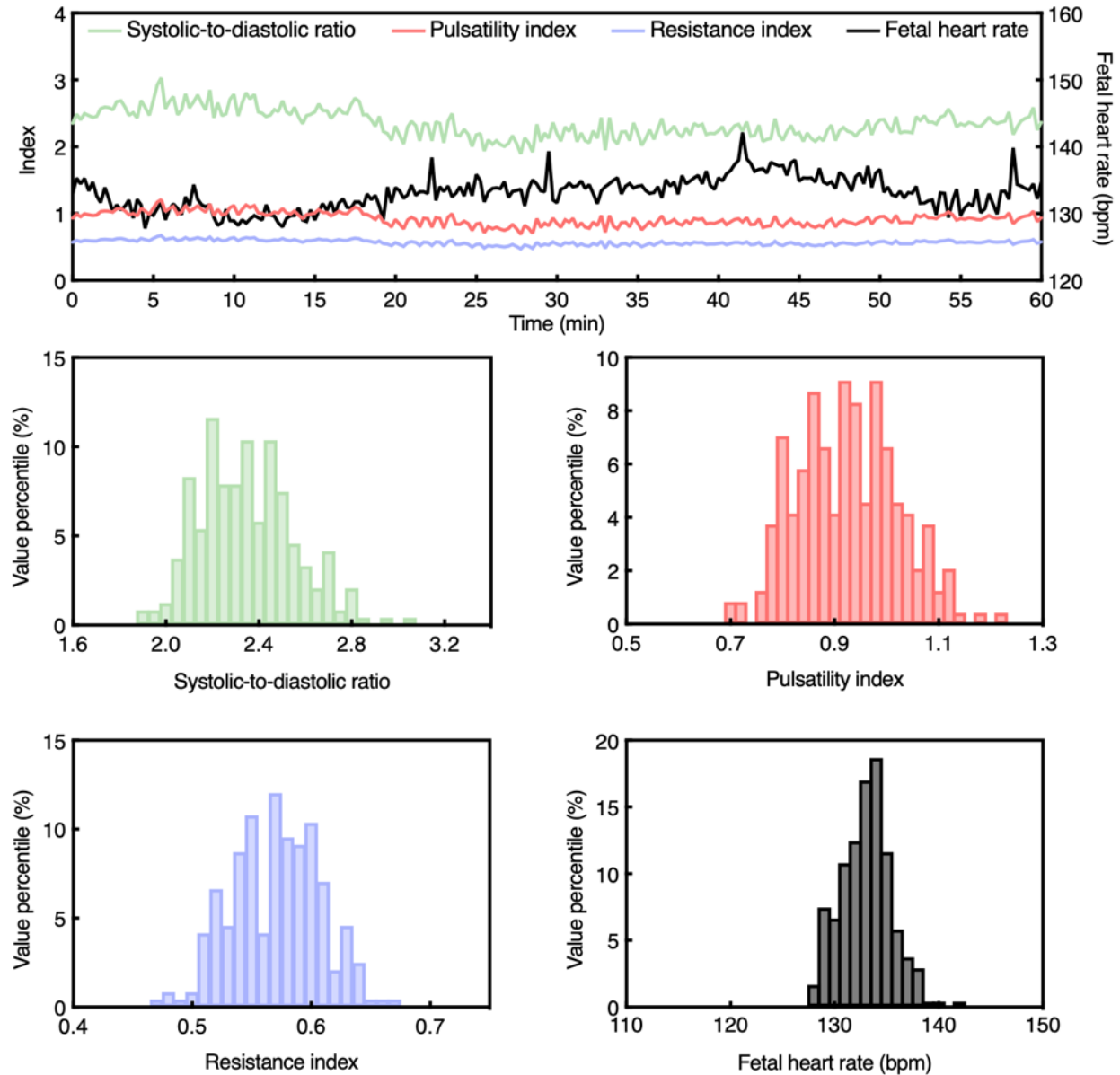


1845
 1846
 1847
 1848
 1849
 1850

Supplementary Fig. 84 | Continuous fetal monitoring using the UPatch in Participant #49. **a**, Time series data from the 1-h continuous monitoring session. Systolic-to-diastolic ratio, pulsatility index, and resistance index are plotted on the left y-axis, and fetal heart rate is plotted on the right y-axis. Histograms of **b**, systolic-to-diastolic ratio, **c**, pulsatility index, **d**, resistance index, and **e**, fetal heart rate over the recording period.

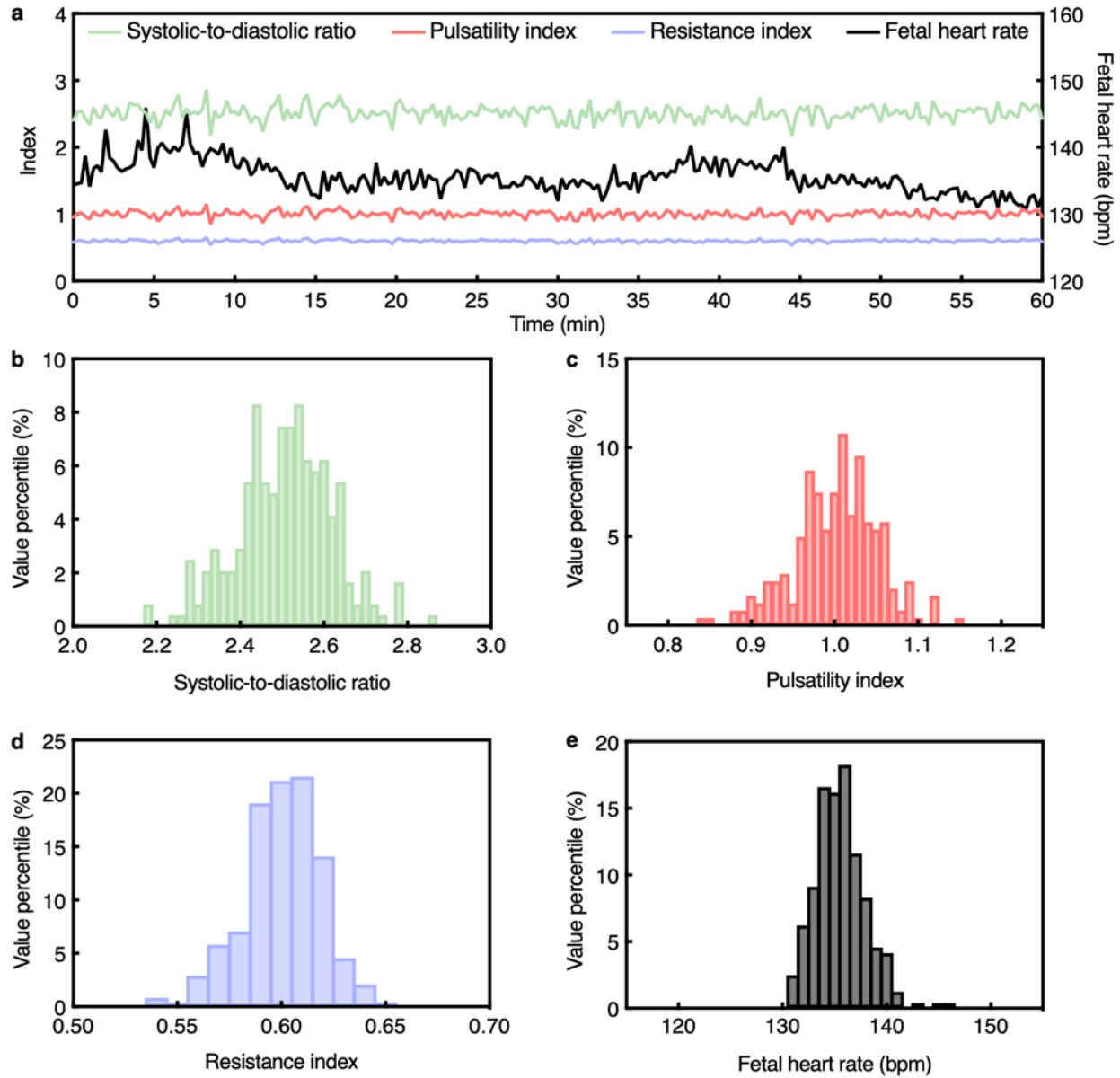


1851
 1852 **Supplementary Fig. 85 | Continuous fetal monitoring using the UPatch in Participant #50.** a,
 1853 Time series data from the 1-h continuous monitoring session. Systolic-to-diastolic ratio, pulsatility
 1854 index, and resistance index are plotted on the left y-axis, and fetal heart rate is plotted on the right
 1855 y-axis. Histograms of b, systolic-to-diastolic ratio, c, pulsatility index, d, resistance index, and e,
 1856 fetal heart rate over the recording period.



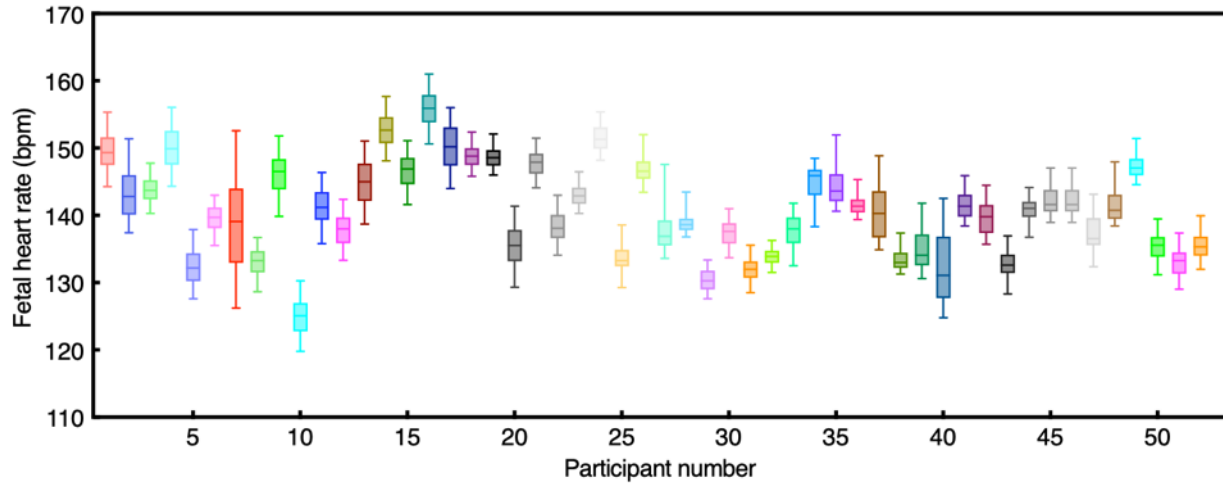
1857
 1858
 1859
 1860
 1861
 1862

Supplementary Fig. 86 | Continuous fetal monitoring using the UPatch in Participant #51. a, Time series data from the 1-h continuous monitoring session. Systolic-to-diastolic ratio, pulsatility index, and resistance index are plotted on the left y-axis, and fetal heart rate is plotted on the right y-axis. Histograms of **b**, systolic-to-diastolic ratio, **c**, pulsatility index, **d**, resistance index, and **e**, fetal heart rate over the recording period.



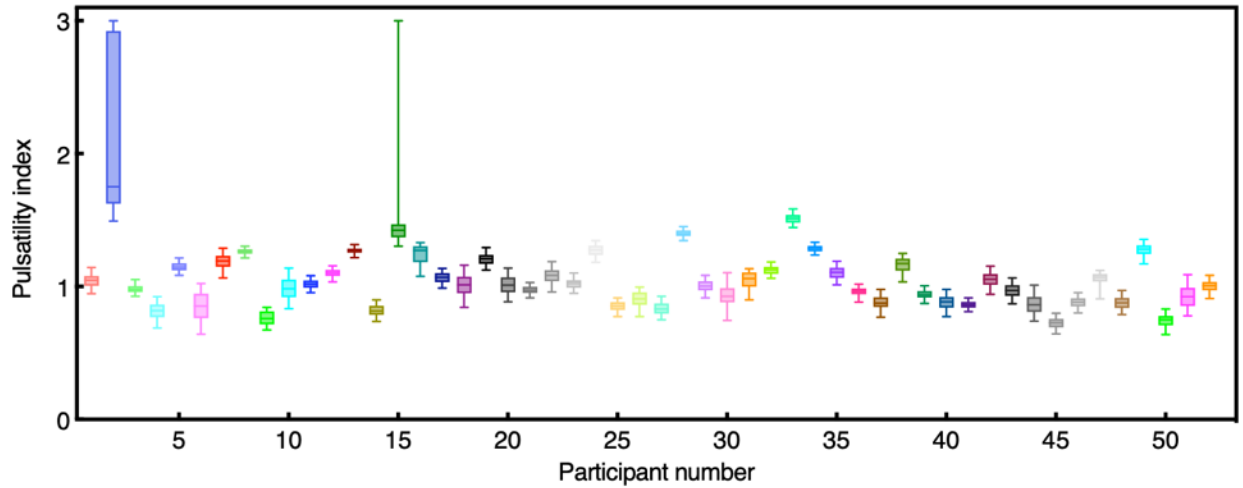
1863
 1864
 1865
 1866
 1867
 1868

Supplementary Fig. 87 | Continuous fetal monitoring using the UPatch in Participant #52. a, Time series data from the 1-h continuous monitoring session. Systolic-to-diastolic ratio, pulsatility index, and resistance index are plotted on the left y-axis, and fetal heart rate is plotted on the right y-axis. Histograms of b, systolic-to-diastolic ratio, c, pulsatility index, d, resistance index, and e, fetal heart rate over the recording period.



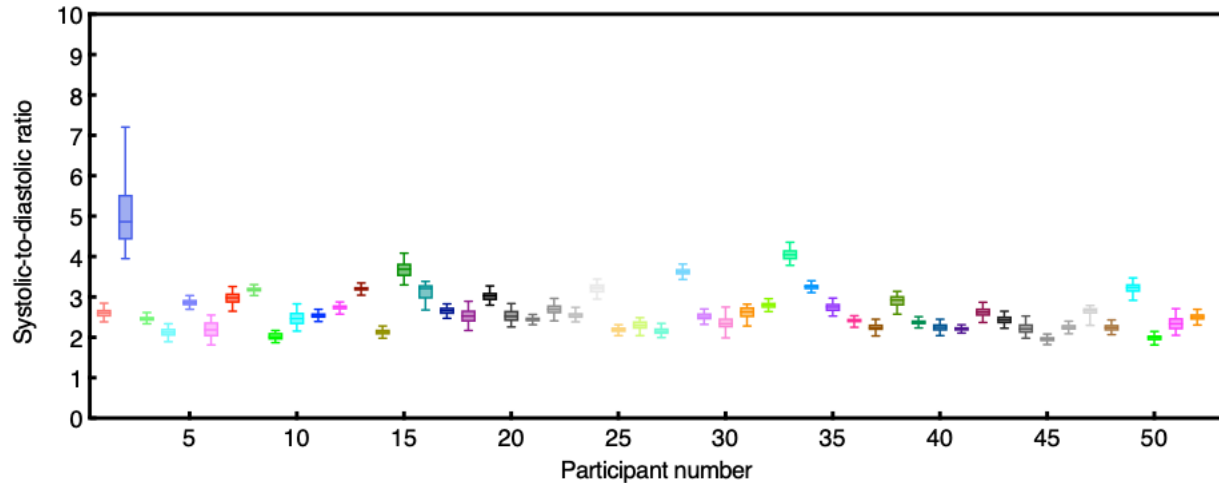
1869
1870
1871
1872
1873
1874

Supplementary Fig. 88 | Box plots of fetal heart rate during continuous monitoring. Distribution of fetal heart rate values across the full monitoring session for all participants. Each box represents the interquartile range (25th to 75th percentiles), the whiskers denote the 5th to 95th percentile range, and the midline indicates the median. The observed variability reflects dynamic physiological changes during the monitoring period.

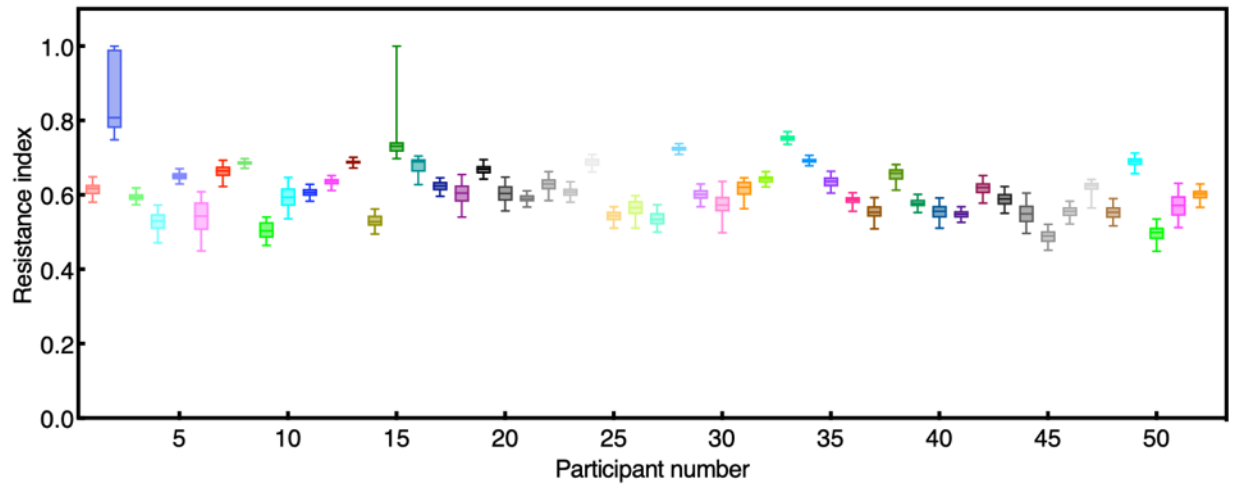


1875
 1876
 1877
 1878
 1879
 1880

Supplementary Fig. 89 | Box plots of pulsatility index during continuous monitoring. Distribution of pulsatility index values across the full monitoring session for all participants. Each box represents the interquartile range (25th to 75th percentiles), the whiskers denote the 5th to 95th percentile range, and the midline indicates the median. The observed variability reflects dynamic physiological changes during the monitoring period.

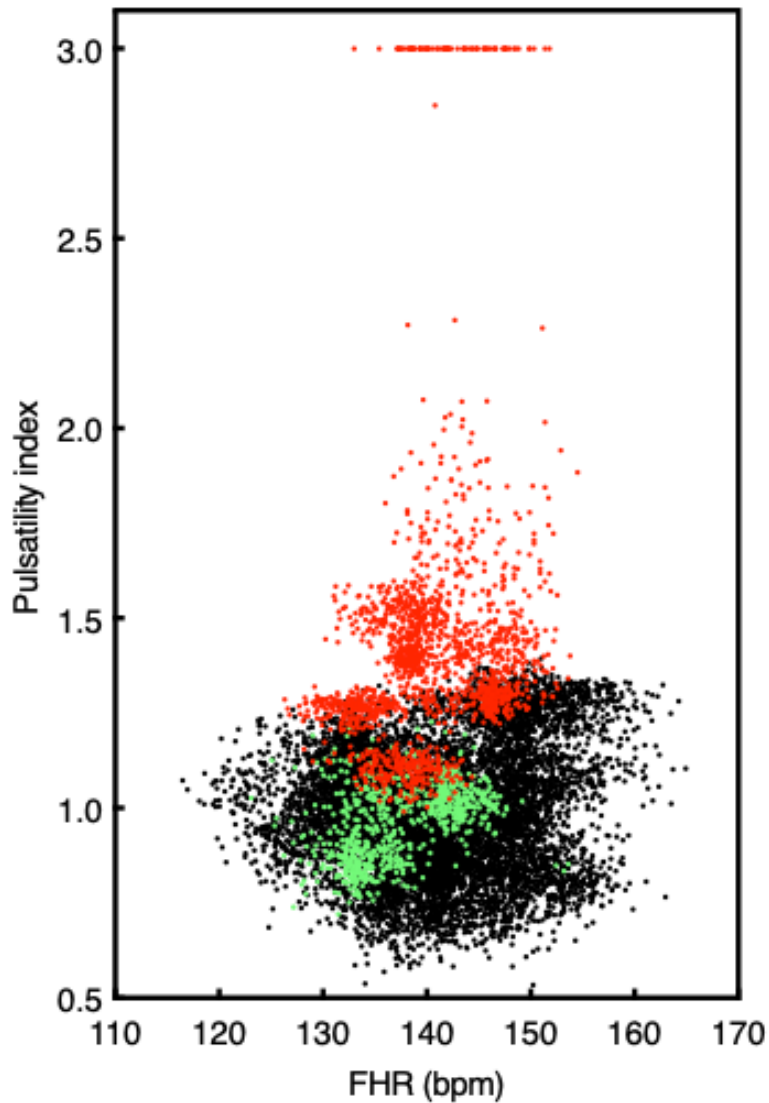


1881
 1882 **Supplementary Fig. 90 | Box plots of systolic-to-diastolic ratio during continuous monitoring.**
 1883 Distribution of systolic-to-diastolic ratio values across the full monitoring session for all
 1884 participants. Each box represents the interquartile range (25th to 75th percentiles), the whiskers
 1885 denote the 5th to 95th percentile range, and the midline indicates the median. The observed
 1886 variability reflects dynamic physiological changes during the monitoring period. In Participants
 1887 #2 and #15, systolic-to-diastolic ratios that could not be computed due to absent end diastolic flow
 1888 were excluded from the analysis; only computable values were included.



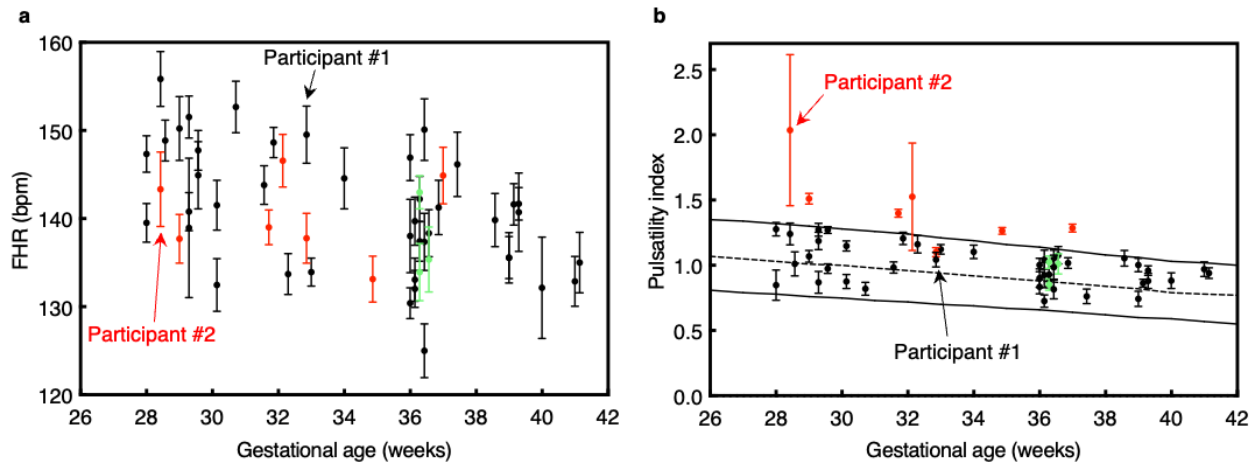
1889
 1890
 1891
 1892
 1893
 1894

Supplementary Fig. 91 | Box plots of resistance index during continuous monitoring. Distribution of resistance index values across the full monitoring session for all participants. Each box represents the interquartile range (25th to 75th percentiles), the whiskers denote the 5th to 95th percentile range, and the midline indicates the median. The observed variability reflects dynamic physiological changes during the monitoring period.

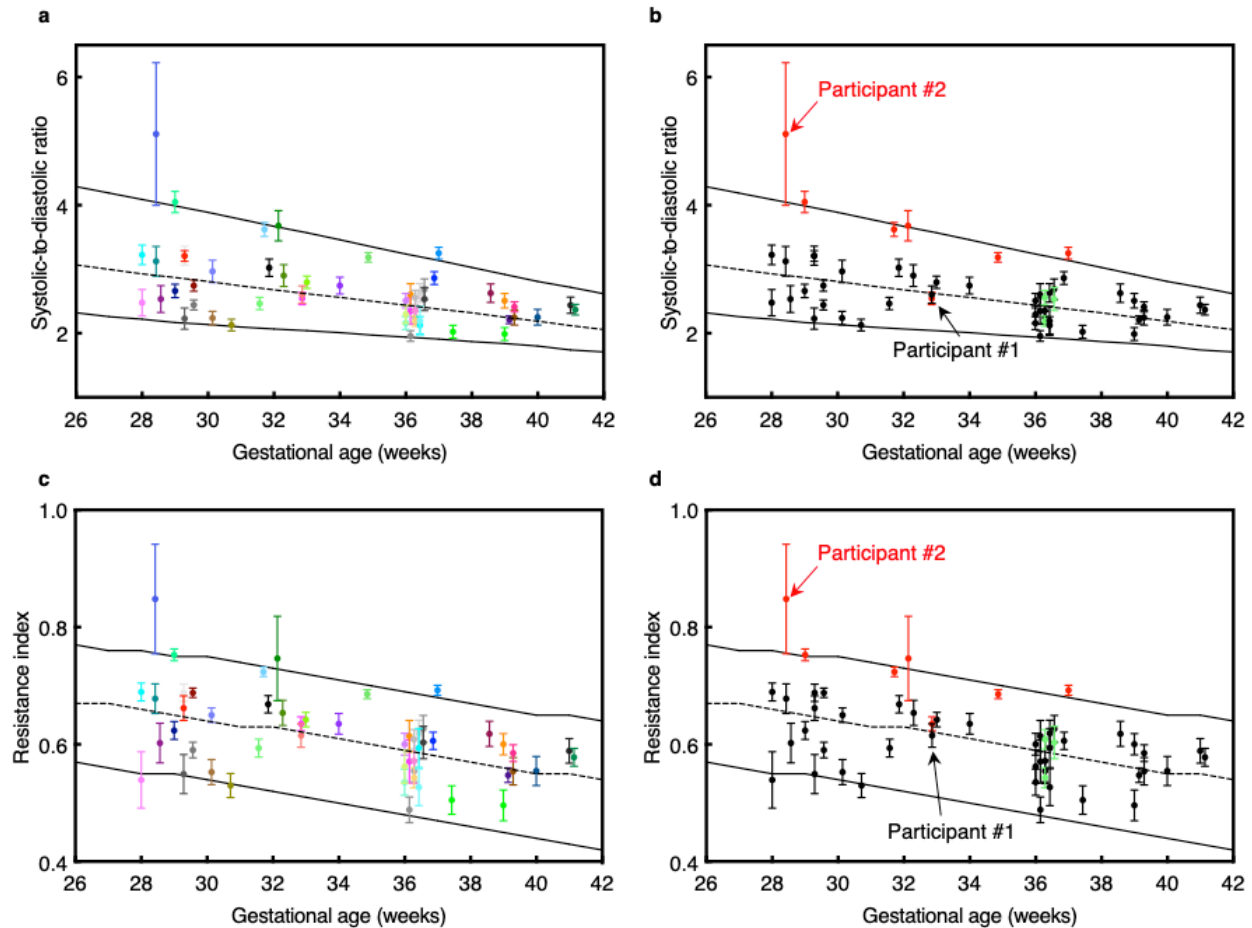


1895
1896
1897
1898
1899
1900

Supplementary Fig. 92 | Scatterplot of pulsatility index against FHR. The color corresponds to perinatal conditions: healthy (black, 42 participants), small for gestational age (red, 7 participants), and large for gestational age (green, 3 participants). Because participants are often presented with multiple co-occurring maternal risk conditions, risk groups were classified solely based on fetal risk conditions.

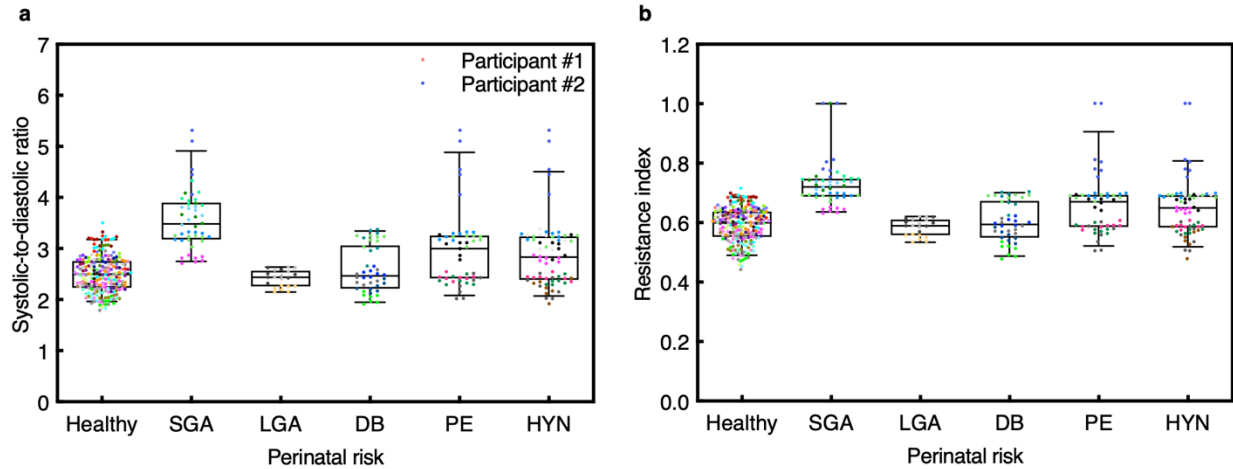


1901
 1902 **Supplementary Fig. 93 | Gestational trends in FHR and pulsatility index.** **a**, FHR plotted
 1903 against gestational age. **b**, Umbilical artery pulsatility index plotted against gestational age. The
 1904 color corresponds to perinatal conditions: healthy (black, 42 participants), small for gestational
 1905 age (red, 7 participants), and large for gestational age (green, 3 participants). The black dashed
 1906 line is the 50th percentile, and the solid black lines are the 5th and 95th percentiles of a widely used
 1907 reference population⁶⁸. Because participants are often presented with multiple co-occurring
 1908 maternal risk conditions, risk groups were classified solely based on fetal risk conditions. Data are
 1909 presented as mean \pm standard deviation ($n = 241$).

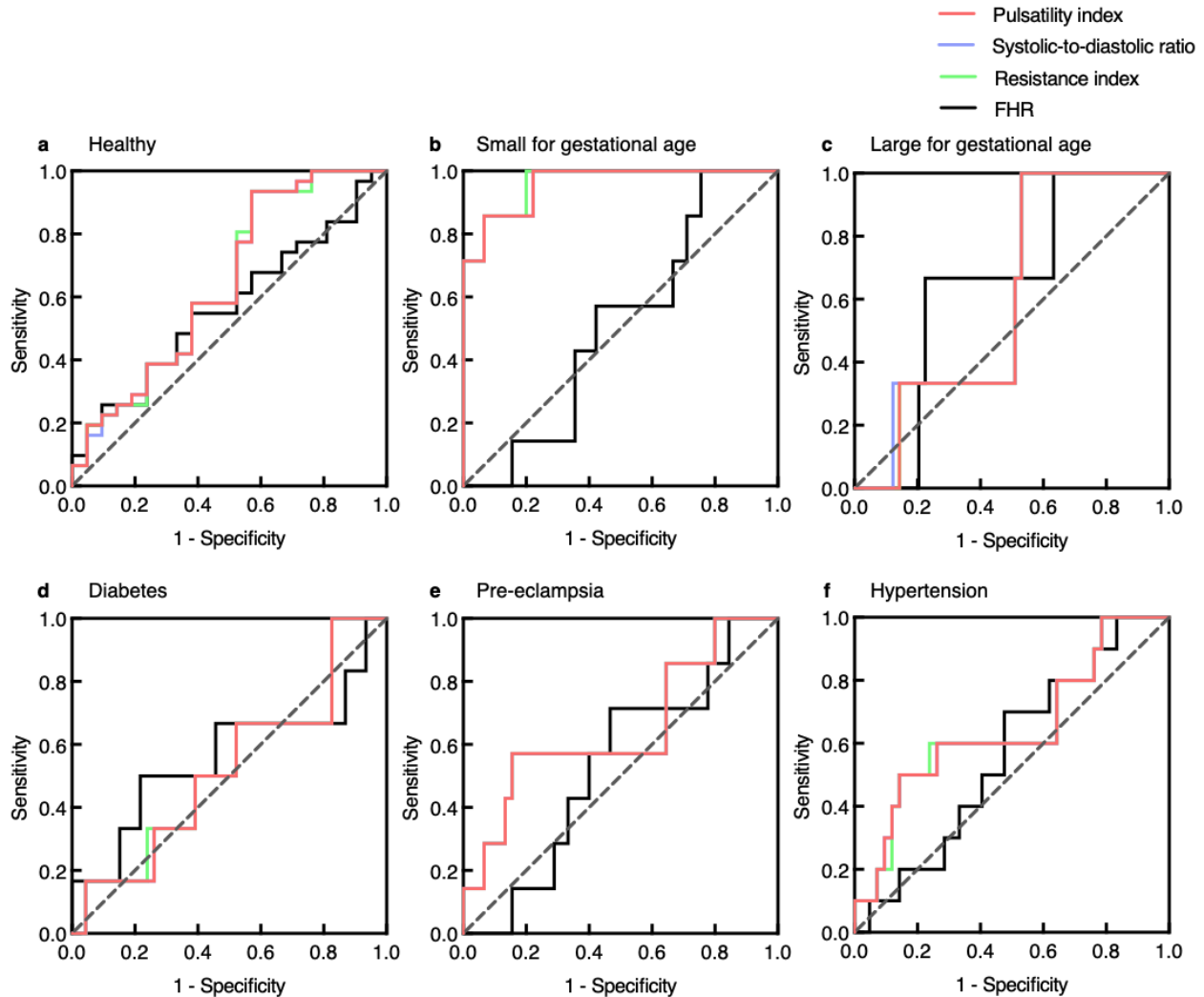


1910
 1911
 1912
 1913
 1914
 1915
 1916
 1917
 1918
 1919
 1920
 1921
 1922

Supplementary Fig. 94 | Gestational trends in systolic-to-diastolic ratio and resistance index. **a,b**, Umbilical artery systolic-to-diastolic ratio plotted against gestational age (**a**) with each color corresponding to an individual participant and (**b**) with each color corresponding to perinatal conditions: healthy (black, 42 participants), small for gestational age (red, 7 participants), and large for gestational age (green, 3 participants). **c,d**, Umbilical artery resistance index plotted against gestational age (**c**) with each color corresponding to an individual participant and (**d**) with each color corresponding to perinatal conditions: healthy (black, 42 participants), small for gestational age (red, 7 participants), and large for gestational age (green, 3 participants). The black dashed line in each plot is the 50th percentile, and the solid black lines are the 5th and 95th percentiles of a widely used reference population⁶⁸. Because participants are often presented with multiple co-occurring maternal risk conditions, risk groups were classified solely based on fetal risk conditions. Data are presented as mean \pm standard deviations ($n = 241$).



1923
 1924 **Supplementary Fig. 95 | Risk stratification in systolic-to-diastolic ratio and resistance index.**
 1925 (a) Box plot of systolic-to-diastolic ratio stratified by perinatal conditions: healthy (31 participants,
 1926 217 data points), small for gestational age (SGA; 7 participants, 46 data points), large for
 1927 gestational age (LGA; 3 participants, 21 data points), diabetes (DB; 6 participants, 42 data points),
 1928 pre-eclampsia (PE; 7 participants, 47 data points), and maternal hypertension (HYN; 10
 1929 participants, 68 data points). In Participants #2 and #15, systolic-to-diastolic ratios that could not
 1930 be computed due to absent end diastolic flow were excluded from the analysis; only computable
 1931 values were included. (b) Box plot of resistance index stratified by perinatal conditions: healthy
 1932 (31 participants, 217 data points), small for gestational age (SGA; 7 participants, 49 data points),
 1933 large for gestational age (LGA; 3 participants, 21 data points), diabetes (DB; 6 participants, 42
 1934 data points), pre-eclampsia (PE; 7 participants, 49 data points), and maternal hypertension (HYN;
 1935 10 participants, 70 data points). Each box represents the interquartile range (25th to 75th percentiles),
 1936 the whiskers denote the 5th to 95th percentile range, and the midline indicates the median. Each
 1937 participant's data was segmented into 10-min intervals ($n = 7$ per participant). Each color in the
 1938 data points corresponds to an individual participant, and the color schemes in **a** and **b** are the same.



1939
1940
1941
1942
1943
1944
1945
1946
1947
1948
1949

Supplementary Fig. 96 | Predictive modeling using logistic regression. Receiver operating characteristic curves from logistic regression analyses for perinatal conditions: a, healthy (31 participants), b, small for gestational age (7 participants), c, large for gestational age (3 participants), d, diabetes (6 participants), e, pre-eclampsia (7 participants), and f, maternal hypertension (10 participants). The plot was constructed using participant-level mean values for pulsatility index, systolic-to-diastolic ratio, resistance index, and fetal heart rate. The dashed diagonal line indicates chance-level performance (AUROC = 0.5). For conditions with limited sample sizes, ROC curves exhibit increased variability, including localized regions below chance-level performance, which is expected for single-feature models constructed from aggregated participant-level data.

1950 **Supplementary Video 1 | Real-time tracking.** The UPatch can monitor the umbilical cord in the
1951 duplex image. The tracking algorithm can register a sample gate on the moving umbilical artery
1952 in real time. Then, blood flow spectra can be recorded from the umbilical arteries.

1953 **References**

1954 1 Rouse, D. J. Antepartum fetal surveillance ACOG practice bulletin, number 229. *Obstet*
1955 *Gynecol* **137**, E116-E127 (2021).

1956 2 Grivell, R. M., Alfirevic, Z., Gyte, G. M. & Devane, D. Antenatal cardiotocography for
1957 fetal assessment. *Cochrane Database of Systematic Reviews* **9**, CD007863 (2015).

1958 3 Warland, J. & Glover, P. Fetal movements: What are we telling women? *Women and*
1959 *Birth* **30**, 23-28 (2017).

1960 4 Khalil, A. *et al.* ISUOG Practice Guidelines: performance of third-trimester obstetric
1961 ultrasound scan. *Ultrasound in Obstetrics & Gynecology* **63**, 131-147 (2024).

1962 5 Maslovich, M. & Burke, L. *Intrauterine Fetal Demise*. (StatPearls Publishing, 2022).

1963 6 Collins, J. H. Umbilical cord accidents: Human studies. *Seminars in Perinatology* **26**, 79-
1964 82 (2002).

1965 7 Oyelese, Y. & Ananth, C. V. Placental Abruptio. *Obstetrics & Gynecology* **108**, 1005-
1966 1016 (2006).

1967 8 Parry, S. & Strauss, J. F. Premature Rupture of the Fetal Membranes. *New England*
1968 *Journal of Medicine* **338**, 663-670 (1998).

1969 9 Marzbanrad, F., Stroux, L. & Clifford, G. D. Cardiotocography and beyond: a review of
1970 one-dimensional Doppler ultrasound application in fetal monitoring. *Physiological*
1971 *Measurement* **39**, 08TR01 (2018).

1972 10 Alim, A. & Imtiaz, M. H. Wearable Sensors for the Monitoring of Maternal Health—A
1973 Systematic Review. *Sensors* **23**, 2411 (2023).

1974 11 Kim, J. *et al.* Skin-interfaced wireless biosensors for perinatal and paediatric health.
1975 *Nature Reviews Bioengineering* **1**, 631-647 (2023).

1976 12 Porter, P. *et al.* Accuracy, interpretability and usability study of a wireless self-guided
1977 fetal heartbeat monitor compared to cardiotocography. *npj Digital Medicine* **5**, 167
1978 (2022).

1979 13 Kamala, B. A. *et al.* Implementation of a novel continuous fetal Doppler (Moyo)
1980 improves quality of intrapartum fetal heart rate monitoring in a resource-limited tertiary
1981 hospital in Tanzania: An observational study. *PLOS ONE* **13**, e0205698 (2018).

1982 14 <https://www.sonoline.com/sonoline-b-fetal-doppler.html>.

1983 15 [https://edanusa.com/wp-content/uploads/sites/12/2020/06/SD1-Series-Specification-](https://edanusa.com/wp-content/uploads/sites/12/2020/06/SD1-Series-Specification-V1.0-20180524-1.pdf)
1984 [V1.0-20180524-1.pdf](https://edanusa.com/wp-content/uploads/sites/12/2020/06/SD1-Series-Specification-V1.0-20180524-1.pdf).

1985 16 <https://lib.store.turbify.net/lib/babybeat/BabyBeatManual.pdf>.

1986 17 Freeman, R. K., Garite, T. J., Nageotte, M. P. & Miller, L. A. *Fetal Heart Rate*
1987 *Monitoring*. (Lippincott Williams & Wilkins, 2012).

1988 18 [https://my.getzhealthcare.com/getzhealthcare/products/ge-healthcare/corometrics-](https://my.getzhealthcare.com/getzhealthcare/products/ge-healthcare/corometrics-250cx/corometrics250cx_datasheet.pdf)
1989 [250cx/corometrics250cx_datasheet.pdf](https://my.getzhealthcare.com/getzhealthcare/products/ge-healthcare/corometrics-250cx/corometrics250cx_datasheet.pdf).

1990 19 <https://www.usa.philips.com/healthcare/product/HC865071/avalon-fm50-fetal-monitor>.

1991 20 Harkey, K. T., Casale, M. B., Pantelopoulos, A. A. & Zurcher, M. A. Assessing the
1992 Clinical Use of a Novel, Mobile Fetal Monitoring Device. *Obstetrics & Gynecology* **123**,
1993 55S (2014).

1994 21 Kawakita, T. *et al.* Neonatal complications associated with use of fetal scalp electrode: a
1995 retrospective study. *BJOG: An International Journal of Obstetrics & Gynaecology* **123**,
1996 1797-1803 (2016).

1997 22 Wilmink, F. A., Wilms, F. F., Heydanus, R., Mol, B. W. J. & Papatsonis, D. N. M. Fetal
1998 complications after placement of an intrauterine pressure catheter: A report of two cases

- 1999 and review of the literature. *The Journal of Maternal-Fetal & Neonatal Medicine* **21**,
2000 880-883 (2008).
- 2001 23 Ryu, D. *et al.* Comprehensive pregnancy monitoring with a network of wireless, soft, and
2002 flexible sensors in high- and low-resource health settings. *Proceedings of the National*
2003 *Academy of Sciences* **118**, e2100466118 (2021).
- 2004 24 Nguyen, K. *et al.* Wearable Fetal Monitoring Solution for Improved Mobility During
2005 Labor & Delivery. *Annu Int Conf IEEE Eng Med Biol Soc* **2018**, 4397-4400 (2018).
- 2006 25 Hayes-Gill, B. R. Monica Healthcare: From the research laboratory to commercial
2007 reality—A real-life case study. *Healthcare Technology Letters* **8**, 1-10 (2021).
- 2008 26 Cohen, W. R. *et al.* Accuracy and reliability of fetal heart rate monitoring using maternal
2009 abdominal surface electrodes. *Acta Obstetrica et Gynecologica Scandinavica* **91**, 1306-
2010 1313 (2012).
- 2011 27 [https://www.usa.philips.com/healthcare/product/HC866488/avalon-beltless-fetal-](https://www.usa.philips.com/healthcare/product/HC866488/avalon-beltless-fetal-monitoring-solution)
2012 [monitoring-solution](https://www.usa.philips.com/healthcare/product/HC866488/avalon-beltless-fetal-monitoring-solution).
- 2013 28 Mhajna, M. *et al.* Wireless, remote solution for home fetal and maternal heart rate
2014 monitoring. *American Journal of Obstetrics & Gynecology MFM* **2**, 100101 (2020).
- 2015 29 <https://www.mindchild.com/assets/22dsp021908-mindchild-patches-data-sheet.pdf>.
- 2016 30 Noirhomme, Q. *et al.* Validation of a new electrophysiological fetal heart rate monitor:
2017 comparison with cardiotocography. *American Journal of Obstetrics and Gynecology* **226**,
2018 S656-S657 (2022).
- 2019 31 Lempersz, C. *et al.* Intrapartum non-invasive electrophysiological monitoring: A
2020 prospective observational study. *Acta Obstetrica et Gynecologica Scandinavica* **99**,
2021 1387-1395 (2020).
- 2022 32 Liu, B., Marler, E., Thilaganathan, B. & Bhide, A. Ambulatory antenatal fetal
2023 electrocardiography in high-risk pregnancies (AMBER): protocol for a pilot prospective
2024 cohort study. *BMJ Open* **13**, e062448 (2023).
- 2025 33 Clifford, G., Sameni, R., Ward, J., Robinson, J. & Wolfberg, A. J. Clinically accurate
2026 fetal ECG parameters acquired from maternal abdominal sensors. *American Journal of*
2027 *Obstetrics and Gynecology* **205**, 47.e41-47.e45 (2011).
- 2028 34 <https://clinicaltrials.gov/study/NCT04876846>.
- 2029 35 Kasap, B. *et al.* Use of A Novel Transabdominal Fetal Pulse Oximeter (TFO) In Human
2030 Pregnancy: A Proof-of-Concept. *American Journal of Obstetrics and Gynecology* **228**,
2031 S100 (2023).
- 2032 36 Gunther, J. E., Jayet, B., Sekar, S. K. V., Kainerstorfer, J. M. & Andersson-Engels, S.
2033 Review of optical methods for fetal monitoring in utero. *Journal of Biophotonics* **15**,
2034 e202100343 (2022).
- 2035 37 Delay, U. *et al.* Novel non-invasive in-house fabricated wearable system with a hybrid
2036 algorithm for fetal movement recognition. *PLOS ONE* **16**, e0254560 (2021).
- 2037 38 Du, Y.-C., Yen, L. B., Kuo, P.-L. & Tsai, P.-Y. A Wearable Device for Evaluation of
2038 Relative Position, Force, and Duration of Fetal Movement for Pregnant Woman Care.
2039 *IEEE Sensors Journal* **21**, 19341-19350 (2021).
- 2040 39 Qin, M., Xu, Y., Liang, Y. & Sun, T. A wearable fetal movement detection system for
2041 pregnant women. *Frontiers in Medicine* **10**, 1160373 (2023).
- 2042 40 Xu, J. *et al.* Fetal Movement Detection by Wearable Accelerometer Duo Based on
2043 Machine Learning. *IEEE Sensors Journal* **22**, 11526-11534 (2022).

- 2044 41 Lai, J. *et al.* Performance of a wearable acoustic system for fetal movement
2045 discrimination. *PLOS ONE* **13**, e0195728 (2018).
- 2046 42 Ghosh, A. K., Catelli, D. S., Wilson, S., Nowlan, N. C. & Vaidyanathan, R. Multi-modal
2047 detection of fetal movements using a wearable monitor. *Information Fusion* **103**, 102124
2048 (2024).
- 2049 43 Kauffmann, T. & Silberman, M. *Fetal Monitoring*. (StatPearls Publishing, 2023).
- 2050 44 Goldenberg, R. L., Harrison, M. S. & McClure, E. M. Stillbirths: The Hidden Birth
2051 Asphyxia — US and Global Perspectives. *Clinics in Perinatology* **43**, 439-453 (2016).
- 2052 45 Freeman, R. K. Problems with intrapartum fetal heart rate monitoring interpretation and
2053 patient management. *Obstet Gynecol* **100**, 813-826 (2002).
- 2054 46 Baschat, A. A. & Gembruch, U. The cerebroplacental Doppler ratio revisited. *Ultrasound
2055 in Obstetrics & Gynecology* **21**, 124-127 (2003).
- 2056 47 Alfirevic, Z., Devane, D., Gyte, G. M. & Cuthbert, A. Continuous cardiotocography
2057 (CTG) as a form of electronic fetal monitoring (EFM) for fetal assessment during labour.
2058 *Cochrane Database Syst Rev* **2**, CD006066-CD006066 (2017).
- 2059 48 Kypros Nicolaidis, G. R., Kurt Hecher, Renato Ximenes. *Doppler in Obstetrics*. (2002).
- 2060 49 Berkley, E., Chauhan, S. P. & Abuhamad, A. Doppler assessment of the fetus with
2061 intrauterine growth restriction. *American Journal of Obstetrics and Gynecology* **206**, 300-
2062 308 (2012).
- 2063 50 Kennedy, A. M. & Woodward, P. J. A Radiologist's Guide to the Performance and
2064 Interpretation of Obstetric Doppler US. *RadioGraphics* **39**, 893-910 (2019).
- 2065 51 Maulik, D. & Lees, C. C. *Doppler Ultrasound in Obstetrics and Gynecology*. (Springer,
2066 2023).
- 2067 52 Dall'asta, A. *et al.* Intrapartum Doppler ultrasound: where are we now? *Minerva Obstet
2068 Gynecol* **73**, 94-102 (2021).
- 2069 53 Woodward, P. J., Kennedy, A. & Sohaey, R. *Diagnostic imaging: obstetrics*. (Elsevier,
2070 2021).
- 2071 54 Nabeshima, Y., Sasaki, J., Mesaki, N., Sohda, S. & Kubo, T. Effect of Maternal Exercise
2072 on Fetal Umbilical Artery Waveforms: The Comparison of IUGR and AFD Fetuses.
2073 *Journal of Obstetrics and Gynaecology Research* **23**, 255-259 (1997).
- 2074 55 Skow, R. J. *et al.* Effects of prenatal exercise on fetal heart rate, umbilical and uterine
2075 blood flow: a systematic review and meta-analysis. *British Journal of Sports Medicine*
2076 **53**, 124-133 (2019).
- 2077 56 Smith, G. C. S. & Fretts, R. C. Stillbirth. *The Lancet* **370**, 1715-1725 (2007).
- 2078 57 Douglas-Escobar, M. & Weiss, M. D. Hypoxic-Ischemic Encephalopathy. *JAMA
2079 Pediatrics* **169**, 397 (2015).
- 2080 58 Nelson, K. B. & Grether, J. K. Causes of cerebral palsy. *Current Opinion in Pediatrics*
2081 **11**, 487-491 (1999).
- 2082 59 Alfirevic, Z., Stampalija, T. & Dowswell, T. Fetal and umbilical Doppler ultrasound in
2083 high-risk pregnancies. *Cochrane Database of Systematic Reviews* **6**, CD007529 (2017).
- 2084 60 Bhide, A. *et al.* ISUOG Practice Guidelines (updated): use of Doppler velocimetry in
2085 obstetrics. *Ultrasound in Obstetrics & Gynecology* **58**, 331-339 (2021).
- 2086 61 Lees, C. C. *et al.* ISUOG Practice Guidelines: diagnosis and management of small-for-
2087 gestational-age fetus and fetal growth restriction. *Ultrasound in Obstetrics &
2088 Gynecology* **56**, 298-312 (2020).

- 2089 62 Sotiriadis, A. *et al.* ISUOG Practice Guidelines: role of ultrasound in screening for and
2090 follow-up of pre-eclampsia. *Ultrasound in Obstetrics & Gynecology* **53**, 7-22 (2019).
- 2091 63 Rouse, D. J., Owen, J., Goldenberg, R. L. & Cliver, S. P. Determinants of the optimal
2092 time in gestation to initiate antenatal fetal testing: a decision-analytic approach. *Am J*
2093 *Obstet Gynecol* **173**, 1357-1363 (1995).
- 2094 64 McClure, E. *et al.* Global Network for Women's and Children's Health Research:
2095 probable causes of stillbirth in low- and middle- income countries using a prospectively
2096 defined classification system. *BJOG: An International Journal of Obstetrics &*
2097 *Gynaecology* **125**, 131-138 (2018).
- 2098 65 Leon, R. L. *et al.* Cerebral Blood Flow Monitoring in High-Risk Fetal and Neonatal
2099 Populations. *Frontiers in Pediatrics* **9**, 748345 (2022).
- 2100 66 Acharya, G., Wilsgaard, T., Berntsen, G. K. R., Maltau, J. M. & Kiserud, T. Reference
2101 ranges for serial measurements of blood velocity and pulsatility index at the intra-
2102 abdominal portion, and fetal and placental ends of the umbilical artery. *Ultrasound in*
2103 *Obstetrics & Gynecology* **26**, 162-169 (2005).
- 2104 67 Acharya, G., Wilsgaard, T., Berntsen, G. K. R., Maltau, J. M. & Kiserud, T. Reference
2105 ranges for serial measurements of umbilical artery Doppler indices in the second half of
2106 pregnancy. *American journal of obstetrics and gynecology* **192**, 937-944 (2005).
- 2107 68 Drukker, L. *et al.* International gestational age-specific centiles for umbilical artery
2108 Doppler indices: a longitudinal prospective cohort study of the INTERGROWTH-21st
2109 Project. *American Journal of Obstetrics and Gynecology* **222**, 602.e601-602.e615 (2020).
- 2110 69 Mari, G. *et al.* Noninvasive Diagnosis by Doppler Ultrasonography of Fetal Anemia Due
2111 to Maternal Red-Cell Alloimmunization. *New England Journal of Medicine* **342**, 9-14
2112 (2000).
- 2113 70 Chudleigh, T., Smith, A. & Cumming, S. *Obstetric & Gynaecological Ultrasound: How,*
2114 *Why and When.* (Elsevier, 2016).
- 2115 71 Ali, S. *et al.* Standardization and quality control of Doppler and fetal biometric
2116 ultrasound measurements in low-income setting. *Ultrasound in Obstetrics & Gynecology*
2117 **61**, 481-487 (2023).
- 2118 72 Hu, H. *et al.* A wearable cardiac ultrasound imager. *Nature* **613**, 667-675 (2023).
- 2119 73 Zhou, S. *et al.* Transcranial volumetric imaging using a conformal ultrasound patch.
2120 *Nature* **629**, 810-818 (2024).
- 2121 74 Gasner, A. & Aatsha, P. *Physiology, Uterus.* (StatPearls Publishing, 2023).
- 2122 75 Basyigit, I. B., Dogan, H. & Helhel, S. The effect of aperture shape, angle of incidence
2123 and polarization on shielding effectiveness of metallic enclosures. *Journal of Microwave*
2124 *Power and Electromagnetic Energy* **53**, 115-127 (2019).
- 2125 76 Li, K., Zeng, D. W., Yung, K. C., Chan, H. L. W. & Choy, C. L. Study on
2126 ceramic/polymer composite fabricated by laser cutting. *Materials Chemistry and Physics*
2127 **75**, 147-150 (2002).
- 2128 77 Lukacs, M. *et al.* Performance and Characterization of New Micromachined High-
2129 Frequency Linear Arrays. *IEEE Transactions on Ultrasonics, Ferroelectrics and*
2130 *Frequency Control* **53**, 1719-1729 (2006).
- 2131 78 Foster, F. S. *et al.* A new 15-50 MHz array-based micro-ultrasound scanner for
2132 preclinical imaging. *Ultrasound Med Biol* **35**, 1700-1708 (2009).
- 2133 79 Zeng, D. W. *et al.* UV laser micromachining of piezoelectric ceramic using a pulsed
2134 Nd:YAG laser. *Applied Physics A* **78**, 415-421 (2004).

2135 80 Yuan, Z., Riaz, A. & Chohan, B. S. Precision Machining by Dicing Blades: A Systematic
2136 Review. *Machines* **11**, 259 (2023).

2137 81 Lu, G. *et al.* Noninvasive imaging-guided ultrasonic neurostimulation with arbitrary 2D
2138 patterns and its application for high-quality vision restoration. *Nature Communications*
2139 **15**, 4481 (2024).

2140 82 Kang, H. *et al.* 2-D Array Design and Fabrication With Pitch-Shifting Interposer at
2141 Frequencies From 4 MHz up to 10 MHz. *IEEE Transactions on Ultrasonics,*
2142 *Ferroelectrics, and Frequency Control* **69**, 3382-3391 (2022).

2143 83 Wodnicki, R. *et al.* Co-Integrated PIN-PMN-PT 2-D Array and Transceiver Electronics
2144 by Direct Assembly Using a 3-D Printed Interposer Grid Frame. *IEEE Transactions on*
2145 *Ultrasonics, Ferroelectrics, and Frequency Control* **67**, 387-401 (2020).

2146 84 <https://www.disco.co.jp/eg/solution/library/dicing/basic.html>.

2147 85 Hoskins, P. R., Martin, K. & Thrush, A. *Diagnostic Ultrasound Physics and Equipment*.
2148 (CRC Press, 2019).

2149 86 Evans, D. H., Jensen, J. A. & Nielsen, M. B. Ultrasonic colour Doppler imaging.
2150 *Interface Focus* **1**, 490-502 (2011).

2151 87 Zhang, L., Du, W., Kim, J.-H., Yu, C.-C. & Dagdeviren, C. An Emerging Era:
2152 Conformable Ultrasound Electronics. *Advanced Materials* **36**, 2307664 (2024).

2153 88 Li, Y., Liang, B., Gu, Z.-M., Zou, X.-Y. & Cheng, J.-C. Reflected wavefront
2154 manipulation based on ultrathin planar acoustic metasurfaces. *Scientific Reports* **3** (2013).

2155 89 Kuhn, C. Impact of extracorporeal shock waves on the human skin with cellulite: A case
2156 study of an unique instance. *Clinical Interventions in Aging* **3**, 201-210 (2008).

2157 90 Gajasinghe, R. W. R. L. *et al.* Experimental study of PDMS bonding to various substrates
2158 for monolithic microfluidic applications. *Journal of Micromechanics and*
2159 *Microengineering* **24**, 075010 (2014).

2160 91 Chang, C. *et al.* Acoustic lens for capacitive micromachined ultrasonic transducers.
2161 *Journal of Micromechanics and Microengineering* **24**, 085007 (2014).

2162 92 Hao, B. *et al.* Focused ultrasound enables selective actuation and Newton-level force
2163 output of untethered soft robots. *Nature Communications* **15**, 5197 (2024).

2164 93 Grand-Perret, V. *et al.* A Novel Microflow Phantom Dedicated to Ultrasound
2165 Microvascular Measurements. *Ultrasonic Imaging* **40**, 325-338 (2018).

2166 94 Di Sieno, L. *et al.* Solid heterogeneous phantoms for multimodal ultrasound and diffuse-
2167 optical imaging: an outcome of the SOLUS project for standardization. in *Novel*
2168 *Biophotonics Techniques and Applications V*. **EB102**, 11075 (2019).

2169 95 Tsou, J. K., Liu, J., Barakat, A. I. & Insana, M. F. Role of Ultrasonic Shear Rate
2170 Estimation Errors in Assessing Inflammatory Response and Vascular Risk. *Ultrasound in*
2171 *Medicine & Biology* **34**, 963-972 (2008).

2172 96 Aksoy, B. *et al.* Shielded soft force sensors. *Nature Communications* **13**, 4649 (2022).

2173 97 <https://www.analog.com/media/en/training-seminars/tutorials/mt-012.pdf>.

2174 98 Ballou, G. *Handbook for Sound Engineers*. (Routledge, 2008).

2175 99 https://download.tek.com/document/3AW_19134_2_MR_Letter.pdf.

2176 100 Nath, M., Maity, S., Avlani, S., Weigand, S. & Sen, S. Inter-body coupling in electro-
2177 quasistatic human body communication: theory and analysis of security and interference
2178 properties. *Scientific Reports* **11**, 4378 (2021).

2179 101 Kibret, B., Teshome, A. & Lai, D. Human Body as Antenna and Its Effect on Human
2180 Body Communications. *Progress In Electromagnetics Research* **148**, 193-207 (2014).

2181 102 Li, J., Nie, Z., Liu, Y., Wang, L. & Hao, Y. Evaluation of Propagation Characteristics
2182 Using the Human Body as an Antenna. *Sensors* **17**, 2878 (2017).

2183 103 Razavi, B. *RF Microelectronics*. (Pearson, 2011).

2184 104 Kledrowetz, V., Fucjik, L., Prokop, R. & Háze, J. A 1 V 92 dB SNDR 10 kHz Bandwidth
2185 Second-Order Asynchronous Delta-Sigma Modulator for Biomedical Signal Processing.
2186 *Sensors* **20**, 4137 (2020).

2187 105 <https://resources.altium.com/p/everything-you-need-know-about-stitching-vias>.

2188 106 Razavi, B. *Design of Analog CMOS Integrated Circuits*. (McGraw-Hill Education, 2017).

2189 107 Ding, N. *et al.* in *Proceedings of the ACM SIGMETRICS/international conference on*
2190 *Measurement and modeling of computer systems* 29–40 (Association for Computing
2191 Machinery, Pittsburgh, PA, USA, 2013).

2192 108 Wu, J. *et al.* A Low-Noise 0.001Hz-1kHz Sample-Level Duty-Cycling Neural Recording
2193 System-on-Chip. in *2023 IEEE International Symposium on Circuits and Systems*
2194 *(ISCAS)*. 1-5 (2023).

2195 109 Horowitz, P. & Hill, W. *The Art of Electronics*. (Cambridge University Press, 2015).

2196 110 Haykin, S. & Moher, M. *Communication Systems*. (John Wiley & Sons, 2009).

2197 111 <https://www.sunuclear.com/uploads/documents/datasheets/068-DS-072120.pdf>.

2198 112 Köşüş, A., Köşüş, N. & Turhan, N. Ö. Is there any relation between umbilical artery and
2199 vein diameter and estimated fetal weight in healthy pregnant women? *Journal of Medical*
2200 *Ultrasonics* **39**, 227-234 (2012).

2201 113 Fitzsimmons, E. D. & Bajaj, T. *Embryology, Amniotic Fluid*. (StatPearls Publishing,
2202 2023).

2203 114 Mark, J. E. *Physical Properties of Polymers Handbook*. (Springer New York, 2007).

2204 115 Formlabs. Elastic 50A.

2205 116 Mencarelli, M., Puggelli, L., Virga, A., Furferi, R. & Volpe, Y. Acoustic velocity and
2206 stability of tissue-mimicking echogenic materials for ultrasound training phantoms.
2207 *Journal of Materials Science* **59**, 6509-6524 (2024).

2208 117 Food and Drug Administration. Marketing clearance of diagnostic ultrasound systems
2209 and transducers: Guidance for industry and food and drug administration staff. *U.S. Food*
2210 *and Drug Administration, Silver Spring, MD, USA*, Tech. Rep. FDA-2017-D-5372
2211 (2023).

2212 118 International Electrotechnical Commission. IEC 62359:2010/AMD1:2017 "Ultrasonics:
2213 Field Characterization—Test Methods for the Determination of Thermal and Mechanical
2214 Indices Related to Medical Diagnostic Ultrasonic Fields". *International Electrotechnical*
2215 *Commission, Geneva, Switzerland*, Ed. 2.1 (2017).

2216 119 International Electrotechnical Commission. IEC 62127-1:2022 "Ultrasonics –
2217 Hydrophones – Part 1: Measurement and characterization of medical ultrasonic fields".
2218 *International Electrotechnical Commission, Geneva, Switzerland*, Ed. 2.0 (2022).

2219 120 Commission, I. E. IEC 62127-1:2022 "Ultrasonics – Hydrophones – Part 1: Measurement
2220 and characterization of medical ultrasonic fields". *International Electrotechnical*
2221 *Commission, Geneva, Switzerland*, Ed. 2.0 (2022).

2222 121 Duck, F. A. Medical and non-medical protection standards for ultrasound and infrasound.
2223 *Progress in Biophysics and Molecular Biology* **93**, 176-191 (2007).

2224 122 Bigelow, T. A. *et al.* The Thermal Index. *Journal of Ultrasound in Medicine* **30**, 714-734
2225 (2011).

- 2226 123 AIUM Official Statement for Recommended Maximum Scanning Times for Displayed
2227 Thermal Index Values. *Journal of Ultrasound in Medicine* **42**, E74-E75 (2023).
- 2228 124 Safety Group of the British Medical Ultrasound Society. Guidelines for the safe use of
2229 diagnostic ultrasound equipment. *Ultrasound* **18**, 52-59 (2010).
- 2230 125 International Electrotechnical Commission. IEC 60601-2-37:2024 “Medical electrical
2231 equipment - Part 2-37: Particular requirements for the basic safety and essential
2232 performance of ultrasonic medical diagnostic and monitoring equipment”. *International
2233 Electrotechnical Commission, Geneva, Switzerland*, Ed. 3.0 (2024).
- 2234 126 Drukker, L., Droste, R., Chatelain, P., Noble, J. A. & Papageorghiou, A. T. Safety
2235 Indices of Ultrasound: Adherence to Recommendations and Awareness During Routine
2236 Obstetric Ultrasound Scanning. *Ultraschall in der Medizin - European Journal of
2237 Ultrasound* **41**, 138-145 (2020).
- 2238 127 SATTAR, N. *et al.* Antenatal Waist Circumference and Hypertension Risk. *Obstetrics &
2239 Gynecology* **97**, 268-271 (2001).
- 2240 128 Sohn, M. & Bye, E. Visual analysis of body shape changes during pregnancy.
2241 *International Journal of Fashion Design, Technology and Education* **5**, 117-128 (2012).
- 2242 129 Ahmadibeni, A., Kashani, P., Hallaj, M. S., Ghanbari, S. & Javadifar, N. The relationship
2243 of pre-pregnancy body mass index with maternal anthropometric indices, weight
2244 retention and the baby’s weight and nutrition in the first 6 months post-partum. *BMC
2245 Pregnancy and Childbirth* **23**, 802 (2023).
- 2246 130 Karlsson, B., Berson, M., Helgason, T., Geirsson, R. T. & Pourcelot, L. Effects of fetal
2247 and maternal breathing on the ultrasonic Doppler signal due to fetal heart movement. *Eur
2248 J Ultrasound* **11**, 47-52 (2000).
- 2249 131 Cahill, L. S. *et al.* Determination of fetal heart rate short-term variation from umbilical
2250 artery Doppler waveforms. *Ultrasound in Obstetrics & Gynecology* **57**, 70-74 (2021).
- 2251 132 Wilson, L. S., Dadd, M. J. & Gill, R. W. Automatic vessel tracking and measurement for
2252 Doppler studies. *Ultrasound Med Biol* **16**, 645-652 (1990).
- 2253 133 Saad, A. A., Loupas, T. & Shapiro, L. G. Computer Vision Approach for Ultrasound
2254 Doppler Angle Estimation. *Journal of Digital Imaging* **22**, 681-688 (2009).
- 2255 134 Lin, M. *et al.* A fully integrated wearable ultrasound system to monitor deep tissues in
2256 moving subjects. *Nature Biotechnology* **42**, 448-457 (2024).
- 2257 135 <https://www.fujifilm.com/de/en/healthcare/ultrasound/arietta/arietta-65/applications>.
- 2258 136 https://www.accessdata.fda.gov/cdrh_docs/pdf20/K202422.pdf.
- 2259 137 https://www.accessdata.fda.gov/cdrh_docs/pdf23/K232145.pdf.
- 2260 138 [https://marketing.webassets.siemens-
2261 healthineers.com/b2b416820d9a212a/a8185f7fda1a/ACUSON-Origin-Brochure.PDF](https://marketing.webassets.siemens-healthineers.com/b2b416820d9a212a/a8185f7fda1a/ACUSON-Origin-Brochure.PDF).
- 2262 139 <https://www.youtube.com/watch?v=-xQGlj5DaPE>.
- 2263 140 <https://echonous.com/kosmos-ai-ultrasound/>.
- 2264 141 <https://www.youtube.com/watch?v=JxDFp59R670>.
- 2265 142 https://www.accessdata.fda.gov/cdrh_docs/pdf23/K233826.pdf.
- 2266 143 Vincent, L. Morphological Area Openings and Closings for Grey-scale Images. **126**,
2267 197-208 (1994).
- 2268 144 Serra, J. & Vincent, L. An overview of morphological filtering. *Circuits, Systems and
2269 Signal Processing* **11**, 47-108 (1992).
- 2270 145 Ferrazzi, E. *et al.* Umbilical vein blood flow in growth-restricted fetuses. *Ultrasound in
2271 Obstetrics & Gynecology* **16**, 432-438 (2000).

- 2272 146 Ma, J. *et al.* Segment anything in medical images. *Nature Communications* **15**, 654
2273 (2024).
- 2274 147 So, H., Chen, J., Yiu, B. & Yu, A. Medical Ultrasound Imaging: To GPU or Not to GPU?
2275 *IEEE Micro* **31**, 54-65 (2011).
- 2276 148 Chang, L. W., Hsu, K. H. & Li, P. C. Graphics Processing Unit-Based High-Frame-Rate
2277 Color Doppler Ultrasound Processing. *IEEE Transactions on Ultrasonics, Ferroelectrics,*
2278 *and Frequency Control* **56**, 1856-1860 (2009).
- 2279 149 AIUM Practice Parameter for the Performance of Standard Diagnostic Obstetric
2280 Ultrasound. *Journal of Ultrasound in Medicine* **43**, E20-E32 (2024).
- 2281 150 Wang, X., Yang, Y.-Q., Cai, S., Li, J.-C. & Wang, H.-Y. Deep-learning-based sampling
2282 position selection on color Doppler sonography images during renal artery ultrasound
2283 scanning. *Scientific Reports* **14**, 11768 (2024).
- 2284 151 Ronneberger, O., Fischer, P. & Brox, T. U-Net: Convolutional Networks for Biomedical
2285 Image Segmentation. in *Medical Image Computing and Computer-Assisted Intervention.*
2286 234-241 (2015).
- 2287 152 Shi, X. *et al.* Convolutional LSTM Network: A Machine Learning Approach for
2288 Precipitation Nowcasting. in *Advances in Neural Information Processing Systems.* **28**,
2289 802-810 (2015).
- 2290 153 Oates, C. *Ultrasound Technology for Clinical Practitioners.* (Wiley, 2023).
- 2291 154 Balkawade, N. U. & Shinde, M. A. Study of Length of Umbilical Cord and Fetal
2292 Outcome: A Study of 1,000 Deliveries. *The Journal of Obstetrics and Gynecology of*
2293 *India* **62**, 520-525 (2012).
- 2294 155 Dunmire, B., Beach, K. W., Labs, K. H., Plett, M. & Strandness, D. E. Cross-beam vector
2295 Doppler ultrasound for angle-independent velocity measurements. *Ultrasound in*
2296 *Medicine & Biology* **26**, 1213-1235 (2000).
- 2297 156 Hartley, C. J., Reddy, A. K., Madala, S., Entman, M. L. & Taffet, G. E. Feasibility of
2298 Dual Doppler Velocity Measurements to Estimate Volume Pulsations of an Arterial
2299 Segment. *Ultrasound in Medicine & Biology* **36**, 1169-1175 (2010).
- 2300 157 Wang, Z. *et al.* Noninvasive Method for Measuring Local Pulse Wave Velocity by Dual
2301 Pulse Wave Doppler: In Vitro and In Vivo Studies. *PLOS ONE* **10**, e0120482 (2015).
- 2302 158 Peronneau, P., Bournat, J., Bugnon, A., Barbet, A. & Xhaard, M. Theoretical and
2303 practical aspects of pulsed Doppler flowmetry: real-time application to the measure of
2304 instantaneous velocity profiles in vitro and in vivo. *Cardiovascular applications of*
2305 *ultrasound* **1**, 66 (1974).
- 2306 159 Peronneau, P., Sandman, W. & Xhaard, M. Blood flow patterns in large arteries.
2307 *Ultrasound in medicine* **3**, 1193-1208 (1977).
- 2308 160 Papadofrangakis, E., Engeler, W. E. & Fakiris, J. A. Measurement of true blood velocity
2309 by an ultrasound system. *The Journal of the Acoustical Society of America* **75**, 1034-1034
2310 (1984).
- 2311 161 Phillips, P. J., Kadi, A. P. & von Ramm, O. T. Feasibility study for a two-dimensional
2312 diagnostic ultrasound velocity mapping system. *Ultrasound in Medicine & Biology* **21**,
2313 217-229 (1995).
- 2314 162 Pilz, N. *et al.* Pulse wave velocity: methodology, clinical applications, and interplay with
2315 heart rate variability. *Reviews in Cardiovascular Medicine* **25**, 266 (2024).

- 2316 163 Spencer, J. A., Price, J. & Lee, A. Influence of fetal breathing and movements on
2317 variability of umbilical Doppler indices using different numbers of waveforms. *Journal*
2318 *of Ultrasound in Medicine* **10**, 37-41 (1991).
- 2319 164 Stroux, L., Redman, C. W., Georgieva, A., Payne, S. J. & Clifford, G. D. Doppler-based
2320 fetal heart rate analysis markers for the detection of early intrauterine growth restriction.
2321 *Acta Obstet Gynecol Scand* **96**, 1322-1329 (2017).
- 2322 165 Pildner Von Steinburg, S. *et al.* What is the “normal” fetal heart rate? *PeerJ* **1**, e82
2323 (2013).
- 2324 166 Oros, D. *et al.* Reference ranges for Doppler indices of umbilical and fetal middle
2325 cerebral arteries and cerebroplacental ratio: systematic review. *Ultrasound in Obstetrics*
2326 *& Gynecology* **53**, 454-464 (2019).
- 2327 167 Zohav, E. *et al.* Third-trimester Reference Ranges for Cerebroplacental Ratio, Middle
2328 Cerebral Artery, and Umbilical Artery Pulsatility Index in Normal-growth Singleton
2329 Fetuses in the Israeli Population. *Rambam Maimonides Medical Journal* **10**, e0025
2330 (2019).
- 2331 168 Khandre, V., Potdar, J. & Keerti, A. Preterm Birth: An Overview. *Cureus* **14**, e33006
2332 (2022).
- 2333 169 Deng, Y., Rouze, N. C., Palmeri, M. L. & Nightingale, K. R. Ultrasonic Shear Wave
2334 Elasticity Imaging Sequencing and Data Processing Using a Verasonics Research
2335 Scanner. *IEEE Transactions on Ultrasonics, Ferroelectrics, and Frequency Control* **64**,
2336 164-176 (2017).
- 2337 170 Yu, J., Yoon, H., Khalifa, Y. M. & Emelianov, S. Y. Design of a Volumetric Imaging
2338 Sequence Using a Vantage-256 Ultrasound Research Platform Multiplexed With a 1024-
2339 Element Fully Sampled Matrix Array. *IEEE Transactions on Ultrasonics, Ferroelectrics,*
2340 *and Frequency Control* **67**, 248-257 (2020).
- 2341 171 Conroy, B. *et al.* Real-time infection prediction with wearable physiological monitoring
2342 and AI to aid military workforce readiness during COVID-19. *Scientific Reports* **12**, 3797
2343 (2022).
- 2344 172 Uwakwe, C. K. *et al.* Longitudinal wearable sensor data enhance precision of Long
2345 COVID detection. *PLOS Digit Health* **4**, e0001093 (2025).
- 2346 173 Subramaniam, S., Faisal, A. I. & Deen, M. J. Wearable Sensor Systems for Fall Risk
2347 Assessment: A Review. *Frontiers in Digital Health* **4**, 921506 (2022).
- 2348 174 Georgieva, A., Abry, P., Nunes, I. & Frasch, M. G. Editorial: Fetal-maternal monitoring
2349 in the age of artificial intelligence and computer-aided decision support: A
2350 multidisciplinary perspective. *Frontiers in Pediatrics* **10**, 2296-2360 (2022).
- 2351 175 Xu, S., Kim, J., Walter, J. R., Ghaffari, R. & Rogers, J. A. Translational gaps and
2352 opportunities for medical wearables in digital health. *Science Translational Medicine* **14**,
2353 eabn6036 (2022).
- 2354 176 Demi, L. Practical Guide to Ultrasound Beam Forming: Beam Pattern and Image
2355 Reconstruction Analysis. *Applied Sciences* **8**, 1544 (2018).
- 2356 177 Chen, C. & Pertijs, M. A. P. Integrated Transceivers for Emerging Medical Ultrasound
2357 Imaging Devices: A Review. *IEEE Open Journal of the Solid-State Circuits Society* **1**,
2358 104-114 (2021).
- 2359 178 Zhang, Y. & Demosthenous, A. Integrated Circuits for Medical Ultrasound Applications:
2360 Imaging and Beyond. *IEEE Transactions on Biomedical Circuits and Systems* **15**, 838-
2361 858 (2021).

- 2362 179 Rodrigues, C. S., Hasenclever, L. & Shimoda, E. The Technological Evolution of Fetal
2363 Monitoring in Pregnancy Care. *Journal Health and Technology* **1**, e1421 (2022).
- 2364 180 Kahankova, R. *et al.* Pregnancy in the time of COVID-19: towards Fetal monitoring 4.0.
2365 *BMC Pregnancy and Childbirth* **23**, 33 (2023).
- 2366 181 Browne, J. E. A review of Doppler ultrasound quality assurance protocols and test
2367 devices. *Physica Medica* **30**, 742-751 (2014).
- 2368 182 <https://www.cirsinc.com/wp-content/uploads/2020/07/769DF-DS-072220.pdf>.
- 2369 183 Calvert, J. & Duck, F. Self-heating of Diagnostic Ultrasound Transducers in Air and in
2370 Contact with Tissue Mimics. *Ultrasound* **14**, 100-108 (2006).
- 2371 184 Hadlock, F. P., Harrist, R. B., Sharman, R. S., Deter, R. L. & Park, S. K. Estimation of
2372 fetal weight with the use of head, body, and femur measurements--a prospective study.
2373 *Am J Obstet Gynecol* **151**, 333-337 (1985).
- 2374